APPLIED COMPUTATIONAL ELECTROMAGNETICS SOCIETY JOURNAL

January 2026
Vol. 41 No. 01
ISSN 1054-4887

The ACES Journal is abstracted in INSPEC, in Engineering Index, DTIC, Science Citation Index Expanded, the Research Alert, and to Current Contents/Engineering, Computing & Technology.

The illustrations on the front cover have been obtained from the ARC research group at the Department of Electrical Engineering, Colorado School of Mines

Published, sold and distributed by: River Publishers, Broagervej 10, 9260 Gistrup, Denmark

JANUARY 2026 REVIEWERS

Ali Al-Azza
Alireza Baghai-Wadji
Dinesh Kumar Reddy Basani
Cai Di
Junbing Duan
Cihan Dogusgen Erbas
Naixing Feng
Srilakshmi Inuganti
Lukasz Knypinski
Mikko Kokkonen
Jake Liu
Xingnan Liu
Andrew Peterson
Manthan Shah
Elisabetta Sieni
Varun Singh
Somchat Sonasang
Waldemar Susek
Nguyen Van Thieu
Seyed Sina Vaezi
Yi Wang
Steven Weiss
Julia Wolff
Mingwen Zhang
Xuemei Zheng

THE APPLIED COMPUTATIONAL ELECTROMAGNETICS SOCIETY JOURNAL

Vol. 41 No. 01 January 2026

TABLE OF CONTENTS

Multi-Objective Optimization of a Rectangular Structured Linear Actuator Based on Taguchi Method

Muhammad Jawad[1], Haitao Yu[1], Fariba Farrokh[2], and Zahoor Ahmad[3]

[1]School of Electrical Engineering
Southeast University, Nanjing, Jiangsu 210096, China
m.jawad35@yahoo.com, htyu@seu.edu.cn

[2]Faculty of Electrical Engineering
Shahid Beheshti University Tehran, Iran
f_farrokh@sbu.ac.ir

[3]Department of Electrical Power Engineering and Mechatronics
Tallinn University of Technology, Tallinn 19086, Estonia
zahoor.ahmad@taltech.ee

Abstract – This paper introduces an innovative rectangular structured Linear Oscillating Machine (LOM) featuring an innovative arrangement of permanent magnets (PMs) which are positioned on the mover. A sinusoidal magnet arrangement (SMA) is chosen to minimize PM materials while ensuring the performance parameter, in terms of electromagnetic force, remains unaffected. The focus of the design is to reduce the cogging force and enhance the electromagnetic force to the PM mass ratio. The optimization is accomplished by utilizing design-of-experiment (DOE) Taguchi method optimization for a linear actuator, along with the finite element method (FEM). A multi-objective optimization approach is employed to refine the parameters of the linear actuator, focusing on the maximum force, the force-to-PM-weight ratio, and minimizing cogging force. By identifying the most effective parameters, an appropriate case with high sensitivity and accuracy is selected. The output parameters, like electromagnetic force and stroke of the proposed optimization approach, score very well, while the design is simply structured due to the utilization of a rectangular structured core part. The proposed design significantly reduces the cogging force to an exceptionally low level, enhancing performance and reliability.

Index Terms – Cogging force reduction, sinusoidal magnet arrangement, Taguchi method of optimization.

I. INTRODUCTION

The Linear Oscillating Machine (LOM) offers an innovative solution for enabling pistons to move back and forth along a single axis without the complexity of screws, gears, or crankshafts. By producing linear oscillatory motion directly within the piston, LOM streamlines the mechanism and eliminates the need for converting rotary motion into linear oscillation. This makes LOM a highly effective alternative for applications that traditionally utilize rotary motors, enhancing efficiency and reducing mechanical complexity [1–6]. The advantages of LOA include a higher oscillation frequency, reduced power consumption, and lower fabrication costs. LOM performs optimally when operated at its resonance frequency, where the excitation frequency aligns perfectly with the mechanical resonance frequency. Under resonance conditions, the armature requires minimal electrical current, which reduces input power while maintaining the same output power, thereby enhancing the system's efficiency [7–9].

Cogging force plays an essential role in the design of conventional PM linear motors. As a result, many innovative methods have been introduced to enhance the accuracy and speed of detent force calculations. These advancements contribute significantly to the optimization of motor performance [10]. The first optimized linear actuator [11] was developed by utilizing design-of-experiment (DOE) and response surface method (RSM) techniques. This approach helps verify the effectiveness of the initial design and enhances its performance characteristics, including output power and compactness. Following this [12], space mapping, manifold mapping, and optimization were implemented for linear actuators. While a Maxwell stress tensor analysis has been applied to the linear actuator, it tends to increase calculation time due to the complexity and nonlinearity of the equations involved [13]. The Taguchi method has been established as the most effective optimization technique

Submitted On: August 21, 2025
Accepted On: January 14, 2026

https://doi.org/10.13052/2026.ACES.J.410101

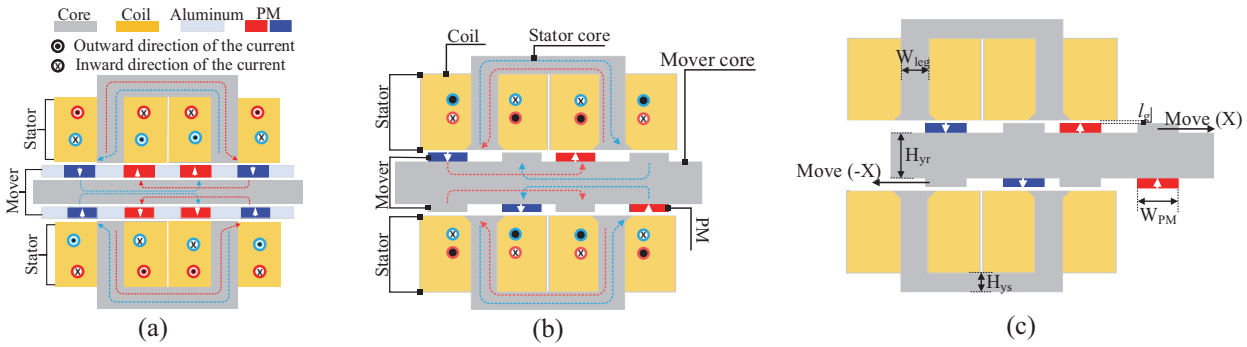

Fig. 1. Topology of the linear actuator: (a) conventional design of the actuator [2], (b) proposed SMA design of the actuator, and (c) optimization parameters of the proposed SMA design of the actuator.

for assessing influential parameters. Research has shown that multi-objective optimization can efficiently identify the key factors affecting electric machines in a short amount of time [14–16]. The inductance-based analytical model in [17] highlights the importance of accurate field prediction in PM linear machines.

Recent research has shown that the Taguchi DOE method is an efficient and reliable tool for optimizing electromagnetic devices with multiple interacting parameters [18]. Reference [19] employed a comprehensive Taguchi-based framework to optimize a coaxial magnetic coupling, demonstrating its ability to reduce computational effort while accurately identifying dominant design variables. Likewise, [19] applied the Taguchi method to optimize an outer-rotor double-PM flux-switching generator, validating the optimized design experimentally and confirming the method's effectiveness in multi-objective performance improvement. Together, these works highlight the suitability of the Taguchi approach for systematic and statistically grounded optimization of complex electrical machine structures.

The main purpose of this paper is to design an optimized linear actuator. The focus is on reducing costs and enhancing the electromagnetic performance of the linear actuator, making it suitable for implementation in conventional actuator structures. The key contributions of this paper include a novel topology that introduces a sinusoidal magnet arrangement (SMA) in the mover for the first time. A new technique of optimization is adopted to optimize the performance. This technique aims to achieve multi-objective optimization, addressing factors such as maximum force, improving the force-to-permanent magnet weight ratio, and minimizing cogging force, all using the Taguchi method. The highlights of this paper are:

(1) The proposal features a linear actuator with an SMA, focusing on low cost and minimum PM material utilization.
(2) DOE optimization utilizing the Taguchi method identifies influential parameters efficiently.
(3) The optimization process adopts a multi-objective approach for a comprehensive outcome.

II. DESIGN AND OPERATING PRINCIPLE

Figure 1 (a) presents a benchmark mark design of the proposed SMA design of the actuator, included to illustrate its significance. The proposed SMA design of the actuator shown in Fig. 1 (b) delivers an identical electromagnetic force while utilizing 50% of the PM materials.

The investigated SMA design includes a C-shaped stator core with a rectangular structure. Coils are wound around both legs of the C-shaped stator core as shown in Figs. 1 (b) and (c). The currents in the coils are arranged to flow in opposite directions, causing the magnetic flux to combine and enter the rotor core. This setup is also adopted for the coils of another stator. The mover is composed of core materials and PMs, which are placed in a sinusoidal pattern. The design parameters are clearly outlined in Table 1.

Table 1: Parameters of the linear actuator

Parameter	**Initial Value**	**Optimized Value**
Height of the actuator [mm]	100	102
Depth of the actuator [mm]	120	
Rotor yoke height [mm]	16	
PM length [mm]	4	3.8
PM width (W_{PM}) [mm]	15	14
Stator yoke height (H_{ys}) [mm]	7	8
Height of the pole shoe [mm]	4	
Length of the pole shoe [mm]	4	
Air gap (l_g) [mm]	1	1.2
Coil width [mm]	20	
Coil height [mm]	30	
Stator leg [mm]	10	

The proposed SMA design operates using single-phase alternating current (AC). During one half-cycle of the AC, the mover adjusts its position to one extreme, providing the least reluctant path for the magnetic flux. During the remaining half cycle of the AC, the mover shifts to the opposite extreme. By maintaining a continuous supply of AC, the mover experiences a linear oscillatory electromagnetic force.

III. MULTI-OBJECTIVE DOE/OPTIMIZATION METHOD

The Taguchi method, a DOE technique, is here applied for the first time to identify effective parameters in linear actuator characteristics. Known for its effectiveness in optimizing electrical machines, the method uses fractional factorial experiments arranged in an "Orthogonal Array." This structure ensures an even distribution of parameter levels across columns and symmetrical combinations for each pair of columns. While the Taguchi method yields optimization results, they may not always be optimal. Increasing the levels of each variable can improve accuracy, but it can also be inefficient and time-consuming. The main goal of this approach is to pinpoint the effective parameters. To comprehensively evaluate the optimization effect of the linear actuator, the overall process is divided into three levels. The structural parameters of both the stator and rotor (shown in Fig. 2) are optimized independently using an improved iterative Taguchi method combined with sensitivity analysis, as illustrated in Fig. 2.

As clearly illustrated in Fig. 2, the optimization procedure is generally carried out in three main stages. The proposed optimization framework integrates the Taguchi method with sensitivity analysis. The primary objective is to systematically identify the influential parameters and evaluate their effects step by step, ensuring a purposeful and targeted optimization process.

In the first stage, the goal is to optimize the geometric dimensions based on three main performance criteria: maximum force, maximum force-to-magnet-weight ratio, and cogging force. Five geometric parameters were examined in this phase, and only the Taguchi method was employed.

The second stage aims to determine the optimal rotor position for start-up. In this phase, the Taguchi method was again applied to optimize two objectives (maximum force and cogging force) at two different magnet positions. By the end of this stage, both the geometry and the rotor position were optimized using the minimum required amount of magnet material.

In the final stage, the position of the second stator was relevant only to the two objectives from the second stage. Sensitivity analysis was therefore used to evaluate and optimize this parameter. The detailed step-by-step implementation of the proposed methodology is comprehensively described in the following section.

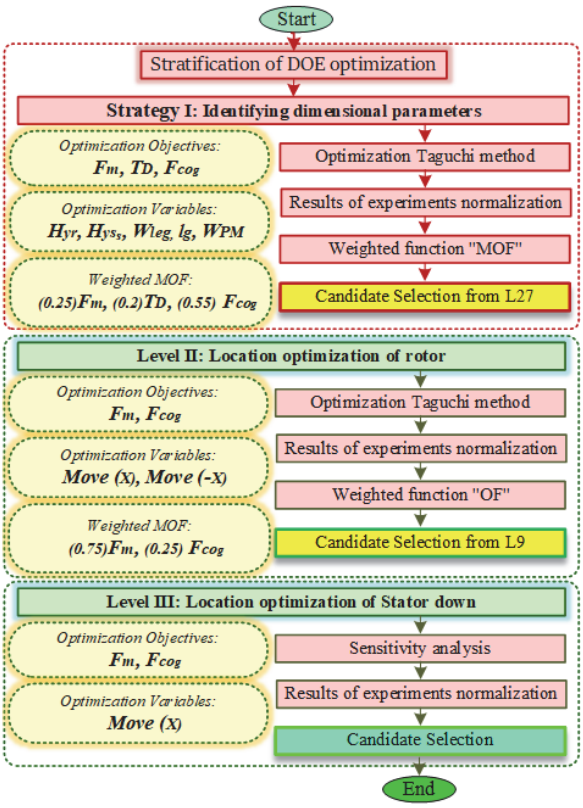

Fig. 2. Flowchart of multi-objective stratification of DOE optimization.

A. Layer I: Optimization of geometric parameters

To improve the working stability of the linear actuator, the maximum force, the force-to-permanent PM weight ratio, and minimizing cogging force are selected as the primary optimization objectives.

Figure 1 (c) shows the parameter model of the linear actuator model, and Table 2 shows the variation range of the design parameters according to the design experience and geometrical limits. The specific values for rotor yoke height (H_{yr}), stator yoke height (H_{ys}), stator leg (W_{leg}), length of the air-gap (l_{ag}), and PM width (W_{PM}) are provided in Table 2. Three levels are considered for each variable, by selecting eight variables at three levels, the Orthogonal Array L27 is established, requiring the performance of 27 experiments. In this paper only five experiments are shown due to space constraint. The corresponding results are analyzed through the finite element method (FEM). The mean effect of various variables on the optimization responses has been assessed. Specifically, the average impact of the selected variables on the optimization responses including maximum force (F_{max}), force-to-PM-weight ratio (T_D), and

Table 2: Combinations of variables using the Taguchi method of optimization

Exp.	H_{yr} (mm)	H_{ys} (mm)	W_{leg} (mm)	l_{ag} (mm)	W_{PM} (mm)	F_m (N)	T_D (N/Kg)	F_{cog} (N)	OF
1	14	7	10	0.8	14	0.94	0.75	0.81	0.83
2	14	7	10	0.8	15	0.88	0.66	0.78	0.788
3	14	7	10	0.8	16	0.87	0.61	0.81	0.785
4	14	8	11	1	14	0.917	0.66	0.66	0.72
5	14	8	11	1	15	0.983	0.765	0.561	0.707
6	14	8	11	1	16	0.956	0.692	0.598	0.706
7	14	9	12	1.2	14	0.844	0.739	0.779	0.787
8	14	9	12	1.2	15	0.883	0.713	0.776	0.79
9	14	9	12	1.2	16	0.870	0.652	0.778	0.775
10	15	7	11	1.2	14	0.812	0.775	0.782	0.789
11	15	7	11	1.2	15	0.797	0.728	0.758	0.762
12	15	7	11	1.2	16	0.806	0.677	0.771	0.761
13	15	8	12	0.8	14	0.999	0.875	0.575	0.741
14	15	8	12	0.8	15	0.999	0.807	0.437	0.652
15	15	8	12	0.8	16	0.999	0.777	0.503	0.682
16	15	9	10	1	14	0.905	0.826	0.914	0.894
17	15	9	10	1	15	0.879	0.769	0.895	0.866
18	15	9	10	1	16	0.841	0.679	0.880	0.83
19	16	7	12	1	14	0.675	0.709	0.971	0.845
20	16	7	12	1	15	0.679	0.648	0.946	0.82
21	16	7	12	1	16	0.692	0.632	0.951	0.823
22	16	8	10	1.2	14	0.794	0.878	0.998	0.923
23	16	8	10	1.2	15	0.780	0.780	1	0.901
24	16	8	10	1.2	16	0.767	0.732	0.998	0.887

cogging force (F_{cog}) has been analyzed and illustrated in Fig. 3. Using the S/N ratio, the impact of each experiment's parameters has been measured. Based on the optimization goal, S/N ratios are calculated as:

$$\frac{S}{N} = -\log\left(\sum_{i=1}^{n}\frac{\frac{1}{Y_i^2}}{n}\right), \tag{1}$$

where n is the number of repeats in each scenario and Y_i is the output of the scenario in ith repetition. In this study, larger is better is specified as SN quality for four object optimizations to analyze the impact of maximum force, the force-to-PM-weight ratio, and minimizing cogging force. Simultaneously, it is aimed to select the one optimal level from three available options. The results of each experiment have been normalized according to:

$$Output_{nor_1} = \frac{|output - best\ output|}{best\ output}, \tag{2}$$

$$Output_{nor_2} = |output_{nor_1} - 1| + (output_{nor_1})_{max}, \tag{3}$$

$$MOF_1 = 0.25F_m + 0.2T_D + 0.55F_{cog}. \tag{4}$$

MOF is defined as the multi-objective function, computed from normalized and weighted values of maximum electromagnetic force, cogging force, and force-to-PM-weight ratio. In a linear actuator, predicting the cogging force is essential. The cogging force is assigned a weight of 0.55, as indicated in equation (4). Next, the maximum force is prioritized with a weight of 0.25. Finally, the force-to-PM-weight ratio is given a weight of 0.2. All metrics are normalized for optimization purposes.

In this regard, Table 2 includes all the experiments. The parameter limits are as follows:

$$\begin{cases} 14 < \text{Hyr} < 16 \\ 7 < \text{Hys} < 8 \\ 10 < \text{W}_{leg} < 12 \\ 0.8 < \text{l}_{ag} < 1.2 \\ 14 < W_{PM} < 16 \end{cases}.$$

Table 2 displays five chosen experiments to optimize manuscript space, highlighting the normalized results for the targeted parameters. Exp. 22, which incorporates at least four parameters ($H_{yr}, W_{leg}, l_g, W_{PM}$) produced the most favorable outcomes. Following this, Exps. 23 and 24 showed improved results with at least three parameters (H_{yr}, W_{leg}, l_g). Therefore, among the 27

experiments derived from Taguchi optimization, Exp. 22 has been selected as the Layer I optimization model.

Figure 3 (a) shows the force for two linear actuators. The maximum force achieved is approximately 794.77 N for the optimized SMA model 1 and 793.52 N for the initial SMA model. Typically, optimizations aimed at reducing cogging result in a decrease in force or torque in machines. However, through multi-objective optimization and the identification of sensitive parameters, the optimal model was chosen to maintain force levels without any reduction. Figure 3 (b) illustrates the cogging force for the two models. The initial SMA model has a cogging force of 395.82 N, while the optimized SMA model 1 has a cogging force of 183.86 N. This means that the optimized SMA model exhibits a 53.5% reduction in cogging force when the winding current is zero.

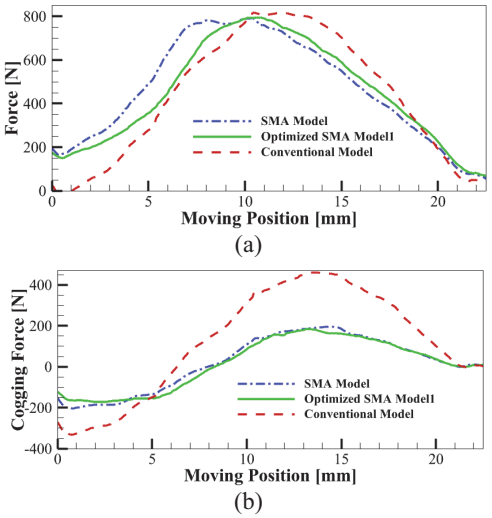

Fig. 3. The force and cogging force of the conventional and SMA actuators after optimization. Layer I: (a) electromagnetic force and (b) cogging force.

B. Layer II: Location optimization of mover

Optimization is continued in Layer II due to the substantial cogging force achieved in the first layer. In this phase, one of the optimization objectives, specifically, the ratio of maximum force to PM weight, has been removed because the geometric parameters in the first layer have already been optimized. Instead, the focus is on optimizing the positions of the upper and lower PMs and the rotor teeth relative to one another. This is done using the Taguchi method to identify their most effective arrangements.

As a result, the optimization objectives in this layer, the targeted parameters are maximum force and minimum cogging force. To facilitate this, L9 orthogonal experiments have been conducted, employing two displacement factors for the upper and lower PMs as well as the rotor teeth. Table 3 illustrates the normalized results of these objectives.

Table 3: Variable combination according to mover's position

Exp.	Move (X) (mm)	Move (-X) (mm)	F_m (N)	F_{cog} (N)	OF
1	1	−1	0.99	0.26	0.807
2	1	−2	0.988	0.4	0.841
3	1	−3	0.973	0.52	0.861
4	2	−1	0.99	0.39	0.84
5	2	−2	0.983	0.54	0.873
6	2	−3	0.953	0.657	0.879
7	3	−1	1	0.633	0.908
8	3	−2	0.981	0.808	0.938
9	3	−3	0.892	1	0.919

The maximum force is assigned to a weight of 0.75, while the cogging force is assigned a weight of 0.25. All metrics are normalized for optimization purposes. Table 3 illustrates the normalized targets for each parameter. Exp. 8, which incorporates at least two parameters, produced the most favorable outcomes. Following this,

Exp. 7 exhibited improved results in maximum force, while Exp. 9 showed enhancements in cogging torque. Therefore, among the nine experiments derived from Taguchi optimization, Exp. 8 has been selected as the optimization model for Layer II. The electromagnetic and cogging force responses of the proposed SMA topology after Layer II optimization are shown in Figs. 4 (a) and (b), respectively.

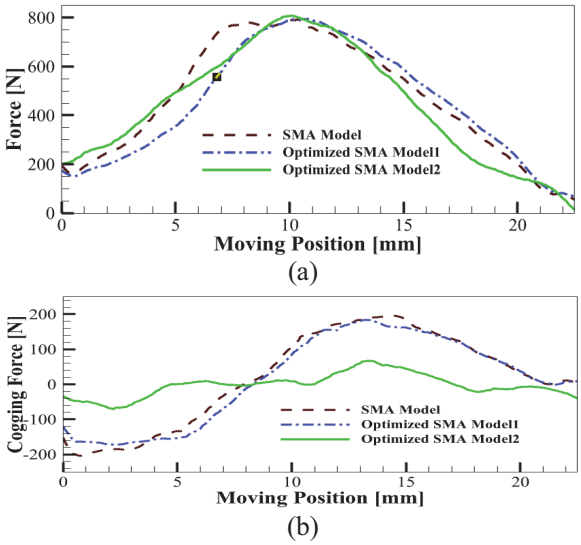

Fig. 4. The force and cogging force of the conventional and SMA actuators after optimization. Layer II: (a) EM force and (b) cogging force.

C. Layer III: Location optimization of stator down

In Layer III, the position of the stator below the actuator, which has two stators and one central mover, significantly affects the optimization objectives. To address this, a sensitivity analysis is conducted at three different optimization levels, focusing on two objectives: maximum force and cogging force. The normalized results of this analysis are presented in Table 4. The results in Table 4 indicate that optimization was achieved in the third layer, positioning the two goals correctly.

Table 4: Variable combination according to the lower stator position relative to the upper stator

Exp.	Move (X) (mm)	F_m (N)	F_{cog} (N)
1	**1**	**1**	**1.081**
2	**2**	**0.921**	**1**
3	**3**	**0.871**	**0.628**

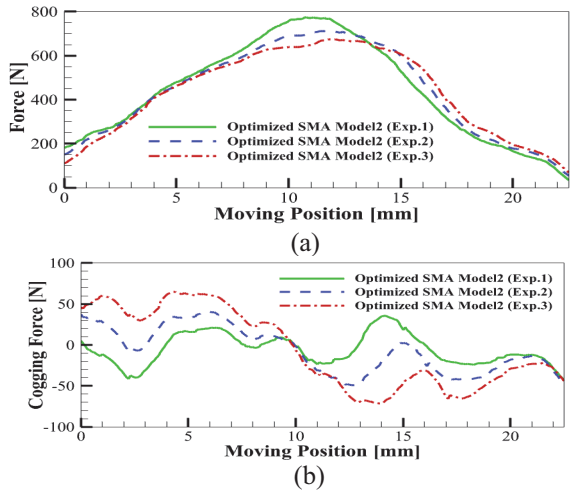

Fig. 5. The force and cogging force of the conventional and SMA actuators after optimization. Layer III: (a) EM force and (b) cogging force.

The results of the last Layer III optimization are presented in Fig. 5. Exp. 1 has much better results than the other two experiments. In the three sensitivity analyses, Exp. 1 demonstrated the highest force and the lowest cogging force, which is why it has been selected as the final model.

D. Summary of the proposed DOE optimization

The normalized results for the targets are summarized in this section. Exp. 22, which incorporates at least four parameters ($H_{yr}, W_{leg}, l_g, W_{PM}$) yielded the most favorable outcomes in Layer I. In Layer II, Exp. 8 demonstrated improved results with at least two parameters: *Mover (x)* and *Mover (-x)*. Consequently, among the 27 experiments in Layer I and the nine experiments in Layer II derived from Taguchi optimization, Exp. 1 has been selected as the final optimization model in Layer III.

IV. FEM SIMULATION AND RESULTS OF THE OPTIMIZED SMA TOPOLOGY

A. FEM model setup and meshing strategy

The proposed model is developed using ANSYS Maxwell, while the optimization process is performed in Minitab. A two-dimensional FEM model of the target actuator is first established in Maxwell to obtain the initial geometric dimensions for preliminary design. The linear motion of the rotor is defined using the motion setup module. An adaptive finite-element meshing strategy is employed to ensure numerical accuracy and convergence, with local mesh refinement applied to critical regions such as the air gap which passes the permanent magnets (PMs), rotor edges, and areas with high magnetic field gradients. In particular, the air-gap region is discretized with a significantly finer mesh to accurately capture flux-density variations and electromagnetic flux during linear motion.

Mesh quality is controlled by limiting element aspect ratios and enforcing minimum element sizes in sensitive regions. A mesh convergence study is conducted to verify that further refinement does not significantly affect key electromagnetic quantities, including flux density, force, and induced voltage.

The initial actuator dimensions and multi-objective optimization goals are processed in Minitab using a multi-stage Taguchi-based DOE approach. Sensitivity analyses identify the most influential parameters at each optimization stage, and these parameters are directly applied to the Maxwell FEM model. Consequently, an effective multi-stage and multi-objective optimization is achieved, and the corresponding FEM simulation results are presented in sections B and C.

B. Flux density distribution and field analysis

The flux density and flux lines of the proposed SMA topology is illustrated in Figs. 6 (a) and (b). The FEM results indicate that the optimized SMA linear actuator does not experience significant magnetic saturation. According to the basic operating principle of a linear actuator, the mover moves to a position where the magnetic flux forms a complete closed path with minimal reluctance. From Fig. 6, the magnetic flux path is completed at extreme mover positions.

C. Electromagnetic and cogging force results

Figures 7 (a) and (b) show the EM force and cogging force of the conventional design of the actuator

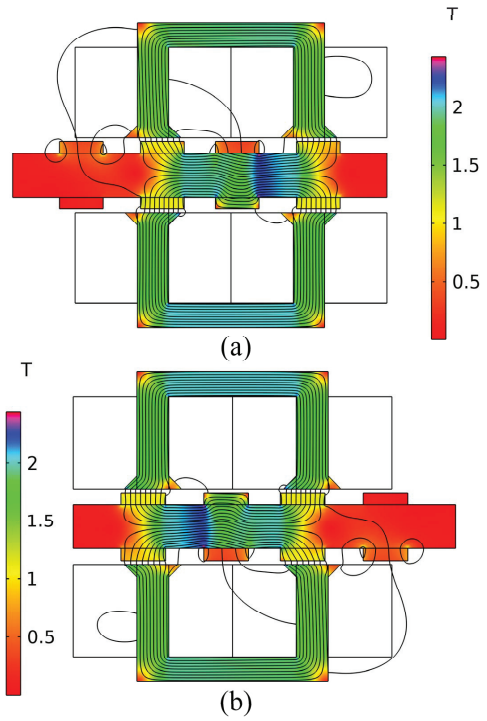

Fig. 6. Flux density distribution and flux lines for the SMA linear actuator at alternate extreme mover positions (a) left extreme mover position, (b) right extreme mover position.

and the proposed SMA actuators, respectively. In the optimized SMA model, the maximum force decreased by 2.53% compared to the initial model and by 5.39% compared to the conventional model. Additionally, the cogging force is reduced in the optimized SMA model, with a decrease of 82.06% compared to the initial model and 92.4% compared to the conventional model. Additionally, the proposed SMA design utilizes around 50% PM materials compared to the conventional design of the actuator.

V. CONCLUSION

The LOM's rectangular structure and sinusoidal arrangement have halved magnet costs compared to traditional designs. Using the Taguchi DOE optimization strategy, key parameters were targeted across three layers. The optimized LOM shows over 92.4% reduction in cogging force and 50% cost savings of the PMs due to comprehensive multi-objective optimization. In addition, the proposed design provides a concept of designing a rectangular topology, an alternative design concept to the conventional tubular topology. The main significance that can be achieved is the fabrication of a laminated core structure. Moreover, the cost of the

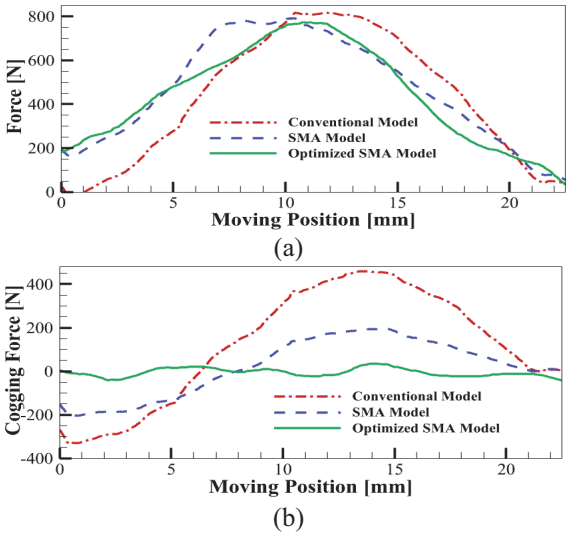

Fig. 7. Force and cogging force of the conventional, SMA, and optimized SMA actuators models. (a) Electromagnetic force and (b) cogging force.

rectangular PM is lower than that of the tubular PM. Furthermore, in the case of the rectangular PM, the desired dimension can be conveniently achieved by attaching numerous small PMs. The proposed SMA linear actuator is a structurally simple, low-cost, and produces feasible output parameters such as electromagnetic force and stroke.

This study has been validated through comprehensive FEM simulations; however, experimental verification has not yet been performed. As part of our future work, we plan to develop an analytical model based on a magnetic equivalent circuit (MEC) formulation to complement the FEM results. Furthermore, a prototype of the proposed linear actuator will be fabricated, and experimental measurements will be carried out to validate the analytical and numerical results.

ACKNOWLEDGEMENT

This work is supported by Haitao Yu.

REFERENCES

[1] A. Hassan, A. Bijanzad, and I. Lazoglu, "Dynamic analysis of a novel moving magnet linear actuator," *IEEE Transactions on Industrial Electronics*, vol. 64, no. 5, 2017.

[2] M. Jawad, H. Yu, Z. Ahmad, B. Ullah, and B. Alghamdi, "Design optimization and resonance analysis of rectangular structured moving magnet linear actuator," *IEEE Access*, vol. 11, 2023.

[3] S. Khalid, F. Khan, B. Ullah, Z. Ahmad, and S. Akbar, "Review of moving magnet linear oscillating actuators for linear compressor application," 2023.

[4] Z. Ahmad, B. Ullah, F. Khan, S. Ullah, and I. Sami, "Electromagnetic performance investigation of rectangular-structured linear actuator with end ferromagnetic poles," *Energies (Basel)*, vol. 16, no. 15, 2023.

[5] H. Zhang, Z. Xu, L. Jin, J. Leng, H. Yu, Z. Shen, B. Ye, and S, Fang, "Electromagnetic calculation of tubular permanent magnet linear oscillation actuator considering corrected air gap permeance," *IEEE Trans Magn*, vol. 59, no. 5, 2023.

[6] H. Zhang, "Detent force reduction design for the C-core single-phase permanent magnet linear oscillation actuator," in *IEEE Transactions on Industry Applications*, 2023.

[7] Z. Ahmad, A. Kallaste, T. Vaimann, and M. U. Sardar, "Design and resonance analysis of tubular structured dual stator linear oscillating actuator," in *2024 International Conference on Electrical Machines, ICEM 2024*, Institute of Electrical and Electronics Engineers Inc., 2024.

[8] S. Khalid, F. Khan, B. Ullah, Z. Ahmad, A. H. Milyani, and S. Alghamdi, "Electromagnetic and experimental analyses of a low-cost miniature tubular moving magnet linear oscillating actuator for miniature compressor applications," *IET Electr Power Appl*, vol. 17, no. 1, 2023.

[9] M. Jawad, Y. Haitao, Z. Ahmad, and Y. Liu, "Design and analysis of a novel linear oscillating actuator with dual stator rectangular geometry," *Appl Comput Electromagn Soc J*, vol. 36, no. 10, 2021.

[10] H. Zhang, "Electromagnetic design of single-phase permanent magnet linear oscillation actuator considering detent force minimum," *IEEE Trans Magn*, vol. 58, no. 8, 2022.

[11] D. J. Lee, K. S. Woo, N. C. Park, and Y. P. Park, "Design and optimization of a linear actuator for subminiature optical storage devices," *IEEE Trans Magn*, vol. 41, no. 2, 2005.

[12] D. Echeverría, D. Lahaye, L. Encica, E. A. Lomonova, P. W. Hemker, and A. J. A. Vandenput, "Manifold-mapping optimization applied to linear actuator design," *IEEE Trans Magn*, vol. 42, no. 4, 2006.

[13] J. Lee, E. M. Dede, D. Banerjee, and H. Iizuka, "Magnetic force enhancement in a linear actuator by air-gap magnetic field distribution optimization and design," *Finite Elements in Analysis and Design*, vol. 58, 2012.

[14] Z. Xing, X. Wang, W. Zhao, X. Li, L. Xiong, and X. Zhang, "Optimization design of interior permanent magnet synchronous motor with u-shaped rotor for low-level torque ripple and electromagnetic vibration," *IEEE Transactions on Transportation Electrification*, vol. 10, no. 1, 2024.

[15] Z. Shi, X. Sun, Y. Cai, and Z. Yang, "Robust design optimization of a five-phase PM hub motor for fault-tolerant operation based on taguchi method," *IEEE Transactions on Energy Conversion*, vol. 35, no. 4, 2020.

[16] J. He, G. Li, R. Zhou, and Q. Wang, "Optimization of permanent-magnet spherical motor based on Taguchi method," *IEEE Trans Magn*, vol. 56, no. 2, 2020

[17] E. Yucel, M. Mutluer, and M. Çunkaş, "Analysis and design of a permanent magnet linear synchronous motor based on inductance calculation," *Archives of Electrical Engineering*, vol. 74, no. 4, pp. 773–794, 2025.

[18] F. Farrokh, A. Ghaheri, and E. Afjei, "A comprehensive DOE-optimization method of coaxial magnetic coupling for aircraft applications," *2024 4th International Conference on Electrical Machines and Drives (ICEMD)*, Tehran, Iran, Islamic Republic of, pp. 1–6, 2024.

[19] M. Farahzadi, S. Ali, S. Mirnikjoo, K. Abbaszadeh, F. Marignetti, and M. Salehi, "Design and experimental validation of a new outer rotor double PM excited flux switching generator for direct drive wind turbines," in *IEEE Access*, vol. 12, pp. 62256–62267, 2024.

Muhammad Jawad was born in Pakistan in 1993. He received his Bachelor of Science degree in Electrical Engineering from UST Bannu in Khyber Pakhtunkhwa, Pakistan, in 2016. He subsequently pursued advanced studies at Southeast University in Nanjing, China, where he completed his master's degree in Electrical Engineering. Currently, he is engaged in doctoral research in Electrical Engineering at Southeast University. His research interests focus on the design of linear actuators.

Haitao Yu, Ph.D., professor, doctoral supervisor, and director of China Energy Society. He received his Ph.D. from Huazhong University of Science and Technology (HUST), China, in 1995. In 1997, he served as an associate professor in the School of Electric Engineering, and 1998–2003 he took part in academic exchange visits to Duke University and Canada. He served as editor of special issue "Ocean Power Generation" in *Advances in Mechanical Engineering* (SCI) and is a reviewer of various IEEE journals.

Fariba Farrokh (Student Senior Member, IEEE) received B.Sc. and M.Sc. degrees in electrical engineering in 2012 and 2014, respectively, and Ph.D. degree in electrical power engineering from Shahrood University of Technology, Shahrood, Iran, in 2024. She is currently with the Faculty of Electrical Engineering at Shahid Beheshti University, Tehran. Her research interests include electrical machine design and optimization, analytical and multi-physics modeling, demagnetization analysis, and development of high-performance permanent magnet machines for electric vehicles, renewable energy systems, and aerospace applications. Farrokh is a Student Senior Member of the IEEE, and has received several research awards, including Best Paper Presentation Award at ICEMD 2024 and Global Research Award 2025.

Zahoor Ahmad (Student Member, IEEE) was born in Khyber Pakhtunkhwa, Pakistan, in 1993. He received a B.S. degree in Electrical Engineering from the University of Science and Technology, Bannu, Khyber Pakhtunkhwa, in 2016 and an M.S. degree in Electrical Engineering from COMSATS University Islamabad at Abbottabad, Pakistan, in 2020. During his M.S. degree program, he worked on the Design and Analysis of Moving Magnet Linear Oscillating Actuators. Currently, he is pursuing a Ph.D. at Tallinn University of Technology, Department of Electrical Power Engineering and Mechatronics. His research interests include Advanced Design Methodology for Additively Manufactured Electrical Machines.

Synthesis of Thinned Linear and Planar Antenna Arrays Using a Taguchi-Enhanced Binary Gold Rush Optimizer

Weibin Kong[1,2], Yiming Zong[1], Lei Wang[1], Wenwen Yang[3], Botong Liu[1], Binghe Sun[4], and Feng Zhou[1]

[1]College of Information Engineering
Yancheng Institute of Technology, Jiangsu Yancheng 224051, China
kongweibin@ycit.cn, 949650915@qq.com, wanglei_ntu@outlook.com,
liubot@ycit.edu.cn, zfycit@163.com

[2]Jiangsu Provincial Engineering Technology Center
Multimodal Perception and Intelligent Control of Offshore Wind Power Systems,
Yancheng 224051, China

[3]School of Science and Technology
Nantong University, Nantong 226019, China
wwyang2008@hotmail.com

[4]Jiangsu Bomin Electronics Co. Ltd, Yancheng 224100, China
bh_sun@bominelec.com

Abstract – In this paper, a Taguchi-enhanced binary gold rush optimizer (TEBGRO) is proposed for designing thinned antenna arrays with a low peak sidelobe level (PSLL). The method integrates the Taguchi orthogonal experimental design into the population initialization phase, generating high-quality initial populations to improve convergence speed and stability. By combining a differential mutation interference factor and a time-varying transfer function, the algorithm further balances global exploration and local exploitation capabilities. Experimental results show that TEBGRO outperforms other binary optimization algorithms for both 100-element linear arrays and 20×10 planar arrays.

Index Terms – Antenna radiation pattern, gold rush optimizer (GRO), thinned array, Taguchi method.

I. INTRODUCTION

Offering advantages such as high signal gain, strong anti-interference capability, and flexible design, antenna arrays are widely used in wireless communication, phased array radar, aerospace, and other fields [1, 2]. Thinned arrays, as compared to traditional uniform arrays, achieve smaller size and weight by selectively removing (or deactivating) certain elements, thereby reducing system costs, power consumption, and complexity of the feeding network. However, the thinning process often results in a decrease in antenna gain and an increase in peak sidelobe levels (PSLL). Thus, the optimization challenge lies in reducing the number of array elements while simultaneously decreasing PSLL.

The thinning of large-scale antenna arrays is a high-dimensional, discrete, non-linear, and non-convex problem. Over the past few decades, numerous methodologies have been proposed to reduce the number of array elements while preserving desired radiation characteristics. To this end, researchers have developed a diverse array of optimization techniques, broadly categorized into two primary classes: deterministic methods and meta-heuristic methods.While deterministic methods like the Iterative Fourier Transform (IFT) are efficient, they are prone to local optima. Meta-heuristic algorithms offer global search capabilities but often face challenges such as reliance on empirical parameter tuning and premature convergence.

To address these limitations,this paper proposes a Taguchi-enhanced binary gold rush optimizer (TEBGRO). Through three enhancement strategies, this approach improves optimization performance for thinning antenna arrays. First, the systematic reasoning capability of the Taguchi method is integrated during population initialization to generate highly representative and uniformly distributed initial solution sets. Second, the time-varying transfer function enables both the mapping of continuous values to discrete states in binary optimization and the balancing of global search with local optimization. Furthermore, a differential mutation

Submitted On: August 03, 2025
Accepted On: January 08, 2026

https://doi.org/10.13052/2026.ACES.J.410102

interference factor is incorporated to strengthen the capability of the algorithm to escape local optima. The effectiveness of TEBGRO is validated through two case studies involving 100-element linear arrays and 20×10 planar arrays, with comparative analysis against optimization results from similar designs reported in other literature.

The main contribution of this work lies in the novel integration of the Taguchi method with the gold rush optimizer (GRO), creating the TEBGRO framework specifically for antenna array thinning. This integration features three synergistic components: Taguchi-enhanced initialization for high-quality binary sequences, a time-varying transfer function for effective continuous-to-binary mapping, and a differential mutation factor for maintaining diversity. Together, they effectively address premature convergence in this high-dimensional binary optimization problem, achieving balance between exploration and exploitation.

II. RELATED WORK

The IFT method stands as a classic deterministic technique. Leveraging the Fourier transform relationship between the array factor and the excitation distribution, this method first optimizes the array factor within the radiation pattern domain and subsequently deactivates specific elements in the aperture domain by nullifying their excitations. These two steps are executed cyclically until a thinned array configuration satisfying the requirements is obtained. While the IFT method is computationally efficient, its performance is heavily dependent on the initial solution. Furthermore, as it is essentially a gradient descent-based approach, it is prone to stagnation in local optima [3, 4].

In parallel, Genetic Algorithms (GA) [5, 6] and Ant Colony Optimization (ACO) [7] were among the earlier meta-heuristic algorithms applied to array thinning. Subsequently, Differential Evolution (DE) [8] and Biogeography-Based Optimization (BBO) [9] demonstrated superior convergence speeds. More recently, advanced algorithms such as the Fruit Fly Optimization Algorithm (FOA) [10] and Cuckoo Search Algorithm (CSA) [11] have been successfully utilized for the optimization of linear and planar arrays. These studies indicate that meta-heuristic algorithms can effectively suppress the PSLL and reduce the element count.

To synergize the strengths of distinct approaches, hybrid methods have emerged. For instance, frameworks combining the rapid convergence of IFT with the global search capability of meta-heuristics have been proposed [12]. In such frameworks, the meta-heuristic algorithm acts as a global explorer responsible for broadly scanning potential regions, while the IFT serves as a local optimizer for rapid fine-tuning; generally, the performance of these hybrid approaches surpasses that of stand-alone algorithms.

Despite the progress achieved by these methods, critical challenges persist, such as the reliance on empirical experience for parameter tuning and limited solution diversity caused by premature convergence.

Meta-heuristic algorithms, by simulating natural physical laws and biological social behaviors, perform global stochastic searches independent of gradient information. Consequently, they exhibit immense potential in solving complex non-linear and non-convex optimization problems. They have been successfully applied across numerous domains, including engineering optimization, scheduling problems, feature selection, and hyperparameter tuning for neural networks [13].

In this context, the GRO [14] has been introduced as a novel meta-heuristic algorithm mimicking the behavior of miners during the 19th-century gold rush. GRO balances exploration and exploitation by simulating the migration of miners towards affluent areas ("cooperative" behavior) and the stochastic exploration for new veins ("selfish" behavior). Characterized by a simple structure and few parameters, GRO has demonstrated outstanding performance on multiple benchmark optimization problems. Although GRO has found applications in other engineering optimization domains [15], it remains relatively new compared to mature algorithms like GA and DE, and its potential in the specific field of antenna thinning remains largely untapped. The intrinsic "cooperative" and "selfish" mechanisms of GRO provide a natural foundation for balancing exploration and exploitation, offering a solid starting point for mitigating premature convergence. Furthermore, the relatively concise structure of GRO facilitates its integration with other optimization strategies, enabling the construction of more robust hybrid models.

However, as the "No Free Lunch" theorem suggests [16], no single algorithm performs optimally on all problems. The versatility of meta-heuristic algorithms is invariably accompanied by inherent limitations. The standard GRO, when addressing high-dimensional binary thinning problems, may still be constrained by the loss of population diversity. Consequently, strategic enhancements are required to adapt GRO effectively for the antenna array thinning optimization.

III. THINNED ARRAY

A. Linear array

The structure of the linear antenna array is illustrated in Fig. 1. The array consists of $2N$ isotropic elements symmetrically arranged along the x-axis. The array factor (AF) of the linear antenna array in the x-z

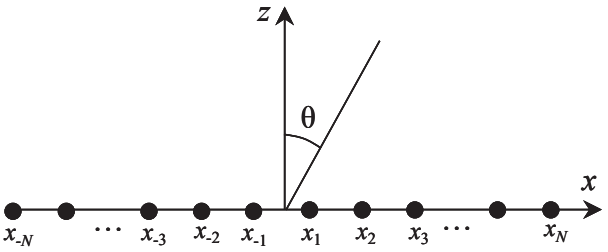

Fig. 1. Geometry of a $2N$-element symmetric linear array.

plane at an angle θ can be expressed as [17]:

$$AF(I,\theta) = \sum_{n=-N}^{-1} I_n e^{j(kx_n \sin\theta + \varphi_n)} + \sum_{n=1}^{N} I_n e^{j(kx_n \sin\theta + \varphi_n)}, \tag{1}$$

where I_n, φ_n and x_n represent the excitation amplitude, phase, and position of element n, respectively. The wave number k is defined as $k = 2\pi/\lambda$, where λ is the wavelength.

In this study, a fixed inter-element spacing of 0.5λ is utilized to mitigate mutual coupling and avoid the formation of grating lobes. $I_n = 1$ if the n-th element is "on," and $I_n = 0$ if it is "off". Assuming symmetric excitation amplitudes ($I_{-n} = I_n$), symmetric element positions ($x_{-n} = -x_n$), and zero excitation phase ($\varphi_n = 0^\circ$). Under these conditions, the two summations in equation (1) are complex conjugates. For a fixed inter-element spacing of 0.5λ with element positions at $x_n = (n-0.5)d$ where $d = \lambda/2$, and $k = 2\pi/\lambda$, Therefore, equation (1) can be expressed as [7, 9]:

$$AF(I,\theta) = 2\sum_{n=1}^{N} I_n \cos(\pi(n-0.5)\sin\theta). \tag{2}$$

B. Planar array

Figure 2 shows the structure of the planar array, which consists of $2N \times 2M$ elements. Each element is isotropic in the x-y plane and symmetric about the x and y axes. Under the same conditions as a linear array, the AF is given by [7, 9]:

$$AF(I,\theta,\varphi) = 4\sum_{n=1}^{N}\sum_{m=1}^{M} I_{nm} \cos(\pi(n-0.5)\sin\theta\cos\varphi) \cdot \cos(\pi(m-0.5)\sin\theta\sin\varphi), \tag{3}$$

where θ is the elevation angle relative to the z-axis and φ is the azimuth angle relative to the x-axis. I_{nm} represents the excitation amplitude, which takes a value of 0 or 1. The array elements in the other three quadrants can be obtained symmetrically based on the position of the array elements in the first quadrant.

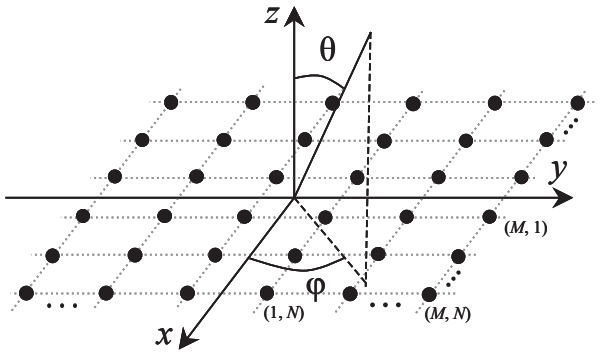

Fig. 2. Geometry of a $2N \times 2M$-element symmetric planar array.

C. Fitness function

As an important performance indicator of array antennas, the expression of PSLL is:

$$PSLL = \max_{\forall\theta\in S}\left(20\log\left|\frac{AF(I,\theta)}{AF_{\max}}\right|\right), \tag{4}$$

where S denotes the side lobe region excluding the main beam and $AF_{\max}$ is the peak of main beam.

To suppress the PSLL, the fitness function is defined as:

$$Fitness = PSLL. \tag{5}$$

The optimization goal is to minimize this Fitness value.

For planar antenna arrays, the fitness function is determined by the higher PSLL value between the $\varphi = 0^\circ$ and $\varphi = 90^\circ$ planes, which can be expressed as:

$$Fitness = \max(PSLL|_{\varphi=0^\circ}, PSLL|_{\varphi=90^\circ}). \tag{6}$$

IV. THE TAGUCHI-ENHANCED BINARY GOLD RUSH OPTIMIZER

A. Taguchi method

Based on statistical experimental design, the Taguchi method systematically optimizes product robustness through parameter design. It employs two core components: orthogonal arrays (OA) for efficient multi-factor analysis and the signal-to-noise ratio (SNR) to measure robustness. Using OA, the method reduces experiments while preserving statistical validity. Meanwhile, the SNR evaluates parameter stability against noise factors. Therefore, this method has been applied to various optimization problems [18–20]. To facilitate understanding, three key concepts used in this paper are

defined as follows:

Levels: These represent the specific values assigned to the design variables. In the context of array synthesis, if a variable represents the excitation amplitude or element position, the "levels" are the candidate values selected for evaluation in each iteration.

OA: It is utilized here as a local search mechanism. The OA is dynamically constructed based on two candidate solutions randomly selected from the current initial population. Each column of the OA represents a dimension (i.e., a binary bit) where the parent vectors differ in value, while each row signifies a new candidate solution formed by the combination of the bit values from the parent vectors.

SNR: It is no longer used to measure robustness; instead, its mathematical form is adopted as a deterministic selection criterion to identify the optimal binary value for each feature dimension. For every position where the two parent solutions differ, the SNR values corresponding to both levels are calculated separately.

Traditional GRO employing random initialization often exhibit poor population diversity and inadequate solution space exploration. This study enhances population initialization by incorporating the Taguchi method.

First, randomly select two individuals, b_1 and b_2, from the initial population. The chance of selecting two individuals with a Hamming distance of 1 is low, and even if this occurs, the negative impact remains relatively limited. The built-in diversity preservation mechanisms in TEBGRO ensure that the search process promptly recovers and continues progressing toward the global optimum. If they differ at w bit positions, a corresponding two-level OA is generated. For each factor $i(i = 1,2\ldots,w)$ in this OA, the standard levels (1 and 2) are substituted with the respective bit values from b_1 and b_2, yielding a modified OA tailored to these individuals.

Subsequently, the SNR is calculated for each run in the modified OA. The use of SNR adapts the classical concept for computational optimization, and it serves as a ranking metric (not a robustness measure) to select the optimal element combination from OA tests based on PSLL performance. Given that the objective function consistently produces negative values, the "smaller-the-better" quality characteristic is adopted for SNR computation, defined as:

$$SNR = -10\log\left(\frac{1}{N_r}\sum_{i=1}^{N} y_i^2\right), \tag{7}$$

where N_r is the number of rows (experimental runs) in the OA, and where y_i is the fitness value (PSLL) obtained from the i-th experimental run.

The construction of the initial population proceeds as follows: in each iteration, two parent solutions are randomly selected. The Taguchi method, utilizing an orthogonal array and the SNR criterion, is then applied to this pair to systematically generate a single, high-quality offspring. This offspring is derived from the optimal combination of the parents' differing element states and is directly accepted into the new population. This iterative process of "select-pair-generate-accept" continues until the newly formed population reaches the predefined target size, ensuring a high-performing starting point for the subsequent optimization.

B. Differential mutation interference factor

The GRO often exhibits limitations when dealing with complex, high-dimensional problems. These include insufficient population diversity during later iterations and limited convergence accuracy. To mitigate these issues, a differential mutation interference factor is incorporated into the cooperative search phase of GRO, formulated as:

$$X(t+1) = X(t) + r\cdot(X_{g2}(t) - X_{g1}(t)) + \gamma, \tag{8}$$

where $X(t+1)$, $X(t)$, and t represent the new position of the feasible solution, current solution and iteration count, respectively. $X_{g2}(t)$ and $X_{g1}(t)$ are two randomly selected gold mining prospectors, r is a random number between [0, 1], and γ is the differential mutation interference factor, represented as:

$$\gamma = \delta\cdot(X_{best}(t) - X(t)), \tag{9}$$

where $X_{best}(t)$ is the current optimal solution, and δ is the adaptive mutation factor, represented as:

$$\delta = \delta_0\cdot 2^{\varepsilon}, \tag{10}$$

$$\varepsilon = \exp\left(1 - \frac{t_{\max}}{t_{\max}+1-t}\right), \tag{11}$$

where δ_0 is the mutation parameter, set to 0.5 in this case. This value was determined through testing and was found to provide an effective trade-off, offering sufficient perturbation without compromising convergence stability. The adaptive nature of δ further reduces dependence on its initial value. The adaptive mutation factor δ starts at $2\delta_0$ and decreases gradually throughout the optimization process, approaching δ_0 as the iteration count reaches the maximum, enabling TEBGRO to more easily escape local optima and avoid premature convergence [21].

C. Time-varying transfer function

GRO and all its operations are based on evaluating solutions using real-valued variables in a continuous search space, which cannot be directly applied to

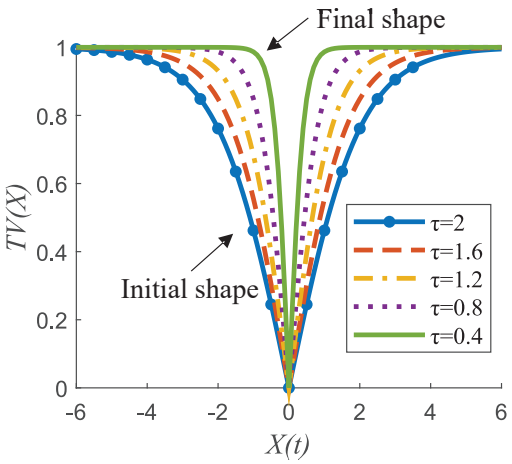

Fig. 3. Demonstration of time-varying transfer function during iteration when $\tau_{\max} = 2$ and $\tau_{\min} = 0.4$.

solve thinned optimization problems for array antennas. Therefore, it is necessary to transform these operations to make them applicable to the binary search space.

Transfer functions effectively convert continuous algorithms into binary ones. The transfer function is independent of the algorithm, does not affect the search behavior of the algorithm, and does not change the computational complexity of the algorithm. A transfer function can play a crucial role in both the exploration and exploitation phases of an optimizer, not just converting a continuous search space into a binary search space [22, 23].

Optimization algorithms should initially prioritize exploration to avoid local optima, transitioning to exploitation in later stages to enhance solution quality. If the transfer function remains unchanged throughout the optimization process, it cannot provide enough diversity, leading to an imbalance between exploration and exploitation. These limitations can be addressed by introducing a time-varying transfer function [24, 25], expressed as follows:

$$TV(X(t)) = \left|\tanh\left(\frac{X(t)}{\tau}\right)\right|, \tag{12}$$

$$X(t+1) = \begin{cases} 1, & r < TV \\ 0, & r > TV \end{cases}, \tag{13}$$

where $TV(X(t))$ is the time-varying transfer function, τ is the time-varying control parameter, which starts from an initial value and gradually decreases with iterations. This is achieved by the following:

$$\tau = \tau_{\max} - t\left(\frac{\tau_{\max} - \tau_{\min}}{t_{\max}}\right), \tag{14}$$

where $\tau_{\max}$ and $\tau_{\min}$ are the bounds on the control parameter τ. The shape of the transfer function changes over time to smoothly transition from the exploration phase to the exploitation phase, depending on different values of τ, as shown in Fig. 3. Here, $\tau_{\max}$ is set to 2, and $\tau_{\min}$ is set to 0.4. A $\tau_{\max}$ larger than 2 would overly flatten the transfer function, inhibiting exploration by preventing $TV(X)$ from approaching 1. A $\tau_{\min}$ smaller than 0.2 would render the transfer function too steep, pushing $TV(X)$ to 1 for most inputs and preventing stable convergence.

To more intuitively illustrate the execution steps of TEBGRO, the flowchart of the improved algorithm is depicted in Fig. 4.

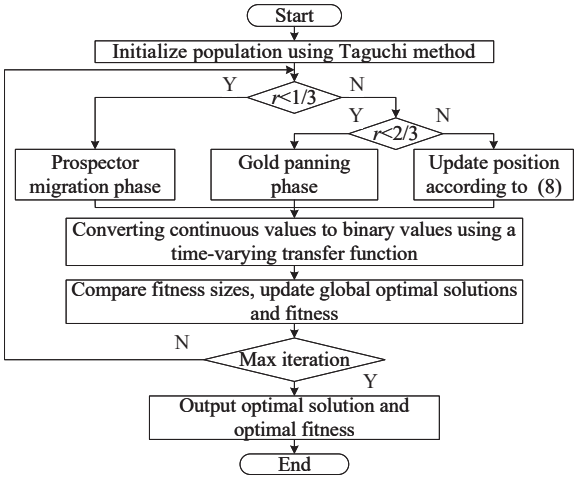

Fig. 4. Flow chart of TEBGRO for array thinning optimization.

V. NUMERICAL RESULTS

In this section, several numerical results are presented to demonstrate the effectiveness of TEBGRO. To ensure a fair comparison, the performance of TEBGRO is evaluated against the best-reported results from the cited literature for the identical linear and planar array specifications.

A. Linear array

The first scenario discusses a 100-element thinned linear array that is symmetrical along the x-axis, with each element spaced at 0.5λ and centered at the origin.

The distribution of excitation amplitude is symmetrical with respect to the center of the linear array, so only half of the amplitude needs to be optimized. The initial population size of TEBGRO is set to 50, and the maximum iteration limit is 300. The optimal value is obtained by running independently for 50 times.

Figure 5 illustrates the distribution of elements in the optimal linear array and provides a comparison of the radiation patterns between the full array and TEBGRO. The PSLL values for TEBGRO and the full array are

−21.29 dB and −13.23 dB, respectively. The thinned array demonstrates a significant reduction in PSLL while concurrently decreasing the number of elements compared to the full array.

Table 1 presents the optimization results of the linear array obtained using TEBGRO. For comparison, the thinning results of the linear arrays obtained by BBO [9], ACO [7], and MICZT [4] are also included in Table 1. The PSLL values for BBO, ACO, and MICZT are −20.84 dB, −20.52 dB, and −21.13 dB, respectively. Among these results, TEBGRO exhibits the lowest PSLL, indicating that it achieves a higher convergence accuracy in the optimization of a linear array with 100 elements.

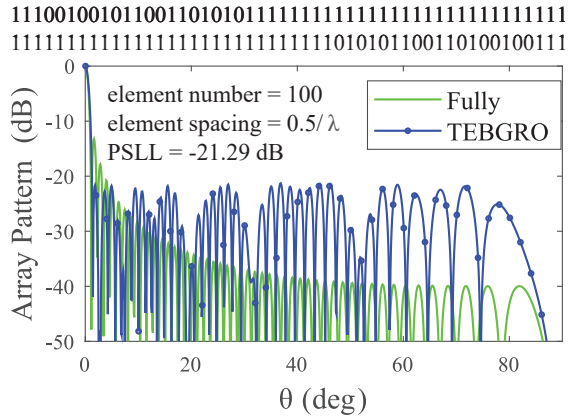

Fig. 5. Element distribution of the optimal linear array and comparison of radiation patterns: Full vs. TEBGRO.

Table 1: Comparison results of linear array

Algorithm	TEBGRO	BBO [9]	ACO [7]	MICZT [4]
PSLL (dB)	−21.29	−20.84	−20.52	−21.13
% of thinning	20	22	20	20

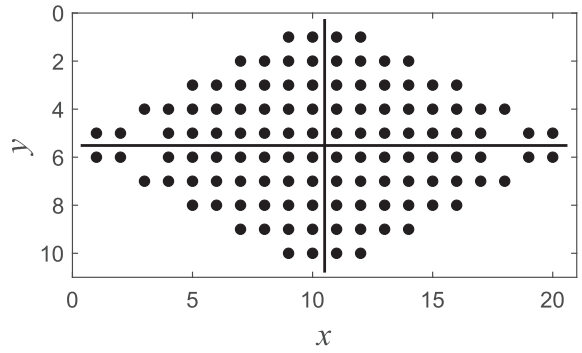

Fig. 6. Element distribution of the optimal planar array.

B. Planar array

In the second example, a planar array with 20 × 10 elements is used for thinning, and the PSLL is suppressed in the $\varphi = 0^\circ$ and $\varphi = 90^\circ$ planes. The excitation amplitude distribution of the planar array exhibits symmetry with respect to the coordinate axes, allowing for optimization of only a quarter of the array. All other experimental parameters remain consistent with those in the initial example.

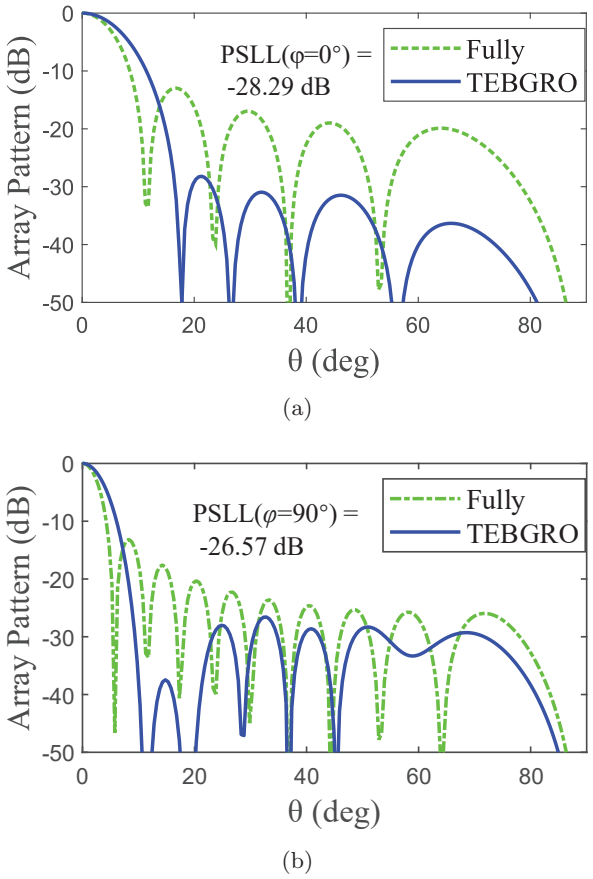

Fig. 7. Planar array radiation pattern comparison (Full vs. TEBGRO) in the (a) $\varphi = 0^\circ$ and (b) $\varphi = 90^\circ$ planes.

Figure 6 illustrates the element distribution of the optimized planar array. For the azimuth angles $\varphi = 0^\circ$ and $\varphi = 90^\circ$, the corresponding radiation patterns of the full array and the TEBGRO optimized array are compared in Fig. 7. The optimization successfully reduced the number of array elements from 200 to 116, while simultaneously lowering the PSLL by 15.33 dB (for the $\varphi = 0^\circ$ plane) and 13.38 dB (for the $\varphi = 90^\circ$ plane).

The same planar array was designed using M-cGA, BDE, and ACO in [6, 8], and [7], respectively. In order to further verify the performance of TEBGRO, the optimal results obtained from TEBGRO, M-cGA, BDE, and ACO are listed in Table 2. The corresponding entry in Table 2 remains blank due to the undisclosed array element arrangement in [6].

In the $\varphi = 0^\circ$ plane, TEBGRO achieved a PSLL of −28.29 dB, outperforming the values of −26.6 dB,

Table 2: Comparison results of planar array

Algorithm	TEBGRO	M-cGA [6]	BDE [8]	ACO [7]
$PSLL\|_{\varphi=0^\circ}$(dB)	−28.29	−26.6	−26.09	−25.76
$PSLL\|_{\varphi=90^\circ}$(dB)	−26.57	−23.8	−25.09	−25.67
% of thinning	42	–	46	32

−26.09 dB, and −25.76 dB reported in [6, 8], and [7], respectively. Similarly, in the $\varphi = 90^\circ$ plane, the PSLL obtained with TEBGRO was −26.57 dB, which is superior to the corresponding values of −23.8 dB, −25.09 dB, and −25.67 dB from the same references. In both evaluated planes, TEBGRO consistently yielded the lowest PSLL. The planar array results again demonstrate that TEBGRO is an effective thinned array optimization technique.

VI. CONCLUSION

This paper presents the design of thinned antenna arrays using TEBGRO, aiming to reduce the number of array elements while minimizing PSLL. To enhance optimization convergence speed and precision, three improvement strategies are proposed: the Taguchi method, time-varying transfer function, and differential mutation interference factor. For a 100-element thinned linear array, TEBGRO achieves a PSLL of −21.29 dB. In the case of a 20×10 thinned planar array, the algorithm obtains a PSLL of −28.29 dB at $\varphi = 0^\circ$ and −26.57 dB at $\varphi = 90^\circ$. The results outperform other binary algorithms, demonstrating TEBGRO's superior optimization capability for array thinning.

ACKNOWLEDGMENT

This work was supported in part by the National Key Research and Development Program of China under Grant 2024YFB2908601, in part by the Natural Science Research Project of Jiangsu Higher Education Institutions under Grant 24KJB510051 and 24KJB140020, in part by the Funding for School-Level Research Projects of Yancheng Institute of Technology under Grant xjr2024036, and in part by the Funding under the "Qinglan Project" for Jiangsu Universities.

REFERENCES

[1] T. Zhang, R. Lian, D. Wu, Y. Li, and J. Zhang, "A broadband high-gain patch antenna array for 5 G millimeter-wave applications," *IEEE Antennas and Wireless Propagation Letters*, vol. 24, no. 4, pp. 803–807, Apr. 2025.

[2] Z. Yu, C. Chen, W. D. Chen, X. Zhang, J. G. Lu, X. L. Zhang, B. J. Che, and Q. Wang, "A low-profile LTCC phased array antenna with wideband and high-gain for X-band satellite communications," *IEEE Transactions on Antennas and Propagation*, vol. 73, no. 1, pp. 659–664, Jan. 2025.

[3] W. P. M. N. Keizer, "Large planar array thinning using iterative FFT techniques," *IEEE Transactions on Antennas and Propagation*, vol. 57, no. 10, pp. 3359–3362, Oct. 2009.

[4] Z. Zhou, C. Zeng, and B. Chen, "Fast low-sidelobe pattern synthesis for linear array thinning utilizing a modified iterative Chirp-Z transform technique," *IEEE Sensors Journal*, vol. 21, no. 20, pp. 23480–23491, Oct. 2021.

[5] R. L. Haupt, "Thinned arrays using genetic algorithms," *IEEE Transactions on Antennas and Propagation*, vol. 42, no. 7, pp. 993–999, July 1994.

[6] B. V. Ha, M. Mussetta, P. Pirinoli, and R. E. Zich, "Modified compact genetic algorithm for thinned array synthesis," *IEEE Antennas and Wireless Propagation Letters*, vol. 15, pp. 1105–1108, Oct. 2016.

[7] O. Quevedo-Teruel and E. Rajo-Iglesias, "Ant colony optimization in thinned array synthesis with minimum sidelobe level," *IEEE Antennas and Wireless Propagation Letters*, vol. 5, pp. 349–352, Aug. 2006.

[8] L. Zhang, Y. C. Jiao, Z. B. Weng, and F. S. Zhang, "Design of planar thinned arrays using a boolean differential evolution algorithm," *IET Microwaves, Antennas & Propagation*, vol. 4, no. 12, pp. 2172–2178, Dec. 2010.

[9] U. Singh and T. S. Kamal, "Optimal synthesis of thinned arrays using biogeography based optimization," *Progress in Electromagnetics Research M*, vol. 24, pp. 141–155, Apr. 2012.

[10] A. Darvish and A. Ebrahimzadeh, "Improved fruit-fly optimization algorithm and its applications in antenna arrays synthesis," *IEEE Transactions on Antennas and Propagation*, vol. 66, no. 4, pp. 1756–1766, Apr. 2018.

[11] G. Sun, Y. Liu, Z. Chen, S. Liang, A. Wang, and Y. Zhang, "Radiation beam pattern synthesis of concentric circular antenna arrays using hybrid approach based on cuckoo search," *IEEE Transactions on Antennas and Propagation*, vol. 66, no. 9, pp. 4563–4576, Sep. 2018.

[12] C. Cui, W. T. Li, X. T. Ye, and X. W. Shi, "Hybrid genetic algorithm and modified iterative fourier transform algorithm for large thinned array synthesis," *IEEE Antennas and Wireless Propagation Letters*, vol. 16, pp. 2150–2154, May 2017.

[13] K. Rajwar, K. Deep, and S. Das, "An exhaustive review of the metaheuristic algorithms for search and optimization: Taxonomy, applications, and open challenges," *Artificial Intelligence Review*, vol. 56, no. 11, pp. 13187–13257, Apr. 2023.

[14] Z. Kamran, "Gold rush optimizer: A new population-based metaheuristic algorithm,"

Operations Research and Decisions, vol. 33, no. 1, pp. 112–150, Apr. 2023.

[15] L. Lyu, G. Kong, F. Yang, L. Li, and J. He, "Augmented gold rush optimizer is used for engineering optimization design problems and UAV path planning," *IEEE Access*, vol. 12, pp. 134304–134339, Aug. 2024.

[16] D. H. Wolpert and W. G. Macready, "No free lunch theorems for optimization," *IEEE Transactions on Evolutionary Computation*, vol. 1, no. 1, pp. 67–82, Apr. 1997.

[17] C. Lin, A. Qing, and Q. Feng, "Synthesis of unequally spaced antenna arrays by using differential evolution," *IEEE Transactions on Antennas and Propagation*, vol. 58, no. 8, pp. 2553–2561, Aug. 2010.

[18] L. Y. Chuang, C. S. Yang, K. C. Wu, and C. H. Yang, "Gene selection and classification using Taguchi chaotic binary particle swarm optimization," *Expert Systems with Applications*, vol. 38, no. 10, pp. 13367–13377, Sep. 2011.

[19] B. Vedik and A. K. Chandel, "Optimal PMU placement for power system observability using Taguchi binary bat algorithm," *Measurement*, vol. 95, pp. 8–20, Jan. 2017.

[20] X. Jia and G. Lu, "A hybrid Taguchi binary particle swarm optimization for antenna designs," *IEEE Antennas and Wireless Propagation Letters*, vol. 18, no. 8, pp. 1581–1585, Aug. 2019.

[21] B. Zhou, Y. Wang, B. Zi, and W. Zhu, "Fuzzy adaptive whale optimization control algorithm for trajectory tracking of a cable-driven parallel robot," *IEEE Transactions on Automation Science and Engineering*, vol. 21, no. 4, pp. 5149–5160, Oct. 2024.

[22] P. Hu, J. S. Pan, and S. C. Chu, "Improved binary grey wolf optimizer and its application for feature selection," *Knowledge-Based Systems*, vol. 195, p. 105746, May 2020.

[23] J. Wang, M. Khishe, M. Kaveh, and H. Mohammadi, "Binary chimp optimization algorithm (BChOA): A new binary meta-heuristic for solving optimization problems," *Cognitive Computation*, vol. 13, pp. 1297–1316, Sep. 2021.

[24] M. J. Islam, X. Li, and Y. Mei, "A time-varying transfer function for balancing the exploration and exploitation ability of a binary PSO," *Applied Soft Computing*, vol. 59, pp. 182–196, Oct. 2017.

[25] M. Mafarja, I. Aljarah, A. A. Heidari, H. Faris, P. F. Viger, X. Li, and S. Mirjalili, "Binary dragonfly optimization for feature selection using time-varying transfer functions," *Knowledge-Based Systems*, vol. 161, pp. 185–204, Dec. 2018.

Weibin Kong received the B.S. degree in mathematics from Qufu Normal University, China, 2007, and the M.S. degree in mathematics from Southeast University, Nanjing, China, in 2010, and the Ph.D. degree in radio engineering from Southeast University, Nanjing, China, in 2015. Since 2020, he has been an associate professor with the College of Information Engineering, Yancheng Institute of Technology, Yancheng. His current research interests include computational electromagnetism, artificial intelligence, and wireless communication.

Yiming Zong received the B.S. degree in electronic information engineering from Yancheng Institute of Technology in 2022. He is currently pursuing the M.Eng. degree in electronic information at Yancheng Institute of Technology. His main research interests focus on computational electromagnetics and artificial intelligence.

Lei Wang received the B.S. degree in integrated circuit design and integrated systems and the Ph.D. degree in information and communication engineering from Nantong University, Nantong, Jiangsu, China, in 2017 and 2023, respectively. Since 2023, he has been a Lecturer with the College of Information Engineering, Yancheng Institute of Technology, Yancheng. His current research interests include artificial intelligence and antenna, millimeter-wave antennas and arrays, and characteristic mode analysis.

Wenwen Yang received the B.Eng. degree in information engineering and the M.Eng. and Ph.D. degrees in electrical engineering from the Southeast University (SEU), Nanjing, China, in 2007, 2010, and 2015, respectively. Since 2015, he has been with the School of Electronics and Information, Nantong University, Nantong, China, where he is currently an Associate Professor.

From August 2018 to August 2019, he was a Visiting Researcher with the Polytechnique Montreal, Montreal, QC, Canada. He has authored or coauthored more than 80 internationally referred journal and conference papers. His research interests include RF, microwave and millimeter-wave passive devices, active antenna array, and antennas for wireless communication.

Botong Liu received the B.S. degrees and M.S. degrees from xidian University, xi'an, China and East China Normal University, shanghai, in 2015 and 2021 respectively. Since 2021, he is a lecturer with the College of Information Engineering, Yancheng Institute of Technology, and Yancheng, China. His research focuses on robotic control and applications, with a specialization in visual simultaneous localization and mapping (VSLAM).

Binghe Sun received the Ph.D. degree in Materials Science from Shanghai Jiao Tong University, Shanghai, China, in 2005. He is currently the Deputy General Manager of Jiangsu Bomin Electronics Technology. He has previously worked at well-known domestic and international companies such as ASE Semiconductor, Autech, and Founder Technology. In 2023, he was recognized as a 'Double Innovation Talent' of Jiangsu Province and was appointed as an industrial professor under the Jiangsu Province Graduate Mentor program. His current research interests include electronic packaging, artificial intelligence, and electromagnetic materials.

Feng Zhou received the B.S. degrees and M.S. degrees from Southeast University, Nanjing, China, in 2004 and 2012 respectively. Since 2023, he is a professor with the College of Information Engineering, Yancheng Institute of Technology, Yancheng, China. His research interests include cooperative communication, satellite communication, cognitive radio, physical layer security and UAV communication.

Enhanced CPML Based on the Autoformer Network for 2D WCS-FDTD Method

Yumeng Wu[1,2], Ning Xu[1,2,*], Yexin Li[1], Kuiwen Xu[1], and Juan Chen[3]

[1]Engineering Research Center of Smart Microsensors and Microsystems
Ministry of Education, Hangzhou Dianzi University, Hangzhou 310018, China
23040531@hdu.edu.cn, 232040214@hdu.edu.cn, kuiwenxu@hdu.edu.cn
*Corresponding Author

[2]State Key Laboratory of Millimeter Waves
Southeast University, Nanjing 210096, China
xuning_10032@hdu.edu.cn

[3]School of Information and Communication Engineering
Xi'an Jiaotong University, Xi'an 710049, China
chen.juan.0201@mail.xjtu.edu.cn

Abstract **–** This paper proposes a novel convolutional perfectly matched layer (CPML) for the weakly conditionally stable finite-difference time-domain (WCSFDTD) method. The Autoformer neural network is introduced to replace the conventional multi-layer CPML. Employing only a single-layer structure, the Auto-former-driven CPML considerably reduces both the computational domain scale and algorithmic complexity. By leveraging sequence decomposition and sparse attention mechanisms, the wave-absorption performance of this method is significantly improved. Integrated into the 2D WCS-FDTD framework, the proposed method overcomes Courant-Friedrichs-Lewy (CFL) stability constraints for FDTD intelligent absorbing boundaries, with its time step size independent of fine grid sizes in any direction. Numerical results demonstrate that the proposed method can achieve excellent wave-absorption performance with high computational efficiency, while maintaining satisfactory robustness in complex scenarios.

Index Terms **–** Autoformer, convolutional perfectly matched layer (CPML), data-driven, weakly conditionally stable finite-difference time-domain (WCS-FDTD).

I. INTRODUCTION

The finite-difference time-domain (FDTD) [1, 2] method, a classical technique for solving Maxwell's equation, is widely applied in engineering scenarios including electromagnetic scattering, antenna design and photonic device simulation. However, constrained by the Courant-Friedrich-Lewy (CFL) stability condition [3, 4], its maximum time step size is strictly determined by the grid sizes in all spatial directions. Consequently, fine-scale structures in simulation objects necessitate a significantly reduced time step size, leading to a substantial increase in the computational time. To overcome this constraint, the weakly conditionally stable finite-difference time-domain (WCS-FDTD) [5–7] method has been proposed. By applying the hybrid implicit explicit technique in the fine directions, the maximum time step size of this method is only related to the coarse grid size in one direction. Therefore, the WCSFDTD method is particularly suitable for simulating electromagnetic devices that have fine structures in two directions.

In time-domain electromagnetic simulations, absorbing boundary conditions (ABCs) [8–16] play a crucial role in truncating computational domains. Among these, the perfectly matched layer (PML) [10] is a classical boundary condition that leverages field splitting to achieve high absorption efficiency. However, multiple layers are required to achieve effective waveabsorption, and the inherent computational complexity of field splitting further degrades its efficiency. To address these limitations, numerous PML variants have been proposed. The uniaxial PML (UPML) [12] simplifies mathematical derivations by introducing uniaxial anisotropic material parameters, while the convolutional PML (CPML) [14] achieves accelerated computation using the recursive convolution method. A further adaptation of the complex-frequency-shifted PML (CFSPML) streamlines the calculation process by incorporating multiple auxiliary variables [15]. Nevertheless, these variants still require multiple layers for effective absorption. It does not resolve the challenge of balancing performance and cost.

Submitted On: August 25, 2025
Accepted On: January 21, 2026

https://doi.org/10.13052/2026.ACES.J.410103

With the rapid advancements in computer science and hardware, recent breakthroughs in machine learning and deep learning have spurred innovations in ABCs. Yao et al. introduced a pioneering PML model based on hyperbolic tangent basis function (HTBF), which utilizes a multi-layer perceptron (MLP) to eliminate auxiliary terms [17], replace the conventional multi-layer CPML with a single layer, and thereby significantly reduce computational complexity. However, this approach suffered from error accumulation in long-term simulations. Subsequently, their team integrated a long short-term memory (LSTM) network, leveraging its temporal modeling capabilities to reduce the pile-up of errors [18]. Subsequently, further innovations demonstrated the potential of these research directions. Zhang et al. proposed a fully machine learning-driven solver that integrates LSTM model for field updating in computational domain and HTBF-PML for boundary absorption [19]. However, this model has not undergone generalization verification. Guo et al. demonstrated that the FDTD can be exactly represented by a recurrent convolutional neural network (RCNN), whose parameters were derived from the original electromagnetic equations [20]. This method requires no training, but its efficiency only improves in large-scale computations. Additionally, Feng's research group proposed a single-layer PML based on deep differentiable forest (DDF) to replace traditional multi-layer CPML [21]. They further applied a neural Turing machine (NTM) model incorporating deep differentiable decision trees (DDT) for effective boundary truncation in 3D microstrip line simulations [22]. They developed the gradient boosted decision trees-perfectly matched monolayer (GBDTPMM) model to tackle subsurface sensing issues [23]. Meanwhile, Ren et al. introduced a neural-networkbased CPML model by using the gated recurrent unit (GRU) [24]. However, its reliance on the multi-layer CPML structure inherently limits computational efficiency.

While the aforementioned ABCs exhibit promising absorption performance, they were primarily developed and validated within the FDTD framework. Their applicability has not been explored in the WCS-FDTD solver, which features a relaxed numerical stability criterion. This paper proposes a novel CPML method based on the Autoformer network for the 2D WCSFDTD framework. The main contributions of this paper are summarized as follows:

(1) An Autoformer-driven intelligent absorbing boundary is proposed to replace the conventional absorbing boundary. Using only a single-cell absorption layer, the Autoformer-based CPML can achieve absorption performance comparable to the conventional 6-layer CPML, while reducing computational time by 60.9%.
(2) Successful integration of the Autoformer-based CPML into the 2D WCS-FDTD framework. The time step size of this method can be set to an arbitrary value, significantly expanding the application scope of intelligent absorbing boundaries in the FDTD framework.
(3) The generalization capability is verified by modeling complex scenarios, including large computational domains, multiple excitation sources, multiple media, and fine-scale structures. Even in simulation environments far beyond the training dataset, the proposed method continues to exhibit stable and excellent wave-absorption performance.

II. FORMULATIONS

A. Conventional WCS-FDTD method with CPML

It is assumed that the fine structures are contained in both the x and z directions. Fig. 1 illustrates the conventional CPML configuration for a 2D transverse magnetic (TM) case. The electromagnetic fields in this CPML region consist of three components (H_x, H_z, E_y). The updated equations for the 2D WCS-FDTD method with the CPML [5, 14] are given as follows:

Step 1:

$$\begin{aligned}&(1+\mathrm{A}_1+B_1)E_y^{n+\frac{1}{2}}(i,j)-A_1E_y^{n+\frac{1}{2}}(i+1,j)-B_1E_y^{n+\frac{1}{2}}(i-1,j)\\&\quad=(1-A_1-B_1)E_y^{n}(i,j)+A_1E_y^{n}(i+1,j)+B_1E_y^{n}(i-1,j)-\chi_1\left[H_z^n\left(i+\frac{1}{2},j\right)-H_z^n\left(i-\frac{1}{2},j\right)\right]+\beta_1\end{aligned}\tag{1}$$

$$\begin{aligned}&H_z^{n+\frac{1}{2}}\left(i+\frac{1}{2},j\right)\\&\quad=H_z^n\left(i+\frac{1}{2},j\right)-\varphi_{hzx}^{n+\frac{1}{2}}(i,j)\Delta t/\mu\\&\qquad-\left[E_y^{n+\frac{1}{2}}(i+1,j)-E_y^{n+\frac{1}{2}}(i+1,j)+E_y^{n}(i+1,j)-E_y^{n}(i+1,j)\right]\Delta t\Big/\left[2\Delta x\mu k\left(i+\frac{1}{2},j\right)\right]\end{aligned}\tag{2}$$

$$H_x^{n+\frac{1}{2}}(i,j) = H_x^n(i,j) \tag{3}$$

$$\begin{cases} \varphi_{hzx}^{n+\frac{1}{2}}\left(i+\frac{1}{2},j\right) = \varphi_{hzx}^{n}\left(i+\frac{1}{2},j\right) b_x\left(i+\frac{1}{2}\right) \\ \qquad + \left[E_y^{\mathrm{n}+\frac{1}{2}}(i+1,j) - E_y^{\mathrm{n}+\frac{1}{2}}(i,j) + E_y^{\mathrm{n}}(i+1,j) - E_y^{\mathrm{n}}(i,j)\right] b_x\left(i+\frac{1}{2}\right) \Big/ (2\Delta x) \\ \varphi_{eyx}^{n+\frac{1}{2}}(i,j) = \varphi_{eyx}^{n}(i,j) b_x(i) + \left[H_z^{\mathrm{n}+\frac{1}{2}}\left(i+\frac{1}{2},j\right)\right. \\ \qquad \left. - H_z^{\mathrm{n}+\frac{1}{2}}\left(i-\frac{1}{2},j\right) + H_z^{\mathrm{n}}\left(i+\frac{1}{2},j\right) - H_z^{\mathrm{n}}\left(i-\frac{1}{2},j\right)\right] a_x(i) \Big/ (2\Delta x) \\ \varphi_{eyz}^{n+\frac{1}{2}}(i,j) = \varphi_{eyz}^{n}(i,j) \\ \varphi_{hxz}^{n+\frac{1}{2}}(i,j) = \varphi_{hxz}^{n}(i,j). \end{cases} \tag{4}$$

Step 2:

$$\begin{aligned} &(1+A_2+B_2)E_y^{n+1}(i,j) - A_2E_y^{n+1}(i,j+1) - B_2E_y^{n+1}(i,j-1) \\ &\quad = (1-A_2-B_2)E_y^{n+\frac{1}{2}}(i,j) + A_2E_y^{n+\frac{1}{2}}(i,j+1) \\ &\qquad + B_2E_y^{n+\frac{1}{2}}(i,j-1) + \chi_2\left[H_x^{n+\frac{1}{2}}\left(i,j+\frac{1}{2}\right) - H_x^{n+\frac{1}{2}}\left(i,j-\frac{1}{2}\right)\right] + \beta_2 \end{aligned} \tag{5}$$

$$\begin{aligned} &H_{\mathrm{x}}^{n+1}\left(i,j+\frac{1}{2}\right) \\ &\quad = H_x^{n+\frac{1}{2}}\left(i,j+\frac{1}{2}\right) + \varphi_{hxz}^{n+1}\left(i,j+\frac{1}{2}\right)\Delta t \Big/ \mu \\ &\qquad + \left[E_y^{n+1}(i,j+1) - E_y^{n+1}(i,j) + E_y^{n+\frac{1}{2}}(i,j+1) - E_y^{n+\frac{1}{2}}(i,j)\right]\Delta t \Big/ \left(2\Delta z \mu k_z\left(j+\frac{1}{2}\right)\right) \end{aligned} \tag{6}$$

$$H_{\mathrm{z}}^{n+1}(i,j) = H_z^{n+\frac{1}{2}}(i,j) \tag{7}$$

$$\begin{cases} \varphi_{hxz}^{n+1}\left(i,j+\frac{1}{2}\right) = \varphi_{hxz}^{n+\frac{1}{2}}\left(i,j+\frac{1}{2}\right) b_z\left(j+\frac{1}{2}\right) \\ \qquad + \left[E_y^{\mathrm{n}+1}(i,j+1) - E_y^{\mathrm{n}+1}(i,j) + E_y^{\mathrm{n}+\frac{1}{2}}(i,j+1) - E_y^{\mathrm{n}+\frac{1}{2}}(i,j)\right] a_z\left(j+\frac{1}{2}\right) \Big/ (2\Delta z) \\ \varphi_{eyz}^{n+1}(i,j) = \varphi_{eyz}^{n+\frac{1}{2}}(i,j) b_z(j) \\ \qquad + \left[H_x^{\mathrm{n}+1}\left(i,j+\frac{1}{2}\right) - H_x^{\mathrm{n}+1}\left(i,j-\frac{1}{2}\right) + H_x^{\mathrm{n}+\frac{1}{2}}\left(i,j+\frac{1}{2}\right) - H_x^{\mathrm{n}+\frac{1}{2}}\left(i,j-\frac{1}{2}\right)\right] a_z(j) \Big/ (2\Delta z) \\ \varphi_{eyx}^{n+1}(i,j) = \varphi_{eyx}^{n+\frac{1}{2}}(i,j) \\ \varphi_{hzx}^{n+1}(i,j) = \varphi_{hzx}^{n+\frac{1}{2}}(i,j). \end{cases} \tag{8}$$

The coefficients in the above equations are defined as follows:

$$\beta_1 = -\frac{\Delta t}{\varepsilon} b_x(i)\varphi_{eyx}^n(i,j) + [1/k_x(i) + a_x(i)]\frac{\Delta t^2}{2\varepsilon\mu\Delta x}\left[b_x\left(i+\frac{1}{2}\right)\varphi_{hzx}^n\left(i+\frac{1}{2},j\right) - b_x\left(i-\frac{1}{2}\right)\varphi_{hzx}^n\left(i-\frac{1}{2},j\right)\right]$$

$$\beta_2 = \frac{\Delta t}{\varepsilon} b_z(j)\varphi_{eyz}^{n+\frac{1}{2}}(i,j) + [1/k_z(j) + a_z(j)]\frac{\Delta t^2}{2\varepsilon\mu\Delta z}\left[b_z\left(j+\frac{1}{2}\right)\varphi_{hxz}^{n+\frac{1}{2}}\left(i,j+\frac{1}{2}\right) - b_z\left(j-\frac{1}{2}\right)\varphi_{hxz}^{n+\frac{1}{2}}\left(i,j-\frac{1}{2}\right)\right]$$

$$A_1 = \frac{\Delta t^2}{4\varepsilon\mu\Delta x^2}\xi_x(i)\xi_x\left(i+\frac{1}{2}\right) \quad B_1 = \frac{\Delta t^2}{4\varepsilon\mu\Delta x^2}\xi_x(i)\xi_x\left(i-\frac{1}{2}\right)$$

$$\chi_1 = \frac{\Delta t}{\varepsilon\Delta x}\xi_x(i) \quad \chi_2 = \frac{\Delta t}{\varepsilon\Delta z}\xi_z(j)$$

$$A_2 = \frac{\Delta t^2}{4\varepsilon\mu\Delta z^2}\xi_z(j)\xi_z\left(j+\frac{1}{2}\right) \quad B_2 = \frac{\Delta t^2}{4\varepsilon\mu\Delta z^2}\xi_z(j)\xi_z\left(j+\frac{1}{2}\right)$$

$$\xi_w(s) = \frac{1}{k_w(s)} + a_w(s) \quad (w = x \text{ or } z, s = i \text{ or } j)$$

$$b_w(s) = \exp\left\{-\frac{\Delta t}{\varepsilon_0}\left[\frac{\sigma_w(s)}{k_w(s)} + \alpha_w\right]\right\} \quad a_w(s) = \frac{(b_w(s)-1)}{k_w(s)(\sigma_w(s)+k_w(s)\alpha_w)}\sigma_w(s)$$

$$k_w(s) = 1 + (k_{\max}-1)\frac{|w-w_0|^m}{d^m} \quad \sigma_w(s) = \sigma_{w\max}\frac{|w-w_0|^m}{d^m} \quad \alpha_w = \alpha_{w\max}\frac{|w-w_0|^m}{d^m}$$

where i and j denote the indices of spatial increments, respectively, in x and z directions. w_0 is the position of interface. d is the CPML thickness. $\sigma_{w\max}$ represents the conductivity at the outer side of CPML layers. m is the order of polynomial. $\alpha_{w\max}$ and $k_{\max}$ are selected according to actual conditions, with their values ranging from 0 to 0.05, and 5 to 10, respectively. ε is the permittivity, and μ is the permeability.

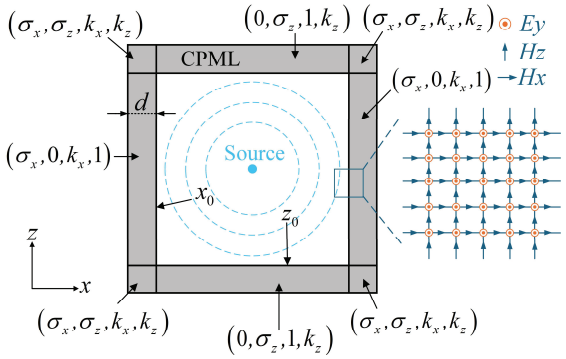

Fig. 1. Conventional CPML method.

Different from the explicit update in FDTD algorithm, the WCS-FDTD method divides one iteration into two sub-time steps. The update of the electric field component $E_y^{n+\frac{1}{2}}$ in Step 1 involves the magnetic field $H_z^{n+\frac{1}{2}}$ at the same time instance, and the update of the electric field E_y^{n+1} in Step 2 requires the concurrent magnetic field component H_x^{n+1}. Both updates necessitate implicit difference calculations. To complete one iteration, it is necessary to solve 2 implicit equations and 6 explicit equations. By adopting the implicit method in the x and z directions, the time step size of the WCS-FDTD method is independent of the grid size along these coordinates. Hence, an arbitrary time step size can be employed in the 2D WCS-FDTD method.

B. Autoformer-driven CPML

As a deep learning network, Autoformer demonstrates excellent efficiency and accuracy in time series forecasting [25, 26]. To balance between prediction accuracy and computational speed in CPML, a compact architecture is used in this paper. Fig. 2 shows its detailed structure. It includes two key modules: (i) a time series decomposition module, which uses two 1D convolutional layers with different kernel sizes to decompose the input sequence into a long-term trend and a short-term seasonal component, enabling the model to capture distinct feature patterns. (ii) an auto-correlation module, which integrates sparse mechanisms and multi-head mechanisms. The sparse mechanism extracts high-score components along the last dimension of the score matrix, facilitating the capture of core sequence features and preventing overfitting. The multi-head mechanism enables parallel output from multiple autocorrelation layers, which are then mapped to the model's dimension via a linear layer to capture sequence information from multiple perspectives. Subsequently, the results are normalized via layer normalization and pass through an attention pooling module for feature refinement. In the attention pooling layer, the attention score matrix is computed by passing the module input through a linear layer. Following this scheme, the matrix is normalized by a SoftMax function and then multiplied with the input sequence. The resulting weighted sequence is finally summed along the last dimension to produce the output.

During the data acquisition phase, let x_{ij}^t denote the input electromagnetic field components at the current time t, where i and j represent the spatial indices of the

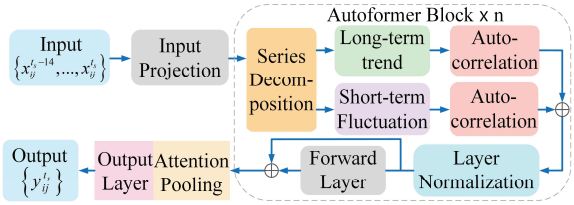

Fig. 2. Autoformer model framework.

grid position. Let y_{ij}^{t+1} denote the output electromagnetic field components at the next time step $t+1$. For each data sample, it consists of an input sequence $X^t = \{x^{t-14},\ldots,x^t\}$ of length 15, which comprises electromagnetic field components from 15 consecutive time steps, and an output label $Y^{t+1} = \{y^{t+1}\}$ representing the field data at the subsequent time step $t+1$.

As depicted in Fig. 3, different data collection strategies are applied to the cells at the corners and edges of the computational boundary. (a) edge cells: data are gathered from a cell on the CPML boundary and its directly adjacent neighbor inside the computational domain; (b) corner cells: data are gathered from the CPML cell and a diagonally adjacent neighbor. To balance prediction accuracy and computational efficiency, the input features are composed of the electromagnetic field components from three adjacent cells, totaling 9 features per time step. The output feature set is defined as the three field components of one boundary cell, which is highlighted in red in Fig. 3. In the conventional CPML implementations for WCS-FDTD method, the calculation for one discrete time step is performed using two sub-procedures. First, the electromagnetic fields at the intermediate time step $n+1/2$ are calculated using the values at time step n. Subsequently, the fields at time step $n+1$ are derived from those at $n+1/2$. While, in the proposed Autoformer-driven CPML, the electromagnetic field values at the intermediate time step $n+1/2$ are not required. Only the field values at time steps n and $n+1$ are collected. The specific input and output data at one time step are as follows:

In edge cells:

$$\begin{cases} x_{ij}^t = [H_z^t(i-3/2,j+1), H_x^t(i-2,j+1/2), \\ \quad E_y^t(i-2,j+1), H_z^t(i-1/2,j+1), \\ \quad H_x^t(i-1,j+1/2), E_y^t(i-1,j+1), \\ \quad H_z^t(i+1/2,j+1), H_x^t(i,j+1/2), \\ \quad E_y^t(i,j+1)] \\ y_{ij}^{t+1} = [H_z^t(i+1/2,j+1), H_x^t(i,j+1/2), \\ \quad E_y^t(i,j+1)]. \end{cases} \tag{9}$$

In corner cells:

$$\begin{cases} x_{ij}^t = [H_z^{t+1}(i-3/2,j+3), H_x^{t+1}(i-2,j+5/2), \\ \quad E_y^{t+1}(i-2,j+3), H_z^{t+1}(i-1/2,j+2), \\ \quad H_x^{t+1}(i-1,j+3/2), E_y^{t+1}(i-1,j+2), \\ \quad H_z^{t+1}(i+1/2,j+1), H_x^{t+1}(i,j+1/2), \\ \quad E_y^{t+1}(i,j+1)] \\ y_{ij}^{t+1} = [H_z^{t+1}(i+1/2,j+1), H_x^{t+1}(i,j+1/2), \\ \quad E_y^{t+1}(i,j+1)]. \end{cases} \tag{10}$$

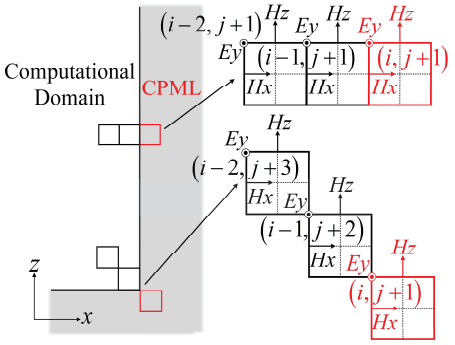

Fig. 3. Data acquisition mechanism for Autoformer-driven CPML.

To ensure the model's generalization capability, multiple electromagnetic simulation scenarios were selected for training data collection, encompassing single-point source, 9-point source, and 13-point source configurations. Each data sample captures 300 time steps of electromagnetic field evolution. Considering the implicit computation, a column-stacking approach was adopted for data acquisition, which enhances storage and update efficiency while remaining applicable to the FDTD framework. The final training dataset comprises input samples with dimensions (106392, 15, 9) and output labels with dimensions (106392, 1, 3), where 106392 denotes the total number of samples, 15 is the sequence length of the input data, 9 is the number of input features, 1 is the sequence length of the output label, and 3 is the number of output features. All training and evaluation processes were implemented using the PyTorch deep learning framework on a system equipped with an AMD Ryzen 9 9950X CPU and an NVIDIA GeForce RTX 4080 Super GPU. The training of this model takes 797 s.

C. Ablation study and parameter selection

To evaluate the contribution of each component in the proposed Autoformer architecture, an ablation study

Table 1: Ablation study for the important components

Method	H_x Error ↓	H_z Error ↓	E_y Error ↓	MSE↓	Time(s)	Params
Autoformer	3.94e-05	**3.80e-05**	5.09e-05	4.28e-5	416.56	35640
w/o Sparse Mechanism	**3.78e-05**	3.87e-05	**4.38e-05**	**4.01e-5**	472.83	35640
w/o Series Decomposition	1.15e-04	3.32e-04	1.97e-04	2.15e-4	369.16	18036
w/o Multi-head Mechanism	3.16e-04	2.13e-04	2.38e-04	2.56e-4	327.61	21006
w/o Attention Polling	4.41e-05	4.75e-05	6.38e-05	5.18e-5	399.45	35612

was performed by assessing the impact of removing the sparse attention, sequence decomposition, multi-head mechanism, and attention pooling modules. Table 1 summarizes the corresponding performance changes in terms of component errors (H_x, H_z, E_y), mean squared error (MSE), inference times, and the number of parameters.

The experimental results indicate that removing either the series decomposition module or the multi-head mechanism leads to significant performance degradation, with the MSE increasing by approximately one order of magnitude. These results highlight the crucial role both components play in enhancing feature representation and improving predictive accuracy. Replacing the sparse attention with a full attention mechanism reduces the overall MSE to 4.01e-4 but markedly increases the inference time, suggesting that sparsification effectively balances computational efficiency and model representational capacity. Furthermore, removing the attention pooling module reduces the parameter count but also leads to notable increases in all error metrics, confirming its essential role in maintaining prediction accuracy.

In neural network construction and training, parameter design is important. The specific parameter configurations are as follows:

(1) *Convolution kernel*: In the series decomposition, a kernel size of 3 is employed to extract short-term fluctuations, while a kernel size of 9 is used for extracting long-term trends.
(2) *Hidden layer size*: An excessively large size may induce overfitting and compromise computational efficiency, whereas an insufficient size fails to adequately capture the nonlinear input-output relationship. After balancing computational efficiency with model capacity, the hidden layer size is set to 27.
(3) *Sparse mechanism factor*: A factor of 0.34 is selected to accelerate both model training and inference while simultaneously mitigating overfitting.
(4) *Number of heads*: Five heads are configured to enable comprehensive extraction of data features across multiple dimensions.
(5) *Training parameters*: The network is trained using the AdamW optimizer with an initial learning rate of 0.003. This pairing represents a standard, well-established choice for training deep neural networks, as it delivers stable convergence and effective regularization.

D. Integration of autoformer-driven CPML with WCS-FDTD

Based on the trained Autoformer network, $\{y_{ij}^{t+1}\}$ can be predicted by $\{x_{ij}^{t-14},\ldots,x_{ij}^{t}\}$ and the electromagnetic fields on the CPML interface at $t+1$ can be further obtained. Then, using $\{y_{ij}^{t+1}\}$, the electromagnetic fields in the object domain at $t+1$ can be obtained via the standard WCS-FDTD process. Meanwhile, the field values within both the CPML layer and its adjacent region in the object domain are stored for use as the input features at $t+2$. By repeating this process, the Autoformer-driven CPML can replace the conventional multi-layer CPML and be integrated into the WCS-FDTD framework. The specific algorithm is shown as follows:

Algorithm: Autoformer-driven CPML on WCSFDTD framework

Data Collection and Training

(1) Collect the dataset $\{x_{ij}^{t_s-14},\ldots,x_{ij}^{t_s}\}$ and $\{y_{ij}^{t_s}\}$ in a columnar fashion.
(2) Train the Autoformer-driven CPML using the collected dataset.

Network Prediction Substitution

Initialization $(k<15)$**:**

(1) Initialize the electromagnetic field values at each time step using WCS-FDTD method.
(2) Collect data at each time step and stack them in the format required for the model input.

kth Iteration $(k\geq 15)$**:**

(3) Update input sequence $X^t=\{x^{t-14},\ldots,x^t\}$ using a sliding window.
(4) Predict boundary fields $\{y^{t+1}\}$ by using Autoformer model.
(5) Update the electromagnetic fields on the first CPML layer with $\{y^{t+1}\}$.
(6) Update the electromagnetic fields in the object domain at $t+1$ using WCS-FDTD method.

III. NUMERICAL EXAMPLES

To evaluate the performance of the proposed method, three distinct scenarios are simulated. Case A is primarily used to validate the wave-absorption performance of Autoformer-driven CPML, whereas cases B and C are designed to assess its generalization capability across various complex scenarios.

A. Single point source

To validate the wave-absorption performance of this Autoformer model, the propagation process of a single source under identical environmental parameters to those in the training dataset is modeled. As illustrated in Fig. 4, the computational domain is 60 mm × 60 mm, with a grid size of 2 mm × 2 mm and a time step size of 2 ps. A sinusoidal point source is located at the center of the computational domain. It should be noted that the conventional CPML requires a multi-layer structure to achieve satisfactory wave-absorption, whereas the proposed Autoformer model only needs one layer.

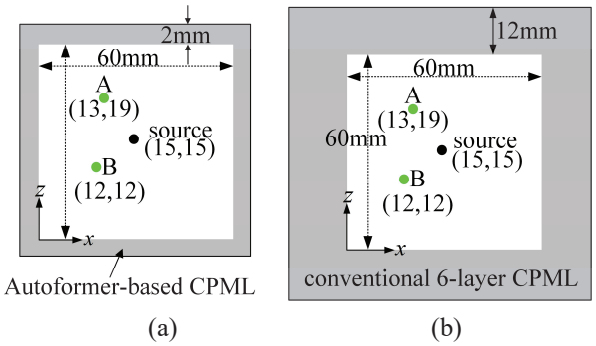

Fig. 4. Profile of a single point source: (a) Autoformer-driven CPML and (b) conventional 6-layer CPML.

To evaluate the performance of the proposed method, the relative error is defined by the following formula:

$$Error(t)_{\mathrm{dB}} = 20 \times \log_{10} \frac{|E_y(t) - E_y^{\mathrm{ref}}(t)|}{|E_y^{\mathrm{ref,max}}(t)|} \tag{11}$$

where $E_y(t)$ is the predicted electric field, $E_y^{\mathrm{ref}}(t)$ is the boundary-reflection-free reference electric field, and $E_y^{\mathrm{ref,max}}(t)$ is the maximum value of the reference electric field.

Figure 5 shows the relative errors of various methods at observation points A and B during the time intervals from $t = 600$ ps to $t = 1000$ ps, and from $t = 3600$ ps to $t = 4000$ ps. For point A, the conventional 1-layer CPML and 6-layer CPML show -11 dB and -37 dB errors, respectively. For comparison, the HTBF-based PML and LSTM-based PML, which are originally developed for the 2D FDTD method, were migrated into the WCS-FDTD framework. The input data structure was reshaped to $(15,9)$ for the LSTM model and $(1,9)$ for the HTBF model, with the output data structure being $(1,3)$ for both. To achieve optimal performance, the hidden layer sizes were set to 27 and 36 for the HTBF and LSTM models, respectively. The maximum errors of the HTBF model and LSTM model are -31 dB and 34 dB, respectively. Meanwhile, the maximum error of the Autoformer-driven CPML is only -40 dB, which is lower than that of both the conventional CPMLs and other machine-learning-driven CPMLs. For point B, the maximum relative errors of conventional 1-layer CPML, 6-layer CPML, HTBF model, LSTM model and Autoformer model are -9 dB, -35 dB, -28 dB, -32 dB and -40 dB, respectively. The Autoformer-driven CPML achieves the best wave-absorption performance.

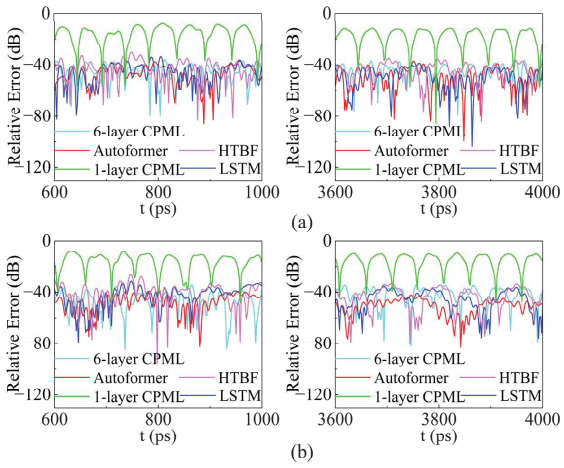

Fig. 5. Error comparison among five methods: (a) relative error at point A and (b) relative error at point B.

Since the algorithm operates in the time domain, a long-term simulation was performed to validate its stability. As shown in Fig. 6, the electric field waveform at observation point A remains stable and consistent with the conventional 120-layer CPML, even after 100,000 time steps. This result confirms that the proposed method retains high predictive stability in prolonged simulations.

To further evaluate the performance of the proposed method, Fig. 7 compares the average relative errors of these five methods across the entire computational domain. The conventional 1-layer CPML shows an average error of -13 dB, indicating ineffective waveabsorption. Moreover, the average errors for other methods are respectively -37 dB for the conventional 6-layer CPML, -30 dB for the HTBF model, -32 dB for the LSTM model and -39 dB for the Autoformer model. The proposed method achieves the lowest absorption error. Compared to the conventional 6-layer CPML, the

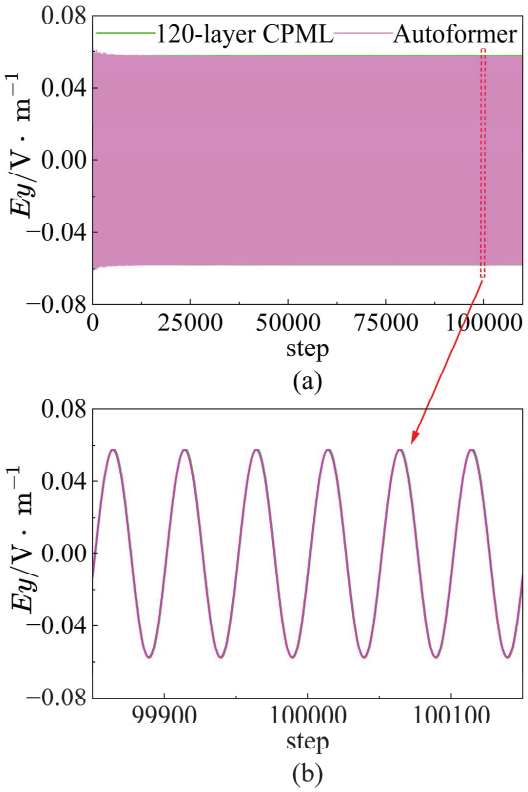

Fig. 6. Long-term stability and accuracy verification of 100,000 time steps: (a) long-term waveform diagram and (b) detailed waveform comparisons at the late stage.

proposed method's absorption effect improves by 2 dB. Besides, it demonstrates 9 dB and 7 dB improvements over the HTBF and LSTM models, respectively.

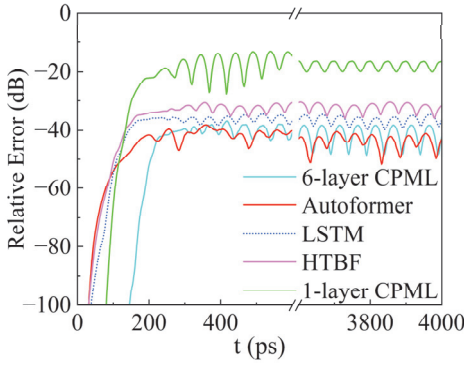

Fig. 7. The average relative error over the entire computational domain.

Table 2 records the single-step computational time for the above five methods. Completing one-step simulation, the conventional 1-layer CPML and 6-layer CPML take 0.00694 s and 0.01187 s, respectively, whereas the Autoformer-driven CPML only spends 0.00464 s. Obviously, the Autoformer-driven CPML achieves a wave-absorbing effect comparable to that of the conventional 6-layer CPML, however, its computational time is reduced by 60.9%. Unfortunately, the computational cost of the Autoformer model is higher than that of HTBF model (0.00268 s) and LSTM model (0.00305 s).

Table 2: Comparison of single-step simulation time between deep learning networks and conventional CPML methods for Case A

Method	**1-layer CPML**	**6-layer CPML**	**HTBF**	**LSTM**	**Autoformer**
Average Time (s)	0.00694	0.01187	0.00268	0.00305	0.00464

To further assess the computational efficiency of the proposed method, Fig. 8 presents the average single-step computational cost across different computational scales. Both the Autoformer-driven CPML and LSTM model are faster than the conventional CPML, and these performance advantages become increasingly significant as the grid scale increases. This is because the conventional CPML needs to calculate convolution terms grid by grid, while the deep learning driven CPMLs only predict the electromagnetic field values on the boundaries. When comparing the LSTM model and the Autoformer model, the LSTM model performs serial operations in the time dimension, whereas the Autoformer model incorporates a GPU-accelerated parallel architecture. This powerful parallel computing capability greatly saves computational time in large-scale computations. As shown in Fig. 8, although the Autoformer model has a higher computational cost than the LSTM model, the performance gap between them is gradually narrowing as the computational scale increases.

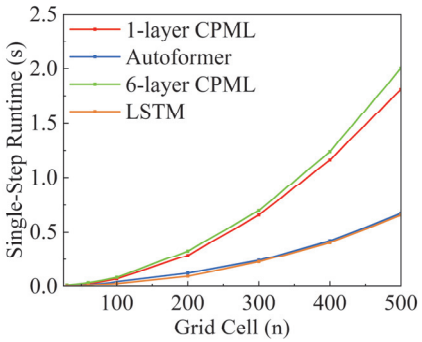

Fig. 8. Single-step simulation time of various methods under different computational scales.

B. Large domain with multiple point sources

To evaluate the generalization ability of the proposed method, a model with a large computational domain containing multiple point sources is established. Different from the training set, the computational

domain of this simulation model is expanded to 140 mm × 140 mm. As shown in Fig. 9, one point source is placed at the center of the computational domain, and the other four point sources exactly form a square. Other simulation parameters are the same as those in single source example.

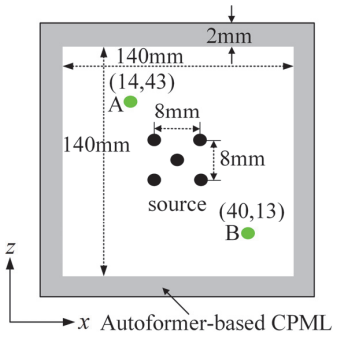

Fig. 9. Large computational domain with multiple point sources.

Figures 10 and 11 compare the relative errors of different methods. As shown in Fig. 10, the maximum relative error of the conventional 1-layer CPML reaches −7 dB at point A and −8 dB at point B, while the conventional 6-layer CPML reaches −35 dB at point A and −36 dB at point B. In contrast, the Autoformer-driven CPML exhibits the lowest errors of −38 dB at point A and −37 dB at point B. The LSTM model yields −30 dB and −32 dB at point A and B, respectively. However, in long-term simulation, the error of the HTBF model suffers from gradual accumulation, resulting in higher errors of −13 dB at point A and −11 dB at point B.

In addition, the average relative errors over the entire computational domain are shown in Fig. 11. The average error of the conventional 1-layer CPML is −13 dB. The HTBF model, due to error accumulation in long-term simulations, also has a high average error of 13 dB. Notably, the Autoformer-driven CPML achieves an average relative error of −38 dB, which is superior to the LSTM model (−33 dB) and the conventional 6-layer CPML (−37 dB).

Furthermore, Table 3 lists the single-step simulation time for each method. For a single-step computation, the conventional 1-layer CPML and conventional 6-layer CPML take 0.03508 s and 0.04565 s, respectively, whereas the LSTM model and Autoformer-driven CPML only require 0.01535 s and 0.02752 s. From the above analysis, it can be observed that when simulating scenarios more complex than those in the training set, the proposed Autoformer-driven CPML maintains high wave-absorption effectiveness with low computational cost. This preliminarily demonstrates the generalization ability of this method.

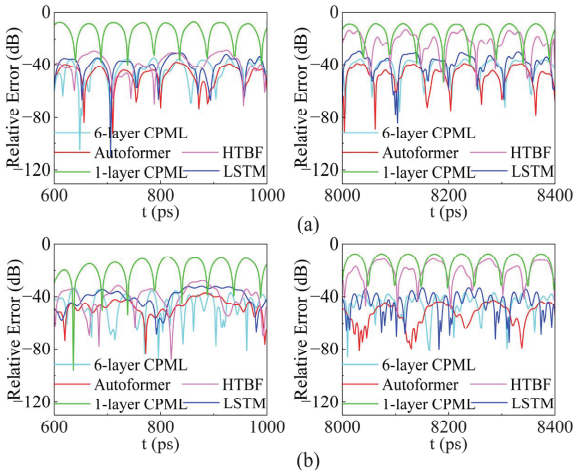

Fig. 10. Relative error of five excitation sources: (a) relative error at point A and (b) relative error at point B.

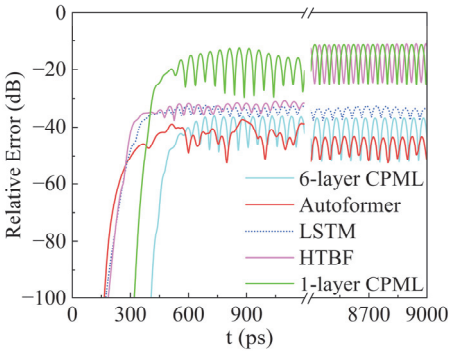

Fig. 11. The average relative error over the entire computational domain.

Table 3: Comparison of single-step simulation time between deep learning networks and conventional CPML methods for Case B

Method	1-layer CPML	6-layer CPML	LSTM	Autoformer
Average Time (s)	0.03508	0.04565	0.01535	0.02752

C. Multi-scale and multi-medium structure

To further evaluate the generalization ability of the proposed method, a complex scenario involving fine metal structures is established. As shown in Fig. 12, the key environmental parameters differing from the training set are summarized as follows:

(1) *Multi-material environment*: Two metallic blocks are introduced to create a multi-material environment, one of which contains fine structural features.

(2) *Multi-scale structures*: Fine meshes with a minimum grid size of $\Delta x_{\min} = \Delta z_{\min} = 0.2$ mm are adopted in both the X and Z directions.
(3) Large time step size: A large time step size of 4 ps is adopted. This value exceeds the limit of the CFL stability condition in the FDTD framework and the time step size used in the training set.
(4) Multiple excitation sources: Five point sources are used as the excitation sources for the simulation model.
(5) Large computational domain: The computational domain is expanded to 140 mm $\times$ 140 mm.

All other simulation parameters remain the same as those in the training set cases.

Figure 13 presents the error analysis of the specified observation points. The HTBF model initially exhibits satisfactory wave-absorption performance. However, its error accumulates over time, resulting in a decline in performance, with maximum relative errors reaching 10 dB at point A and -11 dB at point B. In contrast, other methods maintain stability. The maximum relative errors of the conventional 1-layer CPML, 6-layer CPML, and the LSTM model at point A are -9 dB, -35 dB, and -28 dB, and at point B are -8 dB, -34 dB, and 25 dB, respectively. The Autoformer-driven CPML achieves the lowest errors of -41 dB at point A and -38 dB at point B, demonstrating excellent wave-absorption performance.

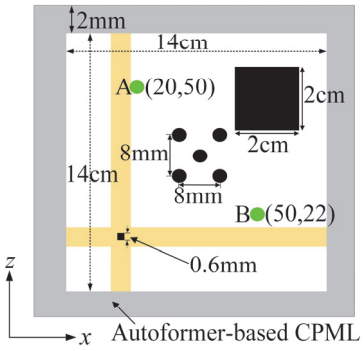

Fig. 12. A complex simulation scenario with five excitation sources, a large computational domain, and multiple metal blocks.

Subsequently, the average relative errors of these methods are discussed. As shown in Fig. 14, the HTBF model gradually accumulates errors after 9000 ps, eventually reaching -13 dB. The error of the LSTM model increases to -27 dB, while the Autoformer model maintains a lower error of -38 dB, comparable to that of the conventional 6-layer CPML (-36 dB). It is evident that the proposed model exhibits excellent wave-absorption performance with a larger time step size. Notably, the

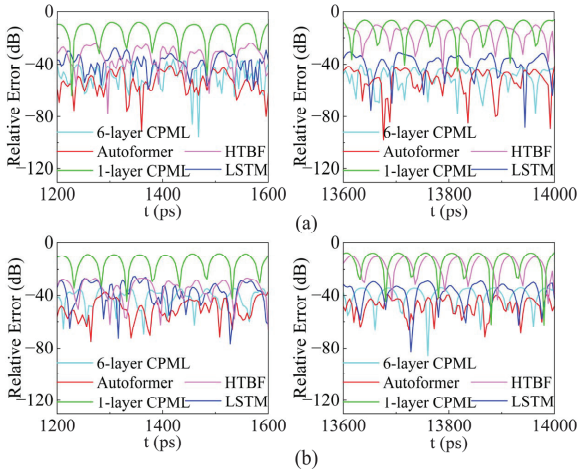

Fig. 13. The relative errors of the five methods: (a) relative error at point A and (b) relative error at point B.

time step size of 4 ps breaks through the CFL limit of the FDTD framework, enabling a significant expansion of the application range for intelligent absorption boundaries.

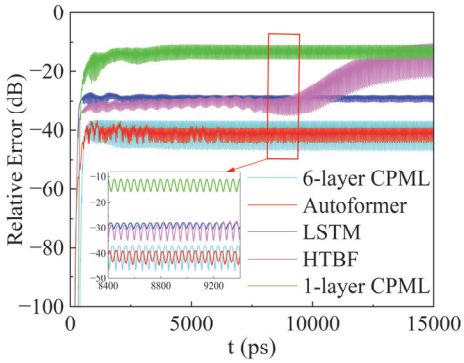

Fig. 14. The average relative error over the entire computational domain.

In addition, as shown in Table 4, for single-step simulation, the Autoformer-driven CPML takes 0.02537 s, which is slightly longer than the 0.01875 s required by the LSTM model, but significantly shorter than the 0.04857 s of the conventional 1-layer CPML and 0.06307 s of the conventional 6-layer CPML. Obviously, compared with conventional CPMLs, the proposed method achieves comparable wave-absorption performance to the conventional 6-layer CPML while reducing computation time by 59.79%. Relative to the LSTM model, it exhibits a 11 dB improvement in wave-absorption performance. Furthermore, as the computational scale increases, the additional time cost decreases from 52.13 % to 35.25%, indicating that the efficiency gap diminishes at larger scales. From the above analysis, it can be concluded that even in scenarios

considerably more complex than the training set, the proposed method maintains excellent wave-absorption performance and fast simulation, which validates the robustness of the proposed method. This robustness holds for electromagnetic environments with multiple media, multiple sources, multiple scales, large time step sizes, and large computational domains, underscoring the method's potential as a practical tool for engineering applications.

Table 4: Comparison of single-step simulation time between deep learning networks and conventional CPML methods for Case C

Method	**1-layer CPML**	**6-layer CPML**	**LSTM**	**Autoformer**
Average Time (s)	0.04857	0.06307	0.01875	0.02537

IV. CONCLUSION

This paper proposes an Autoformer-driven CPML for the WCS-FDTD framework to improve the efficiency of open-region simulations. The Autoformer-based CPML employs a single-layer structure to replace the conventional multi-layer CPML, significantly reducing both the computational domain scale and algorithmic complexity. Compared to the conventional CPMLs and other deep-learning-driven PML approaches, this new model provides superior wave-absorption effectiveness and high computational efficiency. Integrated into the WCS-FDTD framework, this method overcomes CFL stability constraints, substantially expanding the modeling scope of intelligent absorption boundaries. Furthermore, the proposed method exhibits satisfactory wave-absorption performance and excellent generalization capability in complex scenarios involving multi-material environments, multi-source excitations, multi-scale structures, large computational domains, and extended time step sizes. Moreover, by adjusting the sampling strategy and modifying the input-output dimensions, this proposed method can be extended to 3D scenes, which constitutes a key direction for our future work.

ACKNOWLEDGMENT

This work was supported in part by the State Key Laboratory of Millimeter Waves under Grant K202518 and in part by the Zhejiang Provincial Natural Science Foundation of China under Grant LQN25F010010 and LQN25F010011.

REFERENCES

[1] A. Taflove and S. C. Hagness, *Computational Electrodynamics: The Finite-Difference Time-Domain Method*, 3rd ed. Boston, MA, USA: Artech House, 2005.

[2] W. Sun, "Automatic and efficient surface FDTD mesh generation for analysis of EM scattering and radiation," *Applied Computational Electromagnetics Society (ACES) Journal*, vol. 9, no. 2, pp. 162–169, July 2022.

[3] K. S. Yee, "Numerical solution of initial boundary value problems involving Maxwell's equations in isotropic media," *IEEE Trans. Antennas Propagat.*, vol. AP-14, pp. 302–307, 1966.

[4] R. Courant, K. Friedrichs, and H. Lewy, "On the partial difference equations of mathematical physics," *IBM J. Res. Dev.*, vol. 11, no. 2, pp. 215–234, Mar. 1967.

[5] J. Chen and J. Wang, "A novel WCS-FDTD method with weakly conditional stability," *IEEE Trans. Electromagn. Compat.*, vol. 49, no. 2, pp. 419–426, 2007.

[6] J. Chen, "Improved weakly conditionally stable finite-difference time-domain method," *Applied Computational Electromagnetics Society (ACES) Journal*, vol. 27, no. 5, pp. 413–419, Feb. 2022.

[7] J. Chen and H. Mai, "A review of weakly conditional stable finite-difference time-domain method for modeling electromagnetic problems with fine structures," *Int. J. Numer. Model.: Electron. Networks, Devices Fields*, vol. 31, no. 5, p. e2341, 2018.

[8] G. Mur, "Absorbing boundary conditions for the finite-difference approximation of the time-domain electromagnetic-field equations," *IEEE Trans. Electromagn. Compat.*, vol. EMC-23, no. 4, pp. 377–382, 1981.

[9] B. Engquist and A. Majda, "Absorbing boundary conditions for the numerical simulation of waves," *Math. Comput.*, vol. 31, no. 139, pp. 629–651, 1977.

[10] J.-P. Berenger, "A perfectly matched layer for the absorption of electromagnetic waves," *J. Comput. Phys.*, vol. 114, no. 2, pp. 185–200, 1994.

[11] J.-P. Berenger, "Perfectly matched layer for the FDTD solution of wave-structure interaction problems," *IEEE Trans. Antennas Propag.*, vol. 44, no. 1, pp. 110–117, 1996.

[12] A. P. Zhao, "Uniaxial perfectly matched layer media for an unconditionally stable 3-D ADI-FD-TD method," *IEEE Microw. Wireless Compon. Lett.*, vol. 12, no. 12, pp. 497–499, 2002.

[13] L. Bernard, R. R. Torrado, and L. Pichon, "Efficient implementation of the UPML in the generalized finite-difference time-domain method," *IEEE Trans. Magn.*, vol. 46, no. 8, pp. 3492–3495, 2010.

[14] J. A. Roden and S. D. Gedney, "Convolutional PML (CPML): An efficient FDTD implementation of the CFS-PML for arbitrary media," *Microw. Opt. Technol. Lett.*, vol. 27, no. 5, pp. 334–339, 2000.

[15] S. D. Gedney, "An auxiliary differential equation formulation for the complex-frequency shifted PML," *IEEE Trans. Antennas Propag.*, vol. 58, no. 3, pp. 838–847, 2010.
[16] R. Martin and D. Komatitsch, "An unsplit convolutional perfectly matched layer technique improved at grazing incidence for the viscoelastic wave equation," *Geophys. J. Int.*, vol. 179, no. 1, pp. 333–344, 2009.
[17] H. M. Yao and L. Jiang, "Machine-learning-based PML for the FDTD method," *IEEE Antennas Wireless Propag. Lett.*, vol. 18, no. 1, pp. 192–196, 2018.
[18] H. M. Yao and L. Jiang, "Enhanced PML based on the long short-term memory network for the FDTD method," *IEEE Access*, vol. 8, pp. 21028–21035, 2020.
[19] H. H. Zhang, H. M. Yao, L. Jiang, and M. Ng, "Deep long short-term memory networks-based solving method for the FDTD method: 2-D case," *IEEE Microw. Wirel. Technol. Lett.*, vol. 33, no. 5, pp. 499–502, May 2023.
[20] L. Guo, M. Li, S. Xu, F. Yang, and L. Liu, "Electromagnetic modeling using an FDTD-equivalent recurrent convolution neural network: Accurate computing on a deep learning framework," *IEEE Antennas Propag. Mag.*, vol. 65, no. 1, pp. 93–102, Feb. 2023.
[21] N. Feng, Y. Chen, Y. Zhang, M. S. Tong, Q. Zeng, and G. P. Wang, "An expedient DDF-based implementation of perfectly matched monolayer," *IEEE Microwave and Wireless Components Letters*, vol. 31, no. 6, pp. 541–544, June 2021.
[22] Y. Chen, Y. Zhang, H. Wang, N. Feng, L. Yang, and Z. Huang, "Differentiable-decision-tree-based neural Turing machine model integrated into FDTD for implementing EM problems," *IEEE Trans. Electromagn. Compat.*, vol. 65, no. 6, pp. 1579–1586, Dec. 2023.
[23] N. Feng, H. Wang, Z. Zhu, Y. Zhang, L. Yang, and Z. Huang, "Gradient boosting decision tree-based PMM model integrated into FDTD method for solving subsurface sensing problems," *IEEE Transactions on Antennas and Propagation*, vol. 72, no. 7, pp. 5892–5899, July 2024.
[24] H.-Y. Ren, X.-H. Wang, T. Wei, and L. Wang, "Recurrent neural network-assisted truncation of convolutional perfectly matched layers for FDTD," *IEEE Antennas Wireless Propag. Lett.*, vol. 23, no. 5, pp. 1493–1497, 2024.
[25] H. Wu, J. Xu, J. Wang, and M. Long, "Autoformer: Decomposition transformers with auto-correlation for long-term series forecasting," *Adv. Neural Inf. Process. Syst.*, vol. 34, pp. 22419–22430, 2021.
[26] Z. Shen, J. Lu, L. Gui, J. Li, Y. He, D. Yin, and X. Sun, "SSA: A content-based sparse attention mechanism," *Int. Conf. Knowl. Sci. Eng. Manag. Dig.*, pp. 669–680, 2022.

Yumeng Wu was born in Zhejiang, China, in 2004. He is currently working toward the B.S. degree in Electronic Science and Technology at Hangzhou Dianzi University, China. His current research interests include computational electromagnetics and deep learning.

Ning Xu received the Ph.D. degree in electromagnetic fields and microwave techniques at Xi'an Jiaotong University, Xi'an, China, in 2021. She was a visiting student with the On-Chip Electromagnetics Group, School of Electrical and Computer Engineering, Purdue University, West Lafayette, IN, USA. She now serves as a researcher at Hangzhou Dianzi University, China. Her current research interests include computational electromagnetics especially the FDTD method, graphene and terahertz electronics.

Yexin Li was born in Anhui, China. He received the B.E. degree from Anhui Agricultural University, China, in 2019, in electronic information engineering. He is currently pursuing an M.S. degree at Hangzhou Dianzi University. His research interests include computational electromagnetism and deep learning.

Kuiwen Xu (Member, IEEE) received his B.E. degree in Electronics and Information Engineering from Hangzhou Dianzi University, Hangzhou, China, in 2009, and his Ph.D. degree from the Department of Information and Electronic Engineering at Zhejiang University, Hangzhou, 2014. He was invited to the State Key Laboratory of Terahertz and Millimeter Waves, City University of Hong Kong, Hong Kong, as a Visiting Professor, in 2018. Since September 2015, he has been with Hangzhou Dianzi University, Hangzhou, where he is currently a professor. His research interests include electromagnetic inverse problems, RF measurement and microwave imaging, and AI-inspired inverse design of RF devices.

Juan Chen was born in Chongqing, China. She received the Ph.D. degree from Xi'an Jiaotong University, Xi'an, China, in 2008, in electromagnetic field and microwave technology. She is currently working in Xi'an Jiaotong University, Xi'an, as a professor. Her research interests include the computational electromagnetics and microwave device design.

A Hybrid Optimization Strategy of Random Forest and Differential Evolution Algorithm for Wideband Antennas

Gengtao Huang and Chen Ding

School of Information Engineering
Guangdong University of Technology, Guangzhou 510006, China
2112303184@mail2.gdut.edu.cn, cdinghk@outlook.com

Abstract – This paper presents a hybrid optimization strategy for wideband antenna design that leverages the strengths of both Random Forest (RF) and Differential Evolution (DE) algorithms. The strategy employs DE for iteratively updating antenna parameters and RF for feature selection in the process of antenna performance optimization. Initially, DE is applied to update antenna parameters for a predetermined number of iterations, generating a dataset of antenna performance metrics. This dataset is then used to train an RF model, which identifies the importance of each design variable. Feature selection, guided by the RF-derived importance, is applied to reduce the dimensionality of the search space. DE subsequently continues the optimization process within this reduced parameter space. Validation of this hybrid approach is performed through the design of a wideband slot antenna and compared against standalone DE, Genetic Algorithm (GA), Particle Swarm Optimization (PSO), and Simulated Annealing (SA). Results demonstrate that the proposed strategy significantly accelerates convergence, achieving the target reflection coefficient and gain with substantially fewer iterations than the other methods (reductions of 75.56%, 45%, 42.11%, and 50% compared to DE, GA, SA, and PSO, respectively). Furthermore, the hybrid strategy consistently finds superior solutions exhibiting lower loss values compared to the benchmark algorithms. The method offers a computationally efficient, interpretable, and effective approach to antenna optimization.

Index Terms – Antenna, Differential Evolution (DE) algorithm, feature selection, Random Forest (RF) algorithm.

I. INTRODUCTION

Antenna performance critically impacts wireless communication systems' efficiency and reliability [1]. Traditional design methods rely on High Frequency Structure Simulator (HFSS) or Computer Simulation Technology (CST) simulations and empirical adjustments, requiring iterative parameter tuning and hundreds of electromagnetic simulations for optimization a time-intensive process [2]. With emerging technologies like antenna arrays [3, 4] and broadband circularly polarized antennas [5, 6] increasing design complexity, conventional approaches face limitations. This underscores the urgent need for automated optimization methods to enhance design efficiency and address modern performance demands.

Meta-heuristic algorithms, inspired by natural phenomena and physical processes, have gained prominence in AI-driven optimization. These methods fall into four categories: evolutionary (e.g., DE [7], Genetic Algorithm (GA) [8]), swarm-based (e.g., Particle Swarm Optimization (PSO) [9]), human-inspired (e.g., Teaching-Learning-Based Optimization, TLBO [10]), and physics- or chemistry-based (e.g., Simulated Annealing (SA) [11]). While they enhance antenna design accuracy and efficiency, their reliance on thousands of simulation iterations to approach global optima still results in prolonged optimization cycles, limiting time-sensitive applications.

Advances in computing power have driven machine learning (ML) integration in antenna optimization, with approaches like Artificial Neural Network (ANN)-based multi-fidelity modeling [12], Random Forest (RF)-augmented models [13], Support Vector Machine (SVM)-Gaussian hybrids [14] serving as surrogate models and Convolutional Neural Networks (CNN)-aided Reinforcement Learning (RL) [15]. While these surrogates accelerate electromagnetic simulation predictions, they face challenges: limited generalization across environmental conditions and dependence on time-intensive electromagnetic simulation datasets for training [2].

This paper presents a hybrid optimization method for wideband antenna design using RF and Differential Evolution (DE) algorithms. DE generates a dataset by iteratively updating antenna parameters for RF model training. The RF model assesses each design variable's importance for feature selection to reduce search space dimensionality, after which DE optimizes within this

Submitted On: April 07, 2025
Accepted On: February 01, 2026

https://doi.org/10.13052/2026.ACES.J.410104

reduced space. Validation via wideband slot antenna design shows this hybrid method significantly reduces iterations compared to standalone DE, GA, PSO, and SA, and consistently finds better solutions with lower loss. It offers a computationally efficient, interpretable, and effective antenna optimization solution.

The remainder of this paper is organized as follows. Section II introduces DE and RF fundamentals. Section III details the hybrid strategy. Section IV presents a case study, followed by conclusions in section V.

II. FUNDAMENTAL ALGORITHM

A. Random Forest

RF is an ensemble learning method utilizing decision trees with Bagging integration and randomized training [16]. Each tree is trained on distinct data subsets, reducing errors through complementary predictions. Key advantages include high accuracy, robustness, overfitting resistance, and feature importance analysis for high-dimensional data. As shown in Fig. 1, RF aggregates results from multiple trees: classification uses majority voting, while regression employs averaging, ensuring reliable predictions across diverse tasks.

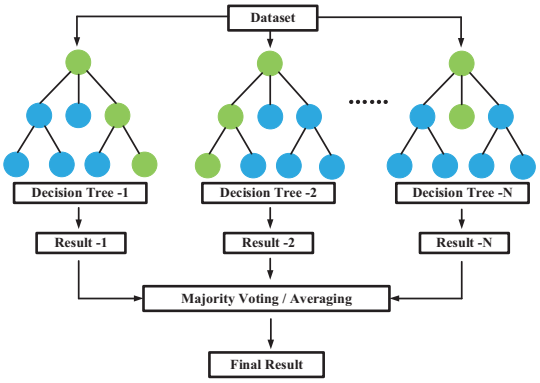

Fig. 1. Workflow of Random Forest.

B. Differential Evolution algorithm

The DE algorithm is a population-based optimization method inspired by natural evolution, employing mutation, crossover, and selection operations to iteratively refine solutions [17]. As shown in Fig. 2, DE initializes a population and iteratively updates it through differential mutation, crossover, and competitive selection until convergence. Its strengths lie in differential vector-driven global exploration, gradient-free optimization for non-differentiable functions, and robustness in escaping local optima within high-dimensional spaces. These attributes, combined with inherent parallelism, make DE particularly effective for complex electromagnetic design problems requiring broad search capabilities and adaptability.

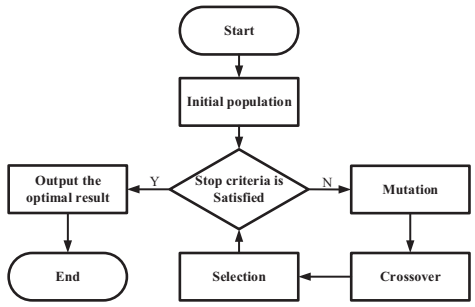

Fig. 2. Workflow of Differential Evolution algorithm.

III. HYBRID OPTIMIZATION STRATEGY

The workflow of the hybrid optimization strategy is illustrated in Fig. 3, and the corresponding pseudo-code is presented in Table 1. The specific steps of the algorithm are as follows.

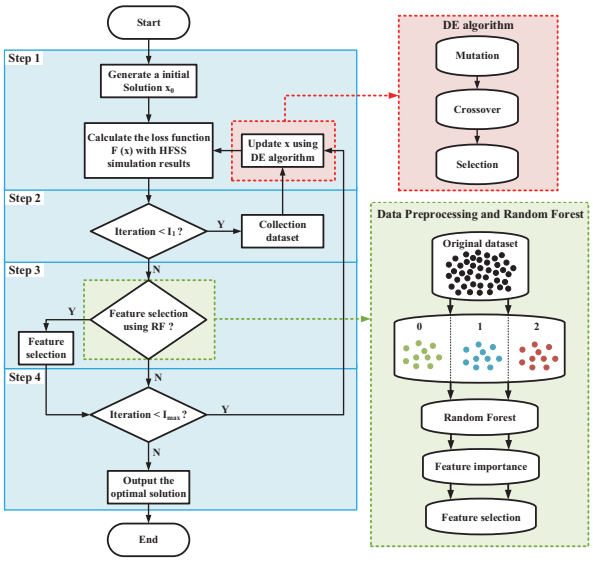

Fig. 3. Workflow of hybrid optimization strategy.

Step 1: Initialization is performed. The initial target x_0, representing the initial values of the antenna optimization variables, is input into HFSS for simulation. The loss function $F(x_0)$ is calculated to obtain the loss value, after which the process proceeds to Step 2.

Step 2: If the iteration count has not reached I_1, store the HFSS simulation data and use the DE algorithm to update the antenna variables through mutation, crossover, and selection, then simulate in HFSS to calculate $F(x)$ and return to Step 2. The process of updating the antenna variables, as shown in the red block diagram in Fig. 1. If the iteration count reaches I_1, then proceed to Step 3.

Step 3: If feature selection using RF is enabled, the dataset from Step 2 is preprocessed and classified into

Table 1: Pseudo-code of the proposed hybrid optimization strategy

	Algorithm: Hybrid Optimization strategy for Antenna Design
1	begin
2	initialize $x = x_0, x_{space}, I_{max}, I_1$ and dataset D
3	for $i = 1$ to I_{max} do
4	if $i < I_1$ then
5	simulate x in HFSS, calculate loss $F(x)$
6	store $(x, S_{11}(x))$ in D
7	update x using DE algorithm
8	else
9	if feature selection is enabled then
10	preprocess D (classify into $0, 1, 2$)
11	train RF model, perform feature selection
12	update x_{space} with feature selection
13	end
14	update x using DE algorithm
15	simulate x in HFSS, calculate loss $F(x)$
16	end
17	end
18	output optimal solution
19	end

0 (bad), 1 (medium), and 2 (good). This classified data is used to train the RF, obtaining feature importance for selection. The process of data preprocessing and RF is shown in the green block diagram in Fig. 1. If not enabled, this step is skipped. (It should be noted that when the dimensions of the antenna are high, Step 3 can be activated multiple times during the algorithm execution process for multiple rounds of feature selection.)

Step 4: If the maximum preset iteration count I_{max} has not been reached, use the DE algorithm to update the antenna optimization variables, calculate the loss function $F(x)$, and return to Step 2. If I_{max} is reached, output the optimal solution and the process is terminated.

IV. CASE STUDY

This section analyzes antenna optimization simulations using hybrid optimization strategies and four benchwork algorithms. The experiment has a preset maximum of 100 iterations ($I_{max} = 100$) and 20 data collection iterations ($I_1 = 20$). Each generation's population size is 10, and a loss value of -60 is acceptable. The hybrid optimization strategy runs three times, with Step 3 performed once per execution due to the antenna's low number of optimization variables.

A. Structure of the wideband slot antenna

The structure, variables, and boundaries of the wideband slot antenna are shown in Fig. 4. The antenna is used to verify the effectiveness of the hybrid optimization strategy [18]. The antenna uses an FR4 substrate with a relative permittivity of 4.4, a loss tangent of 0.02, and a thickness of 1.6 mm. The design involves a square slot on one side of the substrate and a small branch within the slot. To highlight the hybrid strategy's benefits, minor antenna modifications are introduced, expanding the search space by one dimension.

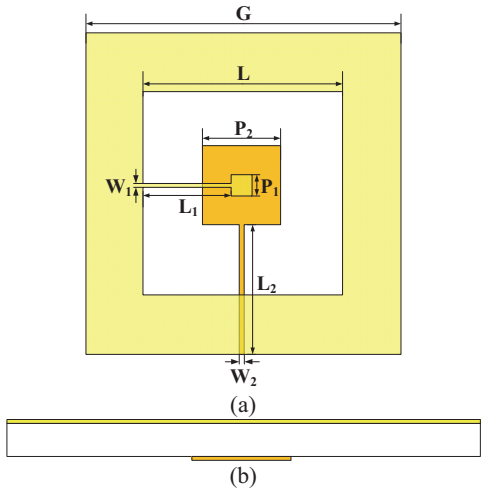

Fig. 4. Wideband slot antenna: (a) perspective and (b) side view.

B. Settings before optimization

Table 2 presents the optimization variables for the antenna, detailing each parameter's search space. The algorithm operates within an 8-dimensional search space. Additionally, two optimization objectives have been established for the antenna. The first objective concerns the antenna reflection coefficient, which must be below -10.0 dB between 1.5 GHz and 4.2 GHz, with a particular emphasis on maintaining an average below -15 dB throughout the entire operating band. The second objective pertains to the antenna gain, requiring an average exceeding 3.8 dB within the operational frequency range.

Table 2: Optimization variable of wideband slot antenna (unit: mm)

Variable	**Boundary**
G	$[75.0, 85.0]$
L	$[44.0, 64.0]$
L_1	$[10.0, 30.0]$
L_2	$[14.0, 45.0]$
W_1	$[0.5, 1.5]$
W_2	$[0.5, 1.5]$
P_1	$[4.0, 10.0]$
P_2	$[16.0, 22.0]$

This optimization involves two inherently coupled performance metrics: S_{11} and Gain. To ensure balanced consideration of both objectives without excessively prioritizing one at the expense of the other, a product-form loss function is employed. To address these requirements, this paper introduces a loss function $F(x)$, as defined in equation (1):

$$F(x) = \omega f_1(x) \times f_2(x), \tag{1}$$

where $x = [G, L, L_1, L_2, W_1, W_2, P_1, P_2]$ is the value of the optimization variable, ω is the weight coefficient, $f_1(x)$ is the function of the optimization objective 1, $f_2(x)$ is the function of the optimization objective 2. The details of $f_1(x)$ and $f_2(x)$ are shown in equations (2) and (3) respectively:

$$f_1(x) = \begin{cases} avg(S_{11}(x) \mid S_{11} < -10\,dB, \\ \qquad f \in [1.5,\ 4.2]), & \text{(I)} \\ avg(S_{11}(x) \mid S_{11} < -10\,dB, \\ \qquad f \notin [1.5,\ 4.2]), & \text{(II)} \\ min(S_{11}(x) \mid S_{11} > -10\,dB), & \text{(III)} \end{cases} \tag{2}$$

$$f_2(x) = avg(Gain(x) \mid f_1(x)) \tag{3}$$

where condition (I) requires that under the optimization variable x, the value of S_{11} in the frequency range [1.5, 4.2] GHz from EM simulation must be less than -10 dB. Here, $f_1(x)$ is defined as the average value of S_{11} below -10 dB, with a weight coefficient ω set to 1. Condition (II) specifies that under the optimization variable x, the value of S_{11} outside the frequency range [1.5, 4.2] GHz from EM simulation must be less than -10 dB. In this case, $f_1(x)$ is also the average value of S_{11} below 10 dB, but the weight coefficient ω is set to 0.5. Condition (III) encompasses all other conditions not covered by Conditions (I) and (II). For this condition, $f_1(x)$ is defined as the minimum value of S_{11}, and the weight coefficient ω is set to 0.1. Equation (3) states that for any condition, $f_2(x)$ is the average gain within the frequency range used by $f_1(x)$ under that same condition. This setting of weight coefficients aims to enhance the loss value for better solutions and worsen it for poorer solutions, thereby improving search efficiency and subsequently boosting the optimization efficiency of the antenna.

C. Feature selection result of slot antenna

Table 3 presents the feature importance, algorithm training accuracy, and feature selection results for the triple hybrid optimization strategy. As indicated by these results, the feature selection for the wideband slot antenna under the three times hybrid optimization strategies are P_2, P_1, and $\{P_1, W_1\}$ for DERF1, DERF2, and DERF3, respectively. These selected features are subsequently removed from the antenna parameters to achieve dimensionality reduction. Through this process, the search space of the antenna is effectively reduced, thereby enhancing the optimization efficiency and speed.

Table 3: Feature importance of hybrid optimization strategy

Feature	DERF1	DERF2	DERF3
G	0.1067	0.0881	0.1117
L	0.1095	0.0990	0.0998
L_1	0.1012	0.0940	0.1105
L_2	0.3134	0.2915	0.2943
W_1	0.1446	0.0928	0.0788
W_2	0.0823	0.1296	0.1312
P_1	0.0808	0.0745	0.0724
P_2	0.0615	0.1305	0.1016
Accuracy	0.9167	0.8667	0.8867
Feature selection	P_2	P_1	P_1, W_1

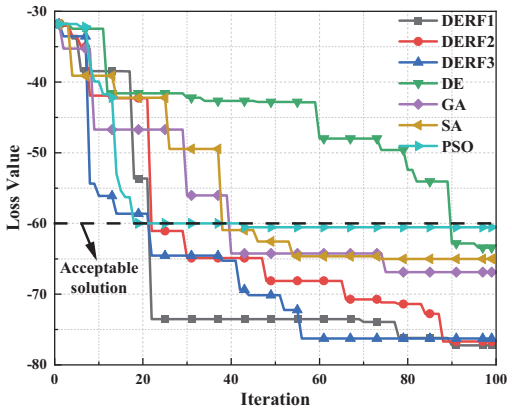

Fig. 5. Loss value with the number of iterations.

D. Results of algorithm comparison

Figure 5 illustrates the comparative iterative loss values for the hybrid optimization strategy and meta-heuristic algorithms. Additionally, Fig. 6 presents the S_{11} and gain graphs for each algorithm. The above simulation results are summarized and analyzed in Table 4. The hybrid strategy converges consistently in three runs, needing 22 iterations to reach the target loss of -60 (with the first 20 for data collection). In comparison, DE, GA, SA, and PSO require 90, 40, 38, and 44 iterations, respectively. The hybrid strategy's loss value exceeds -75, while others reach about -65. Thus, the hybrid optimization strategy reduces iterations for acceptable solutions and finds better solutions in antenna optimization.

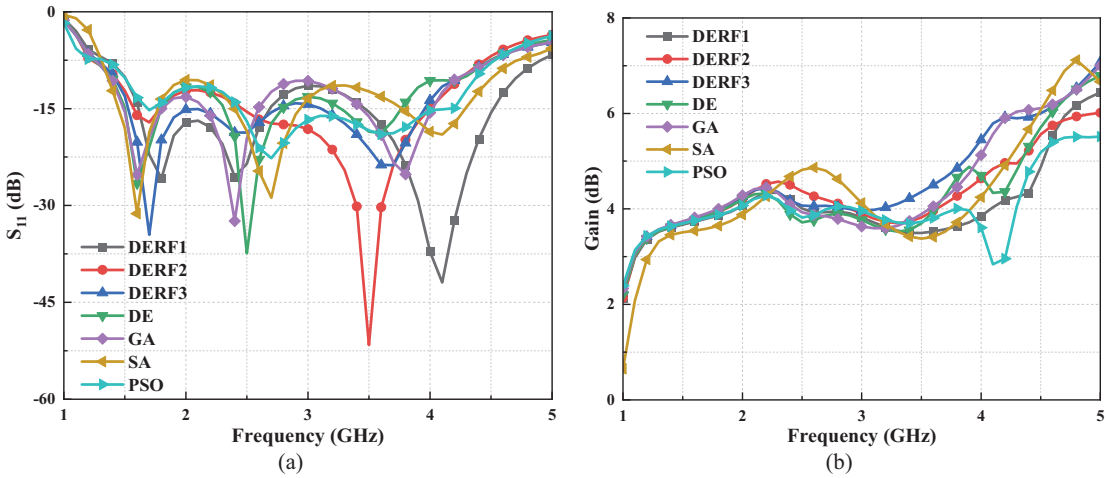

Fig. 6. Simulation (a) S_{11} and (b) Gain.

Table 4: Performance comparison of each algorithm

Algorithm	F(x)	$F(x) < -60$	$S_{11} < -10$ dB	Avg (S_{11})	Avg (Gain)
DERF1	−77.241	22	1.5–4.7 GHz	−19.157	4.032
DERF2	−76.695	22	1.5–4.2 GHz	−18.463	4.154
DERF3	−76.278	22	1.5–4.2 GHz	−17.463	4.368
DE[3]	−63.417	90	1.4–4.2 GHz	−15.874	3.995
GA[4]	−66.872	40	1.4–4.2 GHz	−16.141	4.143
SA[5]	−65.004	38	1.4–4.5 GHz	−15.555	4.179
PSO [7]	−60.528	44	1.5–4.3 GHz	−15.750	3.843

V. CONCLUSION

This paper introduced a hybrid optimization strategy for wideband antenna design, integrating Random Forest (RF) for feature selection with Differential Evolution (DE) for parameter optimization. The DE algorithm generates a dataset of antenna performance metrics, which is then used by RF to rank the importance of each design variable. This ranking enables a dimensionality reduction of the search space through feature selection, significantly accelerating the subsequent DE-driven optimization. The efficacy of this approach was demonstrated through the design of a wideband slot antenna. Comparative studies against standalone DE, GA, PSO, and SA algorithms revealed that the hybrid strategy achieves substantially faster convergence, requiring significantly fewer iterations to reach a target performance level. Moreover, the proposed method consistently discovered higher-quality solutions, as evidenced by lower loss values. The results clearly validate the proposed hybrid DE-RF strategy as a computationally efficient and effective approach for wideband antenna optimization, offering both improved convergence speed and superior solution quality. The interpretability provided by the RF feature importance analysis is an additional advantage, offering insights into the design process.

ACKNOWLEDGMENT

This work is supported by National Natural Science Foundation of China under Grant 62401159, and Guangdong Basic and Applied Basic Research Foundation under grants 2023A1515011334.

REFERENCES

[1] S. Koziel and A. Pietrenko-Dabrowska, "Efficient simulation-based global antenna optimization using characteristic point method and nature-inspired metaheuristics," *IEEE Trans. Antennas Propag.*, vol. 72, no. 4, pp. 3706–3717, Apr. 2024.

[2] Z. Wei, Z. Zhou, P. Wang, J. Ren, Y. Yin, G. F. Pedersen, and M. Shen, "Automated antenna design via domain knowledge-informed reinforcement learning and imitation learning," *IEEE Trans. Antennas Propag.*, vol. 71, no. 7, pp. 5549–5557, July 2023.

[3] C. Zhao, W. Jiang, W. Hu, and Y. Gao, "In-band RCS reduction method for the Vivaldi array antennas based on the manipulation of the antenna mode scattering field," *IEEE Trans. Antennas Propag.*, vol. 72, no. 5, pp. 4687–4692, May 2024.

[4] Y. Gou, Y. Chen, and S. Yang, "Radar cross section reduction of wideband Vivaldi antenna arrays with array-level scattering cancellation," *IEEE Trans.*

Antennas Propag., vol. 70, no. 8, pp. 6740–6750, Aug. 2022.

[5] Y. Cheng and Y. Dong, "Wideband circularly polarized split patch antenna loaded with suspended rods," *IEEE Antennas Wirel. Propag. Lett*., vol. 20, no. 2, pp. 229–233, Feb. 2021.

[6] Z. Qi, Y. Zhu, and X. Li, "Compact wideband circularly polarized patch antenna array using self-sequential rotation technology," *IEEE Antennas Wirel. Propag. Lett*., vol. 21, no. 4, pp. 700–704, Apr. 2022.

[7] Y. Ding, Y.-C. Jiao, L. Zhang, and B. Li, "Solving port selection problem in multiple beam antenna satellite communication system by using Differential Evolution algorithm," *IEEE Trans. Antennas Propag*., vol. 62, no. 10, pp. 5357–5361, Oct. 2014.

[8] A. J. Kerkhoff and H. Ling, "Design of a band-notched planar monopole antenna using Genetic Algorithm optimization," *IEEE Trans. Antennas Propag*., vol. 55, no. 3, pp. 604–610, Mar. 2007.

[9] A. A. Minasian and T. S. Bird, "Particle swarm optimization of microstrip antennas for wireless communication systems," *IEEE Trans. Antennas Propag*., vol. 61, no. 12, pp. 6214–6217, Dec. 2013.

[10] F. Zadehparizi and S. Jam, "Increasing reliability of frequency-reconfigurable antennas," *IEEE Antennas Wirel. Propag. Lett*., vol. 17, no. 5, pp. 920–923, May 2018.

[11] S. J. Freethy, V. F. Shevchenko, and R. G. L. Vann, "Optimization of wide field interferometric arrays via simulated annealing of a beam efficiency function," *IEEE Trans. Antennas Propag*., vol. 60, no. 11, pp. 5442–5446, Nov. 2012.

[12] J. Tan, Y. Shao, J. Zhang, and J. Zhang, "Efficient antenna modeling and optimization using multifidelity stacked neural network," *IEEE Trans. Antennas Propag.*, vol. 72, no. 5, pp. 4658–4663, May 2024.

[13] J. Zhang, J. Xu, Q. Chen, and H. Li, "Machine-learning-assisted antenna optimization with data augmentation," *IEEE Antennas Wirel. Propag. Lett*., vol. 22, no. 8, pp. 1932–1936, Aug. 2023.

[14] J. Gao, Y. Tian, and X. Chen, "Antenna optimization based on co-training algorithm of Gaussian process and support vector machine," *IEEE Access*, vol. 8, pp. 211380–211390, 2020.

[15] J. Dou, "Convolutional neural networks aided reinforcement learning for accelerated optimization of antenna topology," *Applied Computational Electromagnetics Society (ACES) Journal*, vol. 40, no. 01, pp. 35–41, Jan. 2025.

[16] L. Breiman, "Random Forests," *MACH LEARN*, vol. 45, no. 1, pp. 5–32, 2001.

[17] R. Storn and K. Price, "Differential Evolution: A simple and efficient heuristic for global optimization over continuous spaces," *J. Glob. Optim*., vol. 11, no. 4, pp. 341–359, 1997.

[18] Y. Sung, "A printed wide-slot antenna with a modified L-shaped microstrip line for wideband applications," *IEEE Trans. Antennas Propag*., vol. 59, no. 10, pp. 3918–3922, Oct. 2011.

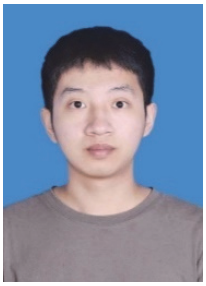

Gengtao Huang was born in Shantou, Guangdong, China, in 2000. He received the B.S. degree in communication engineering from Dongguan University of Technology, Dongguan, in 2023. He is currently pursuing the M.S. degree at Guangdong University of Technology, Guangzhou. His research interests include microwave radar antennas, circularly polarized antennas, and antenna optimization simulation by machine learning.

Chen Ding (S'16–M'20) was born in Weifang, Shandong, China. He received the B.S. degree in Mathematics from the Chinese University of Hong Kong in 2012. He joined the industry as an electronic and software engineer from 2012 to 2014. He received the M.S. degree in Electronic and Information Engineering from City University of Hong Kong in 2015. From 2015 to 2016, he worked as a research assistant with the State Key Laboratory of Millimeter-Waves, City University of Hong Kong. He received the Ph.D. degree in electrical engineering from City University of Hong Kong in 2020.

He joined Guangdong University of Technology as an Associate Professor in 2020. His current research interests include low-profile antennas, millimeter-wave antennas, circularly-polarized antennas, and antenna measurement methods. He was the first prize winner of best student paper award in 2019 IEEE International Symposium on Antennas and Propagation (AP-S 2019) which was held in Atlanta, USA. He was the winner for the Best Student Paper Prize in 2019 Asia-Pacific Microwave Conference (APMC 2019) held in Singapore. He was also the first-prize winner for the Best Student Paper Award in the 9th Asia-Pacific Conference on Antennas and Propagation (APCAP 2020).

A Semi-Supervised Electromagnetic Imaging Algorithm Based on Generative Adversarial Networks

Chun Xia Yang[1], Chi Zhou[1], Shuang Wei[1], and Mei Song Tong[2]

[1]Shanghai Engineering Research Center of Intelligent Education and Bigdata
Shanghai Normal University, Shanghai 200234, China
chunxiay@shnu.edu.cn, 1000528179@smail.shnu.edu.cn, weishuang@shnu.edu.cn

[2]Department of Electronic Science and Technology
Tongji University, Shanghai 201804, China
mstong@tongji.edu.cn

Abstract – In electromagnetic imaging applications, acquiring labeled data for supervised learning poses a significant challenge due to the high cost and time-consuming annotation processes. To address this limitation, we propose a semi-supervised electromagnetic imaging algorithm leveraging generative adversarial networks (GANs), which effectively integrates limited labeled data with abundant unlabeled measurements. Unlike conventional approaches that directly learn from raw scattered data, our method employs diffraction tomography (DT)-generated images as network inputs, thereby embedding spatial prior knowledge of scatterers to mitigate inherent artifacts such as boundary blurring and speckle noise. The framework features a modified U-Net architecture augmented with convolutional block attention modules (CBAMs) and residual blocks, enhancing feature extraction and segmentation robustness. Furthermore, adversarial training is introduced to refine the segmentation network using pseudo-labels generated from unlabeled DT images, enabling the discriminator to enforce physical consistency between labeled and unlabeled domains. Extensive simulations demonstrate the superiority of our method: when trained with only 100 labeled samples and 1,000 unlabeled samples, the proposed algorithm achieves a 23.0% reduction in mean squared error (MSE) compared to purely supervised counterparts. Additional validation on the handwritten digits and the "Austria" profile highlights its strong generalization capability for reconstructing unseen targets. This work bridges the gap between data-driven deep learning and physical priors, offering a practical solution for high-precision electromagnetic imaging under limited supervision.

Index Terms – Generative adversarial network, inverse problems, semi-supervised learning.

I. INTRODUCTION

With the rapid advancement of technology, electromagnetic techniques and theories have shown remarkable vitality. As an important branch of electromagnetic technology, microwave imaging has been widely applied in various fields such as remote sensing [1] and oil exploration [2]. In comparison to conventional cameras, the penetrative ability of electromagnetic waves renders them impervious to darkness or adverse weather conditions, thereby augmenting camera imaging capabilities. Although computed tomography (CT) [3] continues to be indispensable for high-resolution anatomical imaging and rapid diagnostics, microwave imaging provides distinct advantages in specific clinical contexts, such as eliminating exposure to ionizing radiation and facilitating cost-effective repetitive monitoring [4]. This underscores its potential as a complementary modality for applications sensitive to radiation exposure [5].

Traditional physics-based electromagnetic inverse scattering methods can be primarily categorized into two types: (1) linear approximation methods (e.g., Born/Rytov approximations), and (2) iterative optimization frameworks that minimize data-model discrepancies through regularization techniques. Although linear approximation methods provide computational efficiency suitable for real-time imaging, their reliance on approximation conditions limits their applicability scope. For example, the Born approximation, due to its dependence on the weak scattering assumption and neglect of multiple scattering effects, may encounter substantial loss of accuracy when handling electrically large or strongly scattering targets. On the other hand, iterative optimization methods enhance reconstruction fidelity but are accompanied by computationally intensive processes that hinder practical applications. These limitations become particularly critical in biomedical

Submitted On: December 06, 2024
Accepted On: February 09, 2026

https://doi.org/10.13052/2026.ACES.J.410105

dynamic monitoring and time-sensitive remote sensing scenarios, where balancing computational complexity and imaging accuracy remains a challenging issue [6].

Such inherent constraints of traditional physics-driven approaches have driven the exploration of data-driven deep learning frameworks, which aim to bypass iterative computations while retaining the ability to model nonlinear scattering phenomena [7, 8]. Wei and Chen [9] proposed a convolutional neural network (CNN) based on the U-Net architecture to solve the full-wave inverse scattering problem, introducing and comparing several CNN-based training schemes, including the back-propagation scheme (BPS) [10] and the dominant current scheme (DCS). Sanghvi et al. [11] introduced a deep learning-based framework to address the electromagnetic inverse scattering problem. This framework builds upon and extends the capabilities of existing physics-based inversion algorithms. These algorithms, such as contrast source inversion (CSI) [12], subspace optimization methods (SOM) [13], and their variants, often struggle with getting trapped in false local minima when recovering objects with high contrast values. They also proposed a novel CNN architecture called the contrast source network (CS-Net). Xu et al. [14] proposed an inversion method based on U-Net network to solve the phaseless data direct inverse scheme (PD-DIS) for phase free electromagnetic backscatter imaging problems. Ye et al. [15] proposed a linear imaging method for homogeneous background problems and applied a GAN with an attention mechanism to address super-resolution tasks.

Most segmentation frameworks are based on typical segmentation networks, such as U-Net, which extract multi-scale features in a fully supervised manner. Although these methods have demonstrated success, the reliance on extensive measurement data for fully supervised learning approaches is time-consuming and expensive. In electromagnetic imaging, the scarcity of high-quality labeled data presents a substantial obstacle for data-driven reconstruction methods. Semi-supervised learning (SSL) addresses this limitation by leveraging both limited labeled data and abundant unlabeled measurements in a unified framework. Core SSL mechanisms, such as consistency regularization (which enforces prediction invariance under perturbations of unlabeled inputs) [16] and adversarial constraints (which align reconstructions with physical priors through generative-discriminative interactions) [17], facilitate robust feature learning even under weak supervision. These approaches have demonstrated efficacy in domains like medical imaging, where similar low-data conditions prevail [18]. This success provides a strong rationale for adopting SSL principles in microwave imaging, enabling the utilization of unlabeled experimental or simulated data to enhance model generalizability.

The structure of this paper is as follows. Section II introduces the physical model and its mathematical description for the microwave imaging problem. Section III provides a comprehensive explanation of the design and implementation of a semi-supervised imaging network based on GAN. Section IV presents the experimental design, dataset construction, and subsequent analysis of experimental results. Finally, in section V, we conclude with a summary of our findings.

II. ELECTROMAGNETIC IMAGING MODEL

The physical model of the microwave imaging problem is shown in Fig. 1. Within the spatial domain, an imaging region D encompasses scatterers of diverse shapes. Microwave imaging is a non-contact method that employs antennas positioned in an observation region S outside the imaging domain D to transmit and receive electromagnetic waves. When incident electromagnetic waves illuminate the scatterer, a scattered field is generated, which combines with the incident field to form the total field received by the antennas. The microwave imaging problem involves deducing the shape, position, and material properties of scatterers within the imaging region D based on measured scattered data at receiving points.

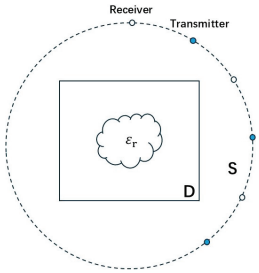

Fig. 1. The physical model of microwave imaging problems.

For the two-dimensional problem, the scattering process is described by the following formula:

$$E^t(r) = E^i(r) + k_b^2 \int_{\mathrm{D}} g(r,r') \cdot \chi(r') E^t(r')\, dr', \quad r \in \mathrm{S} \tag{1}$$

where E^i and E^t denote the incident field and the total field, respectively. k_b is the wave number of the background medium, $g(r,r')$ represents the two-dimensional Green's function in background, r denotes the position of the receiving antenna, r' represents the position of an arbitrary point within the imaging region, and $\chi(r') = \varepsilon(r') - 1$ represents the contrast distribution within the

imaging region with $\varepsilon(r')$ being the relative permittivity at position r'. The function $g(r,r')$ governs wave propagation in the background medium and connects the contrast distribution $\chi(r')$ with scattered field measurements as the integral kernel. The goal of inverse scattering is to determine the contrast distribution in the imaging region using scattered field data from the observation region. The contrast function quantifies permittivity variations and relates to material properties like conductivity and polarization through electromagnetic relations [19]. Analyzing the distribution of $\chi(r')$ is critical for distinguishing material heterogeneity, such as tumors versus healthy tissues in biomedical imaging, and resolving ambiguities in inverse scattering problems. Its magnitude and spatial gradients directly determine scattering field perturbations [20].

To alleviate the learning complexity of neural networks, this study initially employs the diffraction tomography (DT) algorithm [21] to obtain an approximate contrast image, which is subsequently inputted into a segmentation network to generate a refined contrast image with enhanced resolution. The DT algorithm is a linear inversion method based on the Born approximation [22]. In the case of weak scattering intensity, the incident field can be approximated as being equivalent to the total field $E^t(r') \simeq E^i(r')$, allowing equation (1) to be reformulated as

$$\begin{aligned} E^s(r) &= E^t(r) - E^i(r) \\ &\simeq k_b^2 \int_{\mathrm{D}} g(r,r') \cdot \chi(r') E^i(r')\, dr', \quad r \in \mathrm{S} \end{aligned} \tag{2}$$

where E^s denotes the scattered field. After a series of derivations, the above equation can be expressed as

$$E^s(r_R, r_T) \simeq \frac{ik_b}{8\pi\sqrt{|r_R||r_T|}} e^{ik_b(|r_R|+|r_T|)} O(K_R + K_T). \tag{3}$$

In equation (4), both the transmitting and receiving antennas are approximated as ideal line sources, with position vectors r_T and r_R in two-dimensional space, respectively. The Fourier transform of $\chi(r')$, denoted by $O(K_R + K_T)$, is defined as $K_R = k_b \tilde{r}_R$ and $K_T = k_b \tilde{r}_T$. Here, $\tilde{r}_R$ and $\tilde{r}_T$ denote the unit vectors in the directions of r_R and r_T, respectively. Based on the linear approximation in equation (4), the DT algorithm generates initial contrast images under weak scattering conditions. These images often suffer from boundary blurring and speckle noise, especially for strong scatterers. To address this, we use DT images as inputs to the segmentation network instead of raw scattering data. This introduces a physical prior into the network, enabling it to retain target spatial distribution information while focusing on denoising and enhancing the DT images.

III. SEMI-SUPERVISED INVERSION ALGORITHM

The proposed semi-supervised framework, illustrated in Fig. 2, employs a Generative Adversarial Network (GAN) [23] architecture comprising a segmentation generator and a discriminator. The workflow operates in two phases:

A. Supervised pre-training

The segmentation generator is initially trained on limited labeled data to establish baseline mapping capabilities between electromagnetic measurements and target structures.

B. Adversarial refinement with unlabeled data

Pseudo-label Generation: Unlabeled measurements are processed by the pre-trained generator to produce segmentation probability maps (pseudo-labels).

Discriminative Evaluation: The discriminator receives three inputs: (i) ground-truth labels from labeled data, (ii) generator predictions for labeled data, and (iii) pseudo-labels for unlabeled data. It outputs a probability score to assess segmentation plausibility against physical priors.

Adversarial Optimization: Through iterative minimax training, the generator learns to produce segmentation

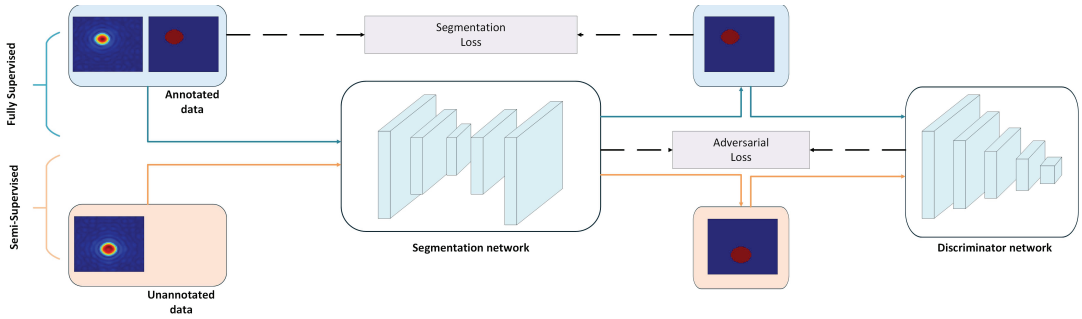

Fig. 2. The semi-supervised imaging network based on GAN.

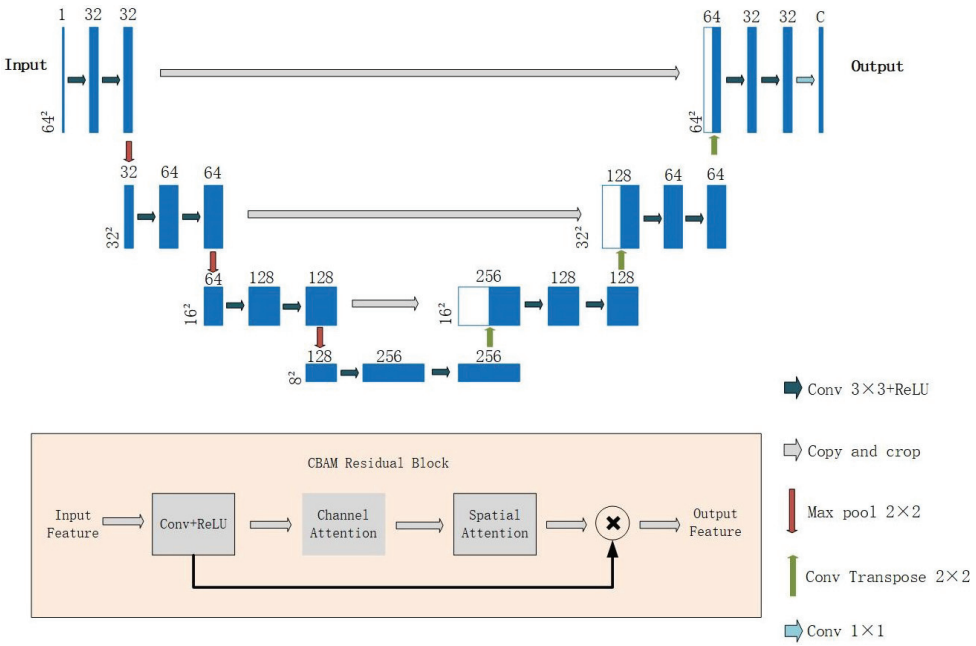

Fig. 3. The structure of the segmentation network.

maps that deceive the discriminator (by aligning with physical priors), while the discriminator improves its ability to distinguish authentic versus generated labels. This dual competition regularizes ill-posed segmentation tasks by enforcing consistency across labeled and unlabeled domains.

Figure 3 shows the schematic of the segmentation network, a modified U-Net for DT image segmentation. The U-Net architecture, originally designed for biomedical image segmentation [24], exhibits intrinsic compatibility with electromagnetic inverse scattering problems due to the following characteristics. (1) Encoder-Decoder Symmetry: The encoder (contracting path) progressively extracts multi-scale scattering features from raw measurement data, while the decoder (expanding path) reconstructs high-resolution permittivity maps through transposed convolutions. This aligns with the ill-posed mapping from sparse measurements to continuous physical properties. (2) Skip Connections: By enabling cross-layer feature fusion between the encoder and decoder, skip connections preserve both low-frequency structural priors and high-frequency details. This effectively addresses the challenges posed by multi-scale scattering phenomena, such as weak single scattering versus strong multiple scattering.

To address the challenges of boundary blurring and noise in DT images, the segmentation network incorporates Convolutional Block Attention Modules (CBAM) [25] and residual blocks [26] into the U-Net architecture. By effectively integrating low-level information, these additions facilitate the generation of enhanced high-level features, thereby aiding in the identification of scatterers from DT images [27]. The CBAM comprises channel attention and spatial attention modules, which enhance the feature extraction capability of CNNs in a more comprehensive and effective manner. Moreover, training deep learning networks can encounter diverse challenges, including instability during the training process. By integrating residual blocks with skip connections, we can effectively stabilize the training of extremely deep neural networks.

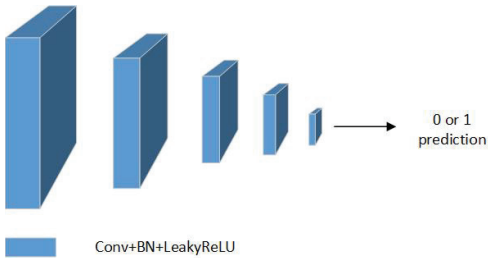

Fig. 4. The structure of the discriminant network.

The architecture of the discriminator network is depicted in Fig. 4 and comprises a straightforward CNN. The discriminator outputs a probability to evaluate the quality of input segmentation results. A value close to 1 denotes high quality, while a value close to 0 indicates low quality.

The segmentation network is trained by minimizing the following loss function:

$$l_s = l_{\text{seg}} + \lambda_{\text{adv}} \cdot l_{\text{adv}}, \tag{4}$$

where l_{seg} and l_{adv} represent the supervised segmentation loss and adversarial loss, respectively. The weight for adversarial learning, denoted as λ_{adv}, is set to 0.02, following the loss function weights specified in [28]. For labeled pairs, the segmentation network G is trained to map DT images $I_{DT}^{labeled}$ to their corresponding ground truth contrast maps I_{GT} by minimizing the supervised loss l_{seg}, which is defined as the pixel-wise mean squared error (MSE). For unlabeled DT images $I_{DT}^{unlabeled}$, the pre-trained generator G produces pseudo-labels $I_{pseudo} = G(I_{DT}^{unlabeled})$. Subsequently, the discriminator D evaluates both the labeled data $G(I_{DT}^{labeled})$ and the pseudo-labeled data I_{pseudo} to calculate the adversarial loss l_{adv}. Equation (4) can be expanded in more detail as:

$$l_s = \frac{1}{N}\sum_{i=1}^{N}(I_{GT(i)} - I_{DT(i)}^{labeled})^2 + \lambda_{\text{adv}} \cdot \big(-\log(D(G(I_{DT})))\big). \tag{5}$$

Where N represents the total number of pixels in the imaging region, $I_{GT(i)}$ and $I_{DT(i)}^{labeled}$ respectively indicate the contrast values at the i-th pixel in the ground truth image and the predicted labeled image. In the adversarial loss term, I_{DT} encompasses both labeled DT images $I_{DT}^{labeled}$ and unlabeled DT images $I_{DT}^{unlabeled}$. Typically, the number of labeled data is significantly smaller than that of unlabeled data, resulting in an inherent imbalance during network training. To address this issue, this study employs data augmentation techniques on the labeled dataset, such as image flipping and rotation, to enhance both diversity and quantity of training samples.

IV. SIMULATION EXPERIMENT AND ANALYSIS

In this experiment, the key parameters, including the imaging domain size, antenna configuration, and operating frequency, are rigorously aligned with the electromagnetic model described in section II. The imaging region is a square area with a side length of 2 m located in free space, which is further divided into a grid consisting of 64×64 pixels. The origin of the coordinate system is located at the center of this imaging region. In the observation region outside the imaging area, there are a total of 16 transmitting antennas and 32 receiving antennas arranged symmetrically around the origin within a radius of 3 m. The incident wave operates at a frequency of 0.4 GHz. In every measurement, each transmitting antenna sequentially emits electromagnetic waves to illuminate the imaging region, while all receivers concurrently capture the scattered waves from the scatterer. This process yields a total of 16×32-dimensional scattering data. In this paper, the Method of Moments (MoM) is used to solve the forward scattering problem, generating synthetic scattering data which are then processed by the DT algorithm to reconstruct preliminary images for the GAN input.

A. Test 1: Circular scatterers

In the first test, the dataset consists of circular scatterers with random sizes and positions. The relative permittivity of the target ranges randomly from 1.1 to 3.0 (contrast ranging from 0.1 to 2.0), with radii between 0.1 and 0.3 m, in intervals of 0.01 m. The coordinates of the center of the targets are within the range of (-0.5 m to 0.5 m, -0.5 m to 0.5 m).

To validate the effectiveness of the proposed network enhancement and semi-supervised learning under the adversarial training mechanism, we conducted a comparative analysis of three models under identical experimental conditions: (1) Basic U-Net: A standard U-Net without CBAM or residual blocks; (2) Supervised GAN: The generator adopts a U-Net architecture integrated with CBAM and residual blocks, and is trained exclusively on labeled data; and (3) GAN-based SSL: The semi-supervised method combining labeled and unlabeled data with adversarial training. The segmentation and the discriminator network are both optimized using the Adam optimizer, with an initial learning rate set to 1×10^{-2}. The training process is iterated for 2000 epochs to ensure convergence is achieved. Through this iterative procedure, the learning rate gradually reduces to 1×10^{-4}. These parameter settings are determined based on optimal values obtained from experimental simulations.

The quality of the segmented image is evaluated by using the MSE and the structural similarity (SSIM) index [29]. The calculation formula for SSIM is as follows:

$$\text{SSIM}(m,n) = \frac{(2\mu_m\mu_n + C_1)(2\sigma_{mn} + C_2)}{(\mu_m^2 + \mu_n^2 + C_1)(\sigma_m^2 + \sigma_n^2 + C_2)} \tag{6}$$

where μ_m and μ_n represent the mean contrast values of images m and n, respectively. Additionally, the variances of the contrast in images m and n are denoted by σ_m^2 and σ_n^2, respectively, while their covariance is indicated by σ_{mn}. The constants C_1 and C_2 are crucial for maintaining stability, where $C_1 = (k_1 L)^2$ and $C_2 = (k_2 L)^2$. Here, L represents the range of pixel values (specifically, the range of relative permittivity values in this experiment), while k_1 and k_2 are assigned as 0.01 and 0.03 respectively.

Three experimental sample sets were established, with 100, 200, and 500 labeled samples allocated to each group respectively, while the number of unlabeled samples was consistently maintained at 1000 across all groups.

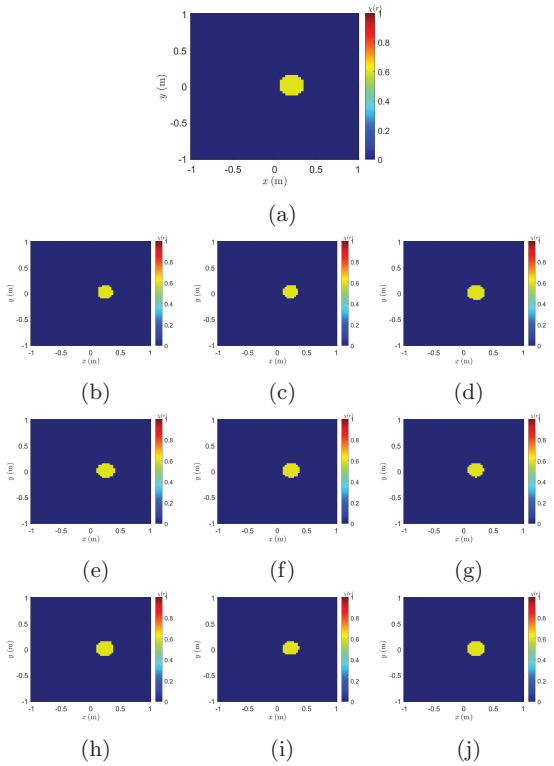

Fig. 5. Imaging results of circular scatterers. (a) Actual target. (b)–(d) Basic U-Net results trained with 100, 200, and 500 labeled datasets. (e)–(g) Supervised GAN results trained with 100, 200, and 500 labeled datasets. (h)–(j) GAN-based SSL results trained with 100, 200, and 500 labeled samples plus 1000 unlabeled samples.

Table 1: MSE values for circular scatterers

Method	**Labeled Samples (1000 Unlabeled)**		
	100	**200**	**500**
Basic U-Net	1.2412	0.8634	0.7180
Supervised GAN	1.0762	0.8023	0.6659
GAN-based SSL	0.8283	0.6711	0.5511
Reduction (SSL vs. Supervised)	**23.0%**	**16.4%**	**17.2%**

Table 2: SSIM values for circular scatterers

Method	**Labeled Samples (1000 Unlabeled)**		
	100	**200**	**500**
Basic U-Net	0.9486	0.9563	0.9599
Supervised GAN	0.9531	0.9611	0.9621
GAN-based SSL	0.9587	0.9639	0.9716

The imaging results for one of the samples are presented in Fig. 5, where the GAN-based SSL method demonstrates the most accurate reconstructions. As shown in Tables 1 and 2, the basic U-Net consistently exhibits the highest MSE and the lowest SSIM across all labeled data settings, indicating its limited ability to address boundary blurring and speckle noise inherent in DT images. By integrating channel attention mechanisms via CBAM and residual blocks, as well as incorporating discriminators, the supervised GAN achieves a significant performance improvement. Nevertheless, the GAN-based SSL method further enhances segmentation accuracy by effectively leveraging unlabeled data. Specifically, compared to the supervised GAN, the semi-supervised approach reduces MSE by 23.0%, 16.4%, and 17.2% for datasets with 100, 200, and 500 labeled samples, respectively. Similarly, SSIM values show substantial increases when unlabeled data is introduced. These findings confirm that both architectural enhancements (CBAM and residual blocks) and semi-supervised adversarial training contribute to improving the model's robustness and precision.

B. Test 2: MNIST digits

To further validate the model's performance and compare it with other semi-supervised methods, we conducted experiments on the MNIST dataset. This dataset contains handwritten digits from 250 individuals, covering all ten numerical symbols ranging from 0 to 9. To augment the sample data and improve the model's generalization capability, each sample was augmented with a randomly sized and positioned circular scatterer. The relative permittivity for all samples was set within the range of 1.1 to 2.0 (with a contrast range of 0.1 to 1.0).

The model was trained and tested on three datasets with labeled-to-unlabeled ratios of 1:9 (1000:9000), 1:4 (2000:8000), and 1:1 (5000:5000). For comparison, we additionally implemented the Mean Teacher method [30], a widely adopted semi-supervised learning approach in computer vision. The Mean Teacher model employed the same U-Net backbone as our segmentation network, with an exponential moving average (EMA) decay rate of 0.99 for the teacher weights. All hyperparameters, including the learning rate and optimizer, were kept consistent across models to ensure a fair comparison.

Table 3: MSE values for handwritten digits

Method	**Labeled Samples (10000 in Total)**		
	1000	**2000**	**5000**
Mean Teacher	1.0339	1.0276	0.7177
Supervised GAN	0.9172	0.8326	0.7087
GAN-based SSL	0.8523	0.7847	0.6891
Reduction (SSL vs. Supervised)	**7.1%**	**5.8%**	**2.8%**

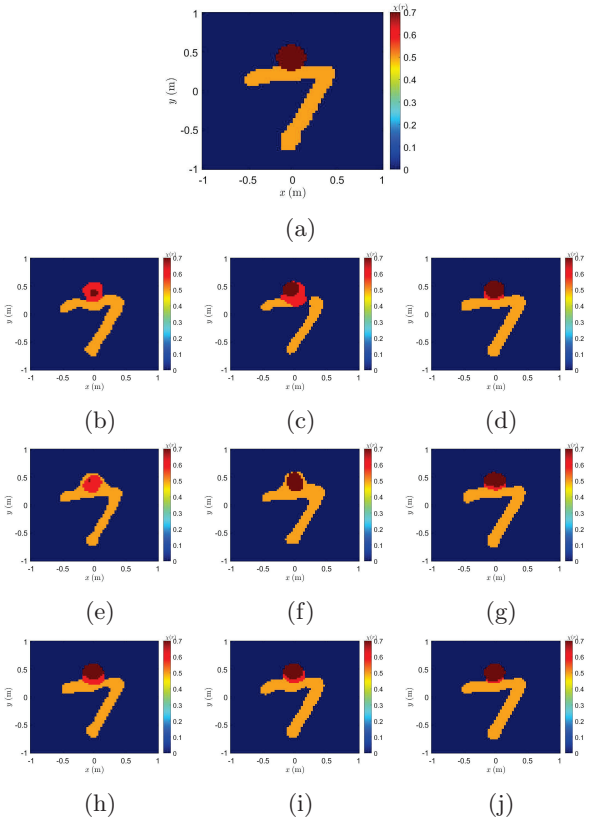

Fig. 6. Imaging results of handwritten digits. (a) Real target. (b)-(d) Supervised GAN results trained on 1000, 2000, and 5000 labeled datasets. (e)-(g) Mean Teacher results trained with labeled to unlabeled data ratios of 1:9, 1:4, and 1:1. (h)-(j) GAN-based SSL results trained with labeled to unlabeled data ratios of 1:9, 1:4, and 1:1.

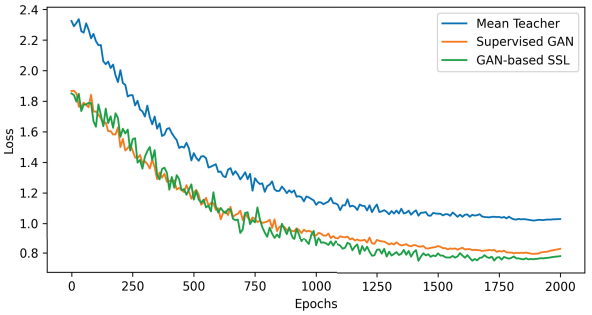

Fig. 7. The curves of training loss versus epochs.

Table 4: SSIM values for handwritten digits

Method	Labeled Samples (10000 in Total)		
	1000	2000	5000
Mean Teacher	0.8780	0.8821	0.9124
Supervised GAN	0.8932	0.9009	0.9149
GAN-based SSL	0.8981	0.9056	0.9172

The experimental results demonstrate that the SSL method based on GAN significantly outperforms both the supervised GAN and the Mean Teacher model on the MNIST dataset. In the imaging results of a representative sample shown in Fig. 6, the GAN-based SSL reconstructs the target edges more accurately and clearly. Figure 7 shows the training loss versus epochs curves for the Mean Teacher, supervised GAN, and GAN-based SSL methods when the ratio of labeled to unlabeled data is 2000:8000. As illustrated in Table 3, under conditions of limited labeled data (1000:9000), the MSE of GAN-based SSL is 7.1% lower than that of the supervised GAN, and it retains a 2.8% advantage even as the amount of labeled data increases (5000:5000). The Mean Teacher model exhibits inferior performance due to issues with pseudo-label noise. Furthermore, the results presented in Table 4 corroborate the GAN-based SSL method achieves the highest SSIM scores across all configurations. These findings underscore the efficacy of SSL in leveraging unlabeled data via adversarial training to enhance boundary clarity, particularly in scenarios with limited labeled data.

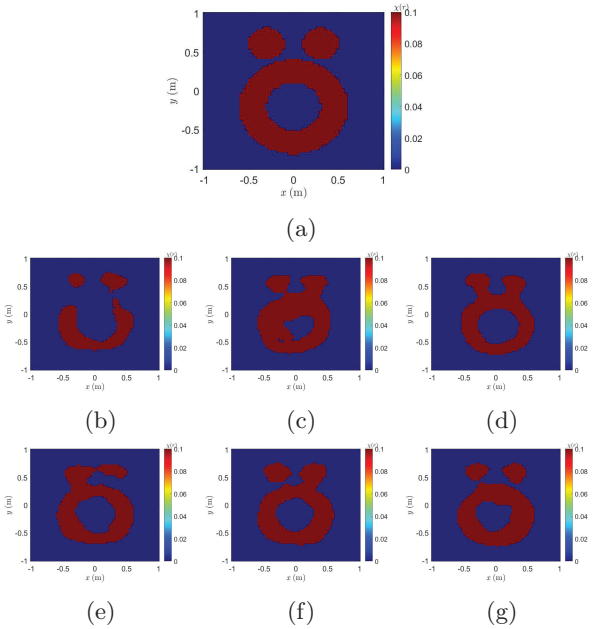

Fig. 8. The imaging results of the "Austria" profile using the MINIST data-trained network. (a) Real profile. (b), (c), and (d) show supervised GAN results trained on 1000, 2000, and 5000 labeled datasets, respectively. (e), (f), and (g) present SSL results from models trained with labeled to unlabeled data ratios of 1:9, 1:4, and 1:1, respectively.

C. Test 3: "Austria" profile

To further validate the generalization capability of the proposed model, we employed a test example

known as the "Austria" profile to evaluate the trained segmentation model. The "Austria" profile differs significantly from the profiles present in the MNIST training database, as shown in Fig. 8 (a). It consists of two disks and a ring. Both disks have radii of 0.2 m and are centered at coordinates (0.3, 0.6) m and (−0.3, 0.6) m, respectively. The inner and outer radii of the ring measure 0.3 m and 0.6 m, respectively. The relative permittivity of the target is specified as 1.1.

The segmentation networks trained on the MNIST dataset in Test 2 were utilized to reconstruct this target. As shown in Fig. 8, the results demonstrate that after incorporating the unlabeled data, the GAN-based SSL can effectively approximate the position, size, and shape of the unseen scattering target. This highlights its superior generalization ability and robustness.

V. CONCLUSION

In this study, we propose a SSL model based on the GAN architecture. This model uses DT images as input instead of scattering data and leverages adversarial generation training to effectively utilize unlabeled data, thereby significantly improving the segmentation quality of scatters in DT images. DT relies on the fast Fourier transform (FFT), with a computational complexity of only $O(N \log N)$. This efficiency satisfies the timeliness requirements for real-time imaging. Regarding GAN components, while the offline training phase is time-consuming, particularly during semi-supervised adversarial training, the online inference phase is relatively rapid. The integration of GPU acceleration and other advanced technologies ensures that the system can effectively meet the demands of real-time imaging. In practical applications, factors such as sensor noise, antenna position errors, and environmental disturbances may degrade image quality. To enhance imaging stability in complex environments, multi-physical field inversion combined with data from other sensors (e.g., optical or infrared) can be explored. In the experimental section, the model's generalization capability for unknown targets has been validated using the MNIST dataset and the "Austria" profile test. However, the diversity of scatterer materials, shapes, and background media in real-world scenarios presents challenges. To address this issue, future work will focus on incorporating more sophisticated physical simulations (such as inhomogeneous backgrounds and multi-target coupling) during the training phase to improve the model's adaptability to complex scenes.

REFERENCES

[1] R. W. King, M. Owens, and T. T. Wu, *Lateral Electromagnetic Waves: Theory and Applications to Communications, Geophysical Exploration, and Remote Sensing*. Berlin: Springer Science & Business Media, 2012.

[2] R. Streich, "Controlled-source electromagnetic approaches for hydrocarbon exploration and monitoring on land," *Surveys in Geophysics*, vol. 37, pp. 47–80, 2016.

[3] R. Kramme, K.-P. Hoffmann, and R. S. Pozos, *Springer Handbook of Medical Technology*. Berlin: Springer Science & Business Media, 2011.

[4] M. Maier, S. Paul, M. Rother, S. Di Meo, M. Pasian, J. Schoebel, and V. Issakov, "Microwave imaging for breast cancer detection-a comparison between VNA and FMCW radar," *IEEE Journal of Microwaves*, vol. 5, no. 2, pp. 291–304, 2025.

[5] R. Chandra, H. Zhou, I. Balasingham, and R. M. Narayanan, "On the opportunities and challenges in microwave medical sensing and imaging," *IEEE Transactions on Biomedical Engineering*, vol. 62, no. 7, pp. 1667–1682, 2015.

[6] M. Salucci, M. Arrebola, T. Shan, and M. Li, "Artificial Intelligence: New frontiers in real-time inverse scattering and electromagnetic imaging," *IEEE Transactions on Antennas and Propagation*, vol. 70, no. 8, pp. 6349–6364, 2022.

[7] X. Liu, K. Zheng, and J. Li, "An electromagnetic scattering mechanism recognition method based on deep learning," *Applied Computational Electromagnetics Society (ACES) Journal*, vol. 40, no. 01, pp. 10–19, Jan. 2025.

[8] C. X. Yang, J. J. Meng, S. Wei, and M. S. Tong, "A dual-input electromagnetic inverse scattering algorithm based on improved U-Net", *Applied Computational Electromagnetics Society (ACES) Journal*, vol. 39, no. 11, pp. 961–969, Nov. 2024.

[9] Z. Wei and X. Chen, "Deep-learning schemes for full-wave nonlinear inverse scattering problems," *IEEE Transactions on Geoscience and Remote Sensing*, vol. 57, no. 4, pp. 1849–1860, 2018.

[10] X. Chen, *Computational Methods for Electromagnetic Inverse Scattering*. Hoboken, NJ: John Wiley & Sons, 2018.

[11] Y. Sanghvi, Y. Kalepu, and U. K. Khankhoje, "Embedding deep learning in inverse scattering problems," *IEEE Transactions on Computational Imaging*, vol. 6, pp. 46–56, 2019.

[12] P. M. Van Den Berg and R. E. Kleinman, "A contrast source inversion method," *Inverse Problems*, vol. 13, no. 6, p. 1607, 1997.

[13] X. Chen, "Subspace-based optimization method for solving inverse-scattering problems," *IEEE Transactions on Geoscience and Remote Sensing*, vol. 48, no. 1, pp. 42–49, 2009.

[14] K. Xu, L. Wu, X. Ye, and X. Chen, "Deep learning-based inversion methods for solving inverse scattering problems with phaseless data," *IEEE Transactions on Antennas and Propagation*, vol. 68, no. 11, pp. 7457–7470, 2020.

[15] X. Ye, N. Du, D. Yang, X. Yuan, R. Song, S. Sun, and D. Fang, "Application of generative adversarial network-based inversion algorithm in imaging 2-D lossy biaxial anisotropic scatterer," *IEEE Transactions on Antennas and Propagation*, vol. 70, no. 9, pp. 8262–8275, 2022.

[16] N. Karaliolios, F. Chabot, C. Dupont, H. Le Borgne, Q.-C. Pham, and R. Audigier, "Generalized pseudo-labeling in consistency regularization for semi-supervised learning," in *2023 IEEE International Conference on Image Processing (ICIP)*, pp. 525–529, 2023.

[17] P. Wang, J. Peng, M. Pedersoli, Y. Zhou, C. Zhang, and C. Desrosiers, "CAT: Constrained adversarial training for anatomically-plausible semi-supervised segmentation," *IEEE Transactions on Medical Imaging*, vol. 42, no. 8, pp. 2146–2161, 2023.

[18] X. Xie, J. Niu, X. Liu, Q. Li, Y. Wang, and S. Tang, "DK-consistency: A domain knowledge guided consistency regularization method for semi-supervised breast cancer diagnosis," in *2021 IEEE International Conference on Bioinformatics and Biomedicine (BIBM)*, pp. 3435–3442, 2021.

[19] W. C. Chew, *Waves and Fields in Inhomogenous Media.* Hoboken, NJ: John Wiley & Sons, 1999.

[20] J. D. Shea, P. Kosmas, S. C. Hagness, and B. D. Van Veen, "Contrast-enhanced microwave breast imaging," in *2009 13th International Symposium on Antenna Technology and Applied Electromagnetics and the Canadian Radio Science Meeting*, pp. 1–4, 2009.

[21] C. Yang, J. Zhang, and M. S. Tong, "An FFT-accelerated particle swarm optimization method for solving far-field inverse scattering problems," *IEEE Transactions on Antennas and Propagation*, vol. 69, no. 2, pp. 1078–1093, 2020.

[22] A. Onufriev, D. A. Case, and D. Bashford, "Effective Born radii in the generalized Born approximation: The importance of being perfect," *Journal of Computational Chemistry*, vol. 23, no. 14, pp. 1297–1304, 2002.

[23] I. Goodfellow, J. Pouget-Abadie, M. Mirza, B. Xu, D. Warde-Farley, S. Ozair, A. Courville, and Y. Bengio, "Generative adversarial networks," *Communications of the ACM*, vol. 63, no. 11, pp. 139–144, 2020.

[24] O. Ronneberger, P. Fischer, and T. Brox, "U-Net: Convolutional networks for biomedical image segmentation," in *Medical Image Computing and Computer-Assisted Intervention–MICCAI 2015: 18th International Conference, Munich, Germany, October 5–9, 2015, Proceedings, Part III 18*, pp. 234–241, 2015.

[25] S. Woo, J. Park, J.-Y. Lee, and I. S. Kweon, "CBAM: Convolutional block attention module," in *Proceedings of the European Conference on Computer Vision (ECCV)*, pp. 3–19, 2018.

[26] K. He, X. Zhang, S. Ren, and J. Sun, "Deep residual learning for image recognition," in *Proceedings of the IEEE Conference on Computer Vision and Pattern Recognition*, pp. 770–778, 2016.

[27] C. X. Yang, X. Yang, J. Zhang, C. Zhou, and M. S. Tong, "An electromagnetic imaging algorithm based on generative adversarial network for limited observation angle," *Applied Computational Electromagnetics Society (ACES) Journal*, vol. 40, no. 8, pp. 702–713, Aug. 2025.

[28] L. Han, Y. Huang, H. Dou, S. Wang, S. Ahamad, H. Luo, Q. Liu, J. Fan, and J. Zhang, "Semi-supervised segmentation of lesion from breast ultrasound images with attentional generative adversarial network," *Computer Methods and Programs in Biomedicine*, vol. 189, p. 105275, 2020.

[29] Z. Wang, A. C. Bovik, H. R. Sheikh, and E. P. Simoncelli, "Image quality assessment: From error visibility to structural similarity," *IEEE Transactions on Image Processing*, vol. 13, no. 4, pp. 60–612, 2004.

[30] A. Tarvainen and H. Valpola, "Mean teachers are better role models: Weight-averaged consistency targets improve semi-supervised deep learning results," *Advances in Neural Information Processing Systems*, vol. 30, 2017.

Chun Xia Yang received the Ph.D. degree in electronic science and technology from Tongji University, Shanghai, China, in 2017. During her doctoral studies, she also conducted research at the Department of Electrical and Computer Engineering, University of Illinois at Urbana-Champaign, Champaign, IL, USA as a visiting student between 2014 and 2016. She is currently an associate professor at the Department of Communication Engineering, Shanghai Normal University, Shanghai, China. Her ongoing research interests primarily revolve around electromagnetic inverse scattering for imaging and computational electromagnetics.

Chi Zhou received the M.S. degree in Electronic Information from Shanghai Normal University, Shanghai, China, in 2025. He is currently affiliated with Wenyin Cloud Computing Co., Ltd, Shanghai, China. His research mainly focuses on electromagnetic inverse scattering.

Shuang Wei received the B.S. degree and the M.S. degree from the Huazhong University of Science and Technology, Wuhan, China, in 2005 and 2007 respectively, and the Ph.D. degree in electrical and computer engineering from the University of Calgary, Calgary, Canada, in 2011. She is now an Associate Professor with College of Information, Mechanical and Electrical Engineering, Shanghai Normal University, Shanghai, China. From 2021 to 2022, she was a Visiting Scholar at the Shanghai Key Laboratory of Navigation and Location-based Services, School of Sensing Science and Engineering, School of Electronic Information and Electrical Engineering, Shanghai Jiao Tong University, Shanghai, China. Her current research interests include array signal processing, signal estimation and detection, computational intelligence, and compressed sensing.

Mei Song Tong received the B.S. and M.S. Degrees from Huazhong University of Science and Technology, Wuhan, China, respectively, and Ph.D. degree from Arizona State University, Tempe, Arizona, USA, all in electrical engineering. He is currently a Humboldt Awardee Professor in the Chair of High-Frequency Engineering, Technical University of Munich, Munich, Germany, and is on leave from the Distinguished/Permanent Professor and Head of Department of Electronic Science and Technology, and Vice Dean of College of Microelectronics, Tongji University, Shanghai, China. He has also held an adjunct professorship at the University of Illinois at Urbana-Champaign, Urbana, Illinois, USA, and an honorary professorship at the University of Hong Kong, China. He has published more than 700 papers in refereed journals and conference proceedings and coauthored eight books or book chapters. His research interests include electromagnetic field theory, antenna theory and technique, modeling and simulation of RF/microwave circuits and devices, interconnect and packaging analysis, inverse electromagnetic scattering for imaging, and computational electromagnetics.

Prof. Tong is a Fellow of IEEE, Fellow of the Electromagnetics Academy, Fellow of the Japan Society for the Promotion of Science (JSPS), and Fellow of International Academy of Artificial Intelligence Sciences (AAIS). He has been the chair of Shanghai Chapter since 2014 and the chair of SIGHT committee in 2018, respectively, in IEEE Antennas and Propagation Society. He has served as an associate editor or guest editor for several well-known international journals, including IEEE Antennas and Propagation Magazine, IEEE Transactions on Antennas and Propagation, IEEE Transactions on Components, Packaging and Manufacturing Technology, International Journal of Numerical Modeling: Electronic Networks, Devices and Fields, Progress in Electromagnetics Research, and Journal of Electromagnetic Waves and Applications. He also frequently served as a session organizer/chair, technical program committee member/chair, and general chair for some prestigious international conferences. He was the recipient of a Visiting Professorship Award from Kyoto University, Japan, in 2012, and from University of Hong Kong, China, 2013. He advised and coauthored 15 papers that received the Best Student Paper Award from different international conferences. He was the recipient of the Travel Fellowship Award of USNC/URSI for the 31th General Assembly and Scientific Symposium (GASS) in 2014, Advance Award of Science and Technology of Shanghai Municipal Government in 2015, Fellowship Award of JSPS in 2016, Innovation Award of Universities' Achievements of Ministry of Education of China in 2017, Innovation Achievement Award of Industry-Academia-Research Collaboration of China in 2019, "Jinqiao" Award of Technology Market Association of China in 2020, Baosteel Education Award of China in 2021, Carl Friedrich von Siemens Research Award of the Alexander von Humboldt Foundation of Germany in 2023, and Technical Achievement Award of Applied Computational Electromagnetic Society (ACES) of USA in 2024. In 2018, he was selected as the Distinguished Lecturer (DL) of IEEE Antennas and Propagation Society for 2019–2022, and in 2024–2025, he was selected to the Top 2% Scientists List for both Career-Long Impact and Single-Year Impact by Elsevier and Stanford University.

A Novel Approach for Early-Stage Breast Cancer Detection

Mohamed Behih[1], Christophe Dumond[2], Farid Bouttout[1], and Tarek Fortaki[3]

[1]EAT Laboratory
Institute of Electronics and Telecommunications,
University of Mohamed El Bachir El Ibrahimi
Bordj Bou Arreridj, Algeria
mohamed.behih@univ-bba.dz, f.bouttout@univ-bba.dz

[2]PRISME Institut
IUT of Chartres, University of Orleans, Orleans, France
christophe.dumond@univ-orleans.fr

[3]AE Laboratory
Departement of Electronics, University of Batna 2,
Mostefa Ben Boulaïd, Batna 05000, Algeria
t.fortaki@univ-batna2.dz

Abstract – This paper presents a novel approach for early-stage breast cancer detection using only a single radiofrequency 3D antenna sensor operating in several frequency bands below Ultra-Wide Band (UWB) frequencies. To this end, an innovative Inverted-F Antenna with Short Circuit-Like (IFA-SCL) is proposed, and the breast to be examined is fully placed inside this antenna between the radiating element and the ground plane. The designed and simulated antenna operates in the two frequency bands (902.8–928.0 MHz and 2.400–2.4835 GHz) of the Industrial, Scientific, and Medical (ISM) bands. After examination of the two patient breasts and by comparison of the antenna's performances considering the return loss ($S_{11} < -10$ dB), tumor presence is detected when the resonance frequencies that cover the operating frequency bands corresponding to an unhealthy breast, are shifted to higher frequencies and the corresponding magnitudes are changed. A spherical shape model of the female breast tissues is created for designing and simulating antenna and tumor detection performances. Also, to test the practicality of the proposed method and detail the tumor detection performances with breast variability, three tests are performed using side-set and teardrop shape breasts. The present approach demonstrates great potential to become a new way for early-stage breast cancer detection, both quickly and with high efficiency. The proposed method, and thus the designed multi-band 3D antenna sensor, exhibits the capability to detect a tumor of spherical shape, of radius only 1 mm and embedded deeply in the breast. Furthermore, it is able to sense tumor presence even with breasts of various sizes and shapes. The patient's safety is ensured by adhering to Specific Absorption Rate (SAR) limits.

Index Terms – 3D antenna, breast cancer detection, dual-band antenna, ISM bands, tumor.

I. INTRODUCTION

Cancerous or malignant tissues are produced due to uncontrolled cell division due to genetic mutations which disrupts the natural cell cycle regulation. Breast cancer is a malignant tumor that originates in the glandular epithelium of the breast and can spread to other parts of the breast. It has emerged as a serious health concern worldwide and the most common cancer among women [1]. For both sexes, breast cancer represents the second leading cause of cancer-related deaths after lung cancer [2–6].

The process of early-stage breast cancer detection is crucial for reducing its deployment in the breast, mortality rates, and improving treatment outcomes. It allows for timely intervention before the disease progresses to advanced stages [4, 7]. The extreme emphasis of early-stage breast cancer detection is reflected by the wide array of methods and strategies used for this objective, from traditional imaging and clinical assessment to emerging molecular, computational, and biomarker-based methods [7–9]. The most common imaging-based methods for breast tumor detection are X-ray mammography imaging [9–11], ultrasound imaging [1, 12, 13],

Submitted On: August 02, 2025
Accepted On: February 01, 2026

https://doi.org/10.13052/2026.ACES.J.410106

magnetic resonance imaging [1, 12, 13], and Microwave Breast Imaging (MWBI) in its two strategies of tomography and radar-based [1, 5, 10, 12, 14–17].

X-ray mammography imaging is a widely used screening tool for breast cancer detection. It utilizes low-dose X-rays to image the breast and is effective for early-stage breast cancer detection. However, it can be uncomfortable, it implies exposure to ionizing radiation, it is less effective for dense breasts, and it leads to false-positive and false-negative results [11].

The ultrasound imaging technique uses sound waves to create images of the breast. It is often used as a complementary process to the X-ray mammograms, especially in dense breasts. Ultrasounds are not able to distinguish between malignant and benign tumors, and they produce low-resolution images [1, 12, 13].

Magnetic resonance imaging uses magnetic fields and radio waves to produce detailed images; it provides high sensitivity in detecting breast cancer, especially in dense breast tissue. This technique is characterized by high cost and variable specificity, leading to more false-positives and a lack of standardized interpretation criteria and protocols [1, 12, 13].

The microwave tomography technique operates by illuminating the breast with low-power microwave signals in the 0.3–10 GHz range using multiple antennas arranged around the breast. The scattered fields are collected, and inverse algorithms reconstruct images that reveal spatial distributions of dielectric permittivity and conductivity. Malignant tissues, due to their higher water and ionic content, show higher permittivity and conductivity, enabling tumor detection. While microwave tomography shows promise as a non-ionizing, patient-friendly technique for breast cancer imaging, its spatial resolution, sensitivity for small or deep-seated tumors, susceptibility to tissue heterogeneity and coupling artifacts, and slow computational performance remain key hurdles for early-stage breast cancer detection. Furthermore, insufficient large-scale clinical validation and lack of standardization limit its transition from research prototype to routine clinical tool [1, 12].

The radar-based MWBI uses low-power and short-duration Ultra-Wide Band (UWB) pulses to scan the breast tissue. A set of antennas placed around the breast is used for both power transmitting, and back-scattered energy collecting. Signals corresponding to the collected power are used to produce a 3D image of the scanned breast [1, 12]. The radar-based MWBI senses the dielectric properties changes between normal and abnormal breast tissues to detect and locate the breast tumors. It is widely applied for breast tumor detection; in fact, it allows the obtaining of high-contrast 3D images using non-ionizing radiation and without breast compression. Radar-based MWBI systems avoid complex computational challenges associated with microwave tomography. However, this method requires a complex and high-cost system; the use of multiple antennas and feeds creates a complex system that can be difficult to manage. This complexity can lead to mutual coupling between antennas, resulting in low resolution and accuracy. In addition, used antennas must be arranged in ring or arc geometries around the pendulant breast [5].

Comparing the various methods and techniques used for breast cancer detection summarized above, it appears that the radar-based MWBI method is most convivial for breast cancer detection; in fact, it presents compelling advantages over X-ray mammography, ultrasound, and MRI, both in terms of underlying physical principles and practical clinical application. The key behind this success is the antenna and its high sensing capability. Unlike the complexity and high cost related to radar-based MWBI systems, their antennas multiplicity, and the accompanied problems and inconvenience as discussed above, using a single antenna with a simple system and procedure for breast cancer detection is very interesting.

Radiofrequency antenna technology is widely used and practiced for various healthcare purposes, e.g., stimulation [18], hyperthermia and tumor ablation [19] for therapeutic ends, biotelemetry [20], wireless power transfer for implants [21], and early-stage breast cancer detection [22]. Herein, the dielectric properties of human body tissues (adding to those abnormal ones) are the keystone.

Radiofrequency antennas operating below UWB frequencies, i.e., below 3.1 GHz, confer several compelling advantages for healthcare applications; electromagnetic waves radiated by such antennas exhibit reduced dielectric loss and greater penetration depth in human body tissues compared to UWB and higher bands. In addition, several frequency bands and services are allocated and reserved for biomedical and healthcare purposes: frequency bands 401–406 MHz of the medical device radiocommunications service, bands 433.1–434.8, 868.0–868.6, and 902.8–928.0 MHz and 2.400–2.4835 GHz of the Industrial, Scientific, and Medical (ISM) bands, and the bands 608–614 MHz, 1.395–1.400, and 1.427–1.432 GHz of the Wireless Medical Telemetry Service [20, 21]. Furthermore, operating at frequencies below UWB frequencies produces lower Specific Absorption Rate (SAR) for a given transmitted power, which reduces the risk of tissue heating and enables continuous or long-duration operation while keeping the SAR below regulatory thresholds.

Using antenna performances in the below UWB frequencies for early-stage breast cancer detection is not widely reported in the literature. Furthermore, proposed and suggested antennas for this purpose are generally

planar and functional in a single band [23–27]. Using these antennas, resonance frequency shifting, reflection coefficient magnitude variation, and impedance bandwidth displacement and changing have been used for tumor detection. Using multi-band antennas allows one to obtain more accurate diagnostic results; a multitude of operating frequency bands increases the antenna sensing capability to detect even minor variation in dielectric properties of breast tissues and, thus, to detect the tumor presence even with the smallest size.

In [23], a single-band and planar array-antenna sensor is proposed for early-stage breast cancer detection; the frequency band of operability is around 2 GHz. This proposed antenna processes a high sensitivity for breast cancer detection, but the sensor operational frequency band is not reserved for medical and healthcare purposes.

In [24], a miniaturized, wearable, planar, and triple-band microstrip antenna is carried out for early-stage breast cancer detection. Operating frequency bands are ISM 2.45 GHz, and around the frequencies of 5.5 and 6.1 GHz. The suggested antenna can't detect breast tumors smaller than 2 mm in radius, and only at a maximum depth of 10 mm using imaging.

A planar patch antenna operating in the frequency band of ISM 2.45 GHz has been designed and simulated for early-stage breast cancer detection in [25]. Only tumors of a radius of 6 mm at least can be detected. Furthermore, the tumor depth influence on detection capability is not discussed.

The planar monopole antenna suggested in [26] for breast cancer detection operates in the frequency band of 1.9–2.1 GHz. The tumor model used simulates a radius of 8 mm. Furthermore, the operating frequency band is not allocated for biomedical and healthcare applications.

Reference [27] describes a metasurface-based planar microstrip array antenna operational in the frequency band of ISM 2.4 GHz. The tumor examined is of a diameter of 1.5 mm.

This work aims to propose a novel and promising approach for early-stage breast cancer detection using non-ionizing electromagnetic waves. It is non-invasive, low-cost, safe, and comfortable for the patient, and sensitive for small and deep-seated tumors. The proposed approach senses tumor presence using performances of an innovative single radiofrequency antenna. The designed and simulated antenna has the following features:

(1) The proposed antenna is of 3D structure, and the breast to be examined is placed inside this antenna, i.e., between the radiating element and the ground plane. By this placing manner, the antenna's performances are strongly linked to any change in dielectric properties of breast tissues, i.e., to any tumor presence. Dielectric properties changing is sensed in both operating frequency bands of ISM 915 MHz and 2.45 GHz based on resonance frequency shifting and the corresponding reflection coefficient magnitude increasing/decreasing.
(2) The designed and simulated antenna sensor is a patch antenna modified by slots inserted in both the radiating element and the short-circuit-like, and open-end slot inserted in the ground plane. The dimensions and the solidity of the designed antenna allow us to facilitate and accelerate the examination procedure with a large degree of freedom for the patient. It may be used sitting, standing, or lying down.
(3) Two frequency bands are targeted for the antenna's operability to increase the antenna sensor capability for smallest tumor detection in any region in the breast; if a tumor presence is not marked clearly in an operating frequency band, it will be sensed more clearly with the antenna's performances in the other operating frequency band. Furthermore, these two frequency bands are reserved and used for medical applications and covered with high impedance matching for each of them. In addition, these two frequency bands are located below the UWB frequencies, which further ensures patient safety, as they are associated with relatively lower losses through the human body tissues.
(4) A spherical shape phantom model of the human female breast is used in the design and simulation of the 3D antenna sensor and in tumor detection performances. The applied dielectric properties of healthy breast tissues and of tumors are based on empirical, approved, and most cited models.
(5) Using a phantom model of the frontal torso and a realistic model of the female human body of VHP-Female version 2.1 [28], the practicality of the proposed method is performed, and simulation outcomes show promise for breast cancer detection using only a single multi-band 3D antenna sensor.

The remainder of this paper is organized as follows. In section II, the breast phantom model, proposed antenna design, and simulation process are presented. In section III, breast cancer detection performances are detailed. Section IV shows practical testing by simulation of the proposed method considering breast variability. In section V, SAR restrictions adherence is described and shown. In section VI, a conclusion for summarizing the main obtained results is given.

II. BREAST MODELING AND ANTENNA DESIGN

As in all electromagnetic problems, designing and simulating antennas for any purpose is based on solving

of Maxwell's equations. Most antenna problems involve complex model geometries and solving these leads to a set of equations unsolvable analytically, e.g., via variable separation and Green's functions. In the problem solved in this paper, the model geometry becomes more and more complex with the using of the three various biological structures of the spherical model of the human female breast, the phantom model of the frontal side of the middle part of the human body, and female human body the realistic model of VHP-Female version 2.1.

Complex electromagnetic problems solving like in the case of the problems solved in this paper requires the use of numerical methods like the finite element method (FEM), used for the design and the simulation of the proposed approach. Herein, the 3D FEM solver within Ansys HFSS software is employed. This package is considered as one of the most powerful tools used for complex electromagnetic problems treatment. To create and solve an electromagnetic problem in HFSS, next steps are performed: creating the model of the problem to be solved, assign boundaries and excitation, set up the solution, solving the problem, and finally post-process the results. Using HFSS, the problem solving implies the automatically subdividing procedure of the whole model geometry into many smaller subsections of tetrahedron shape. The entire collection of these tetrahedrons represents the mesh of the problem. The obtained initial mesh is refined automatically and iteratively using adaptative meshing, focusing on high-error areas for accurate results until a highly precise outcome is met. In all design and simulation processes realized in this paper, the electromagnetic fields within the model mesh elements are solved using first-order basis functions for better accuracy with fewer elements, leading to faster convergence and reduced computational cost.

A. Breast phantom model

For numerical electromagnetic computational purposes such as breast cancer detection, the realistic human breast can be modeled by layered phantom models; each layer simulates a particular breast tissue, its shape, dimensions, thickness, and dielectric properties. A healthy breast is a heterogeneous organ constituted of skin, fat, glandular/fibro-glandular tissues, and a nipple. For an adult woman, the breast is of average full diameter of around 114 mm, and may have various shapes, e.g., round, teardrop [29]. To present the proposed approach for breast cancer detection, the used 3D multi-layer phantom model (Brst_mdl.1) of a healthy female breast is represented in Fig. 1. In this model, skin, fat, and glandular tissue layers are shapes of concentrated half spheres and simulate radii of 55, 53, and 50 mm, respectively. The nipple is also modeled by a half-sphere with a radius of 6 mm.

Dielectric properties of breast tissues, like all human body tissues, are relative permittivity, εr, and conductivity, σ. These two properties are highly frequency-dependent and given by the Cole-Cole empirical model [30].

B. IFA-SCL antenna design and simulation

The dual-band Inverted-F Antenna with Short Circuit-Like (IFA-SCL) antenna sensor designed in this work is tuned to operate in the two frequency bands of ISM 915 MHz and 2.45 GHz with enhanced impedance matching and impedance bandwidth as wide as possible. A 3D and a frontal view of the designed and simulated antenna are shown in Figs. 2 (a) and 2 (b), respectively. The healthy female breast phantom model is placed inside the 3D antenna. This antenna sensor is constituted of three parts, which are a shaped radiating element, a short circuit-like, and a modified ground plane. These antenna's three parts are printed on a substrate, on the side of an internal vertical support, and under a superstrate of Cuflon dielectric material, respectively.

Cuflon is characterized by a relative permittivity εr of 2.05, a loss tangent $\tan\delta$ of 0.00045, and a dielectric thickness of 0.38 mm. The antenna feeding is ensured by a coaxial cable through a Sub-Miniature version A (SMA) connector with a characteristic impedance of 50 Ω.

The shaped radiating element is shown in Fig. 3 (a), and its surficial size is $(X_{RE} \times Y_{RE}) = (111 \times 176.5)$ mm^2. The antenna feed is positioned at the origin of the coordinate system and away from the close edge of the radiating element by 50 mm along the x axis. The substrate corresponding to this radiating element possesses surficial dimensions of $(X_{SUB} \times Y_{SUB}) = (111 \times 180)$ mm^2. This radiating element is modified by the insertion of two meandered slots MS.I and MS.II.

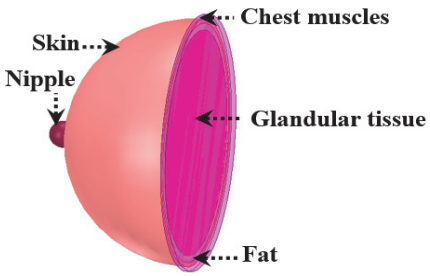

Fig. 1. 3D view of female breast multi-layer phantom model.

The surficial dimensions of the five parts (MS.I_Prt.1 to MS.I_Prt.5) of the first meandered slot MS.I are (41.5 × 1.5), (2.5 × 11), (47 × 2), (1.5 × 8), and (48 × 2) mm^2 for parts from Part.1 to Part.5, respectively. The element MS.I_Prt.1 is away from the

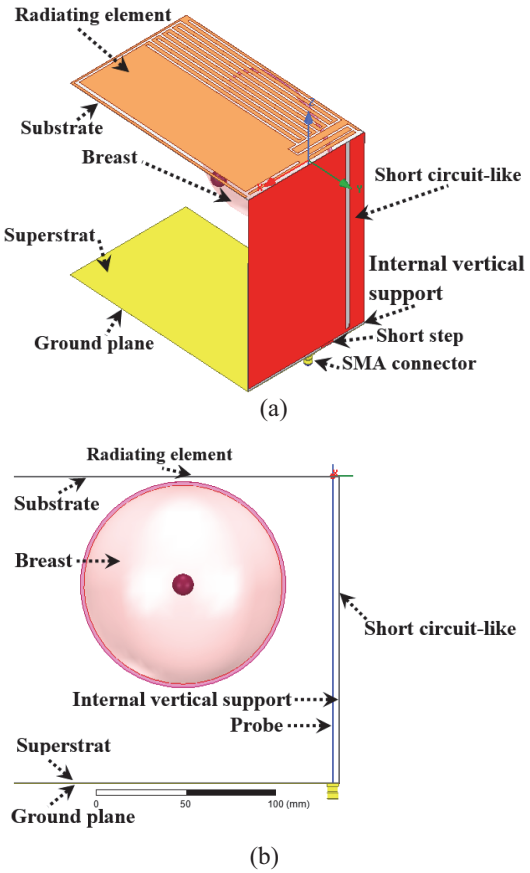

Fig. 2. IFA-SCL antenna sensor structure: (a) 3D view and (b) frontal view.

close edge of the radiating element by 3 mm along the y axis. The element MS.I_Prt.5 branches out to five other slots (MS.I_ST.1 to MS.I_ST.5) in a saw teeth shape. These slots measure surficial dimensions of (2 × 152) mm^2, and they are away from the close edges of the radiating element by 2, 12, 22, 32, and 42 mm along the y axes, respectively.

For the second meandered slot, i.e., MS.II, the length and width of its three parts (MS.II_Prt.1 to MS.II_Prt.3) are (50 × 2.5), (3 × 175), and (99 × 2) mm^2, respectively. The element MS.II_Prt.3 is attached to four slots (MS.II_ST.1 to MS.II_ST.4) in saw teeth shape of dimensions of (2 × 152) mm^2 for each of them. These four slots are away from the close edge of the radiating element by 7 mm for the slot MS.II_ST.1, 17 mm for the slot MS.II_ST.2, 27 mm for the slot MS.II_ST.3, and 37 mm for the slot MS.II_ST.4 along the x axis. The element MS.II_Prt.1 is distant from close edges of the radiating element by 5, and 2 mm along the x and y axes, respectively.

The short circuit-like is depicted in Fig. 3 (b). This antenna constituent measures surficial dimensions of $(X_{SCL} \times Z_{SCL}) = (111 \times 167.6)$ mm^2. The length and the width of the slot inserted in this short circuit-like are 165 and 4 mm, respectively. Also, the surficial dimensions of the rectangular short step used to connect the short circuit-like to the ground plane are (11 × 2.4) mm^2. The slot and the rectangular short step are away from the close edge of the short circuit-like by 14 and 30 mm along the x axis, respectively. The internal vertical support corresponding to the short circuit-like is to enforce the antenna solidity. Its dimensions are $(X_{IVS} \times Z_{IVS}) = (111 \times 169.6)$ mm^2. Figure 3 (c) illustrates the ground plane and the corresponding superstrate. Their dimensions are $(X_{GND} \times Y_{GND}) = (X_{SUP} \times Y_{SUP}) = (111 \times 180.4)$ mm^2. The surficial dimensions of the open-end slot inserted to reformulate the ground plane are (44 × 2) mm^2. This open-end slot is away from the close edge of the ground plane by 3.9 mm along the y axis.

The final structure of the IFA-SCL antenna is the outcome of the design process that can be summarized in three principal steps. The simulation is performed using the 3D full-wave software of High-Frequency Structure Simulator (HFSS), which is based on the finite element method to solve electromagnetic problems. Also, the simulation run-time is very high due to the heterogeneity of the breast phantom model, and also due to the large dimensions of the designed 3D antenna. Furthermore, this time increases from one design step to the next.

Figure 4 shows the radiating element, the short circuit-like, and the ground plane structures issuing from successive design and simulation steps. To validate each step, the reflection coefficient representation is adopted as indicated by Fig. 5. The design and simulation steps are as follows:

First, using two Cuflon dielectric Printed Circuit Boards (PCBs) of size (111 × 180 × 0.38) mm^3 and copper thickness of 18 μm for each of them, a patch antenna with a full ground plane and rectangular radiating element is designed and simulated. The first PCB is used to print the radiating element; however, the second PCB is used to print the ground plane as depicted in Fig. 4 (a).

The radiating element is connected to a coax-feed via a SMA connector with a probe of full length of 170 mm and radius of 0.38 mm (Fig. 2 (b)), which yields a 3D patch antenna. The breast (Brst_mdl.1) to be examined is placed inside the antenna. The computed reflection coefficient that corresponds to this first step is represented by Fig. 5 (First step). In the frequency range of interest, i.e., from 0.85 to 2.8 GHz, three resonance frequencies are obtained at frequencies of 0.96 GHz, 1.76 GHz, and 2.64 GHz. For the lower resonance, it is close to the first targeted frequency band of ISM 915 MHz, but its impedance matching is not sufficient. The third resonance is close to the second targeted frequency band of ISM 2.45 GHz and presents a practical

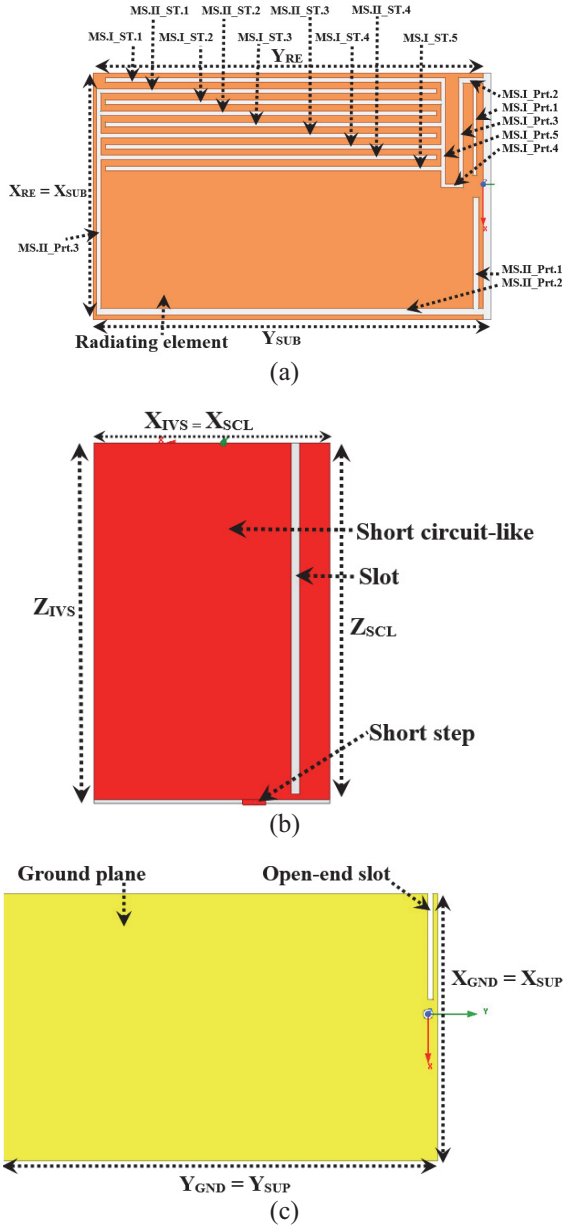

Fig. 3. 2D view of the designed 3D antenna sensor elements: (a) radiating element, (b) short circuit-like, and (c) ground plane.

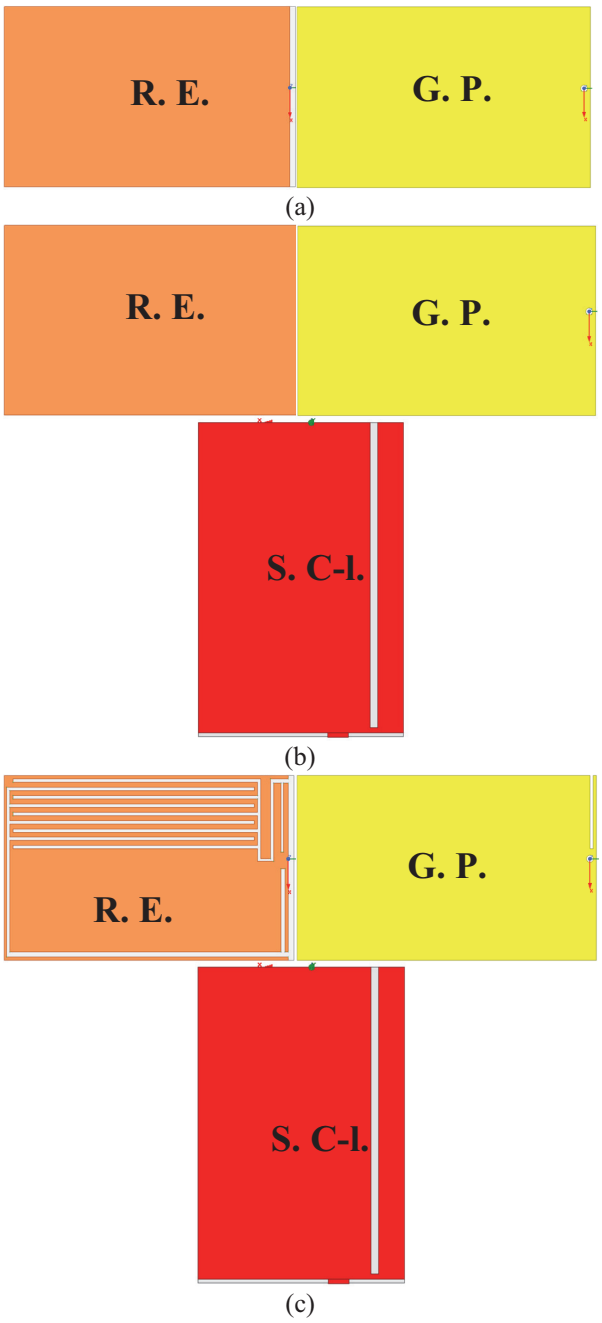

Fig. 4. Design and simulation process steps: (a) first step, (b) second step, and (c) third and final step. R.E. Radiating element, G.P. Ground plane, S.C-l. Short circuit-like.

impedance matching. In the next design and simulation steps, these first and third resonance frequencies will be reduced and tuned to cover the two targeted frequency bands with enhanced impedance matching as possible.

Second, a short circuit-like is inserted in the antenna between the radiating element and the ground plane and connected to the ground plane by a rectangular short step. In addition, to enforce the solidity of the 3D antenna, the short circuit-like is printed on the side of an internal vertical support of Cuflon dielectric material. To reduce the first and third resonance frequencies obtained in the precedent design step, a rectangular slot is inserted in this short circuit-like as shown by Fig. 4 (b).

The reflection coefficient corresponding to this step is represented by Fig. 5 (Second step). A shift to lower frequencies is obtained for the first resonance frequency, and the first targeted frequency band of ISM 915 MHz is partially covered with a practical impedance matching. Furthermore, the third resonance frequency obtained in

the first step of this design is also reduced, leading to covering the second targeted frequency band of ISM 2.45 GHz with a satisfactory impedance matching.

Finally, to cover the two targeted frequency bands with impedance bandwidth as wide as possible and improved impedance matching as possible, two meandered slots constituted of five parts for the first and three for the second are inserted in the radiating element as represented in Fig. 4 (c). Also, these two meandered slots are enforced by five and four other slots shaped like saw teeth. These two shaped like saw teeth aim to increase the antenna sensing to dielectric properties changing and, thus, tumor(s) presence. In addition, an open-end slot is inserted in the ground plane. Finally, dimensions are tuned to yield the best design and simulation results.

The simulated reflection coefficient obtained from this third and final step is represented by Fig. 5 (Third step, Final design). The final design yields a 3D antenna operating in two frequency bands allocated for medical devices, which are ISM 915 MHz and 2.45 GHz. The first frequency band is covered with a resonance at a frequency of 0.875 GHz; the corresponding magnitude of the reflection coefficient (S_{11}) is -30.94 dB, and the achieved impedance bandwidth is around 80 MHz. For the second frequency band, the corresponding resonance is at a frequency of 2.465 GHz, the magnitude of the reflection coefficient (S_{11}) is -32.29 dB, and the available impedance bandwidth is 50 MHz.

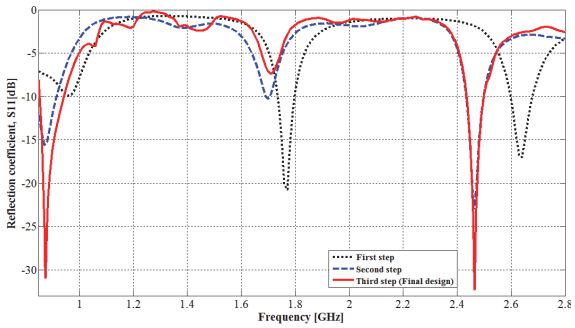

Fig. 5. Reflection coefficient corresponding to design and simulation steps.

III. TUMOR DETECTION PERFORMANCES

In pathologic cases, breast tumors are generally produced in the glandular tissue. Electromagnetically, the tumor is characterized by particular dielectric properties, which are completely different from those of the healthy tissue. Dielectric properties of breast tumors used in this work are from the most agreed-upon and used empirical model [31]. Malignant tissues are characterized by different water and ionic content than other human body tissues, which leads to particular permittivity and conductivity and thus enables tumor detection.

A. Tumor detection and its size effect

It must be noted here that, while breasts are similar, very slight differences in size, shape, and internal structure are very common and normal for most women due to natural variations in tissue (fat/glandular) distribution, hormones, and genetics. The proposed approach is based on the reality that breast cancer is typically unilateral, meaning it starts in one breast, with bilateral (both breasts) cases occurring in only 1–3 % of patients [32, 33]. Thus, breast cancer detection with the proposed approach entails the examination of the two breasts of the patient and then comparing the shifting and magnitude of resonance frequencies covering the two operating frequency bands.

To evaluate the performances of the proposed IFA_SCL antenna sensor for tumor detection, the adopted scenario is given by Fig. 6 (a). The tumor to be detected is supposed to be of spherical shape with radii of 1, 2, and 5 mm and placed deeply in the glandular layer of the female breast phantom model (Brst_mdl.1) presented in section II, part A. Figure 6 (b) shows the obtained mesh of breast skin part corresponding to solved problem of this scenario. The entire model geometry is discretized into 469066 tetrahedrons, with the tumor divided into 649 finite elements having a minimum volume of 2.25794×10^{-5} mm^3. The corresponding reflection coefficient is shown in Fig. 7. By comparison with the reflection coefficient corresponding to the final design obtained in section II, part B, which is also represented in this figure, the tumor presence produces a resonance frequency shift and return loss modification in both lower and higher resonance frequencies covering the two operating frequency bands.

For the lower functional frequency band, the resonance frequency shifts from 0.875 GHz to higher frequencies of 0.879, 0.880, and 0.880 GHz for tumor radii of 1, 2, and 5 mm, respectively. Also, the simulated return loss (S_{11}) changes from -30.94 dB to -31.38, -29.75 and -29.54 dB for these same tumor radii. For the higher operating frequency band, the resonance frequency shifts also occur to higher frequencies but it is less remarkable especially for the tumor radius of 1 mm. For this higher operating frequency band, the resonance frequency shifting and the corresponding amplitude are from (2.465 GHz, -32.29 dB) to values of (2.465, -33.94), (2.466, -34.91), and (2.467, -39.62) (GHz, dB) for tumor radii of 1, 2, and 5 mm, respectively.

From the obtained outcomes, a tumor presence with a radius of only 1 mm is detectable based on the resonance frequency shifting and the corresponding

return loss magnitude changing. Effectively, the tumor presence is sensed in both operating frequency bands with some difference in sensing ability. Thus, the use of a multi-band antenna sensor allows for the efficient sensing of the tumor presence with remarkable resonance frequency shifting and/or return loss magnitude changing in at least one of their operating frequency bands. From the simulation performed in this section, tumor presence produces a shifting of value of at least 4 MHz for the resonance frequency that covers the ISM band of 915 MHz. This shifting value is very remarkable which means that this lower operating frequency is more sensitive to tumor presence in considered breast shape and size. Obtaining remarkable values allows practitioners to confirm easily the tumor presence. In addition, tumors of various sizes are also detectable. In fact, a tumor size increase leads to more resonance frequency shifting and/or more impedance matching in at least in one of the two operating frequency bands. Tumor presence produces variations in the impedance bandwidth corresponding to the two operating bands.

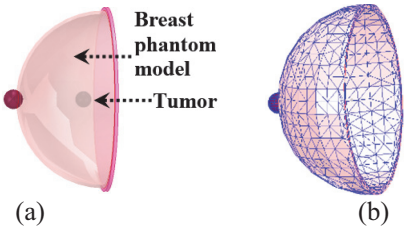

Fig. 6. Tumor detection using designed IFA_SCL antenna: (a) tumor to be detected and (b) skin part meshing.

B. Multiple tumors detection

In the breast, the tumor can appear in various regions of glandular tissue. The scenario of the parallel presence of six spherical shape tumors with same radius is examined using the breast model Brst_mdl.1 as shown in Fig. 8. To study the mentioned scenario, three stages are considered by varying the six tumors the same radius from 1, 2, to 5 mm in each stage. The corresponding simulated reflection coefficient is shown in Fig. 9. Effectively, multiple tumor presences are also detectable considering the resonance frequency shifting and the corresponding magnitude changing. For tumors with radius of 1 mm, the resonance frequency amplitude changes by 8.04 dB within the ISM band of 2.45 GHz without a shift in the resonance frequency, and for the ISM band of 915 MHz, a shifting of 4 MHz is simulated for the resonance frequency. A radius of 2 mm leads to resonance frequency shifting by around 4 MHz within the two ISM frequency bands. With the radius of 5 mm, the shifting is clearer within the frequency

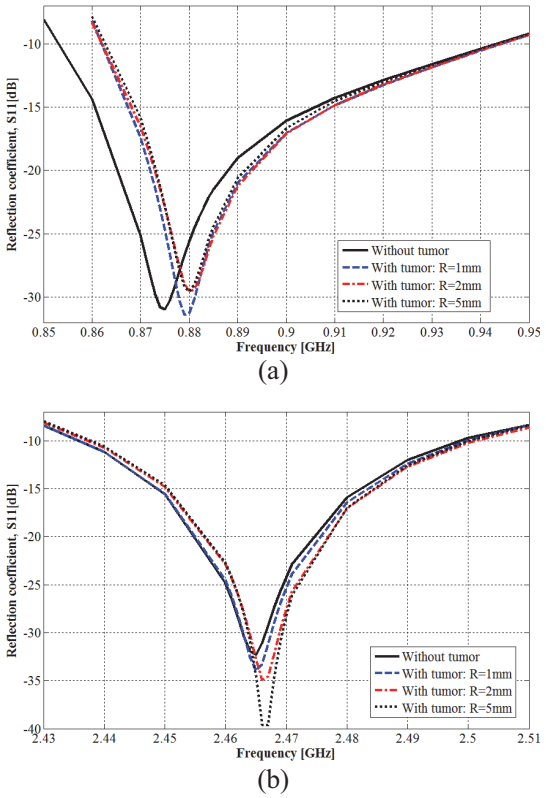

Fig. 7. Effect of tumor presence on reflection coefficient: (a) ISM band of 915 MHz and (b) ISM band of 2.45 GHz.

band of 2.45 GHz where a shifting of around 6 MHz is simulated. Thus, multiple tumors lead to more resonance frequency shifting for both resonance frequency, and the six tumors presence is sensed more in the ISM frequency band of 915 MHz.

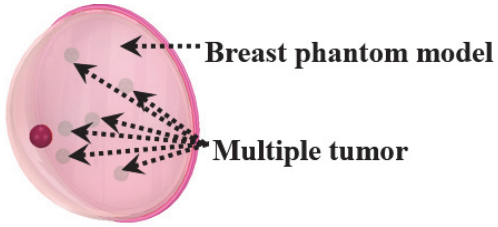

Fig. 8. Multiple tumor detection scenario.

C. Breast size effect

Breast size and shape may change naturally from one individual to another. These differences are influenced by genetics, related body weight, and age, and can also be affected by hormonal fluctuations, pregnancy, and weight changes. Because breasts are composed of fatty tissue, weight gain or loss directly impacts size. For these reasons, the antenna sensor must be usable with various sizes and shapes.

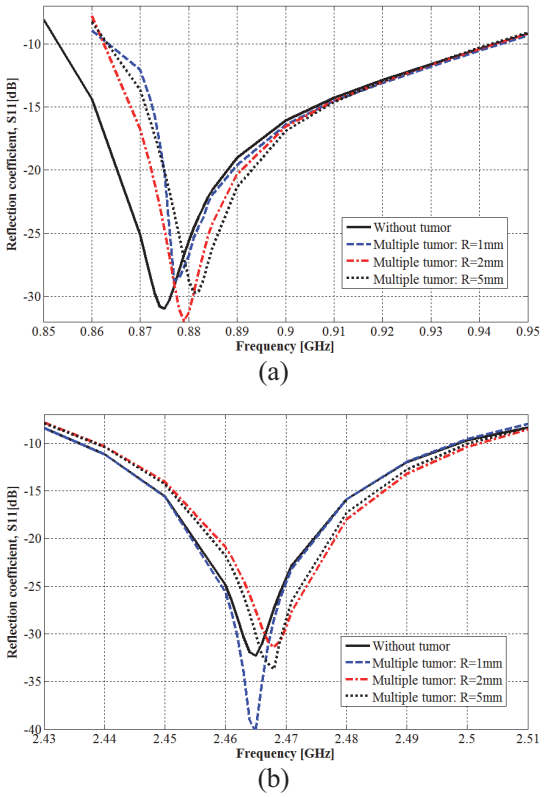

Fig. 9. Multiple tumor effect on the IFA_SCL antenna performances: (a) ISM band of 915 MHz and (b) ISM band of 2.45 GHz.

To simulate the detection ability of the proposed method considering the breast size variability, the spherical shape breast model Brst_mdl.1 used previously is added to two other spherical shape breast models: Brst_mdl.2 and Brst_mdl.3. The model Brst_mdl.2 has skin, fat, and glandular layers of radii of 51, 48.5, and 47 mm, respectively. The skin, fat, and glandular layers radii of the model Brst_mdl.3 are 47, 46, and 44.5 mm, respectively.

The simulated reflection coefficients corresponding to these three models are given in Fig. 10. Herein, the tumor is also suggested to be of spherical shape with a radius of 1 mm and placed deep within the glandular tissue.

Without a tumor and based on performed simulations, breast size and structure variations lead to different resonance frequencies for both the lower and upper operating frequency bands. While the spherical shape breast model of Brst_mdl.1 simulates resonance frequencies of 0.875 GHz and 2.465 GHz for lower and higher operating frequency bands, the model Brst_mdl.2 yields resonance frequencies of 0.881 GHz and 2.465 GHz, and the model Brst_mdl.3 produces resonance frequencies of 0.877 GHz and 2.464 GHz. Despite the distinguished resonance frequencies obtained with various breast spherical models, the two operating frequency bands of ISM 915 MHz and 2.45 GHz remain covered with high impedance matching. Thus, the 3D antenna sensor is usable with breasts of various sizes.

With a tumor and also based on performed simulations, the breast spherical model Brst_mdl.2 shifts the resonance frequencies from 0.881 to 0.882 GHz and from 2.465 to 2.466 GHz for the first and second operating frequency bands. The shifted resonance frequency corresponding to the higher frequency band is accompanied by amplitude changing of value of 3.32 dB and it is more than the amplitude changing (1.55 dB) corresponding to shifted resonance frequency within the lower frequency band. Thus, with this breast model of Brst_mdl.2, the ISM frequency band of 2.45 GHz is more sensitive to tumor presence. Also, for the breast spherical model Brst_mdl.3, the resonance frequencies shift from 0.877 to 0.879 GHz, and from 2.464 to 2.465 GHz for the first and the second operating frequency bands, respectively. The resonance frequency shifting observed with all three breast phantom models is accompanied by changes in the corresponding reflection coefficient magnitudes. From these various breast spherical models, the proposed approach and thus the proposed dual-band 3D antenna sensor have the potential to be used with breasts of various sizes.

From simulations affected in this section, the breast cancer detection ability of the proposed method is demonstrated by its capability to detect minor tumors even those with a radius only of 1 mm, either in single or multiple locations, and across various considered breast sizes. Tumor presence results in a significant frequency shift at least in one resonance frequency within two covered frequency bands of ISM 915 MHz and 2.45 GHz. The simulated value of resonance frequency shifting may reach 6 MHz, which is a very remarkable value. Furthermore, this shifting is accompanied by a change in the corresponding magnitudes with difference values until 7.33 dB.

Since both the antenna's electrical and radiation performances are significantly related to the surrounding material's dielectric properties, the resonance frequencies and their magnitudes of the proposed 3D antenna are exploited to sense variations in dielectric properties of breast tissues due to the tumor presence. By placing the breast under examination between the radiation element and the ground plane, it becomes part of the effective substrate of the 3D antenna which leads to reach high sensing capability for variations in the breast's dielectric properties.

To better show the detection ability of the proposed method, the next section designs and simulates this ability using breasts of teardrop and side-set shapes.

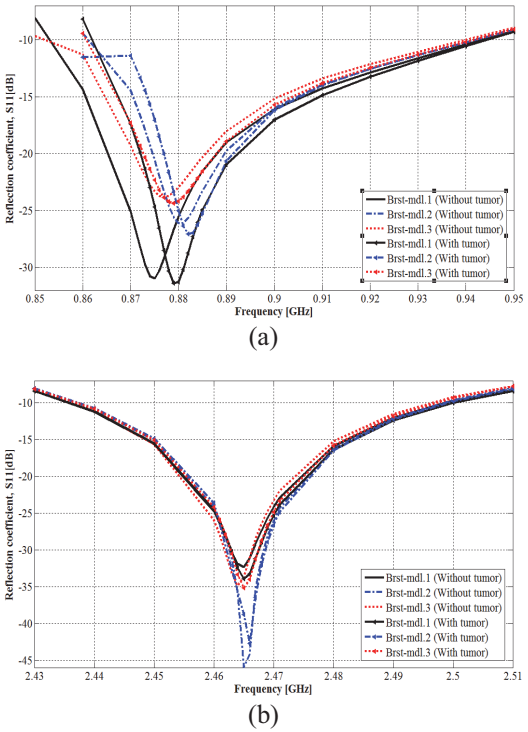

Fig. 10. Breast size effect on tumor detection: (a) in the ISM 915 MHz frequency band and (b) in the ISM 2.45 GHz frequency band.

IV. PRACTICAL TESTS AND TUMOR DETECTION USING MORE BREAST VARIABILITY SIMULATION

For both testing the clinical applicability and demonstrating the performance of the tumor detection with more breast shapes using the proposed method, two realistic human female breast models in side-set and teardrop shapes are simulated. A human tissues model, denoted Tbrst_mdl, is obtained by merging the side-set shape within a frontal torso phantom model, while the teardrop shape breast is included in the middle part of the computational and realistic female human body of VHP-Female version 2.1 and the resulting human tissues model is denoted Vbrst_mdl. The frontal torso is constituted of muscle, fat, and skin tissues. The entire version 2.1 of the VHP-Female realistic model contains 25 individual tissues distributed in 203 tissue parts. As in previous, the dielectric properties of various tissues are based on the Cole-Cole model.

A top and lateral view of the model Tbrst_mdl and the side-set shape breast tissues are depicted in Figs. 11 (a), (b) and (c). A top and lateral view of the model Vbrst_mdl, and the teardrop shape breast tissues are shown by Figs. 12 (a), (b) and (c).

Figure 13 (a) presents the application of the 3D antenna sensor for tumor detection in practical testing

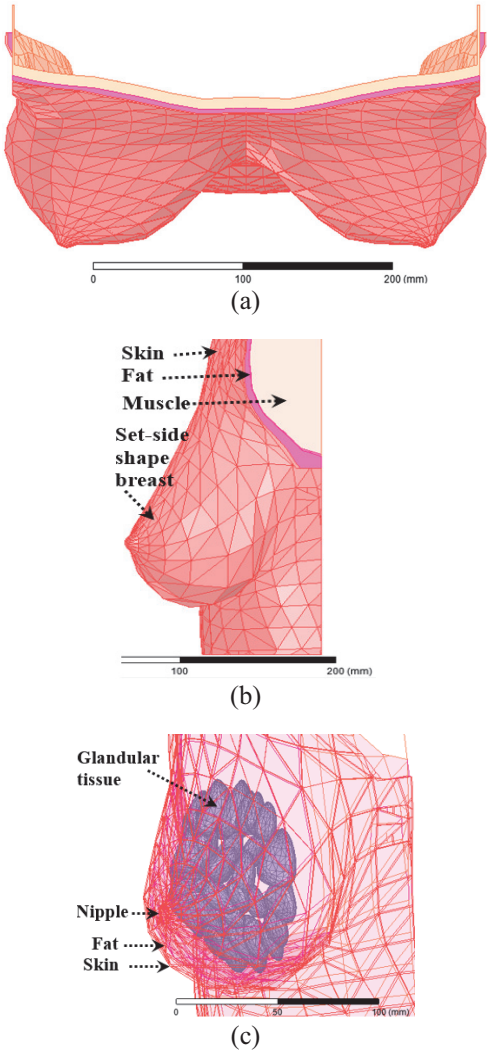

Fig. 11. Tbrst_mdl model: (a) top view, (b) lateral view, and (c) side-set shape breast tissues.

for the Tbrst_mdl model, while Fig. 13 (b) shows this testing with the Vbrst_mdl model. The mesh corresponding to the geometry of the solved model depicted in Fig. 13 (b) is represented by Fig. 13 (c). Herein, the full mesh is constituted of 703454 tetrahedrons. The tumor is discretized into 766 tetrahedra finite elements with a minimum volume of 7.61211×10^{-6} mm^3.

The tumor to be detected is positioned within the side-set shape breast of the Tbrst_mdl model as illustrated in Fig. 14 (a). For the teardrop shape breast of the model Vbrst_mdl examination, tumor presence is positioned in two different locations (upper and lower) as indicated in Figs. 14 (b) and (c). In all cases, the tumor is spherical, located within the glandular tissue, and has radii of 1, 2, or 5 mm.

As a function of tumor radius, simulated reflection coefficients obtained with the side-set and teardrop

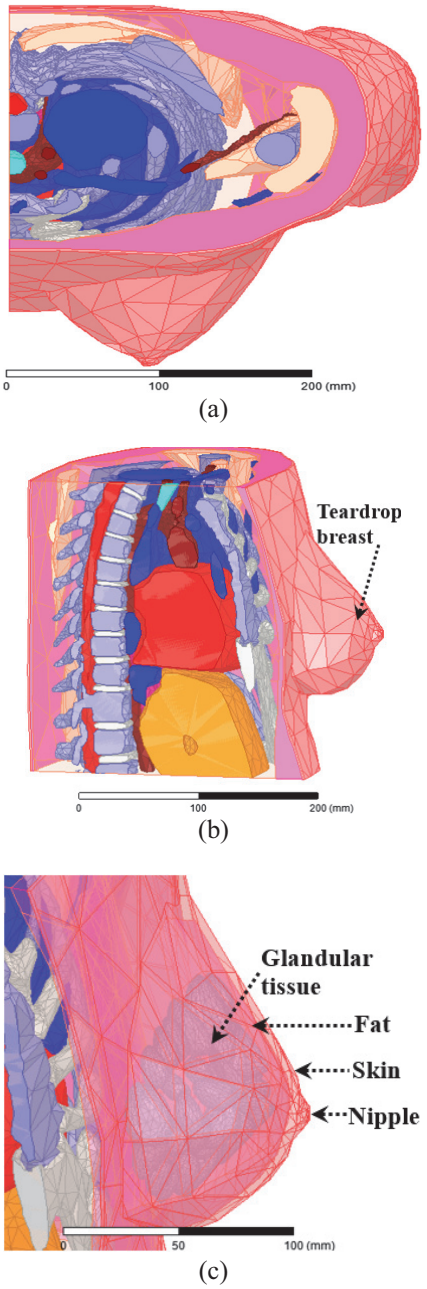

Fig. 12. Vbrst_mdl model: (a) top view, (b) lateral view, and (c) teardrop shape breast tissues.

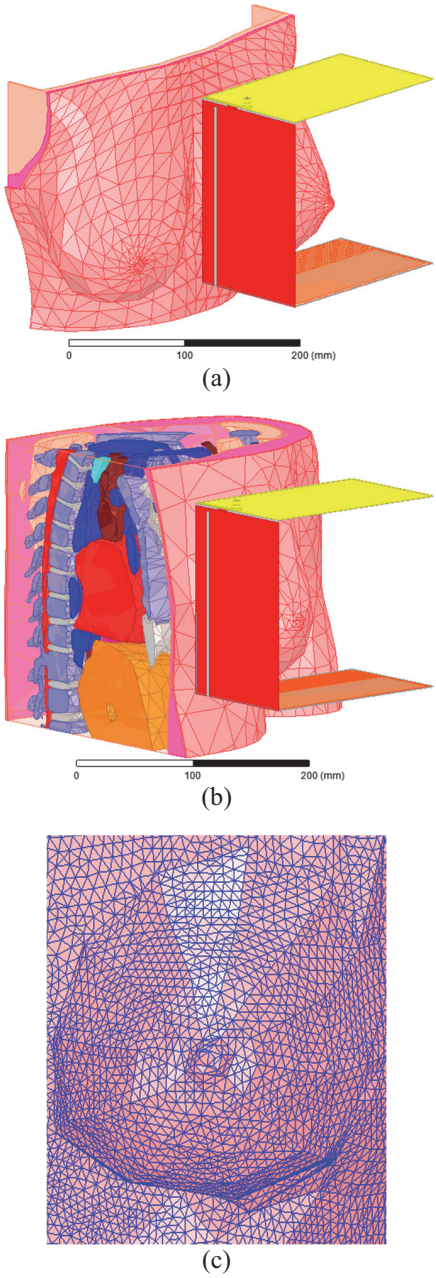

Fig. 13. Clinical testing of the 3D antenna sensor with breast variability: (a) side-set shape breast examination, (b) teardrop shape examination, and (c) breast skin part meshing.

shape breast are shown in Figs. 15 (a, b), and Figs. 16 (a, b), with the tumor in the upper location for the latter.

Depending on the tumor location, simulated reflection coefficients obtained with the teardrop shape breast are shown in Figs. 17 (a) and (b), with the tumor radius fixed at 1 mm.

Herein, it must be noted that the required time for problem analysis and solving increases from the Tbrst_mdl to the Vbrst_mdl models due to the more model geometry complexity of this letter.

As precisely indicated in Fig. 15, the presence of a tumor within the breast model (Tbrst_mdl) results in a shift to higher frequencies (and changes in amplitude) for both lower and higher resonance frequencies of the 3D antenna sensor. The lower resonance frequency shifts (amplitude changes) from 0.870 GHz (−21.15 dB) to 0.880 (−20.17), 0.880 (−20.29), and 0.880 GHz (−20.62 dB) when the tumor radius is of 1, 2, and

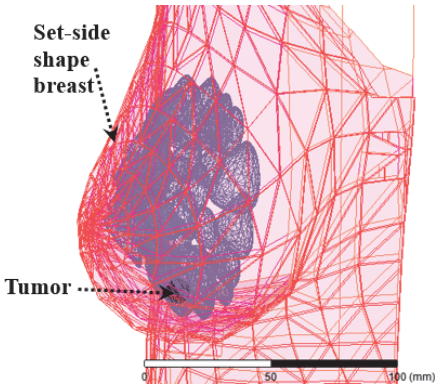

(a)

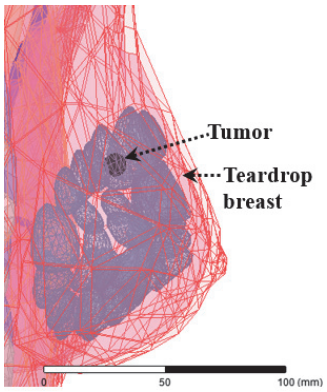

(b)

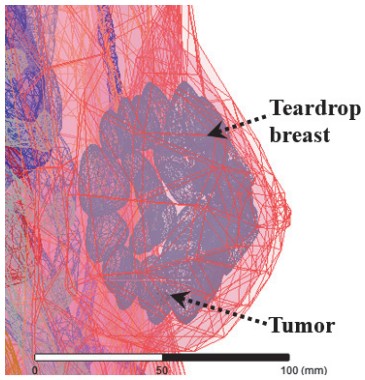

(c)

Fig. 14. Tumor presence in glandular tissue: (a) tumor in side-set shape breast, (b) tumor in upper location in teardrop shape breast, and (c) tumor in lower location in teardrop shape breast.

5 mm, respectively. The higher resonance frequency shifts (amplitude changes) from 2.450 GHz (−23.68 dB) to 2.470 (−19.67), 2.460 (−26.44), and 2.460 GHz (−23.63 dB) also when the tumor radius is 1, 2, and 5 mm, respectively. Thus, the tumor presence is sensed significantly in both operating frequency bands with more remarkable shifting within the ISM frequency band of 2.45 GHz.

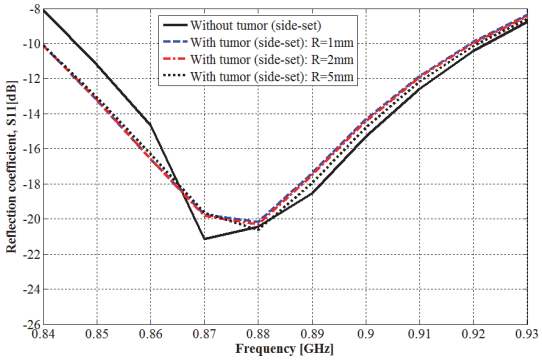

(a)

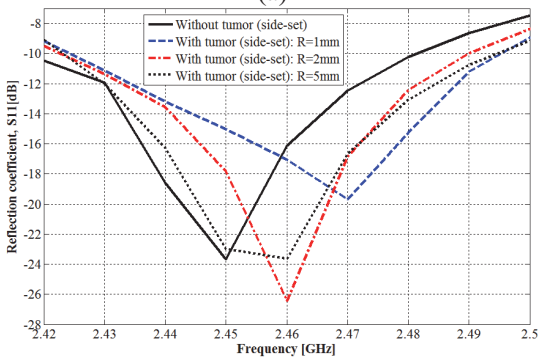

(b)

Fig. 15. Tumor detection in side-set shape breast: (a) 915 MHz ISM band and (b) 2.45 GHz ISM band.

From Fig. 16, when the tumor is placed in the upper location within the teardrop shaped breast, both resonance frequencies shift to higher frequencies, which also yields a change in amplitude. The lower resonance frequency shifts (and amplitude changes) from 0.870 GHz (−24.21 dB) to 0.880 (−25.40), 0.880 (−23.92) and 0.880 GHz (−23.61 dB), and the higher resonance frequency shifts (and amplitude changes) from 2.460 GHz (−25.29 dB) to 2.470 (−21.45), 2.470 (−23.69) and 2.480 MHz (−20.47 dB). Tumor radius is of value at 1, 2, and 5 mm consecutively. Detection ability is more remarkable within the frequency band of 2.45 GHz, especially with tumor radius of 5 mm.

As shown in Fig. 17, the presence of a spherical tumor with a 1 mm radius in the lower location was detected by the 3D antenna sensor. A shift in the two resonance frequencies and a change in amplitude were obtained for various reached resonance frequencies. For the lower resonance frequency, the frequency shift (and the amplitude change) is from 0.870 GHz (−24.21 dB) to 0.880 GHz (−21.86 dB); the higher resonance frequency shifts (and amplitude changes) from 2.460 GHz (−25.29 dB) to 2.470 GHz (−18.43 dB).

For various simulations corresponding to this section, tumor presence introduces a significant shift of at least of 10 MHz in at least resonance frequency.

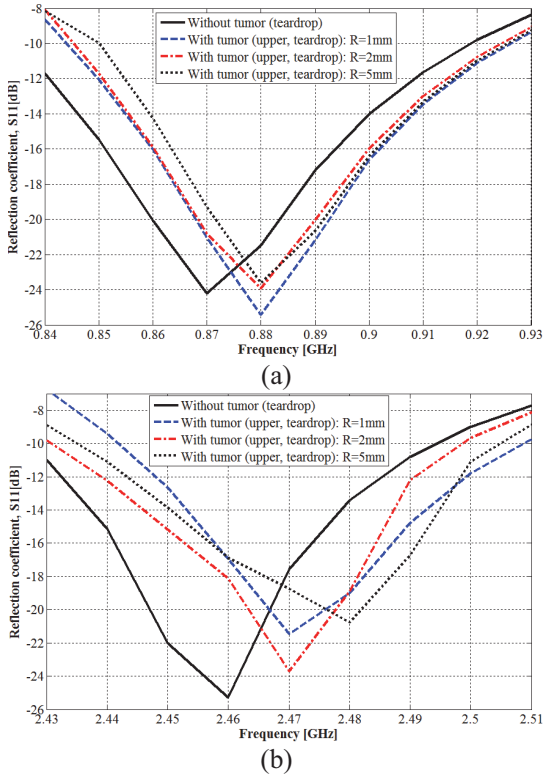

Fig. 16. Tumor detection in teardrop shape breast: (a) 915 MHz ISM band and (b) 2.45 GHz ISM band.

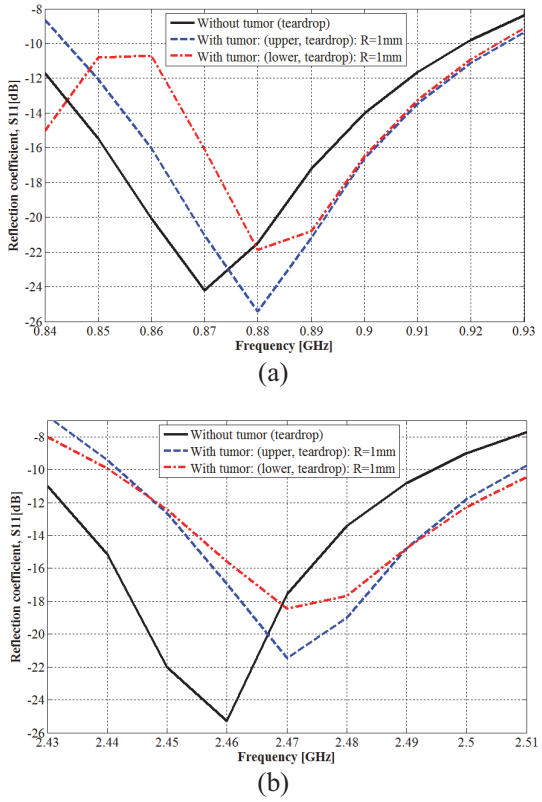

Fig. 17. Tumor location effect on tumor detection: (a) 915 MHz ISM band and (b) 2.45 GHz ISM band.

Based on reflection coefficients obtained by simulation with various breast spherical models (Brst_mdl.1, Brst_mdl.2, and Brst_mdl.3) used in sections II and III, as well as the side-set shape breast of the Tbrst_mdl model and the teardrop shape breast of the Vbrst_mdl model used in this section, it can be deduced that, despite the influence of the breast variability on the resonance frequencies and their amplitudes, the operating frequency bands remain covered and the 3D antenna sensor maintains its full-power for tumor detection. A tumor with radius of only 1 mm can be sensed and, in all cases, at least one resonance frequency shift by a remarkable value of few MHz is simulated.

The detection ability of the proposed method was confirmed in the two simulated practical tests, where remarkable frequency shifts were obtained. For both first and second tests, simulated frequency shifting is of minimum value of 10 MHz and a maximum value of 20 MHz were achieved for the two ISM frequency bands of 915 MHz and 2.45 GHz. Additionally, the shifted resonance frequency magnitude increases by up to 6.86 dB for the second test. Therefore, after examination of a woman's breasts and by comparing the corresponding reflection coefficients, practitioners can deduce a tumor's presence if there's a remarkable difference in resonance frequency at least in one operating frequency band. The unhealthy breast is that which exhibits the higher resonance frequency (or frequencies).

V. PATIENT SAFETY CONFIRMATION

In any interaction between human body tissues and electromagnetic waves, the patient's safety must be ensured. To reach this goal, the general public exposure is restricted by the two standards of IEEE C95.1-1999 (1-g Averaged SAR $\leq$ 1.6 W/Kg) [34] and IEEE C95.1-2005 (10-g Averaged SAR $\leq$ 2 W/Kg) [35]. For the proposed approach, the net-input power of the 3D antenna sensor should not exceed the corresponding value for each limit. Since the first limit is the most restricted, it will be used in this work.

Proposed experimental and clinical systems used in breast cancer detection using radar-based MWBI commonly operate at very low power levels where the power transmitted by antennas is within the 0.1 (-10 dBm) to 10 mW ($+10$ dBm) range. More exactly, many systems settle near 1 mW (0 dBm) as a practical balance point.

To verify patient safety during examination for early-stage breast cancer detection using the proposed antenna sensor, its net-input power is set to 1 mW. The simulated maximum 1-g averaged SAR values at resonance frequencies that cover the two interested

frequency bands using the breast phantom model Brst_mdl.1 are given by Table 1.

Table 1: Simulated maximum 1-g averaged SAR in breast phantom model Brst_mdl.1 tissues

Frequency [GHz]	Tissue	Max 1-g Avg. SAR [mW/Kg]
0.875	Skin	1.93
	Fat	2.83
	Glandular	2.40
	Muscle	2.24
2.465	Skin	3.79
	Fat	3.68
	Glandular	2.00
	Muscle	3.15

From simulated maximum values of averaged SAR using the 1-g standard, patient safety remains ensured even as the antenna net-input power rises until 422.16 mW, which is much higher than the experimental transmitted power by radar-based MWBI antennas.

VI. CONCLUSION

The present work discusses and presents a novel approach for early-stage breast cancer detection using only a single radiofrequency 3D antenna sensor. The simulated, designed, and used IFA-SCL antenna is of an innovative structure that allows placing the entire breast to be examined inside between its radiating element and ground plane, this enables efficient sensing of the dielectric properties of the breast under examination.

The proposed antenna is operational in two allocated frequency bands for medical applications, which are ISM 915 MHz and 2.45 GHz. Based on the shifting of resonance frequencies corresponding to these two bands and the related return loss magnitude changing, tumor presence and thus its detection is realized. A tumor with a radius of only 1 mm and placed deeply in the glandular tissue is detectable with various sizes of a spherical shape breast model; a shifting of 4 MHz in the resonance frequency that covers the ISM 915 MHz is obtained. Testing by simulation of the proposed approach with realistic and variable breasts yields very satisfactory results for practical use. From these tests, a significant and a remarkable resonance frequency shifting of 20 MHz is simulated within the frequency band of ISM 2.45 GHz. From simulated results, the 3D antenna sensor is able to sense tumor presence with variable breast shapes and sizes.

With the proposed approach, tumor detection is easy, fast, less painful, safe and comfortable, and with low-cost. In addition, false-positive (a suspicious area that appears to be cancerous, but no cancer is present) and false-negative (incorrectly suggesting no cancer is present, when a tumor is actually present) results are fully detected by the proposed 3D antenna sensor, which may allow this novel approach to become a promising and alternative way for early-stage breast cancer detection.

REFERENCES

[1] H. M. E. Misilmani, T. Naous, S. K. A. Khatib, and K. Y. Kabalan, "A survey on antenna designs for breast cancer detection using microwave imaging," *IEEE Access*, vol. 8, pp. 102570–102594, 2020.

[2] N. Rezaei, *Breast Cancer Treatment: An Interdisciplinary Approach*. Switzerland: Springer Nature, 2024.

[3] Y. Bakar and A. Tugral, *Managing Side Effects of Breast Cancer Treatment*. Switzerland: Springer Nature, 2024.

[4] K. V. Ramani, H. Ramani, S. S. Alurkar, B. S. Ajaikumar, and R. G. Trivedi, *Breast Cancer: Medical Treatment, Side Effects and Complementary Therapies*. New York: Momentum Press, 2017.

[5] U. Veronesi, A. Goldhirsch, P. Veronesi, O. D. Gentilini, and M. C. Leonardi, *Breast Cancer: Innovations in Research and Management*. Switzerland: Springer International Publishing, 2017.

[6] O. Al Jarroudi, K. El Bairi, and G. Curigliano, *Breast Cancer Research and Treatment*. Switzerland: Springer Nature, 2023.

[7] K. H. R. Tkaczuk, S. B. Kesmodel, and S. J. Feigenberg, *Handbook of Breast Cancer and Related Breast Disease*. New York: Demos Medical Publishing, 2017.

[8] G. Gasparini and D. F. Hayes, *Biomarkers in Breast Cancer: Molecular Diagnostics for Predicting and Monitoring Therapeutic Effect*. New Jersey: Humana Press, 2006.

[9] E. Bombardieri, G. Bonadonna, and L. Gianni, *Breast Cancer: Nuclear Medicine in Diagnosis and Therapeutic Options*. Berlin Heidelberg: Springer-Verlag, 2008.

[10] S. Mallick and C. K. Sharma, *Evidence in Breast Cancer*. Singapore: Springer Nature, 2024.

[11] S. J. Nass, I. C. Henderson, and J. C. Lashof, *Mammography and Beyond: Developing Technologies for the Early Detection of Breast Cancer*. Washington DC: National Academic Press, 2001.

[12] M. Z. Mahmud, M. T. Islam, N. Misran, S. Kibria, and M. Samsuzzaman, "Microwave imaging for breast tumor detection using uniplanar AMC based CPW-fed microstrip antenna," *IEEE Access*, vol. 6, pp. 44763–44775, 2018.

[13] D. N. Elsheakh, O. M. Fahmy, M. Farouk, K. Ezzat, and A. R. Eldamak, "An early breast cancer detection by using wearable flexible sensors and artificial intelligent," *IEEE Access*, vol. 12, pp. 48511–48529, 2024.

[14] N. Nithya and M. S. K. Manikandan, "Enhancement of multifrequency microwave tomography breast imaging system using flexible preconditioner based Krylov subspace methods," *Applied Computational Electromagnetics Society (ACES) Journal*, vol. 37, no. 6, pp. 664–671, June 2022.

[15] A. K. Alqallaf, R. K. Dib, and S. F. Mahmoud, "Microwave imaging using synthetic radar scheme processing for the detection of breast tumors," *Applied Computational Electromagnetics Society (ACES) Journal*, vol. 31, no. 2, pp. 98–105, Feb. 2016.

[16] B. Guetaf, A. Chaabane, A. Khalfallaoui, and H. Attia, "Narrow-band circularly polarized antenna for medical microwave imaging and health monitoring applications," *Applied Computational Electromagnetics Society (ACES) Journal*, vol. 38, no. 6, pp. 424–438, June 2023.

[17] I. Unal, B. Türetken, and C. Canbay, "Spherical conformal bow-tie antenna for ultra-wide band microwave imaging of breast cancer tumor," *Applied Computational Electromagnetics Society (ACES) Journal*, vol. 29, no. 2, pp. 124–133, Feb. 2014.

[18] R. A. Petrella, K. H. Schoenbach, and S. Xiao, "A dielectric rod antenna for picosecond pulse stimulation of neurological tissue," *IEEE Transactions on Plasma Science*, vol. 44, no. 4, pp. 708–714, Apr. 2016.

[19] M. R. S. Ramu and K. Arunachalam, "Miniaturized 434 MHz cavity encapsulated patch antenna for superficial hyperthermia treatment," *IEEE Journal of Electromagnetics, RF and Microwaves in Medicine and Biology*, vol. 7, no. 4, pp. 392–399, Dec. 2023.

[20] M. Behih, F. Bouttout, T. Fortaki, and C. Dumond, "A novel wideband and multiband implantable antenna design for biomedical telemetry," *Applied Computational Electromagnetics Society (ACES) Journal*, vol. 37, no. 04, pp. 441–457, Apr. 2022.

[21] M. Behih, F. Bouttout, T. Fortaki, and C. Dumond, "A novel multifunction implantable antenna design for biomedical telemetry," in *2021 International Applied Computational Electromagnetics Society Symposium (ACES)*, Hamilton, ON, Canada, pp. 1–4, 2021.

[22] N. Hammouch, A. Rghioui, and H. Ammor, "A low-cost UWB microwave imaging system for early-stage breast cancer detection," *Multimed. Tools Appl.*, July 2024.

[23] M. A. Aldhaeebi, T. Almoneef, S. Bamatraf, A. O. Aldhaibain, O. Bakhalah, S. Alhdad, S. Bakhalah, and M. K. Saleem, "Near-field metasurface sensor for an early-stage breast cancer detection," *Sensors International Journal*, vol. 6, 2025.

[24] S. Reelekshmi and S. P. Sankar, "Design and analysis of novel miniaturised triple band antenna for breast cancer detection," *Microsyst. Technol. Journal*, vol. 28, pp. 1715–1726, 2022.

[25] I. Jahan and M. A. Kabir, "Microstrip patch antenna for breast cancer detection," in *5th International Conference on Electrical Information and Communication Technology (EICT)*, Khulna, Bangladesh, Dec. 2021.

[26] T. Lanka, D. Chaturvedi, M. V. L. Bhavani, and A. Kumar, "Design of PRS enabled monopole slotted-antenna sensor for breast tumor detection," *Scientific Reports*, vol. 15, 2025.

[27] K. Youssef, M. A. Zahhad, H. Kanaya, and A. H. El-Malek, "A unified approach for breast cancer discrimination using metasurface-based microwave technology," *Discover Applied Sciences*, vol. 6, July 2024.

[28] S. N. Makarov, G. M. Noetscher, J. Yana-Madala, M. W. Piazza, S. Louie, A. Proko, A. Nazarian, and A. Nummenmaa, "Virtual human models for electromagnetic studies and their applications," *IEEE Reviews in Biomedical Engineering*, vol. 10, pp. 95–121, Dec. 2017.

[29] V. R. Nawati, B. K. Sujatha, and G. S. Karthikeya, "A compact dual-polarized probe-fed UWB antenna system for breast cancer detection applications," *Wireless Netw.*, vol. 30, pp. 3039–3050, 2024.

[30] S. Gabriel, R. W. Lau, and C. Gabriel, "The dielectric properties of biological tissues," *Phys. Med. Biol.*, vol. 41, pp. 2231–2293, 1996.

[31] M. Lazebnik, L. McCartney, D. Popovic, C. B. Watkins, M. J. Lindstrom, J. Harter, S. Sewall, A. Magliocco, J. H. Booske, M. Okoniewski, and S. C. Hagne, "A large-scale study of the ultrawide band microwave dielectric properties of normal breast tissue obtained from reduction surgeries," *Phys. Med. Biol.*, vol. 52, no. 10, pp. 2637–2656, 2007.

[32] M. Nameur, "Unilateral versus bilateral breast cancers, synchronous versus non-synchronous bilateral breast cancers: Results of a long survey (25 years) concerning 3632 patients," *Journal of Clinical Oncology*, vol. 22, pp. 729–729, 2004.

[33] J. Oh and B. Park, "Bilateral breast cancer," *Journal of Clinical Oncology*, vol. 25, pp. 17073–17073, June 2007.

[34] *Safety Levels with Respect to Human Exposure to Radiofrequency Electromagnetic Fields, 3 kHz to 300 GHz*, IEEE Standard C95.1, 1999.

[35] *Safety Levels with Respect to Human Exposure to Radiofrequency Electromagnetic Fields, 3 kHz to 300 GHz*, IEEE Standard C95.1, 2005.

Mohamed Behih was born in Bordj Bou Arreridj, Algeria, in 1981. He received the Engineer degree in electronic engineering and Magister degree in communication from Setif University, in 2004 and 2007, respectively, and the Ph.D. degree in communication engineering from the University of Batna 2, in 2024. Presently, he is a doctor at the Institute of Electronics and Telecommunications, University of Bordj Bou Arreridj. His fields of research include telecommunications systems and networks, biomedical engineering, interaction between electromagnetic wave and human body, and medical devices and antennas.

Christophe Dumond was born in Tulle, France, on 22 October 1966. He received the Ph.D. in Optic Communications and Microwaves from University of Limoges in 1994. His works concern the electromagnetic answer of wire structures to fast transient perturbations. In 2007, he joined the Institut Pluridisciplinaire de Recherche en Ingénierie des Systèmes Mécaniques et Energétique (PRISME) of University of Orléans. His fields of research include fractal antennas, high Tc superconducting microstrip patch, phased arrays and implantable antennas for biotelemetry. He is also a teacher and head of the electrical engineering department at the Institut Universitaire de Technologie (IUT) of Chartres.

Farid Bouttout received the B.Sc. and M.Sc. degrees in electronic engineering from the University of Constantine, Constantine, Algeria, in 1994 and 1997, respectively, and the Ph.D. degree in electronic engineering from the University of Setif in 2001. He was granted a three-year postdoc study on design of planar antennas for medical applications at the Commissariat à l'Energie Atomique (CEA) and at the University of Paris VI, France. He is currently a professor with the Institute of Electronics and Telecommunications, University of Bordj Bou Arreridj. His current research interests include planar and cylindrical microstrip antennas and transmission lines, computational electromagnetics, high performance computing, neural networks, and fuzzy logic.

Tarek Fortaki was born in Constantine, Algeria, in 1972. He received the State Engineer, M.Sc., and Ph.D. degrees in electronics and communications engineering from the University of Constantine, Constantine, Algeria, in 1995, 1999, and 2004, respectively. He joined the Department of Electronics at University of Batna in 2000; he was promoted to full professor in 2010. He has supervised 21 Ph.D. theses (including 19 defended). He has authored or co-authored more than 150 research publications in peer-reviewed journals and conference proceedings. He has served as a TPC/IPC member for different international conferences, alongside a reviewer for several prestigious scientific journals. He has been invited to deliver numerous keynote or plenary talks in international conferences. He is widely recognized for his contributions to the numerical modelling of patch antennas embedded in multilayered anisotropic media. His current research interests include microwave electronics, numerical and analytical techniques for electromagnetic modelling, antennas, HF propagation, complex media, artificial materials, computational intelligence, and intelligent design of microwave devices.

Absorbed Power in Human Head Skin Due to Near-Field Exposure up to 100 GHz

Fatih Kaburcuk[1] and Atef Z. Elsherbeni[2]

[1]Department of Electrical and Electronic Engineering
Sivas University of Science and Technology, Sivas 58000, Turkey
fkaburcuk@sivas.edu.tr

[2]Department of Electrical Engineering
Colorado School of Mines, Golden 80401, USA
aelsherb@mines.edu

Abstract – To prevent excessive skin temperature rise from overexposure due to near-field sources for frequencies from 6 to 300 GHz, international safety guidelines and standards for limiting exposure to electromagnetic (EM) waves introduce an incident power density (IPD) as an exposure reference limit and an absorbed power density (APD) as a basic restriction. At frequencies above 6 GHz, the penetration depth of EM waves in the human body model is particularly less, since EM wave penetration is more superficial in tissues. Therefore, the thickness of outermost tissues such as skin, which has different thicknesses in different realistic regions of a three-dimensional (3D) realistic human body, is a critical factor for the accuracy of EM dosimetry analysis. In this paper, the effect of skin thickness in a 3D planar head model on the spatially averaged APD over 1 cm^2 and 4 cm^2 areas due to near-field sources are investigated for the frequency range from 10 to 100 GHz. These investigations are performed using the finite-difference time-domain (FDTD) method considering different separation distances from the near-field source to the model of the skin surface. Numerical results show that skin thickness is the primary parameter in evaluating EM field exposure and the accuracy of EM dosimetry analysis.

Index Terms – Absorbed power density, electromagnetic dosimetry analysis, FDTD method, incident power density, millimeter wave exposure, planar head model.

I. INTRODUCTION

In electromagnetic (EM) dosimetry analysis, skin thickness of a human body directly affects how much EM power is absorbed by the tissues due to lower penetration depth of EM fields in tissues at frequencies above 6 GHz. Therefore, it is necessary to investigate the relationship between skin thickness and absorbed power by the skin tissue for the accuracy of the EM dosimetry analysis, especially for predicting potential thermal effects and evaluating EM safety standards in [1, 2]. These standards, called as IEEE International Committee on Electromagnetic Safety (ICES) [1] and the International Commission on Nonionizing Radiation Protection (ICNIRP) [2], provide basic restrictions such as specific absorption rate (SAR_{1g} and SAR_{10g}) averaged over 1g and 10g of tissues and absorbed power density (APD) for assessing human safety from EM radiation.

For frequencies below 6 GHz [3–10], EM waves penetrate deep into tissues, therefore, SAR_{1g} and SAR_{10g} have been used as basic restrictions to prevent excessive temperature rise on the surface and internal tissues due to different types of EM sources. However, the penetration of the EM waves and resulting temperature rise for frequencies above 6 GHz becomes more significant in superficial tissues [1, 2], especially within the skin tissue. Therefore, APD over 1 cm^2 and 4 cm^2 averaging areas on the skin surface determined in [1, 2] is a useful exposure metric to evaluate EM dosimetry instead of SAR_{1g} and SAR_{10g}. The APD limits recommended in [1, 2] are 20 W/m^2 over a 4 cm^2 surface area in the 6–300 GHz frequency range and 40 W/m^2 over a 1 cm^2 surface area in the 30–300 GHz frequency range. The spatially averaged incident power densities (IPD) over 1 cm^2 and 4 cm^2 areas, calculated in the free space without the presence of the human body model, is defined as an exposure reference level (ERL) [1] or reference level (RL) [2].

Assessment of EM dosimetry analysis due to antenna sources above 6 GHz has been extensively studied in [11–25]. However, the relationship between the spatially averaged IPD/APD and resulting temperature rise due to different exposure types has been studied by only a few research groups in [14, 15] and [22]. The correlation between the spatially averaged IPD and resulting temperature rise in a homogeneous planar skin

Submitted On: June 05, 2025
Accepted On: February 01, 2026

https://doi.org/10.13052/2026.ACES.J.410107

model [11–19] due to EM exposure from the antennas. Furthermore, the APD, which correlates well with the superficial temperature rise in the tissues compared to IPD, due to different antenna types has been calculated in [18–25] for the frequencies above 6 GHz. An intercomparison study reported in [14] investigated the effect of the incident angle on the IPD and resulting temperature rise due to different types of array antennas with different body separation distances. In [15], another intercomparison study has been performed by six different research groups using the finite-difference time-domain (FDTD) method, Galerkin-Bubnov indirect boundary element method (GB-IBEM), and finite integration technique (FIT) to calculate the IPD and resulting temperature rise in a human body model due to different antenna sources operating at the frequencies from 10 to 90 GHz. Furthermore, the spatially averaged APD in planar human body models with a single skin tissue and three different tissues (skin, fat, and muscle) has been calculated due to a single dipole and array dipole antennas operating at frequencies from 10 to 90 GHz in [22]. The intercomparison study in [22] has been performed by 11 different research groups using the different numerical methods (i.e. FDTD method, finite element method (FEM), FIT, transmission line method (TLM), and GB-IBEM).

EM dosimetry evaluation of a three-dimensional (3D) realistic human body model at frequencies above 6 GHz requires huge computational time and large computer resources due to cell size restriction in FDTD method. Therefore, a 3D multi-layered planar human model, instead of the 3D realistic human model, has been analyzed [11–25] above 6 GHz. In most studies, the human body model was considered to have a skin tissue of 1.5 or 2 mm thick. However, thickness of skin tissue in different regions of a realistic human body is not the same [25–29] and is known to vary between roughly 0.5 mm and 2 mm, especially on different regions of the human head as seen in Table 1. The realistic skin thickness values [28, 29] on the different anatomical regions (forehead, eyelid, cheek, chin, neck) of the realistic human head are tabulated for male and female in Table 1. They can also vary significantly across age groups, races, and genders. Since, it is a well-known fact that most of the EM fields emitted by far-field and near-field sources are absorbed by the outer tissues in the human body, especially by skin tissue. Therefore, some studies in [25–27] showed that accuracy of EM dosimetry at frequencies up to 100 GHz has been significantly affected by the skin thickness in the human body model. In [25], the effect of the skin thickness of a head model on APD above 6 GHz was investigated when the dipole antenna was placed at 15- and 45-mm distance from the model. In [26, 27], EM dosimetry analysis of one-dimensional human body models with different skin thicknesses have been investigated up to 100 GHz. However, the effect of skin thickness of the 3D human body model on EM dosimetry analysis has not been investigated sufficiently up to 100 GHz when the antenna is placed very close to the head model.

Table 1: Skin thickness in different regions of the realistic human head [28, 29]

Regions	Male (mm)	Female (mm)
Forehead	0.900	0.835
Eyelid	0.569	0.473
Cheek	1.237	1.044
Chin	0.891	0.746
Neck	1.561	1.255
Postauricular	0.766	0.657
Temple	1.795	–
Nasal Dorsum	2.016	–
Malar	1.086	–
Scalp	1.383	–
Vertex	0.957	–

In this paper, the effect of skin thickness in a 3D planar head model on the spatially averaged APD and IPD have been analyzed using a dispersive formulation of the FDTD method for the frequency range from 10 to 100 GHz. The electrical parameters of each tissue are accurately represented by a three-term Debye model to accurately access the tissues dispersiveness properties on the numerically obtained results. To verify the accuracy of our FDTD codes [30] for EM dosimetry analysis, the spatially averaged IPD and APD values obtained in this study are compared to the mean values of them obtained by different research groups using different numerical methods in the intercomparison studies [15, 22]. Finally, the effects of separation distances between the antenna and the planar head model on the spatially averaged APD over the skin surface of the model are investigated for each frequency of interest.

II. MODEL, METHOD, AND EXPOSURE METRICS

A. Multilayered planar head model

A 3D planar multi-layered head model shown in Fig. 1 is used for the EM dosimetry analysis in this study. This model contains nine different head tissues (skin, fat, muscle, bone cortical, bone marrow, dura, CSF, gray and white matter). The arrangement of these tissues in the planar head model is shown in Fig. 1, and their corresponding thickness values (Th) are provided in Table 2. The side length (L) and thickness (T) of the multi-layered planar head model are provided in Table 3 for each frequency of interest from 10 to 100 GHz.

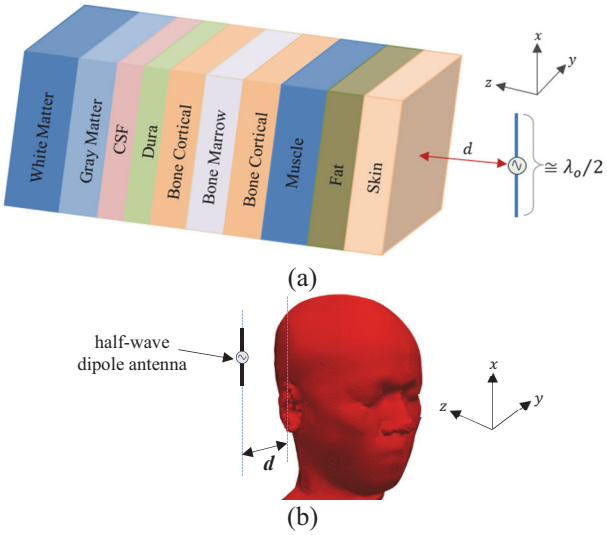

Fig. 1. (a) a 3D planar head model and (b) a 3D realistic head model with a half-wave dipole antenna at the separation distance of d.

Table 2: Thickness (Th) and three-term Debye coefficients of head tissues

Tissues	Th (mm)	ε_∞	ε_{s1}	ε_{s2}	ε_{s3}	τ_1 (ps)	τ_2 (ps)	τ_3 (ps)
Skin	1.5	4.03	0.12	32.41	22.83	1.44	7.23	160.7
Fat	1.5	2.56	0.33	1.18	1.42	1.32	4.98	16.94
Muscle	2.5	4.48	3.79	29.74	19.35	1.60	5.79	17.36
Bone Cortical	1.5	2.64	0.69	2.68	6.16	1.35	5.56	19.22
Bone Marrow	1.5	2.56	0.33	1.15	1.40	1.30	4.91	16.16
Dura	1	4.60	3.75	19.03	19.51	1.47	5.55	18.60
CSF	1	4.61	4.71	39.89	31.69	1.71	6.386	24.34
Gray Matter	3	4.42	3.12	2.58	2.03	1.62	6.12	18.66
White Matter	10	4.31	2.21	18.09	14.50	1.59	6.05	17.76

Table 3: Size and resolution of the planar head model and length of antennas operated between 10 and 100 GHz

Frequency (GHz)	Resolution (mm)	T (mm)	L (mm)	Antenna Length (mm)
10	0.25	25	100	13
20		25	100	9
30		25	100	6
40	0.125	25	50	4
50		25	50	3
60		25	50	2.3
70		25	50	15
80	0.0625	25	25	1.2
90		25	25	1
100		25	25	0.8

The 3D planar multilayer head model in Fig. 1 (a) provides ease of computation and enables efficient EM dosimetry analysis. Furthermore, this planar model was chosen to ensure its applicability in FDTD analyses up to 100 GHz, where the required spatial cell size (<0.1 mm) and time step constraints exist. The planar model can accurately represent EM field distributions and exposures across layered tissues; however, it cannot represent the detailed curvature and heterogeneous structure of a 3D realistic head model in Fig. 1 (b), which requires a very large computational domain and a very long computational time for EM dosimetry analysis at frequencies up to 100 GHz. Therefore, although the planar model is suitable for preliminary or comparative evaluations as in [15] and [22], anatomically detailed and realistic 3D head models could be used in future studies to provide higher spatial accuracy and better representation of realistic conditions.

B. Electrical properties of tissues

The electrical parameters (relative permittivity-ε_r and conductivity-σ) of the head tissues in Fig. 1 are frequency dependent. They can be obtained in (1) by using the three-term Debye coefficients of these tissues (ε_∞ relative permittivity at infinite frequency, ε_{sk} static relative permittivity, τ_k relaxation time at k^{th} term). These three-term Debye coefficients, which are available for the frequency range between 20 and 100 GHz, are provided in [31] and given in Table 2.

$$\varepsilon_r^*(\omega) = \varepsilon_r'(\omega) + j\varepsilon_r''(\omega) = \varepsilon_\infty + \sum_{k=1}^{3} \frac{\varepsilon_{sk} - \varepsilon_\infty}{1 + j\omega\tau_k}, \tag{1a}$$

$$\sigma(\omega) = -\varepsilon_r''(\omega) * \omega * \varepsilon_o. \tag{1b}$$

C. Electromagnetic dosimetry analysis

EM dosimetry analysis of the human model exposed to a near-field source was performed using the dispersive formulation of the FDTD method in [9, 10] which is suitable for the EM analysis of inhomogeneous and complex structures such as the human body models. The FDTD problem domain, which includes the 3D planar head model, a near-field source, and 15-cell air layer, is truncated by a 10-cell convolution perfectly matched layer (CPML) [32]. The spatial resolution of the FDTD problem domain with the head model must be at least one-tenth of the minimum wavelength (λ_{min}) in the tissues to satisfy the Courant-Friedrichs-Lewy (CFL) stability condition [30]. Therefore, the spatial resolutions different for all frequencies of interest between 10 and 100 GHz are given in Table 3.

D. Near field exposure

A single half-wave dipole used as a near-field source in the EM dosimetry analysis was designed at all frequencies of interest from 10 to 100 GHz. The lengths of the dipole antennas, which are half of the free-space wavelength (λ_o) at the desired frequencies, were given in Table 3 and adjusted to have maximum radiation power emitted from the dipole antenna. The half-wave dipole antenna was placed at a separation distance of d from the skin surface of the head model as shown in Fig. 1. It would have been optimal to use a source antenna that covers the entire frequency band from 10 GHz to 100 GHz, then the FDTD simulation would have run only once. However, the design of such antenna is outside the scope of this paper. The use of the dispersive type FDTD formulation [9, 10] yields more accurate results even if one uses different dipole antenna centered at a specific frequency as the dipole antenna radiates at other frequencies but without the same strength, thus a dispersive type of analysis is warranted.

The total input power radiated by a single half-wave dipole antenna is set to 10 mW, which represents the typical input power of antennas used in common wireless consumer devices [33]. For example, smartphones and wearable electronic devices typically radiate between 5 and 20 mW during active transmission (Wi-Fi or Bluetooth modes). Therefore, the modeled level of 10 mW approximates an average realistic usage scenario, consistent with previous studies [15, 22, 34].

E. Exposure metrics for evaluation

The spatially averaged normal IPD (IPD_n) and total IPD (IPD_t) of the time-averaged power density on the evaluation plane at various distances from the antennas has been calculated in the absence of the head model using the complex electric (E) and magnetic (H) fields in equation (2).

$$IPD_n = \frac{1}{2A}\iint_A Real\{E \times H^*\} \cdot \hat{n} dA, \tag{2a}$$

$$IPD_t = \frac{1}{2A}\iint_A \|Real\{E \times H^*\}\| dA, \tag{2b}$$

where * shows the complex conjugate, A refers to the averaging areas over 1 cm^2 and 4 cm^2, $\hat{n}$ shows the unit vector normal to the evaluation plane, $\|\cdot\|$ denotes the norm symbol, and dA is the variable of integration. The spatially averaged APD on the skin surface of the head model placed at different separation distance of d from the antenna has been calculated in equation (3) which is recommended by ICNIRP guidelines [1] and written in the following form:

$$APD = \frac{1}{2A}\iint_A Real\{E \times H^*\} \cdot \hat{n} dA, \tag{3}$$

where $\hat{n}dA$ shows the unit vector normal to the integral area of A on the skin surface of the planar head model.

III. NUMERICAL EVALUATION

In this study, assuming that the skin thickness in different regions of the head model given in Table 1 varies between 0.5 mm and 1.5 mm, peak spatially averaged APD values were calculated depending on the skin thickness of 0.5, 1, and 1.5 mm, the frequency of 10–100 GHz and the separation distance of 2.5–15 mm. Additionally, the peak spatially averaged IPD_n and IPD_t over averaged areas of 1 cm^2 and 4 cm^2 due to a half-wave dipole antenna are calculated as a function of frequency up to 100 GHz and separation distance, and compared with the results in [22].

A. Performance of the antenna with and without a planar head model

The input reflection coefficients (S_{11}) of the half-wave dipole antennas operated at 20 and 60 GHz frequencies with and without a 3D planar head model are shown in Fig. 2. In the simulation with the planar head model, the separation distance of d between the antenna and the skin surface was assumed to be 5 mm, and the skin thickness (t_{skin}) was assumed to be 0.5, 1, and 1.5 mm. As can be seen from Fig. 2, the S_{11} values are really affected by the presence of the planar head model and the change in its skin thickness, especially at the frequency of 20 GHz.

B. Comparison of the results obtained with existing studies

In order to satisfy the accuracy of our FDTD code, the values of peak spatially averaged IPD_n, IPD_t, and APD over 1 cm^2 and 4 cm^2 areas obtained in the intercomparison study [22] due to a half-wave dipole antenna are compared to the results obtained in this study. In [22], the mean values of peak spatial averaged IPD_n, IPD_t, and APD over areas of 1 cm^2 and 4 cm^2 obtained by 11 different research groups have been calculated for the frequencies of 10, 30, and 90 GHz. These research groups used different numerical methods for the EM dosimetry analysis of the planar single and three-layered models. In Table 4, the mean values of peak spatial averaged IPD_n, IPD_t, and APD calculated in [22] for the three-layered model with the skin thickness of 1.5 mm are compared to the results obtained in this study. The results in Table 4 show good agreement.

C. IPD as a function of frequency

The peak values of spatially averaged IPD (IPD_n and IPD_t) over 1 cm^2 and 4 cm^2 areas due to a half-wave dipole antenna are calculated on an evaluation plane and

they are shown in Fig. 3 as a function of frequencies from 10 to 100 GHz when the separation distance of d is 2, 5, and 10 mm. As can be seen from Fig. 3, IPD_n and IPD_t over 1 cm^2 and 4 cm^2 areas gradually increase up to 30 GHz, then their increase slows down and reaches steady-state values. As expected, the peak values of IPD_t are higher than those of IPD_n for both each frequency of interest and each separation distance, and these values also decrease as the separation distance of d increases.

D. IPD as a function of separation distance

The peak values of spatially averaged IPD_n and IPD_t over areas of 1 cm^2 and 4 cm^2 shown in Fig. 4 are calculated as a function of separation distance from 1 to 20 mm for the frequencies of 10, 30, 60, and 100 GHz. As seen in Fig. 4, since EM radiation decreases with distance from the source, the IPD_n and IPD_t values decrease exponentially as the separation distance increases.

E. APD as a function of frequency and skin thickness

To show the effect of skin thickness on the spatially averaged APD values over 1 cm^2 and 4 cm^2 areas, the planar head model with the adjacent half-wave dipole antenna operated at frequencies from 10 to 100 GHz is analyzed using the FDTD method. Figure 5 shows the APD values as a function of frequency from 10 GHz to 100 GHz when the skin thickness is 1.5, 1, and 0.5 mm and the separation distance is 5 and 10 mm. The compared results show that APD values are affected by the changes in skin thickness of the human head, operating frequency of the antenna, and the separation distance between the human body and antenna. As expected, APD values decrease as the separation distance from the antenna increases. There is a relationship between APD values and operating frequency, but it would be difficult

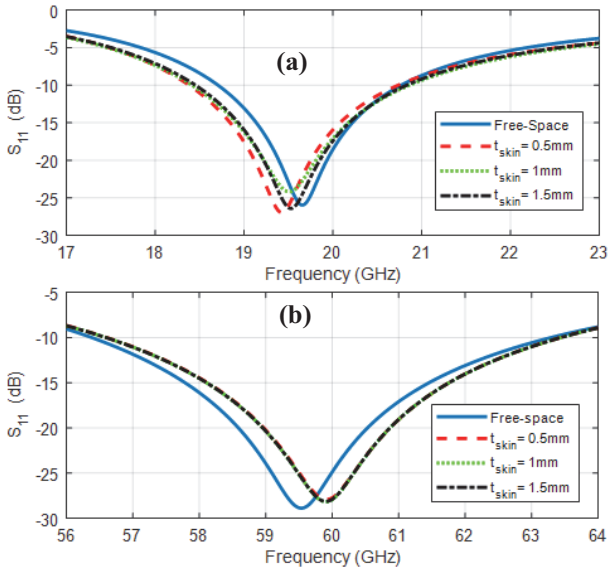

Fig. 2. S_{11} of the antenna operated at (a) 20 and (b) 60 GHz with and without the 3D planar head model.

Table 4: Comparison of peak spatially averaged IPD_n, IPD_t, and APD over 1 cm^2 and 4 cm^2 areas with separation distances of 2, 5, 10, and 15 mm at frequency of 10, 30, and 90 GHz

Dist. (mm)	Freq. (GHz)	Ref.	IPD_n (W/m^2)		IPD_t (W/m^2)		APD (W/m^2)	
			1 cm^2	4 cm^2	1 cm^2	4 cm^2	1 cm^2	4 cm^2
2	90	[22]	36.99	10.83	56.53	20.38	24.76	6.71
		This Work	36.86	10.82	56.48	20.42	24.96	6.68
5	10	[22]	18.04	8.23	20.62	11.28	9.62	3.85
		This Work	18.01	8.23	20.61	11.29	10.02	3.98
	30	[22]	21.31	8.46	25.34	12.09	11.93	4.38
		This Work	21.05	8.42	25.02	12.04	11.46	4.23
	90	[22]	21.92	8.55	26.30	12.31	14.29	5.24
		This Work	21.83	8.51	26.22	12.27	13.96	5.08
10	10	[22]	8.26	5.19	8.72	6.09	2.34	1.40
		This Work	8.27	5.19	8.73	6.10	2.38	1.36
	30	[22]	9.36	5.43	9.99	6.51	4.91	2.79
		This Work	9.23	5.39	9.85	6.46	4.78	2.68
	90	[22]	9.55	5.49	10.23	6.62	6.25	3.54
		This Work	9.49	5.46	10.14	6.56	6.28	3.49
15	10	[22]	4.53	3.37	4.66	3.70	1.57	1.16
		This Work	4.52	3.36	4.65	3.70	1.65	1.18
	30	[22]	4.91	3.52	5.08	3.91	2.53	1.81
		This Work	4.84	3.49	5.00	3.87	2.38	1.72

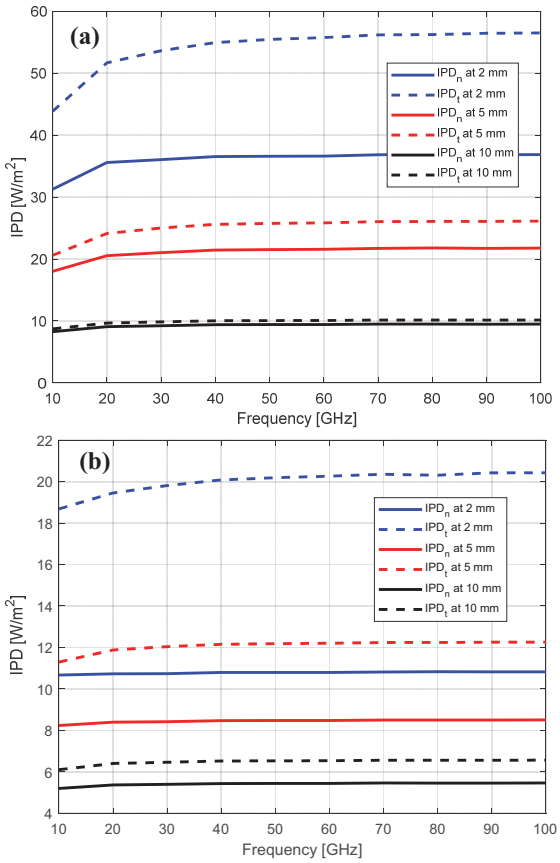

Fig. 3. IPD_n and IPD_t values [W/m^2] over (a) 1 cm^2 and (b) 4 cm^2 averaged areas as a function of frequency with the separation distance of 2, 5, and 10 mm.

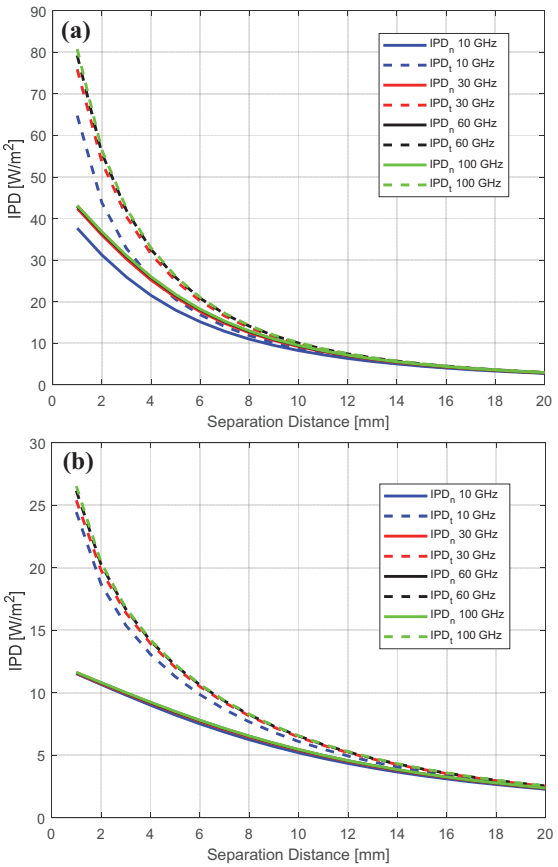

Fig. 4. IPD_n and IPD_t values [W/m^2] over (a) 1 cm^2 and (b) 4 cm^2 averaged areas as a function of separation distance at 10, 30, 60, and 100 GHz.

to make an inference between the operating frequency of the antenna in the 20–100 GHz range and the APD values. However, it can be observed that APD tends to increase as frequency increases, especially from 20 GHz to 90 GHz. This is expected because the energy of the EM wave increases with frequency. The APD values over 1 cm^2 averaging area generally shows higher than those over 4 cm^2 averaging area, especially at higher frequencies, because smaller averaging areas lead to local hotspots or more localized absorption.

As can be seen from Fig. 5, thinner skin leads to higher APD values, especially at 10 GHz, because it allows more EM waves to penetrate deeper tissues and causes higher energy absorption in superficial tissues. However, thicker skin resulting in lower APD allows EM waves to penetrate less deeply into tissues because the energy is attenuated more when reaching deeper tissues. Furthermore, the penetration depth at frequencies of 30 and 60 GHz is less than 1 mm and 0.5 mm [1], respectively. Therefore, APD values are more affected by skin thickness changes from 1.5 mm to 1 mm at 30 GHz and from 1.5 mm to 0.5 mm at 60 GHz. As the separation distance between the antenna and the skin surface increases from 5 mm to 10 mm, the APD values decrease because the power density of the antenna decreases as the separation distance increases due to the inverse square law of EM radiation.

Figure 6 shows the relative percentage change rate (RPCR) in APD values as a function of frequency for skin thickness of 1.5 mm and 0.5 mm at the separation distance of 5 mm. In RPCR calculation, the APD values of 1.5 mm and 0.5 mm skin thickness are compared with the APD values of 1 mm skin thickness when d is 5 mm. As seen in Fig. 5, changes in skin thickness can cause significant changes in APD values in the frequency range of 10–100 GHz, especially at frequencies up to 30 GHz for 1.5 mm skin thickness and up to 60 GHz for 0.5 mm skin thickness. Furthermore, it can be realized that APD is more sensitive to frequency changes for 1.5 mm skin thickness at frequency below 30 GHz and for 0.5 mm skin thickness at frequency below 60 GHz.

$$\text{RPCR} = \left| \frac{APD_{1\text{mm}} - APD_{0.5 \text{ or } 1.5 \text{ mm}}}{APD_{1\text{mm}}} \right| \times 100\%. \quad (4)$$

F. APD as a function of separation distance and skin thickness

In Fig. 7, the peak spatially averaged APD values at 20 and 60 GHz are shown as a function of the separation distance from 2.5 mm to 20 mm. The APD values decrease as the separation distance increases from 2.5 mm to 20 mm. This follows the inverse square law of EM radiation. As seen in Fig. 7, APD values decrease sharply, especially at short distances between 2.5–5 mm, and gradually decrease at long distances between 10–20 mm. As expected, the APD averaged over 1 cm^2 is significantly higher than that averaged over 4 cm^2 at short separation distances. Moreover, as the separation distance increases, the influence of skin thickness on the APD values becomes negligible.

G. APD normalized by skin thickness

APD values normalized to skin thickness in equation (5) allow comparison of how absorbed power scales per unit skin thickness. This is useful for comparing absorption behavior over 1 cm^2 and 4 cm^2 areas with different skin thicknesses. Figure 8 shows the absorbed power density (NAPD) normalized to skin thickness (0.5 mm, 1 mm, and 1.5 mm) over 1 cm^2 and 4 cm^2 averaged areas at four operating frequencies (10, 30, 60, and 90 GHz). At both averaging areas, the NAPD decreases with increasing skin thickness and frequency, indicating stronger EM wave attenuation and reduced penetration depth at higher frequencies.

$$NAPD = \frac{APD\ (W/m^2)}{t_{skin}(mm)}. \tag{5}$$

Although this study focuses on EM analysis of the planar head model due to the dipole antenna to show the effect of skin thickness on APD values, it is crucial to recognize its potential biological implications such as local tissue heating and thermal effect on tissues not investigated in this work. It is well known from [1, 2] that APD values correlate well with surface temperature rise and are an indicator of maximum skin temperature rise at frequencies above 10 GHz. Therefore, it can be concluded that skin thickness has a significant impact on APD values and may also have an impact on the temperature increase resulting from APD values.

The results obtained from this study can help understand the effect of skin thickness on APD levels due to wearable devices such as smartwatches, headsets, or smart glasses. For wearable devices, understanding the skin thickness effect on APD distributions helps assess the thermal safety of the device, ensuring that users are not exposed to harmful levels of EM radiation. Various factors such as bone structure, vascularity, hair and ambient temperature can change the electrical

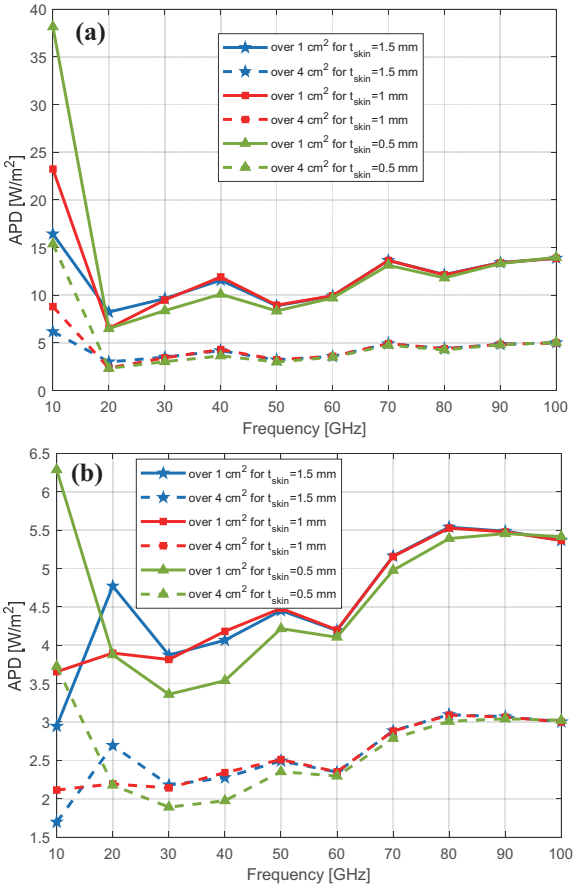

Fig. 5. APD over 1 cm^2 and 4 cm^2 averaged areas as a function of frequency with the skin thickness of 0.5, 1, 1.5 mm for (a) $d = 5$ mm and (b) $d = 10$ mm.

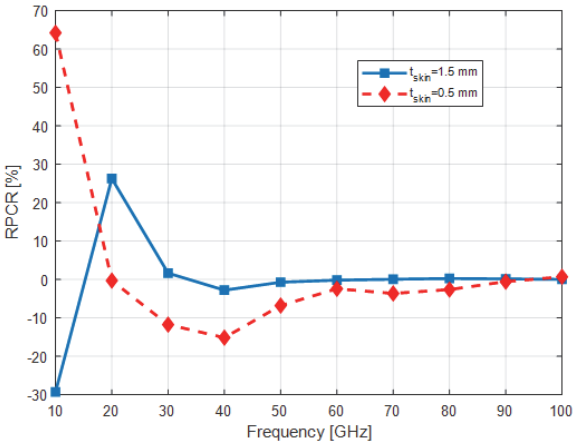

Fig. 6. RPCR values based on the APD results for a skin thickness of 1 mm.

parameters of tissues and these changes can affect the EM dosimetry analysis of the human body, however the effect of these factors was not considered in this study. It can be realized from the numerical results that the APD

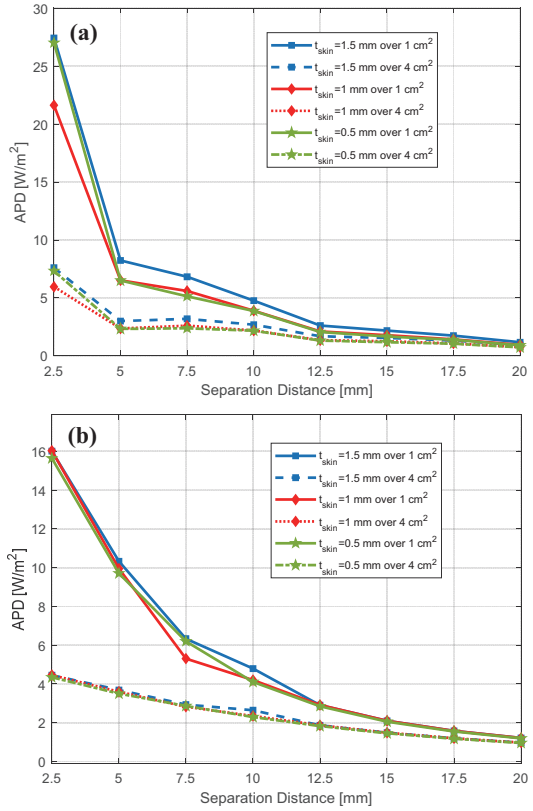

Fig. 7. APD over 1 cm^2 and 4 cm^2 averaged areas at frequencies of (a) 20 and (b) 60 GHz as a function of the separation distance for 0.5, 1, and 1.5 mm skin thickness.

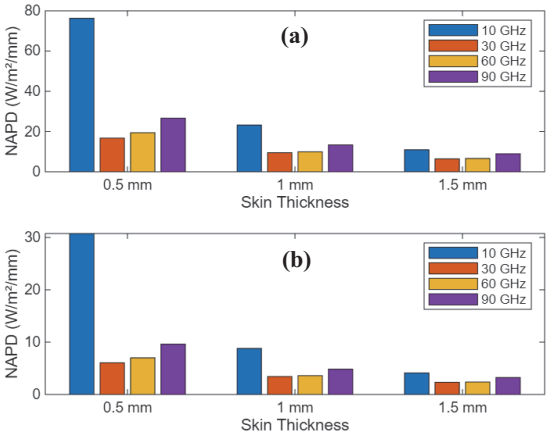

Fig. 8. NAPD as a function of skin thickness (0.5 mm, 1.0 mm, and 1.5 mm) at four frequencies (10, 30, 60, and 90 GHz) over averaging areas of (a) 1 cm^2 and (b) 4 cm^2.

values over 1 cm^2 and 4 cm^2 averaged areas for skin thickness between 0.5 mm and 1.5 mm obtained from this study are lower than the safety limits recommended by [1, 2] for assessing the significance for public health and regulatory compliance.

IV. CONCLUSION

In this paper, the effects of skin thickness in the planar head model on the spatially averaged APD values over 1 cm^2 and 4 cm^2 areas have been investigated using the FDTD method due to a half-wave dipole antenna at operating frequencies from 10 to 100 GHz. It has been realized from the numerical results in this study that the APD values over areas of 1 cm^2 and 4 cm^2 are not only affected by the changes in skin thickness on the 3D human head, but also by changing the operation frequency of the antennas and the separation distance between the antenna and the human body model. As skin thickness decreases from 1.5 to 0.5 mm in the human head, APD values increase significantly at 10 GHz and then decrease at frequencies above 10 GHz. Consequently, since the skin is the most exposed organ to EM waves, skin thickness becomes the primary parameter affecting EM power absorption. Therefore, accurate skin thickness modeling is crucial for EM dosimetry evaluation. In addition, spatially averaged IPD values calculated on the evaluation plane placed at a certain distance from the antenna have been investigated at all frequencies of interest. This work clarifies EM safety limitation assessments by presenting a comprehensive parametric study investigating the dependence of APD values on skin thickness, frequency up to 100 GHz, and distance from the antenna to the skin surface. Future studies could investigate EM dosimetry analysis of a realistic 3D head model, rather than a 3D planar head model, to better model anatomical complexity and validate results. Additionally, the effects of skin thickness on APD, resulting temperature increase, and other exposure metrics due to different EM exposure scenarios from 5G/6G technologies up to 100 GHz can be investigated.

REFERENCES

[1] *Safety Levels with Respect to Human Exposure to Electric, Magnetic and Electromagnetic Fields, 0 Hz to 300 GHz*, IEEE Standard C95.1, 2019.

[2] International Commission on Non-Ionizing Radiation Protection, "Guidelines for limiting exposure to electromagnetic fields (100 kHz to 300 GHz)," *Health Phys.*, vol. 118, no. 5, pp. 483–524, May 2020.

[3] J. Wang and O. Fujiwara, "FDTD computation of temperature rise in the human head for portable telephones," *IEEE Trans. Microwave Theory Tech.*, vol. 47, pp. 1528–1534, Aug. 1999.

[4] P. Bernardi, M. Cavagnaro, S. Pisa, and E. Piuzzi, "Specific absorption rate and temperature increases in the head of a cellular-phone user," *IEEE Trans. Microwave Theory Tech.*, vol. 48, no. 7, pp. 1118–1126, July 2000.

[5] A. Hirata, S. Matsuyama, and T. Shiozawa, "Temperature rise in the human eye exposed to

EM waves in the frequency range 0.6–6 GHz," *IEEE Trans. Electromag. Compat.*, vol. 42, no. 4, pp. 386–393, Nov. 2000.

[6] A. Hirata, M. Morita, and T. Shiozawa, "Temperature increase in the human head due to a dipole antenna at microwave frequencies," *IEEE Trans. Electromag. Compat.*, vol. 45, no. 1, pp. 109–116, Feb. 2003.

[7] A. Hirata and O. Fujiwara, "The correlation between mass averaged SAR and temperature elevation in the human head model exposed to RF near-fields from 1 to 6 GHz," *Phys. Med. Biol.*, vol. 54, no. 23, pp. 7227–7238, Dec. 2009.

[8] A. Hirata, I. Laakso, T. Oizumi, R. Hanatani, K. H. Chan, and J. Wiart, "The relationship between specific absorption rate and temperature elevation in anatomically based human body models for plane wave exposure from 30 MHz to 6 GHz," *Phys. Med. Biol.*, vol. 58, no. 4, pp. 903–921, 2013.

[9] F. Kaburcuk and A. Z. Elsherbeni, "Temperature rise and SAR distribution at wide range of frequencies in a human head due to an antenna radiation," *Applied Computational Electromagnetics Society (ACES) Journal*, vol. 33, no. 4, pp. 367–372, Apr. 2018.

[10] F. Kaburcuk and A. Z. Elsherbeni, "Efficient computation of SAR and temperature rise distributions in a human head at wide range of frequencies due to 5G RF field exposure," *Applied Computational Electromagnetics Society (ACES) Journal*, vol. 33, no. 11, pp. 1236–1242, Nov. 2018.

[11] Y. Hashimoto, A. Hirata, R. Morimoto, S. Aonuma, I. Laakso, K. Jokela, and K. R. Foster, "On the averaging area for incident power density for human exposure limits at frequencies over 6 GHz," *Phys. Med. Biol.*, vol. 62, no. 8, pp. 3124–3138, Apr. 2017.

[12] D. Funahashi, T. Ito, A. Hirata, T. Iyama, and T. Onishi, "Averaging area of incident power density for human exposure from patch antenna arrays," *IEICE Trans. Electron.*, vol. E101.C, no. 8, pp. 644–646, Aug. 2018.

[13] T. Nakae, D. Funahashi, J. Higashiyama, T. Onishi, and A. Hirata, "Skin temperature elevation for incident power densities from dipole arrays at 28 GHz," *IEEE Access*, vol. 8, pp. 26863–26871, 2020.

[14] Y. Diao, K. Li, K. Sasaki, S. Kodera, I. Laakso, W. E. Hajj, and A. Hirata, "Effect of incidence angle on the spatial-average of incident power density definition to correlate skin temperature rise for millimeter wave exposures," *IEEE Trans. Electromagn. Compat.*, vol. 63, no. 5, pp. 1709–1716, Oct. 2021.

[15] K. Li, Y. Diao, K. Sasaki, A. Prokop, D. Poljak, V. Doric, J. Xi, S. Kodera, A. Hirata, and W. E. Hajj, "Intercomparison of calculated incident power density and temperature rise for exposure from different antennas at 10–90 GHz," *IEEE Access*, vol. 9, pp. 151654–151666, 2021.

[16] A. L. Kapetanoviæ and D. Poljak, "Assessment of incident power density on spherical head model up to 100 GHz," *IEEE Trans. Electromagn. Compat.*, vol. 64, no. 5, pp. 1296–1303, Oct. 2022.

[17] R. Morimoto and A. Hirata, "Assessment of incident power density in different shapes of averaging area for radio-frequency exposure above 6 GHz," *Phys. Med. Biol.*, vol. 67, no. 21, Oct. 2022, Art. no. 215014.

[18] D. Funahashi, A. Hirata, S. Kodera, and K. R. Foster, "Area-averaged transmitted power density at skin surface as metric to estimate surface temperature elevation," *IEEE Access*, vol. 6, pp. 77665–77674, 2018.

[19] Y. Diao and A. Hirata, "Exposure assessment of array antennas at 28 GHz using hybrid spherical near-field transformation and FDTD method," *IEEE Trans. Electromagn. Compat.*, vol. 63, no. 5, pp. 1690–1698, Oct. 2021.

[20] D. Funahashi, A. Hirata, S. Kodera, and K. R. Foster, "Area-averaged transmitted power density at skin surface as metric to estimate surface temperature elevation," *IEEE Access*, vol. 6, pp. 77665–77674, 2018.

[21] K. Li, K. Sasaki, K. Wake, T. Onishi, and S. Watanabe, "Quantitative comparison of power densities related to electromagnetic near-field exposures with safety guidelines from 6 to 100 GHz," *IEEE Access*, vol. 9, pp. 115801–115812, 2021.

[22] K. Li, S. Kodera, D. Poljak, Y. Diao, K. Sasaki, A. Susnjara, A. Prokop, K. Taguchi, J. Xi, S. Zhang, M. Yao, G. Sacco, M. Zhadobov, W. E. Hajj, and A. Hirata, "Calculated epithelial/absorbed power density for exposure from antennas at 10–90 GHz: Intercomparison study using a planar skin model," *IEEE Access*, vol. 11, pp. 7420–7435, 2023.

[23] N. Miura, S. Kodera, Y. Diao, J. Higashiyama, Y. Suzuki, and A. Hirata, "Power absorption and skin temperature rise from simultaneous near-field exposure at 2 and 28 GHz," *IEEE Access*, vol. 9, pp. 152140–152149, 2021.

[24] Y. Diao, E. A. Rashed, and A. Hirata, "Assessment of absorbed power density and temperature rise for nonplanar body model under electromagnetic exposure above 6 GHz," *Phys. Med. Biol.*, vol. 65, no. 22, Art. no. 224001, 2020.

[25] K. Taguchi, S. Kodera, A. Hirata, and T. Kashiwa, "Computation of absorbed power densities in high-resolution head models by considering skin thickness in quasi-millimeter and millimeter wave bands," *IEEE J. Electromagn. RF Microw. Med. Biol.*, vol. 6, no. 4, pp. 516–523, Dec. 2022.

[26] S. Kodera, K. Taguchi, Y. Diao, T. Kashiwa, and A. Hirata, "Computation of whole-body average SAR in realistic human models from 1 to

100 GHz," *IEEE Trans. Microwave Theory Tech.*, vol. 72, no. 1, pp. 91–100, Jan. 2024.

[27] F. Kaburcuk, "Effect of skin thickness on electromagnetic dosimetry analysis of a human body model up to 100 GHz," *International Journal of Microwave and Wireless Technologies*, vol. 18, no. 8, pp. 1373–1380, 2024.

[28] E. A. Rashed, J. Gomez-Tames, and A. Hirata, "Human head skin thickness modeling for electromagnetic dosimetry," *IEEE Access*, vol. 7, pp. 46176–46186, 2019.

[29] Y. Lee and K. Hwang, "Skin thickness of Korean adults," *Surg. Radiol. Anat.*, vol. 24, pp. 183–189, 2002.

[30] A. Z. Elsherbeni and V. Demir, *The Finite-Difference Time-Domain Method for Electromagnetics with MATLAB Simulations*, 2nd ed. Edison, NJ: SciTech Publishing, an Imprint of IET, 2016.

[31] R. Lumnitzer, A. Tanner, and A. Z. Elsherbeni, "Debye coefficients for biological tissues from 100 MHz to 100 GHz," in *2020 International Applied Computational Electromagnetics Society Symposium (ACES)*, pp. 1–2, 2020.

[32] J. Roden and S. Gedney, "Convolution PML (CPML): An efficient FDTD implementation of the CFS-PML for arbitrary media," *Microwave and Optical Technology Letters*, vol. 27, no. 5, pp. 334–339, 2000.

[33] *IEEE Guide for the Definition of Incident Power Density to Correlate Surface Temperature Elevation*, IEEE Std 2889TM, Dec. 2021.

[34] *IEEE Guide for the Definition of Incident Power Density to Correlate Surface Temperature Elevation*, IEEE Std 2889-2021.

Fatih Kaburcuk received the M.Sc. and Ph.D. degrees in electrical engineering from Syracuse University, Syracuse, NY, USA, in 2011 and 2014, respectively. In 2014, he was a Visiting Research Scholar with the Department of Electrical Engineering at Colorado School of Mines, Golden, CO, USA. He joined Erzurum Technical University in 2015 and Sivas Cumhuriyet University in 2019. In August 2024, he joined the Department of Electrical and Electronics Engineering at Sivas University of Science and Technology, Sivas, Turkiye, where he is currently serving as a Full Professor. Dr. Kaburcuk is an Associate Editor of the *Applied Computational Electromagnetics Society (ACES) Journal*. His research interests include numerical methods in electromagnetics, biological effects of electromagnetic radiation, and finite-difference time-domain analysis of antennas and RF devices.

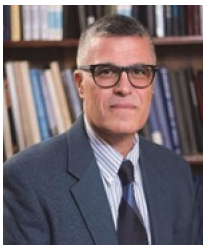

Atef Z. Elsherbeni received his Ph.D. degree in Electrical Engineering from Manitoba University, Winnipeg, Manitoba, Canada, in 1987. He started his engineering career as a part time Software and System Design Engineer from March 1980 to December 1982 at the Automated Data System Center, Cairo, Egypt. From January to August 1987, he was a Post-Doctoral Fellow at Manitoba University. Elsherbeni joined the faculty at the University of Mississippi in August 1987 as an Assistant Professor of Electrical Engineering and progressed to the full professor and the Associate Dean of the College of Engineering for Research and Graduate Programs. He then joined the Electrical Engineering and Computer Science (EECS) Department at Colorado School of Mines in August 2013. Elsherbeni is an IEEE Life Fellow and ACES Fellow. He is the Editor-in-Chief for *Applied Computational Electromagnetics Society (ACES) Journal*, and a past Associate Editor to the *Radio Science Journal*. He was the Chair of the Engineering and Physics Division of the Mississippi Academy of Science, the Chair of the Educational Activity Committee for IEEE Region 3 Section, and the past President of ACES Society. He received the 2023 IEEE APS Harington-Mittra Award for his contribution to computational electromagnetics with hardware acceleration and the ACES 2025 Computational Electromagnetics Award.

Numerical Analysis of Large-Scale Phased Array Calibration Using a Kronecker Product Formulation

Jake W. Liu

Department of Electronic Engineering, National Taipei University of Technology, Taipei 10608, Taiwan
jwliu@ntut.edu.tw

Abstract – This paper proposes a calibration method for large-scale phased arrays based on a Kronecker product formulation, termed the Kronecker Product Method (KPM). Unlike the conventional Phase Toggling Method (PTM), which excites one element per measurement and suffers from limited measurement diversity, KPM employs simultaneous binary-phase excitation across all elements. This structure enhances robustness against noise and error accumulation, particularly in large arrays or high Signal-to-Noise Ratio (SNR) conditions. KPM retains PTM's simplicity and 1-bit phase control compatibility while offering superior theoretical properties and practical performance.

Index Terms – Far-field calibration method, Kronecker product, large arrays, phase toggling method, phased array calibration.

I. INTRODUCTION

Accurate calibration is essential for phased arrays, especially in applications demanding precise beamforming and null control [1–4]. Practical systems suffer from phase and amplitude errors, requiring calibration to maintain pattern fidelity.

Early techniques used near-field scans [5, 6], later improved by PWS-based Backward Transformation Methods (BTM) [7–9], but both are complex and scale poorly. In contrast, far-field methods offer better efficiency in calibration since no mechanical scan is required. Among these, the Phase Toggling Method (PTM) [10] is widely used due to its simplicity and compatibility with 1-bit digital phase shifters (DPSs). However, its element-wise toggling leads to poor signal diversity and degraded performance in large arrays or high-SNR conditions. Rotating-Element Electric-Field Vector Method (REVM) [11] offers phase-free calibration using total field magnitudes, enabling amplitude-only measurements.

Recent works improve efficiency via structured, multi-element excitations [12–14]. Multiple REVM [14] uses Fourier decomposition but is limited by model and resolution. Group-wise amplitude-only methods [15] enhance low-SNR performance. Others employ binary-phase modulation and harmonic analysis [16] or optimize matrix design [17]. A general framework in [18] builds excitation matrices recursively. While the proposed method shares this formulation, it differs by systematically constructing the excitation matrix as a Kronecker product of a 2×2 Hadamard base, offering compactness, scalability, and tractable error analysis.

Despite recent advances, PTM remains a baseline for its simplicity and binary control. Its limited diversity, however, constrains scalability. The proposed Kronecker Product Method (KPM) addresses this by enabling joint multi-element modulation using a structured matrix that remains linearly independent across array sizes. Like PTM, KPM uses only 0 and π phase shifts, preserving hardware simplicity and making it suitable for low-bit systems [19–21].

The rest of the paper is organized as follows: Section II introduces the system model and KPM formulation with error analysis. Section III presents simulation results. Section IV concludes.

II. THEORETICAL FORMULATION

A. System model

Consider a linear array of N elements, each connected to a DPS with b control bits. The DPS supports 2^b discrete phase states, equally spaced over $[-\pi, \pi)$. The n^{th} element introduces an unknown complex excitation modeled as:

$$x_n = a_n e^{ip_n}, \tag{1}$$

where $a_n \in \mathbb{R}$ and $p_n \in [-\pi, \pi)$ represent the amplitude and phase deviations, respectively. These quantities are to be estimated through external measurements.

The array is excited using a set of phase control tables $\Phi \in \mathbb{R}^{M\times N}$, where each row specifies a DPS phase state for a corresponding measurement. The received scalar response for the m^{th} measurement is given by:

$$y_m = \sum_{n=1}^{N} x_n e^{i\varphi_{mn}} + w_m, \tag{2}$$

Submitted On: August 15, 2025
Accepted On: February 10, 2026

https://doi.org/10.13052/2026.ACES.J.410108

where φ_{mn} is the phase applied to the n^{th} element in the m^{th} measurement, and w_m is additive measurement noise. In the model, noise is added to each simulated measurement to evaluate its impact on calibration accuracy.

The model assumes far-field boresight measurements and neglects element positions and patterns to isolate core calibration effects. The received signal is a coherent sum with known phase states and unknown errors, enabling clear comparison of calibration methods despite omitted practical factors.

Although the system model is presented using a linear array for clarity, the proposed KPM is directly applicable to two-dimensional planar arrays. In such cases, the array excitation vector can be formed by lexicographically stacking the element indices. Therefore, the proposed method naturally extends to two-dimensional arrays without modification to the core formulation.

B. The KPM formulation

The PTM operates by applying two measurement states per element: one with all phases set to zero (reference) and one with the target element toggled by 180°. For an N-element array, this results in $N+1$ measurements. The phase and amplitude errors are estimated from the difference between the reference and toggled measurements. Although simple, PTM only modulates one element at a time, leading to reduced signal diversity and increased vulnerability to noise in large arrays.

The proposed KPM constructs the excitation matrix by generating a unitary matrix $\mathbf{S} \in \mathbb{C}^{M\times N}$ from Kronecker products of a 2×2 DFT matrix (also known as the Hadamard matrices). Specifically, we first define

$$\mathbf{D} = \begin{bmatrix} 1 & 1 \\ 1 & -1 \end{bmatrix}. \tag{3}$$

A sequence of Kronecker products is then applied m - 1 times:

$$\mathbf{S}' = \mathbf{D} \otimes \mathbf{D} \otimes \cdots \otimes \mathbf{D} = \mathbf{D}^{\otimes m}, \tag{4}$$

until the resulting matrix $\mathbf{S}'$ has dimension $M \times M$, where $M = 2^m$ is the smallest power of two such that $M \geq N$. Since $\mathbf{D}$ is full-rank, and the Kronecker product of full-rank matrices preserves rank multiplicatively, $\mathbf{S}'$ has full rank M. As a result, all rows and columns of $\mathbf{S}'$ are linearly independent.

To construct $\mathbf{S}$, the first N rows and N columns of $\mathbf{S}'$ are extracted, resulting in a square submatrix:

$$\mathbf{S} = \mathbf{S}'[1:N, 1:N]. \tag{5}$$

Since the rows of $\mathbf{S}'$ span $\mathbb{C}^M$, any $N \leq M$ linearly independent rows (or columns) form a full-rank submatrix. In particular, the leading $N \times N$ principal submatrix $\mathbf{S}$ remains invertible, ensuring that the Kronecker-based measurement matrix admits a stable inverse for accurate error reconstruction.

To align this with the DPS hardware, the continuous phases of $\mathbf{S}$ are quantized to the nearest valid DPS state. Since $\mathbf{S}$ is constructed via 2×2 DFT matrix, all elements in $\mathbf{S}$ are either 1 or -1, which is the same as PTM. Thus, only 1 bit (2 states) is needed in KPM. The corresponding measurement vector $\mathbf{y} \in \mathbb{C}^N$ is collected, and the element-wise excitations are recovered by applying the inverse of $\mathbf{S}$:

$$\hat{\mathbf{x}} = \mathbf{S}^{-1}\mathbf{y}, \tag{6}$$

where the hat symbol in $\hat{\mathbf{x}}$ denotes the reconstructed value. Unlike PTM, which toggles one element at a time, KPM modulates all elements simultaneously using a structured excitation matrix. This enhances measurement diversity, improving noise robustness and system conditioning.

C. Accuracy study under additive Gaussian noise

To better understand the calibration accuracy limits under noise, we derive a closed-form expression for the expected root-mean-square error (RMSE) in the presence of additive complex Gaussian noise. Recall the measurement model:

$$\mathbf{y} = \mathbf{S}\mathbf{x} + \mathbf{w}, \tag{7}$$

where $\mathbf{y} \in \mathbb{C}^N$ is the measured data, $\mathbf{x} \in \mathbb{C}^N$ is the true excitation, $\mathbf{S} \in \mathbb{C}^{N\times N}$ is the measurement matrix, and $\mathbf{w} \in \mathbb{C}^N$ is additive noise. In the ideal case ($\mathbf{w} = \mathbf{0}$), both PTM and KPM recover $\mathbf{x}$ exactly since $\mathbf{S}$ is full-rank. In practice, noise degrades accuracy. We model $\mathbf{w}$ as complex Gaussian and derive a closed-form RMSE for $\hat{\mathbf{x}}$ as a function of SNR and array size.

Let us assume that the noise term takes the form of

$$\mathbf{w} \sim \mathcal{N}_c(0, \sigma^2\mathbf{I}), \tag{8}$$

meaning each entry is independently drawn from a circular symmetric complex Gaussian distribution with zero mean and variance σ^2. The calibration estimate is obtained by matrix inversion:

$$\hat{\mathbf{x}} = \mathbf{S}^{-1}\mathbf{y} = \mathbf{x} + \mathbf{S}^{-1}\mathbf{w}. \tag{9}$$

The estimation error is therefore:

$$\mathbf{e} = \hat{\mathbf{x}} - \mathbf{x} = \mathbf{S}^{-1}\mathbf{w}. \tag{10}$$

Since the noise $\mathbf{w}$ is zero-mean, the estimator is unbiased with $\mathbb{E}[\hat{\mathbf{x}}] = \mathbf{x}$. To compute the expected RMSE, we consider the squared norm of the error vector and use

properties of the complex Gaussian distribution and the linearity of expectation:

$$\mathbb{E}[\|\hat{\mathbf{x}}-\mathbf{x}\|^2] = \mathbb{E}[\|\mathbf{S}^{-1}\mathbf{w}\|^2] = \mathbb{E}[\mathbf{w}^H(\mathbf{S}^{-1})^H\mathbf{S}^{-1}\mathbf{w}] = \sigma^2\,\mathrm{tr}[\mathbf{S}^{-1}(\mathbf{S}^{-1})^H]. \tag{11}$$

where $\mathrm{tr}[\cdot]$ denotes the trace of a matrix. Thus, we define the average RMSE as the square root of the mean squared error normalized by the number of elements N as:

$$\mathrm{RMSE}_{\text{noise}} = \sigma\sqrt{\frac{\mathrm{tr}[\mathbf{S}^{-1}(\mathbf{S}^{-1})^H]}{N}}. \tag{12}$$

This expression reveals how the noise level σ and the structure of the inverse matrix $\mathbf{S}^{-1}$ jointly determine the expected calibration error.

D. Effect of phase quantization error in DPS

Unlike additive Gaussian noise, phase quantization errors in DPS affect the measurement matrix $\mathbf{S}$ through structured perturbations. To simplify analysis, we adopt a first-order perturbation model assuming small phase deviations and no additive noise.

In practice, phase shifters deviate slightly from their ideal discrete values due to hardware imperfections. We model this by assuming the applied phase is perturbed as:

$$\varphi_{mn} = \varphi_{mn}^{\text{ideal}} + \delta_{mn}, \quad \delta_{mn} \sim \mathcal{N}(0,\xi^2), \tag{13}$$

where δ_{mn} is a small, zero mean Gaussian error with standard deviation ξ (often specified as RMS phase error in a DPS datasheet), and, in the case of KPM (and PTM as well), $\varphi_{mn}^{\text{ideal}} \in \{0,\pi\}$. The elementwise impact on the measurement matrix is then modeled as:

$$\mathbf{S}^* = \mathbf{S}\circ\mathbf{E}, \tag{14}$$

where, using the first-order argument approximation,

$$E_{mn} = e^{i\delta_{mn}} \approx 1 + i\delta_{mn}. \tag{15}$$

The operator $\circ$ denotes elementwise (Hadamard) multiplication. Using the approximation in (15), the perturbed matrix becomes:

$$\mathbf{S}^* \approx \mathbf{S} + i(\mathbf{S}\circ\boldsymbol{\delta}), \tag{16}$$

where $\boldsymbol{\delta} \in \mathbb{R}^{N\times N}$ contains independent and identically distributed (i.i.d.) Gaussian entries. Because $\mathbf{S}$ contains only ±1 entries, the elementwise product $\mathbf{S}\circ\boldsymbol{\delta}$ preserves the statistical properties of , up to a sign flip, that is,

$$(\mathbf{S}\circ\boldsymbol{\delta})_{mn} = S_{mn}\cdot\delta_{mn} \in \{-\delta_{mn},\delta_{mn}\}. \tag{17}$$

Hence, in second-order statistics, we may treat $\mathbf{S}\circ\boldsymbol{\delta}$ as a matrix of i.i.d. Gaussian entries with zero mean and variance ξ^2. The estimated excitation vector, following the inverse operation in (6), becomes:

$$\tilde{\mathbf{x}} = \mathbf{S}^{-1}(\mathbf{S}^*\mathbf{x}) \approx \mathbf{x} + i\mathbf{S}^{-1}(\mathbf{S}\circ\boldsymbol{\delta})\mathbf{x}. \tag{18}$$

The resulting estimation error due solely to quantization is:

$$\mathbf{q} = \tilde{\mathbf{x}} - \mathbf{x} = i\mathbf{S}^{-1}(\mathbf{S}\circ\boldsymbol{\delta})\mathbf{x}. \tag{19}$$

Compare this with (10), we can see that the error caused by the DPSs is coupled with the excitation. Since the elements of $\mathbf{S}\circ\boldsymbol{\delta}$ are just δ_{mn} with random signs, and the signs are independent of the Gaussian variables and the entries of $\mathbf{x}$, this means the distribution of $\mathbf{S}\circ\boldsymbol{\delta}$ is the same as δ_{mn} in mean-square sense. So, we can treat the product $\mathbf{S}^{-1}(\mathbf{S}\circ\boldsymbol{\delta})\mathbf{x}$ as:

$$\mathbf{S}^{-1}(\mathbf{S}\circ\boldsymbol{\delta})\mathbf{x} \approx \mathbf{S}^{-1}\boldsymbol{\delta}\cdot\mathbf{x}, \quad \boldsymbol{\delta} \sim \mathcal{N}(0,\xi^2). \tag{20}$$

Hence, using the fact that $\boldsymbol{\delta}\cdot\mathbf{x}$ is a random vector with covariance $\xi^2\cdot\mathrm{diag}(|x_1|^2,\ldots,|x_N|^2)$, we get:

$$\mathrm{RMSE}_{\text{quant}} = \xi\sqrt{\frac{\mathrm{tr}[\mathbf{S}^{-1}\,\mathrm{diag}(|x_n|^2)(\mathbf{S}^{-1})^H]}{N}}. \tag{21}$$

Further assumption can be made if the excitation amplitudes are unit-magnitude (no amplitude variation across the entire array, an ideal case), i.e., $|x_n|^2 = a_n^2 = 1$, then (21) becomes:

$$\mathrm{RMSE}_{\text{quant (uniform)}} \approx \xi\sqrt{\mathrm{tr}[\mathbf{S}^{-1}(\mathbf{S}^{-1})^H]}. \tag{22}$$

In this case, the RMSE is not dependent on the element number N and the excitation vector $\mathbf{x}$.

The above analysis involves simplifications for tractability. However, since KPM modulates all elements simultaneously, it accumulates more phase errors per measurement than PTM, which perturbs one element at a time. Consequently, KPM is expected to exhibit higher quantization-induced error under equal conditions, a trend further examined via numerical experiments.

E. Complexity analysis and storage considerations

This subsection compares PTM and KPM in terms of measurement overhead, computational complexity, and hardware requirements, providing insight for practical system design.

1. Measurement complexity

The PTM requires $N+1$ measurements for an N-element array: one reference and N individual toggled states, yielding $\mathcal{O}(N)$ measurement cost. In contrast, KPM employs a structured excitation matrix $\mathbf{S}$, modulating all elements simultaneously. Using Kronecker products of 2×2 blocks, it requires exactly N measurements, also $\mathcal{O}(N)$, but with higher signal diversity per measurement and no reference measurement.

2. Computational complexity

In PTM, each element's excitation is obtained by subtracting the reference from the $(n+1)^{\text{th}}$ measurement, giving $\mathcal{O}(N)$ complexity without matrix inversion.

For KPM, the excitation vector is computed via matrix inversion and multiplication in (6). An unstructured $\mathbf{S}$ requires $\mathcal{O}(N^3)$ operations. However, with a structured 2×2 DFT-based matrix for $N = 2^n$, the inverse can be computed efficiently:

$$\mathbf{C} = \mathbf{D}^{-1} = \frac{1}{2}\begin{bmatrix} 1 & 1 \\ 1 & -1 \end{bmatrix}, \tag{23}$$

$$\mathbf{S}^{-1} = \mathbf{C}^{\otimes m}, \quad M = N = 2^n. \tag{24}$$

Using recursive Kronecker multiplications (similar to the Fast Walsh-Hadamard Transform), $\mathbf{S}^{-1}$ can be obtained with $\mathcal{O}(N \log N)$ complexity [22]. Matrix-vector multiplication $\mathbf{S}^{-1}\mathbf{y}$ requires $\mathcal{O}(N^2)$ operations.

To summarize, from a computational perspective, PTM requires only simple subtraction operations and thus has $\mathcal{O}(N)$ computational complexity, while KPM involves matrix-vector operations with complexity $\mathcal{O}(N^2)$ (or $\mathcal{O}(N \log N)$ using fast Kronecker implementations). However, in practical calibration systems, the dominant time cost arises from phase-shifter reconfiguration and measurement acquisition rather than digital post-processing. In typical implementations, the additional computation time of KPM is negligible compared to the measurement time, while the improved accuracy and robustness justify the modest increase in computation.

3. Storage and hardware considerations

Both PTM and KPM use 1-bit phase control (0 or π), reducing hardware complexity and eliminating high-resolution phase shifters. Unlike other multi-element calibration methods requiring arbitrary or multi-bit phases, PTM and KPM operate with binary phase matrices. This simplifies excitation generation and storage, making the methods efficient and practical for low-bit phased arrays.

III. NUMERICAL RESULTS

In our examples, we simulate a linear array with known excitations to evaluate KPM and PTM. Amplitudes $a_n \sim \mathcal{U}[0.5, 1.5)$ and phases $p_n \sim \mathcal{U}[-\pi/2, \pi/2)$, with phase referenced to the first element. Numerical experiments include additive complex Gaussian noise with standard deviation σ and random phase from $\mathcal{U}[-\pi, \pi)$.

A. RMSE evaluation over array size and SNR with ideal DPS

We evaluate the average RMSE of KPM and PTM over 10,000 trials under two scenarios: varying array size N at fixed SNR, and varying SNR at fixed N. The KPM numerical results are compared with the analytic prediction in (12) with no DPS quantization error.

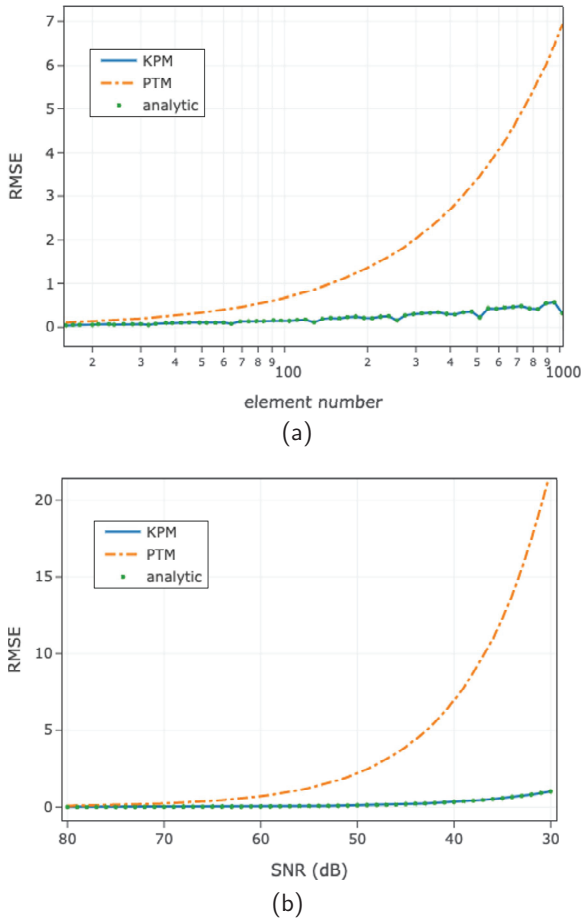

Fig. 1. RMSE performance of KPM and PTM across (a) fixed SNR with various array sizes and (b) fixed array size with various SNR values. KPM shows superior scalability and noise resilience.

Figure 1 (a) shows RMSE versus array size N (16 to 1024) at a fixed SNR of 40 dB. As N increases, both methods exhibit rising RMSE due to more unknowns under constant noise. However, PTM shows a steeper increase, while KPM maintains RMSE below 1, with mild quasi-periodic fluctuations attributed to Kronecker structure conditioning. At $N = 1024$, KPM achieves RMSE nearly 5% of PTM, demonstrating better scalability.

Figure 1 (b) shows RMSE versus SNR (30–80 dB) at fixed $N = 1024$. While both methods improve with

increasing SNR, KPM consistently outperforms PTM, especially below 60 dB where PTM struggles due to limited signal diversity. At 30 dB, KPM's RMSE is only 4% of PTM's, confirming superior noise robustness. In both cases, simulation results align with the analytical model in (12).

B. RMSE evaluation over DPS quantization error

This subsection validates the analytical results by isolating the effect of DPS quantization error. To remove additive noise, the SNR is set to infinity. The RMSE phase error (ξ) is varied from 0.1° to 5° in 0.1° steps, with the array size fixed at $N = 1024$. In this subsection, the numerical results of the KPM are compared with the analytical prediction derived in (22), which assumes a uniform array for analytical tractability.

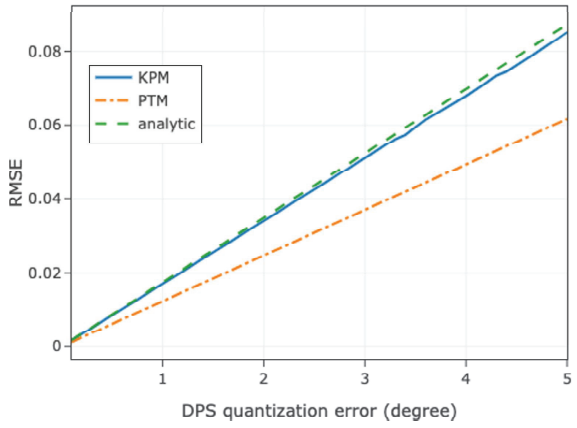

(a)

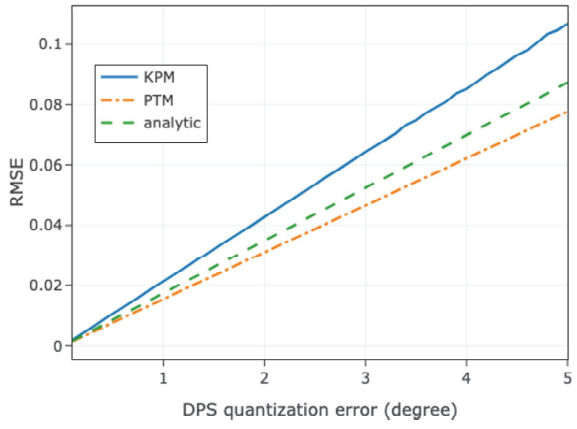

(b)

Fig. 2. Average RMSE of KPM and PTM over 10,000 trials under varying DPS phase quantization error ξ, with SNR $\to \infty$ to isolate quantization effects. (a) Uniform array and (b) non-uniform amplitudes.

We first consider a uniform array with unit amplitudes. Figure 2 (a) shows average RMSE over 10,000 trials. As expected, RMSE for both KPM and PTM increases linearly with DPS phase error. KPM exhibits slightly higher RMSE than PTM, consistent with the cumulative effect of phase errors in multi-element modulation. The KPM RMSE closely follows the analytical prediction in (22), with minor deviations due to the first-order approximation in (15). Figure 2 (b) considers amplitudes uniformly distributed between 0.5 and 1.5. Both methods show slightly higher RMSE than the uniform-amplitude case, indicating additional error from amplitude variation. Here, the prediction in (22) no longer aligns with KPM results, as it assumes $a_n = 1$. In practice, unknown excitations limit the applicability of (22).

C. Overall RMSE analysis

Lastly, we evaluate the RMSE of KPM calibration by jointly considering array size N, SNR, and DPS quantization error ξ. While individual effects of noise and quantization were analyzed analytically, a unified closed-form expression is intractable due to nonlinear interactions. Therefore, we construct numerical error maps for practical estimation.

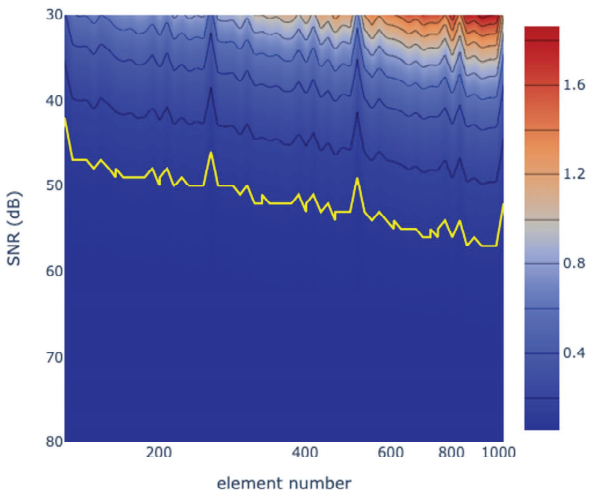

Fig. 3. Contour plot of the average RMSE for the KPM calibration as a function of array size N (ranging from 128 to 1024) and SNR (ranging from 80 dB to 30 dB), with DPS phase quantization error fixed at $\xi = 2.5°$.

Figure 3 shows a contour plot of average RMSE (10,000 trials) versus array size ($N = 128$ to 1024) and SNR (30–80 dB), with fixed quantization error $\xi = 2.5°$. Along the x-axis (increasing N), RMSE trends are similar to Fig. 1 (a), driven by N and $\mathrm{tr}[\mathbf{S}^{-1}(\mathbf{S}^{-1})^H]$, but exhibit more oscillations due to phase quantization, including nulls at power-of-two sizes. Along the SNR axis, RMSE increases with decreasing SNR, as expected.

IV. CONCLUSION

This paper proposes a phased array calibration method using a Kronecker product formulation with binary phase modulation to enable simultaneous multi-element excitation. We analytically prove that the resulting measurement matrix is full rank for any array size, ensuring stable recovery. Theoretical analysis includes closed-form RMSE expressions under additive noise and first-order perturbation analysis of DPS quantization effects. A numerical RMSE map is constructed to evaluate joint impacts of noise, quantization, and array size. Compared to the PTM, the proposed method achieves improved accuracy while maintaining compatibility with low-bit hardware under various array sizes and noise levels. Simulation results confirm its performance under diverse conditions. Experimental validation is planned.

REFERENCES

[1] R. Hansen, *Phased Array Antennas*. Hoboken, NJ: John Wiley & Sons, 2009.

[2] S. Kim, H.-J. Dong, J.-W. Yu, and H. Lee, "Phased array calibration system with high accuracy and low complexity," *Alexandria Engineering Journal*, vol. 69, pp. 759–770, 2023.

[3] J. J. Schuss, T. V. Sikina, J. E. Hilliard, P. J. Makridakis, J. Upton, J. C. Yeh, and S. M. Sparagna, "Large-scale phased array calibration," *IEEE Transactions on Antennas and Propagation*, vol. 67, no. 9, pp. 5919–5933, 2019.

[4] L. Zhu, W. Ma, and R. Zhang, "Movable-antenna array enhanced beamforming: achieving full array gain with null steering," *IEEE Communications Letters*, vol. 27, no. 12, pp. 3340–3344, 2023.

[5] A. Yaghjian, "An overview of near-field antenna measurements," *IEEE Transactions on Antennas and Propagation*, vol. 34, no. 1, pp. 30–45, 1986.

[6] F. Ferrara, C. Gennarelli, and R. Guerriero, "Near-field antenna measurement techniques," in *Handbook of Antenna Technologies*, Z. N. Chen, Ed. Singapore: Springer, pp. 2107–2163, 2016.

[7] J. Lee, E. Ferren, D. Woollen, and K. Lee, "Near-field probe used as a diagnostic tool to locate defective elements in an array antenna," *IEEE Transactions on Antennas and Propagation*, vol. 36, no. 6, pp. 884–889, 1988.

[8] Y. Lu, L. Zhou, M. Cui, X. Du, and Y. Hu, "A method for planar phased array calibration," *Progress In Electromagnetics Research Letters*, vol. 94, pp. 19–25, 2020.

[9] Y. Lu, S. Shi, M. Cui, and L. Zhou, "Probe distance error analysis for phased array calibration based on BTM," *Microwave and Optical Technology Letters*, vol. 64, no. 3, pp. 496–499, 2022.

[10] K. Lee, R. Chu, and S. Liu, "A performance monitoring/fault isolation and correction system of a phased array antenna using transmission-line signal injection with phase toggling method," in *IEEE Antennas and Propagation Society International Symposium 1992 Digest*, pp. 429–432, 1992.

[11] S. Mano and T. Katagi, "A method for measuring amplitude and phase of each radiating element of a phased array antenna," *Electronics and Communications in Japan (Part I: Communications)*, vol. 65, no. 5, pp. 58–64, 1982.

[12] W. Keizer, "Fast and accurate array calibration using a synthetic array approach," *IEEE Transactions on Antennas and Propagation*, vol. 59, no. 11, pp. 4115–4122, 2011.

[13] R. Sorace, "Phased array calibration," *IEEE Transactions on Antennas and Propagation*, vol. 49, no. 4, pp. 517–525, 2002.

[14] T. Takahashi, Y. Konishi, S. Makino, H. Ohmine, and H. Nakaguro, "Fast measurement technique for phased array calibration," *IEEE Transactions on Antennas and Propagation*, vol. 56, no. 7, pp. 1888–1899, 2008.

[15] W. Fan, Y. Zhang, Z. Wang, and F. Zhang, "Large-scale phased array calibration based on amplitude-only measurement with the multiround grouped-REV method," *IEEE Transactions on Antennas and Propagation*, vol. 72, no. 1, pp. 454–465, 2023.

[16] G. Hampson and A. Smolders, "A fast and accurate scheme for calibration of active phased-array antennas," in *IEEE Antennas and Propagation Society International Symposium. 1999 Digest. Held in conjunction with: USNC/URSI National Radio Science Meeting (Cat. No. 99CH37010)*, vol. 2, pp. 1040–1043, 1999.

[17] C. He, X. Liang, J. Geng, and R. Jin, "Parallel calibration method for phased array with harmonic characteristic analysis," *IEEE Transactions on Antennas and Propagation*, vol. 62, no. 10, pp. 5029–5036, 2014.

[18] R. Long, J. Ouyang, F. Yang, W. Han, and L. Zhou, "Multi-element phased array calibration method by solving linear equations," *IEEE Transactions on Antennas and Propagation*, vol. 65, no. 6, pp. 2931–2939, 2017.

[19] A. Graham, *Kronecker Products and Matrix Calculus: With Applications*. New York: Courier Dover Publications, 2018.

[20] M. Cheng, Q. Wu, C. Yu, H. Wang, and W. Hong, "A prephased electronically steered phased array that uses very-low-resolution phase shifters and a hybrid phasing method," *IEEE Transactions on Antennas and Propagation*, vol. 71, no. 9, pp. 7310–7322, 2023.

[21] M. Xiang, Y. Xiao, J. Deng, S. Xu, F. Yang, and H. Sun, "A low-profile programmable 2-bit array based on a novel highly integrated element," *IEEE Transactions on Antennas and Propagation*, vol. 73, no. 5, pp. 3418–3423, 2025.

[22] L. Wang and S. Zhao, "Fast reconstructed and high-quality ghost imaging with fast Walsh-Hadamard transform," *Photonics Research*, vol. 4, no. 6, pp. 240–244, 2016.

Jake W. Liu was born in Hualien, Taiwan, in 1995. He received the B.S. degree in Electrical Engineering from National Taiwan University, Taipei, Taiwan, in 2017, and the Ph.D. degree from the Graduate Institute of Communication Engineering at the same university in 2022. His research interests include antenna measurement theory, calibration of phased arrays at millimeter-wave frequencies, and computational electromagnetics. He is currently an Assistant Professor in the Department of Electronic Engineering at National Taipei University of Technology.

Electromagnetic Shielding Effectiveness Prediction of Stacked Chassis Based on Snow Ablation Optimizer Algorithm

Sen Wang[1], Hong Jiang[1], Xinbo Li[1], Xiaohui Wang[2], and Fengtao Xu[2]

[1]College of Communication Engineering
Jilin University, Changchun, 130012, China
wangsen23@mails.jlu.edu.cn, jiangh@jlu.edu.cn, xb_li@jlu.edu.cn

[2]Research and Development Department
China Academy of Launch Vehicle Technology, Beijing, 100076, China
wang98421@163.com, sunshine-taotao@163.com

Abstract – Stacked chassis has wide application in aerospace integrated electronic systems. However, with irregular enclosure structure and multi-module integrated into small space, its electromagnetic shielding effectiveness (SE) prediction is a challenge problem. In this paper, a novel method of SE prediction for stacked chassis is proposed based on snow-ablation optimizer (SAO) algorithm. First, a dedicated model of stacked chassis is selected and the SE at five internal sampling points is obtained via full-wave numerical simulation. Then, building on the Robinson equivalent model combined with the generalized Baum-Liu-Tesche (BLT) equations, and exploiting the initial simulation data as priors, the characteristic parameters of the stacked chassis are achieved via the SAO algorithm. On this basis and under vertically polarized and normally incident plane wave, the SE is predicted at all the positions across the central axis normal to the incident face of the chassis. The prediction results enable identification of the optimal SE distribution along frequency axis inside the chassis, thereby informing the internal layout and placement of sensitive devices. The prediction curves agree well with the simulation results, which can overcome the large-error limitations of conventional analytical approaches for complex cavities.

Index Terms – Electromagnetic shielding, Robinson equivalent model, shielding effectiveness prediction, snow-ablation optimizer, stacked chassis.

I. INTRODUCTION

Electromagnetic shielding is one of the most widely used techniques for protecting electronic equipment. The performance of a shielded enclosure is quantified by its shielding effectiveness (SE), which is the ratio of the electric field intensities at the locations of the monitoring point without and with the shielded case [1].

At present, there are three main methods to calculate the SE of the shielded cavities: experimental measurement, numerical simulation, and analytical algorithm. Measurements can better restore the real working scene of the shielding cavity and obtain more accurate measurement results. However, shielding rooms, microwave dark rooms, spectrum analyzers, and other experimental sites and expensive instruments are usually required. Hence, its cost is relatively high and, when the shielding cavity is located in a more complex environment, the experimental conditions are difficult to simulate and the limitations are greater.

Numerical calculation methods mainly include finite-difference time-domain (FDTD) algorithm [2–5], method of moments (MoM) [6–8], transmission line matrix (TLM) algorithm [9–11], finite element method (FEM) [12] and some hybrid numerical algorithms [13–18], which generally simulate the experimental scenarios through the simulation software, accurately build the complex model, and obtain the SE of the shielded cavity through the solution algorithm. However, to obtain accurate calculation results, the simulation process occupies a large amount of memory, takes long computation time, and requires high computer performance.

The analytical method occupies less memory with high computational efficiency, and is convenient for analyzing the effect of different parameter changes on the SE of the cavity. However, it is necessary to perform the equivalent processing of the shielding cavity during the modeling process. When the shielding cavity structure is relatively complex, the modeling process cannot be performed accurately, which is prone to cause deviations in the calculation results. A representative algorithm for the analytical calculation of SE of open rectangular cavities under plane wave irradiation is the cavity equivalent circuit model method proposed by Robinson et al. [19]. Many researchers have proposed improved analytical methods on this basis [20–24].

Submitted On: November 18, 2025
Accepted On: January 25, 2026

https://doi.org/10.13052/2026.ACES.J.410109

In recent years, driven by the demands of aerospace integrated electronic systems for "high integration, small form factor, and rapid deployment," stacked-architecture chassis technology has rapidly progressed from proof-of-concept to engineering application. The stacked chassis consists of multiple functional modules stacked vertically and locked as a single assembly by four long through-bolts; internal board-to-board high-speed connectors mate directly to carry data and power. A typical unit is more compact than comparable VITA46 standardized VPX chassis and employs fully conduction-cooled thermal management. The structural features and operating environment of the stacked chassis are highly complex, making experimental measurements stringent and costly.

In this paper, to address the limitations of existing approaches, a novel method is presented for the SE prediction of a stacked-architecture chassis. First, a specific stacked chassis model is selected, and the SE at five internal sampling points is obtained via numerical simulation using the software of computer simulation technology (CST) [25]. Next, a mathematical model for SE calculation is formulated based on the Robinson equivalent model combined with the Baum-Liu-Tesche (BLT) equations. Using the initial simulation results as priors, the characteristic parameters of the stacked chassis are estimated through the snow-ablation optimizer (SAO) algorithm, thereby enabling SE prediction. The proposed method is low-cost and easy to implement compared with the experimental measurements; it avoids repeated modeling and substantially reduces computational resources relative to the numerical simulation approaches.

II. STACKED CHASSIS MODEL AND PROBLEM FORMULATION

A. Stacked-architecture chassis model

In this paper, a dedicated stacked-architecture chassis is selected as the research subject. Its model is shown in Fig. 1, and the chassis dimensions and connector cut-out locations are provided in Fig. 2. We can observe that, originating from a real engineering prototype, the chassis exhibits irregular distributions of apertures and seams as well as a complex internal structure, making conventional analytical approaches inadequate for accurately evaluating its SE. To address this, the apertures and seams are equivalently modeled using the Robinson equivalent-circuit method in conjunction with the BLT equations, and the characteristic parameters of the chassis equivalent circuit are estimated via the SAO algorithm. On this basis, the SE at all the positions along the central axis normal to the incidence face inside the chassis can be predicted.

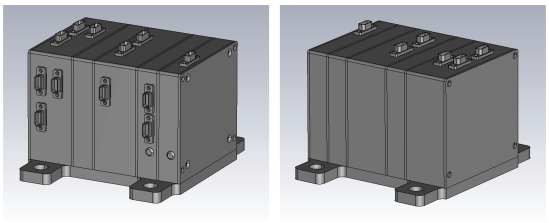

Fig. 1. Front and rear views of the stacked chassis model.

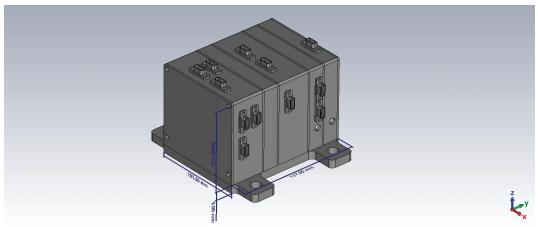

Fig. 2. Dimensional schematic of the stacked chassis model.

B. SE calculation model based on Robinson equivalent model and BLT equations

The SE calculation for a simple shielded cavity using the Robinson equivalent model and BLT equations is first reviewed, after which it is refined for the stacked chassis characteristics and its characteristic parameters are optimized.

Based on the TLM theory, Robinson et al. proposed an equivalent transmission line model for a regular aperture-seam shielded cavity, and the SE of the shielded cavity can be calculated based on the equivalent model. Figure 3 shows a rectangular shielded cavity model, and Fig. 4 is its equivalent transmission line circuit of the shielded cavity. The dimensions of the shielded cavity are $a \times b \times d$, the thickness is t, and the dimensions of the rectangular aperture slit on the cavity surface are $l \times w$. Assume that the plane wave is incident vertically from the direction of the plane where the aperture slit is located, and the observation point P is in the center axis of the plane wave incidence plane and is at a distance from the plane wave incidence plane.

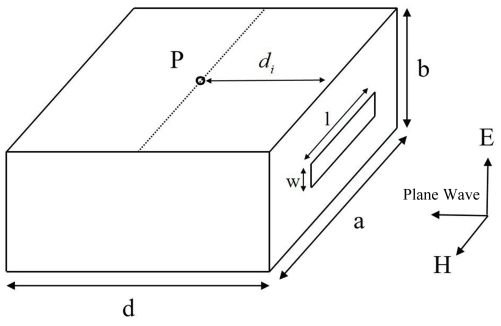

Fig. 3. A rectangular shielded cavity model.

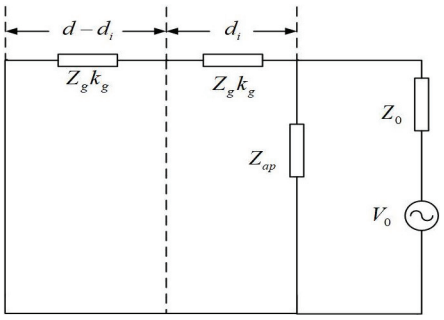

Fig. 4. Equivalent circuit of the shielded cavity based on transmission line equivalence method.

Equating the plane wave to a voltage source V_0 and an impedance $Z_0 = 377\ \Omega$, the aperture in the shielded cavity is equivalent to the impedance, which is expressed as

$$Z_{ap} = \frac{1}{2}\frac{l}{a} j Z_{0s} \tan\frac{k_0 l}{2}, \tag{1}$$

where $k_0 = 2\pi/\lambda$, and

$$Z_{0s} = 120\pi^2 \left[\ln\left(2\frac{1+\sqrt[4]{1-(w_e/b)^2}}{1-\sqrt[4]{1-(w_e/b)^2}}\right)\right]^{-1}, \tag{2}$$

$$w_e = w - \frac{5t}{4\pi}\left(1+\ln\frac{4\pi w}{t}\right). \tag{3}$$

Considering the shielded cavity as a waveguide, if only the TE_{10} mode is propagated, the characteristic impedance of the shielded cavity and the propagation constant are respectively shown as

$$Z_g = Z_0/\sqrt{1-(\lambda/2a)^2}, \tag{4}$$

$$k_g = k_0\sqrt{1-(\lambda/2a)^2}. \tag{5}$$

Based on this, we can effectively compute the SE of an ideal enclosure with a central slot.

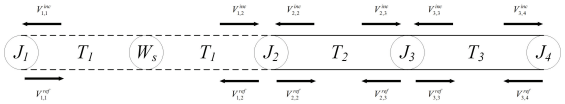

Fig. 5. The corresponding signal-flow graph.

According to the circuit model in Fig. 4, the corresponding signal-flow graph is drawn as Fig. 5. Here, node J_1 denotes the external observation point of the enclosure, J_2 denotes the aperture, J_3 denotes the internal observation point, and J_4 denotes the rear end of the enclosure. W_s represents the source in the equivalent circuit. Tube 1 corresponds to free-space wave propagation outside the enclosure, while Tubes 2 and 3 represent wave propagation inside the enclosure. V^{inc} indicates the incident wave at a node, and V^{ref} indicates the reflected wave.

Let $\mathbf{S}_1$ and $\mathbf{S}_2$ represent the scattering matrices at nodes J_2 and J_3, respectively, written as

$$\mathbf{S}_1 = \begin{bmatrix} \dfrac{Y_0 - Y_g - Y_{ap}}{Y_0 + Y_g + Y_{ap}} & \dfrac{2Y_g}{Y_0 + Y_g + Y_{ap}} \\ \dfrac{2Y_0}{Y_0 + Y_g + Y_{ap}} & \dfrac{Y_g - Y_0 - Y_{ap}}{Y_0 + Y_g + Y_{ap}} \end{bmatrix}, \tag{6}$$

$$\mathbf{S}_2 = \begin{bmatrix} 0 & 1 \\ 1 & 0 \end{bmatrix}, \tag{7}$$

where Y_0, Y_g, Y_{ap} denote the admittances of the free space, transmission line, and aperture, respectively.

Based on the propagation characteristics of waves in free space and inside the waveguide, the system propagation relation equations is derived as

$$\begin{bmatrix} V_{1,1}^{ref} \\ V_{1,2}^{ref} \\ V_{2,2}^{ref} \\ V_{2,3}^{ref} \\ V_{3,3}^{ref} \\ V_{3,4}^{ref} \end{bmatrix} = \begin{bmatrix} 0 & e^{\gamma_0 l_0} & 0 & 0 & 0 & 0 \\ e^{\gamma_0 l_0} & 0 & 0 & 0 & 0 & 0 \\ 0 & 0 & 0 & e^{\gamma_0 d_i} & 0 & 0 \\ 0 & 0 & e^{\gamma_0 d_i} & 0 & 0 & 0 \\ 0 & 0 & 0 & 0 & 0 & e^{\gamma_0 (d-d_i)} \\ 0 & 0 & 0 & 0 & e^{\gamma_0 (d-d_i)} & 0 \end{bmatrix} \times \begin{bmatrix} V_{1,1}^{inc} \\ V_{1,2}^{inc} \\ V_{2,2}^{inc} \\ V_{2,3}^{inc} \\ V_{3,3}^{inc} \\ V_{3,4}^{inc} \end{bmatrix} - \begin{bmatrix} V_0 \\ 0 \\ 0 \\ 0 \\ 0 \\ 0 \end{bmatrix} \tag{8}$$

where l_0 is the distance from the incident wave to the enclosure, and $\gamma_0 = jk_0$ denotes the free-space propagation constant. The 6×6 square matrix in (8) is the propagation matrix. Let γ_g denote the waveguide propagation constant, i.e.,

$$\gamma_g = jk_g = jk_0\sqrt{1-(\lambda/2a)^2}, \tag{9}$$

and define the node reflection coefficient ρ as

$$\rho \triangleq \frac{V^{ref}}{V^{inc}}, \tag{10}$$

$$\rho = \frac{Z_L - Z_C}{Z_L + Z_C}, \tag{11}$$

where Z_L is the load impedance and Z_C is the characteristic impedance. From the relationships between the incident and reflected waves at each node, the scattering-relation equations can be obtained as

$$\begin{bmatrix} V_{1,1}^{ref} \\ V_{1,2}^{ref} \\ V_{2,2}^{ref} \\ V_{2,3}^{ref} \\ V_{3,3}^{ref} \\ V_{3,4}^{ref} \end{bmatrix} = \begin{bmatrix} \rho_1 & 0 & 0 & 0 & 0 & 0 \\ 0 & S_{11}^1 & S_{12}^1 & 0 & 0 & 0 \\ 0 & S_{21}^1 & S_{22}^1 & 0 & 0 & 0 \\ 0 & 0 & 0 & S_{11}^2 & S_{12}^2 & 0 \\ 0 & 0 & 0 & S_{21}^2 & S_{22}^2 & 0 \\ 0 & 0 & 0 & 0 & 0 & \rho_4 \end{bmatrix} \begin{bmatrix} V_{1,1}^{inc} \\ V_{1,2}^{inc} \\ V_{2,2}^{inc} \\ V_{2,3}^{inc} \\ V_{3,3}^{inc} \\ V_{3,4}^{inc} \end{bmatrix}, \tag{12}$$

where ρ_1 denotes the reflection coefficient at node 1, $\rho_1 = 0$. ρ_4 is the reflection coefficient at node 4, $\rho_4 = -1$. The 6×6 matrix in (12) composes a total scattering matrix $\mathbf{S}$.

$$\begin{aligned} \begin{bmatrix} V_{1,1} \\ V_{1,2} \\ V_{2,2} \\ V_{2,3} \\ V_{3,3} \\ V_{3,4} \end{bmatrix} = & \begin{bmatrix} 1+\rho_1 & 0 & 0 & 0 & 0 & 0 \\ 0 & 1+S_{11}^1 & S_{12}^1 & 0 & 0 & 0 \\ 0 & S_{21}^1 & 1+S_{22}^1 & 0 & 0 & 0 \\ 0 & 0 & 0 & 1+S_{11}^2 & S_{12}^2 & 0 \\ 0 & 0 & 0 & S_{21}^2 & 1+S_{22}^2 & 0 \\ 0 & 0 & 0 & 0 & 0 & 1+\rho_4 \end{bmatrix} \\ & \times \begin{bmatrix} -\rho_1 & e^{\gamma_0 l_0} & 0 & 0 & 0 & 0 \\ e^{\gamma_0 l_0} & -S_{11}^1 & -S_{12}^1 & 0 & 0 & 0 \\ 0 & -S_{21}^1 & -S_{22}^1 & e^{\gamma_0 d_i} & 0 & 0 \\ 0 & 0 & e^{\gamma_0 d_i} & -S_{11}^2 & -S_{12}^2 & 0 \\ 0 & 0 & 0 & -S_{21}^2 & -S_{22}^2 & e^{\gamma_0 (d-d_i)} \\ 0 & 0 & 0 & 0 & e^{\gamma_0 (d-d_i)} & -\rho_4 \end{bmatrix}^{-1} \begin{bmatrix} 0.5V_0 e^{\gamma_0 (l_0/2)} \\ -0.5V_0 e^{\gamma_0 (l_0/2)} \\ 0 \\ 0 \\ 0 \\ 0 \end{bmatrix} \end{aligned} \tag{13}$$

The synthesized voltage at nodes $V(x)$ is defined as (13), where $V_{3,3}$ is the voltage at the internal observation point P, denoted as V_p, and the voltage at the observation point when the enclosure is absent is represented as $V_p^{'}$. Here $\mathbf{S}_1$ and $\mathbf{S}_2$ are respectively denoted as

$$\mathbf{S}_1 = \begin{bmatrix} S_{11}^1 & S_{12}^1 \\ S_{21}^1 & S_{22}^1 \end{bmatrix}, \tag{14}$$

$$\mathbf{S}_1 = \begin{bmatrix} S_{11}^2 & S_{12}^2 \\ S_{21}^2 & S_{22}^2 \end{bmatrix}. \tag{15}$$

Then the SE at the observation point can be calculated by

$$SE = -20\log(V_p/V_p^{'}). \tag{16}$$

C. Problem formulation

The cavity model in the previous section is assumed to be an ideal shielding body with a single aperture seam, which is a rectangular body with a regular shape except for the structure of the aperture seam. However, the surface of the stacked-architecture chassis to be studied has small irregular aperture seams. Its structure is complicated, the transmission line equivalent model obtained by the above-mentioned method has low accuracy, and the results of the shielding SE have a large deviation. So it is necessary to improve the equivalent model to enhance its accuracy.

According to the equivalent transmission-line model, the equivalent impedances of the aperture/slot and of the shielded cavity are the primary factors governing model accuracy. Therefore, (1), (2), (4), and (5) are modified so that they capture the characteristics of a stacked-architecture chassis. Let k_1 denote the aperture-location parameter of the stacked chassis; k_2 and k_3 the aperture-shape parameters, and k_4 an enclosure structural parameter. By incorporating k_1, k_2, k_3, k_4 into (1), (2), (4), and (5), the accuracy of the stacked-chassis equivalent model can be improved.

The resulting SE calculation model for the stacked-architecture chassis is shown in (17),

$$
\begin{cases}
Z_{ap} = \dfrac{1}{2}\dfrac{k_1 k_2}{a} jZ_{0s} \tan\dfrac{k_0 k_2}{2} \\
Z_{0s} = 120\pi^2 \left[\ln\left(2\dfrac{1+\sqrt[4]{1-(k_3/b)^2}}{1-\sqrt[4]{1-(k_3/b)^2}} \right) \right]^{-1} \\
Z_g = Z_0 / \left(k_4 \sqrt{1-(\lambda/2a)^2} \right) \\
k_g = k_0 k_4 \sqrt{1-(\lambda/2a)^2} \\
\begin{bmatrix} V_{1,1} \\ V_{1,2} \\ V_{2,2} \\ V_{2,3} \\ V_{3,3} \\ V_{3,4} \end{bmatrix} = \begin{bmatrix} 1+\rho_1 & 0 & 0 & 0 & 0 & 0 \\ 0 & 1+S_{11}^1 & S_{12}^1 & 0 & 0 & 0 \\ 0 & S_{21}^1 & 1+S_{22}^1 & 0 & 0 & 0 \\ 0 & 0 & 0 & 1+S_{11}^2 & S_{12}^2 & 0 \\ 0 & 0 & 0 & S_{21}^2 & 1+S_{22}^2 & 0 \\ 0 & 0 & 0 & 0 & 0 & 1+\rho_4 \end{bmatrix} \\
\qquad \times \begin{bmatrix} -\rho_1 & e^{jk_0 d_0} & 0 & 0 & 0 & 0 \\ e^{jk_0 d_0} & -S_{11}^1 & -S_{12}^1 & 0 & 0 & 0 \\ 0 & -S_{21}^1 & -S_{22}^1 & e^{jk_g d_1} & 0 & 0 \\ 0 & 0 & e^{jk_g d_1} & -S_{11}^2 & -S_{12}^2 & 0 \\ 0 & 0 & 0 & -S_{21}^2 & -S_{22}^2 & e^{jk_g d_2} \\ 0 & 0 & 0 & 0 & e^{jk_g d_2} & -\rho_4 \end{bmatrix}^{-1} \begin{bmatrix} 0.5V_0 e^{\gamma_0 (l_0/2)} \\ -0.5V_0 e^{\gamma_0 (l_0/2)} \\ 0 \\ 0 \\ 0 \\ 0 \end{bmatrix} \\
SE = -20\log_{10}(V_0/V_{3,3})
\end{cases}
\tag{17}
$$

where V_0 is the equivalent voltage source of the incident wave; $k_0 = 2\pi/\lambda$ is the free-space propagation constant; Z_0 is the intrinsic impedance of free space; $\lambda = c/f$ is the incident wavelength; f is the incident frequency; c is the speed of light; a is the height of chassis; and b is the length of the chassis bottom edge on the plane-wave incident face, where

$$
\begin{cases}
S_{11}^1 = \left(\dfrac{1}{Z_0} - \dfrac{1}{Z_g} - \dfrac{1}{Z_{ap}} \right) / \left(\dfrac{1}{Z_0} + \dfrac{1}{Z_g} + \dfrac{1}{Z_{ap}} \right) \\
S_{12}^1 = \left(2 \times \dfrac{1}{Z_g} \right) / \left(\dfrac{1}{Z_0} + \dfrac{1}{Z_g} + \dfrac{1}{Z_{ap}} \right) \\
S_{21}^1 = \left(2 \times \dfrac{1}{Z_0} \right) / \left(\dfrac{1}{Z_0} + \dfrac{1}{Z_g} + \dfrac{1}{Z_{ap}} \right) \\
S_{22}^1 = \left(\dfrac{1}{Z_g} - \dfrac{1}{Z_0} - \dfrac{1}{Z_{ap}} \right) / \left(\dfrac{1}{Z_0} + \dfrac{1}{Z_g} + \dfrac{1}{Z_{ap}} \right),
\end{cases}
\tag{18}
$$

$$
\begin{cases}
S_{11}^2 = S_{22}^2 = 0 \\
S_{21}^2 = S_{21}^2 = 1.
\end{cases}
\tag{19}
$$

Since the stacked chassis consists of multiple structurally similar and relatively enclosed modules, this work predicts SE using a single module as a representative case. The enclosure's characteristic parameters are identified from SE data at five interior sampling points within the module. The procedure is as follows.

(1) Sample the simulated SE at five sampling points located along the central axis of the incident face of the stacked-chassis module. Denote the resulting data by the matrix $\mathbf{S}$; these samples specify the target locations for identifying the enclosure characteristic parameters of the selected module.
(2) Determine the enclosure's characteristic parameters using the above SE prediction model for the stacked chassis, and compute the theoretical SE of the selected module. Denote the computed results as the matrix $\mathbf{S}'$, which serves as the predicted SE for the selected module enclosure.
(3) Formulate an objective function to drive the position-parameter vector toward the target. The objective function is given by

$$\min P = |\mathbf{S}(n) - \mathbf{S}'(n,i)|^2, \tag{20}$$

where $\mathbf{S}(n)$ denotes the sampled value of the SE at the n-th frequency point, and $\mathbf{S}'(n,i)$ denotes the theoretically computed SE for the i-th individual in the population at the n-th frequency point.
(4) The fitness evaluation function is defined as

$$F(n,i) \triangleq \frac{1}{\tau + P(n,i)}, \tag{21}$$

where $\tau = 0.001$. A larger $F(n,i)$ (corresponding to a smaller $P(n,i)$) indicates stronger fitness, whereas a smaller $F(n,i)$ (corresponding to a larger $P(n,i)$) indicates weaker fitness.

III. ALGORITHM TO SOLVE SHIELDING EFFECTIVENESS PREDICTION PROBLEM

A. Basic CST simulation settings

A Gaussian electromagnetic pulse from the CST electromagnetic simulation software is used as the simulated signal source. The pulse has a higher electric field intensity and allows frequency-domain coverage and field intensity of the waveform to be customized through the operating frequency, thereby simulating more severe and complex electromagnetic environment. The approximate expression of the Gaussian electromagnetic pulse is

$$f(t) = \frac{\kappa A}{\pi(t-c)} \sin\left(\frac{(B_H - B_L)(t-c)}{2}\right) \times e^{j\frac{(B_H+B_L)(t-c)}{2}}, \tag{22}$$

where $A = 20$ V/m is the peak value of the electric field strength, κ is the correction factor, B_H and B_L are the maximum and minimum frequencies, and c is the time shift amount. The time-domain and frequency-domain waveforms of the Gaussian electromagnetic pulse are shown in Fig. 6.

The SE at internal monitoring points of the chassis under vertically polarized and vertically incident plane waves is simulated using CST electromagnetic software, where the electric field intensity at these points before and after adding the chassis is obtained and used to calculate the SE. The simulation frequency range is set from 0 to 18 GHz, and the chassis material is set to PEC. The simulation diagram is shown in Fig. 7.

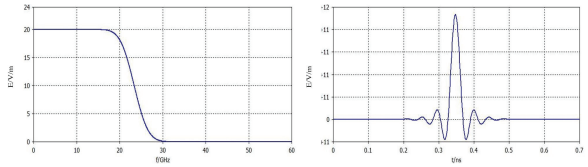

Fig. 6. The frequency-domain and time-domain waveforms of the Gaussian electromagnetic pulse.

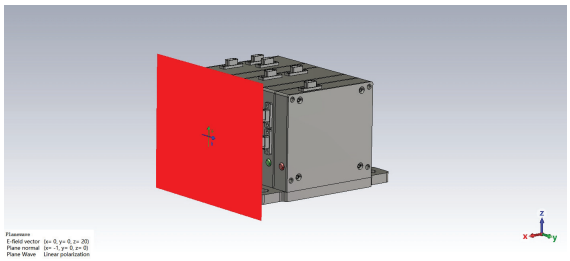

Fig. 7. The simulation diagram using CST.

B. Snow ablation optimizer algorithm for SE prediction

Over the past two decades, metaheuristic algorithms (MAs) have been widely employed across numerous fields to solve a broad range of complex engineering problems. In particular, when tackling nonconvex, highly nonlinear, nonsmooth, and even dynamic real-world problems, MAs exhibit greater general applicability than traditional mathematical optimization methods owing to their gradient-free nature and structural simplicity [26, 27].

The snow ablation optimizer [28, 29] aims to balance global exploration and local exploitation in the solution space, improving convergence efficiency while preserving population diversity, thereby addressing the shortcomings of existing methods on complex problems. It can mitigate premature convergence compared with traditional algorithms such as particle swarm optimization (PSO).

Inspired by snow ablation, SAO maps physical phase-change behaviors to search strategies: sublimation corresponds to dispersed global exploration, melting corresponds to local exploitation around elite solutions, and evaporation represents an adaptive adjustment between these two modes. During optimization, the algorithm dynamically coordinates diffusive exploration and focused exploitation.

(1) Population

In the SAO optimization process, the population consists of N candidate solutions maintained in parallel and is represented by the position matrix

$$\mathbf{Z}^{(t)} = [z_{i,j}^{(t)}]_{N\times Dim} = [\mathbf{z}_1^{(t)^T}, \cdots, \mathbf{z}_N^{(t)^T}]^T, \tag{23}$$

where $\mathbf{z}_i^{(t)} = [z_{i,1}^{(t)}, z_{i,2}^{(t)}, \cdots, z_{i,Dim}^{(t)}]$ denotes the parameter vector of the i-th individual at iteration t, and Dim is the dimension of the decision variables. In this paper, $Dim = 4$ for four parameters. The initial population is generated uniformly at random within the lower and upper bounds $\mathbf{L}$ and $\mathbf{U}$:

$$\mathbf{Z}^{(0)} = \mathbf{L} + \mathbf{R} \odot (\mathbf{U} - \mathbf{L}), \tag{24}$$

where $\mathbf{R} \in [0,1]_{N\times Dim}$ and $\odot$ denotes the element-wise (Hadamard) product. To balance global exploration and local exploitation, SAO dynamically partitions the population index set into an exploration subpopulation and an exploitation subpopulation.

Meanwhile, the population centroid is computed to characterize the overall distribution and assist the position update:

$$\bar{\mathbf{z}}^{(t)} = \frac{1}{N}\sum_{i=1}^{N} \mathbf{z}_i^{(t)}. \tag{25}$$

This design enables the algorithm to rapidly locate promising regions in the early stage while maintaining diversity in later iterations to mitigate premature convergence.

(2) Fitness function

At the n-th discrete frequency point, the CST post-processed SE at the m-th sampling location ($m = 1, \cdots, 5$) is denoted by $\mathbf{S}_m(n)$. For the i-th individual (candidate parameter vector) $\mathbf{z}_i$ in the population, the SE predicted by the Robinson-equivalent model and BLT equations is $\mathbf{S}'_m(n,i)$. The objective function is defined as the sum of squared errors over the five sampling locations:

$$P(n,i) = \sum_{m=1}^{5} \left(\mathbf{S}_m(n) - \mathbf{S}'_m(n,i)\right)^2. \tag{26}$$

Since SAO is implemented as a fitness-maximization scheme (larger fitness is better), the fitness function is constructed by mapping the objective value as

$$F(n,i) = \frac{1}{\varepsilon + P(n,i)}, \tag{27}$$

where $\varepsilon = 0.001$ is introduced to avoid division by zero when $P(n,i) \to 0$ and to improve numerical stability. Therefore, a larger $F(n,i)$ (i.e., a smaller $P(n,i)$) indicates better agreement between the model prediction and the CST results at the five sampling points. In each iteration, SAO evaluates $F(n,i)$ for all individuals and selects the one with the maximum fitness as the current best solution for subsequent updates and elitist guidance.

(3) Sublimation, melting, and evaporation

Sublimation (exploration phase):

The sublimation phase corresponds to the physical process in which snow (or meltwater derived from snow) transforms into vapor. The resulting irregular particle motion leads to a highly dispersed search behavior; therefore, SAO models it as global exploration using Brownian motion. For standard Brownian motion, the step length is drawn from a standard normal distribution with probability density function

$$f_{BM}(x;0,1) = \frac{1}{\sqrt{2\pi}} e^{-\frac{x^2}{2}}. \tag{28}$$

Accordingly, the position-update equation for each individual in the exploration phase is given by (29),

$$\mathbf{z}_{n,i}{}^{(t+1)} = Elite_n(t) + BM_{n,i}(t) \odot \Big(R_1 \cdot (\mathbf{g}_n(t) - \mathbf{z}_{n,i}{}^{(t)}) + (1-R_1)\cdot(\bar{\mathbf{z}}_n^{(t)} - \mathbf{z}_{n,i}{}^{(t)})\Big) \tag{29}$$

where $\mathbf{z}_{n,i}{}^{(t)}$ denotes the position (candidate parameter vector) of the i-th individual at iteration t for the n-th frequency point; $BM_{n,i}(t)$ is the Brownian-motion random step vector, $BM_{n,t}(t) \sim \mathbb{N}(0,1)$; $R_1 \in [0,1]$ is a random factor that weights two guidance directions; $\mathbf{g}_n(t)$ is the current global-best individual at the n-th frequency point; $Elite_n(t)$ denotes an individual randomly selected from the elite pool at the n-th frequency point (the elite pool consists of the best, second-best, and third-best individuals); $\bar{\mathbf{z}}_n^{(t)}$ is the population centroid for the n-th frequency point. As shown in (29), the sublimation operator enables dispersed exploration via Brownian diffusion while incorporating elitist and population-level guidance, thereby improving global search capability and alleviating premature convergence.

Melting (exploitation phase):

The melting phase corresponds to the heating-induced transition from snow to liquid water, and it is mapped

in SAO to local exploitation around the current best solutions. In this phase, search agents are encouraged to perform denser, fine-grained searches in the neighborhood of the current global best, while information exchange with the population centroid helps accelerate convergence toward high-quality regions and reduces stagnation in a single basin of attraction. To model the progressively strengthened exploitation pressure over iterations, the classical degree-day snowmelt model is adopted. Its general form is

$$M = DDF \times (T - T_1), \tag{30}$$

where M denotes the snowmelt rate, T is the daily mean air temperature, and T_1 is the base (threshold) temperature, typically set to $0°C$. By setting $T_1 = 0$, (30) becomes

$$M = DDF \times T, \tag{31}$$

where DDF denotes the degree-day factor. To introduce a time-varying exploitation schedule, the DDF is updated as

$$DDF_n(t) = 0.35 + 0.25 \times \frac{e^{\frac{t}{iter_{\max}}} - 1}{e - 1}, \tag{32}$$

where $iter_{\max}$ is the maximum number of iterations, and t is the current iteration. Defining

$$T(t) = e^{-\frac{t}{iter_{\max}}}, \tag{33}$$

the snowmelt rate at the n-th frequency point is written as

$$M_n(t) = DDF_n(t) \times T(t). \tag{34}$$

Subsequently, within the melting operator, the position-update equation for each individual is given by (35),

$$\begin{aligned} \mathbf{z}_{n,i}{}^{(t+1)} = {} & M_n(t) \cdot \mathbf{g}_n(t) + BM_{n,i}(t) \\ & \odot \Big(R_1 \cdot (\mathbf{g}_n(t) - \mathbf{z}_{n,i}{}^{(t)}) \\ & + (1 - R_1) \cdot (\bar{\mathbf{z}}_n^{(t)} - \mathbf{z}_{n,i}{}^{(t)}) \Big) \end{aligned} \tag{35}$$

where R_2 is a random number in $[-1, 1]$ used to enhance information exchange among individuals. As indicated in (35), the melting operator strengthens exploitation through the time-varying factor $M_n(t)$ while maintaining necessary activity via mild stochastic perturbations, thereby enabling efficient refinement around promising regions.

Evaporation (dynamic adjustment):

The evaporation phase corresponds to the physical process in which meltwater further evaporates into vapor. Algorithmically, SAO maps this process to a dynamic adjustment of the exploration–exploitation balance: as iterations proceed, the algorithm gradually increases the tendency toward irregular, highly dispersed motion (vapor-like diffusion), which helps maintain population diversity, suppress overly aggressive convergence, and strengthen global search capability.

To implement this mechanism, a dual-subpopulation scheme is used in the SAO. At iteration t for the n-th frequency point optimization, the whole population P is randomly partitioned into an exploration subpopulation $P_a^{(t)}$ (sublimation) and an exploitation subpopulation $P_b^{(t)}$ (melting):

$$\begin{gathered} P = P_a^{(t)} \cup P_b^{(t)},\ P_a^{(t)} \cap P_b^{(t)} = \emptyset, \\ |P_a^{(t)}| = N_a(t),\ |P_b^{(t)}| = N_b(t),\ N_a(t) + N_b(t) = N. \end{gathered} \tag{36}$$

Initially, the two subpopulations are of equal size:

$$N_a(1) = N_b(1) = \frac{N}{2}. \tag{37}$$

Then, a linear schedule is applied to gradually enlarge exploration while reduce exploitation (consistent with the MATLAB implementation):

$$N_a(t+1) = \min(N, N_a(t) + 1), \tag{38}$$

$$N_b(t+1) = N - N_a(t+1). \tag{39}$$

Accordingly, the exploration and exploitation ratios are

$$\rho_a(t) = \frac{N_a(t)}{N}, \quad \rho_b(t) = \frac{N_b(t)}{N} = 1 - \rho_a(t), \tag{40}$$

where $\rho_a(t)$ increases with t. Under this "evaporation–diffusion" metaphor, the algorithm realizes a temporal scheduling of the exploration–exploitation ratio and promotes coordination between global and local search throughout the run.

(4) Complete position-update

The complete position-update equation of the SAO is given by (41). The entire population is effectively represented as a position matrix. Accordingly, in the foregoing equation, $index_a$ and $index_b$ denote the index sets of individuals belonging to P_a and P_b, respectively, within this matrix.

$$\begin{cases} Elite_n(t) + BM_{n,i}(t) \odot \Big(R_1 \cdot (\mathbf{g}_n(t) - \mathbf{z}_{n,i}{}^{(t)}) \\ \quad + (1 - R_1) \cdot (\bar{\mathbf{z}}_n^{(t)} - \mathbf{z}_{n,i}{}^{(t)}) \Big),\ i \in index_a \\ M_n(t) \cdot \mathbf{g}_n(t) + BM_{n,i}(t) \odot \Big(R_1 \cdot (\mathbf{g}_n(t) - \mathbf{z}_{n,i}{}^{(t)}) \\ \quad + (1 - R_1) \cdot (\bar{\mathbf{z}}_n^{(t)} - \mathbf{z}_{n,i}{}^{(t)}) \Big),\ i \in index_b \end{cases} \tag{41}$$

In the SAO algorithm, after updating the positions, the fitness values of all individuals associated with each frequency point are evaluated. If the maximum fitness in the current generation exceeds the pre-update maximum, the original position parameters of the corresponding individual are replaced with its current position parameters; otherwise, the original individual is retained. The procedure then proceeds to the next iteration, and the update operation is repeated cyclically.

IV. GLOBAL ALGORITHM DESIGN

Based on the above problem model established in this paper and the introduction of the solution algorithm, the global algorithm design is carried out for the problem model. The flowchart of the SAO algorithm for SE prediction is shown in Fig. 8.

The main steps of the algorithm are as follows:

Step 1, evaluation the SE of five sampling points using CST. Since the stacked-architecture chassis comprises multiple similar, relatively enclosed modules, we take the module enclosure shown in Fig. 9 as a representative example. Along the central axis normal to the plane-wave incident face inside this module, five reference points, labeled A, B, C, D, and E, are selected. The excitation is a short-duration pulsed plane wave with a peak electric-field strength of 20 V/m; the frequency range is set from 10 kHz to 18 GHz, and the polarization is vertical. Using the simulation, we obtain the SE curves at the five sampling points inside the module enclosure. The locations of A–E are shown in Fig. 9. These curves are then discretely sampled and arranged into a matrix **S**, which serves as the target data for identifying the characteristic parameters of the module enclosure. The sampled curves are shown in Fig. 10.

Step 2, SAO parameter settings and population initialization. The decision-variable dimension and physical constraints are first determined, and lower/upper bounds are specified accordingly. Meanwhile, the target matrix **S** obtained in Step 1 is indexed by the unified discrete frequency list to form frequency-wise target data for subsequent per-frequency optimization. SAO control parameters are then specified (e.g., population size $N = 100$ and number of maximum iteration $iter_{\max} = 200$ in this work). The population is randomly initialized within the prescribed bounds to ensure feasibility and adequate coverage: each individual carries four decision variables corresponding to the chassis characteristic parameters in the equivalent model, and the Brownian random vector is generated from a standard normal distribution. After initialization, fitness values are evaluated once and an elite pool (e.g., best/second-best/third-best individuals) is formed to support elitist guidance in subsequent updates. The population representation, initialization, and the definitions of centroid follow the preceding SAO description.

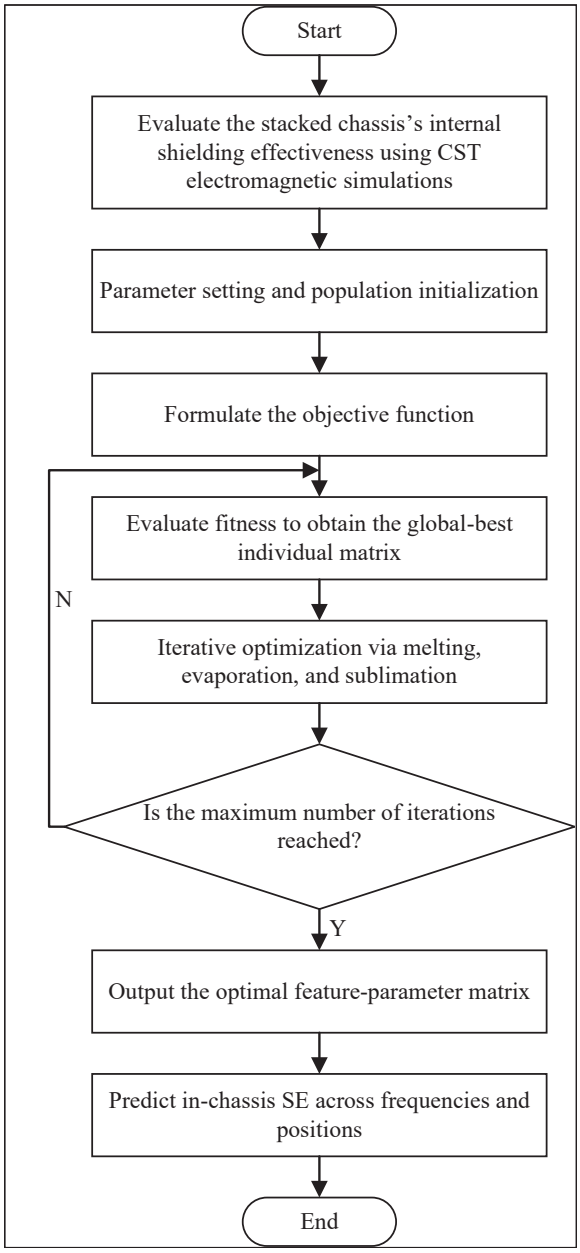

Fig. 8. Overall algorithm flowchart.

Step 3, equivalent-model evaluation, fitness construction, and fitness assessment. For each discrete frequency point, the candidate parameter vector of an individual is used to evaluate the equivalent model: based on the Robinson equivalent-circuit representation combined with the BLT equations, the model-predicted SE at the five sampling points is obtained at that frequency. Using the objective and fitness definitions in (26) and (27), the mismatch between the predicted SE and the target SE values (the corresponding column of **S**) is

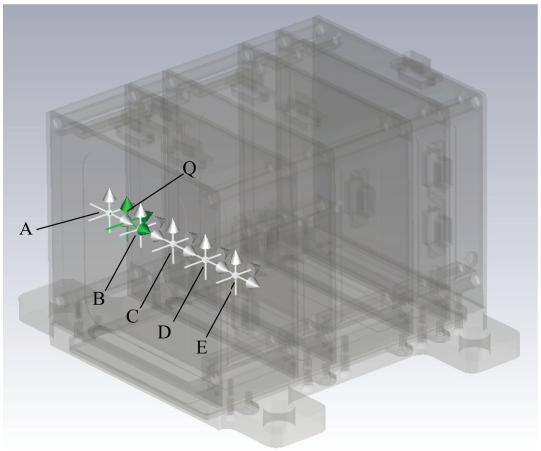

Fig. 9. Locations of the five sampling points (A–E).

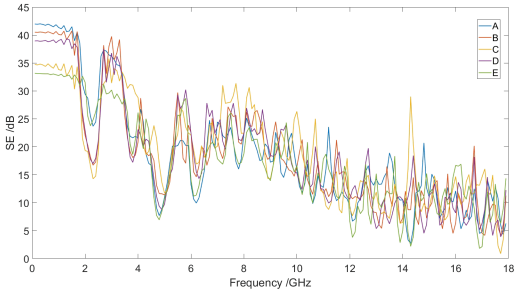

Fig. 10. Shielding-effectiveness sampling curves at the selected sampling points inside the module enclosure.

computed to yield the fitness of each individual. At the end of each iteration, the current best and historical best solutions are updated, and the elite pool and required population statistics (e.g., centroid) are refreshed to provide best/elite/centroid guidance for the next update.

Step 4, update each individual's position via the three SAO operators: sublimation, melting, and evaporation. At each iteration, the evaporation mechanism dynamically partitions the population into an exploration subpopulation and an exploitation subpopulation, and different update operators are applied accordingly. To ensure physical feasibility, boundary-constraint handling is applied to the individual parameters after each position update, followed by the next round of fitness evaluation and elitist retention.

Step 5, the algorithm halts when the SAO reaches the preset maximum number of iterations. The best individual in the population attains the highest fitness and exhibits the closest agreement with the simulated SE results. Across all frequency points, the position parameters of the optimal individuals are assembled into a feature-parameter matrix comprising four groups of features, denoted $k_{n1}, k_{n2}, k_{n3}, k_{n4}$, where n indexes the n-th frequency point. Here, k_{n1} represents the aperture-location parameters of the stacked chassis, k_{n2} and k_{n3} represent the aperture-shape parameters, and k_{n4} represents the chassis structural parameters. This set can be expressed by an $n_{\max} \times 4$ matrix $\mathbf{Z}\_best$, denoted as

$$\mathbf{Z}\_best = \begin{bmatrix} k_{1,1} & k_{1,2} & k_{1,3} & k_{1,4} \\ k_{2,1} & k_{2,2} & k_{2,3} & k_{2,4} \\ \vdots & \vdots & \vdots & \vdots \\ k_{n_{\max},1} & k_{n_{\max},2} & k_{n_{\max},3} & k_{n_{\max},4} \end{bmatrix}, \quad (42)$$

where $n_{\max}$ denotes the total number of selected frequency points. Using the global optimum identified by the SAO, namely, the optimal individual matrix Z_{best}, we can compute the SE at the Q designated points within the selected module enclosure.

Step 6: Using the extracted feature-parameter matrix, analytically compute the SE at the predesignated Q locations inside the selected module enclosure, and the resulting analytical SE values are validated by comparison with the CST simulation results at the same Q locations.

Step 7: Based on the extracted feature-parameter matrix, the SE distribution at multiple interior locations of the selected module is predicted across different frequency points. Regions exhibiting superior electromagnetic shielding at each frequency are identified, thereby providing guidance for internal cable routing and for the placement of sensitive components/modules within the chassis.

V. ALGORITHM PERFORMANCE ANALYSIS

A. Analysis of sample size and computational resource usage

First, the two frequency-domain electric-field intensity curves at each sampling location—measured with and without the chassis protection—are post-processed in CST to obtain the corresponding SE spectrum at the sampling locations. The resulting SE frequency-domain data are then exported in ASCII format for external processing. In MATLAB, the exported SE spectrum contains a total of 1859 frequency samples. The data are subsequently resampled onto a uniform frequency grid, ranging from 0.1 GHz to 18 GHz with a step size of 0.1 GHz, yielding 180 frequency-domain samples used for the SAO iterations. At each discrete frequency point, the SAO optimizer takes the simulated SE values at the five sampling locations as the target outputs and performs the parameter update accordingly. Therefore, five data values are used per frequency point, and the optimization is carried out sequentially over all frequency points, resulting in a total of 900 frequency-domain scalar samples used in the overall procedure.

Table 1: Comparison of runtime and peak memory usage between the full-wave CST simulation and the proposed SAO-assisted analytical method

Method	Runtime	Peak Memory
Full-wave CST simulation	110 min 33 s	1413 MB
Proposed method	73.38 s	4444.48 MB

The overall computational cost is primarily determined by the number of fitness evaluations, and is approximately proportional to the product of the number of frequency points, population size, maximum number of iterations, and number of sampling points. When a denser frequency grid is adopted during sampling, the SAO algorithm must perform a larger number of independent per-frequency iterative optimizations; however, this also yields a denser discrete sequence of "frequency–enclosure characteristic parameters," enabling the subsequent frequency-domain SE prediction to better match the simulation results and thereby reducing errors introduced by frequency discretization and interpolation.

Compared with performing a full-wave numerical simulation of the chassis directly in CST, the proposed approach shifts the computational burden from "full-wave broadband solving of a complex 3D structure" to "a single full-wave simulation to obtain SE spectra at a small number of sampling points + parameter identification based on an equivalent model + fast analytical prediction." Specifically, the CST full-wave simulation uses the time-domain solver Hexahedral TLM, which discretizes the computational domain into a hexahedral mesh equivalently represented by a transmission-line network and updates the electromagnetic fields in the time domain through iterative node scattering and link propagation to obtain a broadband response. However, such time-domain grid-based methods typically require a sufficiently fine mesh and long time stepping to satisfy accuracy and energy-decay termination criteria, resulting in a high computational time cost. As summarized in Table 1, under the same hardware conditions, a single CST simulation for obtaining the SE spectrum at the probe locations takes approximately 110 min 33 s with a peak memory usage of about 1413 MB. In contrast, our MATLAB implementation performs uniform-frequency resampling of the exported SE spectrum, and applies SAO-based iterative identification at each frequency point using the SE values at five sampling locations as target outputs; the complete work-flow of "parameter extraction + SE prediction" takes approximately 73.38 s with a peak memory usage of about 4444.48 MB. Therefore, relative to a single full-wave CST simulation, the proposed approach can reduce the runtime by roughly one order of magnitude, at the expense of increased memory consumption due to population-based iterations and data-structure storage. More importantly, when SE must be evaluated repeatedly for multiple interior locations and layout schemes, the cost of full-wave CST simulations scales approximately linearly with the number of cases, whereas the proposed method requires only a small amount of full-wave data as priors and can rapidly generate broadband, multi-location SE predictions, thereby significantly reducing the overall computational cost for iterative engineering design.

B. Analysis of prediction results

Based on the extracted feature-parameter matrix, the SE at the Q-point within the selected module enclosure is predicted and compared with the CST simulation results at the same location to verify predictive accuracy. The Q-point location is shown previously in Fig. 9. A comparison between the predicted and simulated SE at the Q-point is presented in Fig. 11. The two SE curves exhibit a high degree of agreement, sharing the same overall trend with limited discrepancies, thereby demonstrating the accuracy and validity of the predictions.

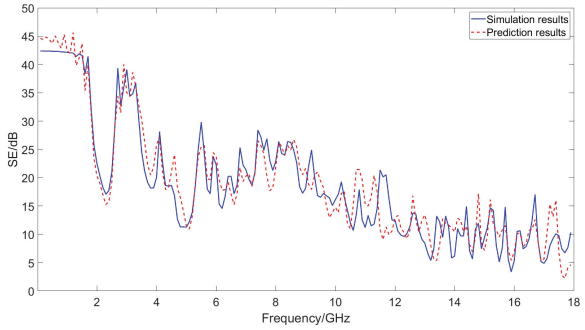

Fig. 11. Comparison of the predicted and the simulated shielding effectiveness at Q-point location.

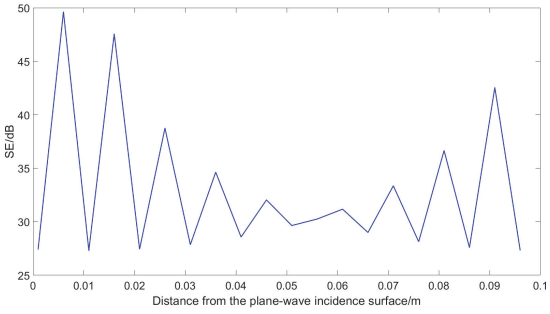

Fig. 12. Effect of distance from plane wave incident surface on shielding effectiveness at 4 GHz frequency point.

Based on the extracted feature-parameter matrix, the SE at other interior locations of the selected module enclosure is predicted across different frequency points. Locations exhibiting relative advantages and disadvantages in SE at each frequency are analyzed to provide guidance for internal routing and for the placement of sensitive components.

As shown in Fig. 12, at 4 GHz the dependence of SE on the distance from the plane-wave incidence surface is presented. The results indicate that, at 4 GHz, the SE inside the selected module enclosure is generally between 25 dB and 35 dB; at distances of 0.006 m, 0.016 m, 0.081 m, and 0.091 m from the incidence surface, the enclosure exhibits comparatively higher SE. The maximum SE of 49 dB occurs at a distance of 0.006 m. Accordingly, sensitive components may be preferentially placed within 0–0.03 m from the plane-wave incidence surface.

As shown in Fig. 13, at 16 GHz the dependence of SE on the distance from the plane-wave incidence surface is presented. The results indicate that, at 16 GHz, the SE inside the selected module enclosure is generally between 5 dB and 20 dB; at distances of 0.016 m and 0.056 m from the incidence surface, the enclosure exhibits comparatively higher SE. The maximum SE of 29 dB occurs at 0.016 m. Accordingly, sensitive components may be preferentially placed near 0.016 m and 0.056 m from the plane-wave incidence surface.

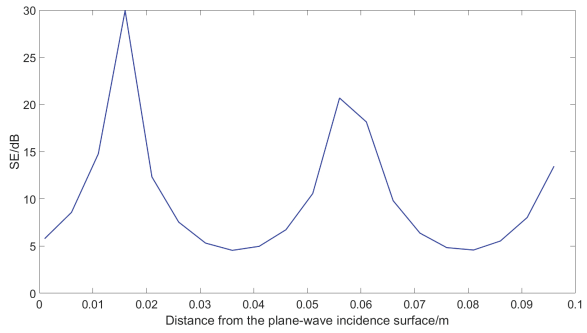

Fig. 13. Effect of distance from plane wave incident surface on shielding effectiveness at 16 GHz frequency point.

Taking 9 GHz frequency point as an example, the fitness value at each iteration is obtained to compare the SAO with the conventional PSO algorithm, thereby evaluating the convergence behavior of the SAO. The resulting convergence curves are shown in Fig. 14. As can be seen from Fig. 14, our SAO-based algorithm converges significantly faster than the PSO: the SAO reaches the global optimum at the 19th iteration, whereas the PSO does not find the optimum until the 86th iteration. These results indicate that the SAO exhibits clearly superior convergence performance compared with the commonly used PSO algorithm.

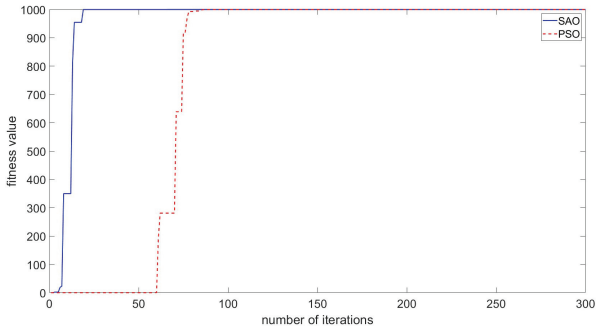

Fig. 14. Convergence performance comparison of SAO and PSO algorithms.

VI. CONCLUSION

We investigated the prediction of SE for the stacked chassis in this paper. An optimization problem model for the stacked chassis is formulated and the SAO-based solver is developed. The proposed approach balances exploration and exploitation, mitigates premature convergence, and better avoids local optima in complex search spaces, thereby improving equivalent-modeling prediction accuracy while substantially reducing computational cost. It can predict the SE of stacked chassis in complex environment, and yield SE prediction curves at multiple interior locations across frequencies. These results provide guidance for internal wiring and the placement of sensitive components.

REFERENCES

[1] J. E. Bridges, "Proposed recommended practices for the measurement of shielding effectiveness of high-performance shielding enclosures," *IEEE Transactions on Electromagnetic Compatibility*, vol. EMC-10, pp. 82–94, 1968.

[2] B. Jinjun, Z. Gang, and W. Lixin, "EMC simulation based on FDTD analysis considering uncertain inputs with arbitrary probability density," *IEEE Transactions on Electromagnetic Compatibility*, vol. 34, pp. 82–94, 2019.

[3] A. Taflove, "Review of the formulation and applications of the finite-difference time-domain method for numerical modeling of electromagnetic wave interactions with arbitrary structures," *Wave Motion*, vol. 10, pp. 547–582, 1988.

[4] N. V. Kantartzis, "Multi-frequency higher-order Adi-FDTD solvers for signal integrity predictions and interference modeling in general

EMC applications," *Wave Motion*, vol. 25, pp. 1046–1060, 2010.

[5] L. Avazpour, S. W. Belling, M. L. King, S. Schmidt, and I. Knezevic, "Field–potential finite-difference time-domain (FiPo FDTD) technique for computational electromagnetics," *Journal of Computational Electronics*, vol. 24, p. 119, 2025.

[6] J. Bai, G. Zhang, L. Wang, and T. Wang, "Uncertainty analysis in EMC simulation based on improved method of moments," *Applied Computational Electromagnetics Society (ACES) Journal*, vol. 31, pp. 66–71, 2016.

[7] D. Omri, M. Aidi, and T. Aguili, "A comparison of three temporal basis functions for the time-domain method of moments (TD-MoM)," *Journal of Computational Electronics*, vol. 19, pp. 750–758, 2020.

[8] J. Bai, B. Hu, H. Cao, and J. Zhou, "Uncertainty analysis method for EMC simulation based on the complex number method of moments," *Progress in Electromagnetics Research Letters*, vol. 121, pp. 7–12, 2024.

[9] W. J. R. Hoefer, "The transmission-line matrix method-theory and applications," *IEEE Transactions on Microwave Theory and Techniques*, vol. 33, pp. 7–12, 1985.

[10] P. Russer and J. A. Russer, "Application of the transmission line matrix (TLM) method to EMC problems," in *2012 Asia-Pacific Symposium on Electromagnetic Compatibility*, pp. 141–144, 2012.

[11] N. S. Dončov, B. Milovanovic, and Z. Stanković, "Extension of compact TLM airvent model on rectangular and hexagonal apertures," *Applied Computational Electromagnetics Society (ACES) Journal*, vol. 26, pp. 64–72, 2011.

[12] Z. Kubik and J. Skala, "Shielding effectiveness simulation of small perforated shielding enclosures using FEM," *Energies*, vol. 9, p. 129, 2016.

[13] F. Chao and S. Zhongxiang, "A hybrid FD-MoM technique for predicting shielding effectiveness of metallic enclosures with apertures," *IEEE Transactions on Electromagnetic Compatibility*, vol. 47, pp. 456–462, 2005.

[14] M. Ranasinghe and V. Dinavahi, "Massively parallel hybrid TLM-PEEC solver and model order reduction for 3D nonlinear electromagnetic transient analysis," *IEEE Transactions on Electromagnetic Compatibility*, vol. 67, pp. 667–678, 2025.

[15] X. Q. Zheng, Z. Y. Huang, Y. Q. Liang, and H. Y. Duan, "Rapid calculation method of ultrathin dielectric layer shielding efficiency based on CNTD-FDTD method," in *2024 IEEE International Conference on Computational Electromagnetics (ICCEM)*, pp. 1–3, Apr. 2024.

[16] R. Qi, Y. Ding, Y. Du, H. Cai, L. Jia, and X. Xiao, "Hybrid TDPEEC/FDTD method for lightning transient analysis in solar panels," *IEEJ Transactions on Electrical Electronic Engineering*, vol. 17, p. 1, 2022.

[17] X. He, M. Chen, and B. Wei, "A hybrid algorithm of 3-D explicit unconditionally stable FDTD and traditional FDTD methods," *IEEE Antennas and Wireless Propagation Letters*, vol. 23, pp. 1–5, 2024.

[18] A. A. Lodhi, Y. Zhu, and O. Gassab, "Improved hybrid FDTD method for complex thin wire structures inside enclosure for accurate differential-mode prediction," *IEEE Transactions on Electromagnetic Compatibility*, vol. 67, pp. 1–13, 2025.

[19] M. P. Robinson, "Analytical formulation for the shielding effectiveness of enclosures with apertures," *IEEE Transactions on Electromagnetic Compatibility*, vol. 40, pp. 240–248, 1998.

[20] A. Rabat, P. Bonnet, K. E. K. Drissi, and S. Girard, "Analytical formulation for shielding effectiveness of a lossy enclosure containing apertures," *IEEE Transactions on Electromagnetic Compatibility*, vol. 60, pp. 1384–1392, 2018.

[21] A. A. Ivanov, A. V. Demakov, M. E. Komnatnov, and T. R. Gazizov, "Semi-analytical approach for calculating shielding effectiveness of an enclosure with a filled aperture," *Electrica*, vol. 22, 2022.

[22] A. A. Ivanov, M. E. Komnatnov, and T. R. Gazizov, "Analytical model for evaluating shielding effectiveness of an enclosure populated with conducting plates," *IEEE Transactions on Electromagnetic Compatibility*, vol. 62, pp. 2307–2310, 2020.

[23] A. Rabat, P. Bonnet, K. E. K. Drissi, and S. Girard, "An analytical evaluation of the shielding effectiveness of enclosures containing complex apertures," *IEEE Access*, vol. 9, pp. 147191–147200, 2021.

[24] J.-C. Zhou and X.-T. Wang, "An efficient method for predicting the shielding effectiveness of an apertured enclosure with an interior enclosure based on electromagnetic topology," *Applied Computational Electromagnetics Society (ACES) Journal*, vol. 37, pp. 1014–1020, 2022.

[25] CST Studio Suite [Online]. Available: http://www.cst.com

[26] Q. Li, S.-Y. Liu, and X.-S. Yang, "Influence of initialization on the performance of metaheuristic optimizers," *Applied Soft Computing*, vol. 91, p. 106193, 2020.

[27] H. Su, D. Zhao, A. A. Heidari, L. Liu, X. Zhang, M. Mafarja, and H. Chen, "RIME: A physics-based optimization," *Neurocomputing*, vol. 532, pp. 183–214, 2023.

[28] L. Deng and S. Liu, "Snow ablation optimizer: A novel metaheuristic technique for numerical optimization and engineering design," *Expert Systems With Applications,* vol. 225, p. 120069, 2023.

[29] W. Chen, Z. Wang, Y. Yang, S. Wang, H. Wang, and Y. Ayaz, "Research on path planning of mobile robots based on snow ablation optimizer," in *2024 43rd Chinese Control Conference (CCC)*, Kunming, China, pp. 4351–4356, 2024.

Sen Wang received the B.S. degree in Electronic Information Engineering from Tianjin University of Technology, Tianjin, China, in 2023. He is currently pursuing the M.S. degree in New-Generation Electronic Information Technology with Jilin University, Changchun, China. His current research interests include simulation analysis of electromagnetic environmental effects, electromagnetic compatibility, and electromagnetic protection for electronic equipment.

Hong Jiang (corresponding author) received the B.S. degree in Radio Technology from Tianjin University, Tianjin, China, in 1989, the M.S. degree in Communication and Electronic System from Jilin University of Technology, Changchun, China, in 1996, and the Ph.D. degree in Communication and Information System from Jilin University, Changchun, China, in 2005. From 2010 to 2011, she worked as a visiting research fellow at McMaster University, Canada. Currently, she is a professor at the College of Communication Engineering, Jilin University, China. Her research fields focus on electromagnetic compatibility and signal processing for radar and wireless communications.

Xinbo Li received the B.S. degree in Automation from Jilin University, Changchun, China, in 2002 and the M.S. and Ph.D. degrees in Control Theory and Control Engineering from Jilin University, Changchun, China, in 2005 and 2009, respectively. Currently, he is a professor at the College of Communication Engineering, Jilin University, China. His research interests focus on electromagnetic protection, electromagnetic environment perception, intelligent signal recognition and processing.

Xiaohui Wang received the M.S. degree in China. He is currently a researcher in Research and Development Center, China Academy of Launch Vehicle Technology, Beijing, China. He is engaged in long-term research on advanced integrated electronic optimization design.

Fengtao Xu received the M.S. degree in mechanics from Xi'an Jiaotong University, China. He is currently a senior engineer at the Research and Development Center, China Academy of Launch Vehicle Technology, Beijing, China. He is primarily engaged in integrated design-related fields such as overall design of electromechanical systems, electrical design, and electromagnetic design.

Optimization Design of Active and Passive Hybrid Shielding for Electric Vehicle's Wireless Power Transfer System

Yangyun Wu[1], Tianhao Wang[1], Quanyi Yu[1], Gang Lv[2], Yaodan Chi[3], and Shanshan Guan[1]

[1]College of Instrumentation and Electrical Engineering
Jilin University, Changchun 130021, China
wuyy21@mails.jlu.edu.cn, wangtianhao@jlu.edu.cn,
qyyu20@mails.jlu.edu.cn, guanshanshan@jlu.edu.cn

[2]EMC Department National Automotive Quality Supervision and Inspection Center
Changchun 130011, China
lvgang@catc.com.cn

[3]Jilin Provincial Key Laboratory of Architectural Electricity and Comprehensive Energy Saving
Jilin Jianzhu University, Changchun 130118, China
chiyaodan@jlju.edu.cn

Abstract – Targeting the issues of electromagnetic exposure safety in the application of an electric vehicle's wireless power transmission (WPT), this study proposes a surrounding active shield coils structure, laying on the four sides of the WPT system, which effectively reduces the lateral magnetic leakage field while supplementing the magnetic field inside the transmission channel. At the same time, this study proposes a ferrite groove structure as the passive shielding, achieving reduction of the vertical magnetic leakage field. On this basis, the paper takes system transfer efficiency and surrounding magnetic leakage field density as the optimization objectives, combining the extreme learning machine (ELM) surrogate model with multi-objective optimization algorithm for hybrid shielding structural design, realizing the further improvement of power transfer and electromagnetic shielding capability. A numerical simulation test is carried out and the results show that the proposed shielding scheme can ensure the system transfer efficiency, meanwhile reducing the magnetic leakage from all directions, and providing effective electromagnetic exposure safety protection for the human body.

Index Terms – Electromagnetic exposure safety, extreme learning machine, hybrid shielding structural design, multi-objective optimization algorithm, wireless power transmission.

I. INTRODUCTION

Developing the electric vehicles industry is an essential strategy for protecting the ecological environment as well as saving fossil energy. In recent years, charging technology has been research hotspot in the field of electric vehicles. With the development of electric vehicles gradually moving towards intelligent networking, the commonly used wired charging station is hardly able to meet the needs of intelligent driving in the future [1, 2]. In contrast, wireless power transmission (WPT) brings convenience and features strong environmental adaptability in its practical application, which makes it a highly suitable charging form for intelligent driving [3, 4]. However, electromagnetic exposure safety issues of the WPT process are gradually emerging as the technology enters the market, which becomes the focus of attention for researchers [5]. To alleviate the electromagnetic fields (EMFs) caused by WPT systems, most existing methods focus on the two categories of active and passive shielding.

Regarding active shielding methods, Cruciani et al. proposed a method to identify the suitable excitation of active coils. The proposed method permits the mitigation of the magnetic leakage in a specific point, the shielding effectiveness (SE) can achieve 20 dB on the considered area with minor losses of efficiency [6]. Cruciani et al. proposed a shielding structure composed of multiple active coils to mitigate the magnetic leakage field of WPT systems, then used a gradient descent algorithm to obtain the most suitable excitation for the active coils. Thus, the magnetic leakage field in the protection area was reduced by nearly half [7]. Mi et al. proposed a double-loop active shield coil directly connected in series with the primary side coil, which reduced the leakage level of the WPT system while eliminating

Submitted On: February 19, 2025
Accepted On: January 14, 2026

https://doi.org/10.13052/2026.ACES.J.410110

the additional coupling between the shield coil and secondary side coil [8]. Campi et al. proposed a novel design of active coil to reduce the magnetic leakage field generated by the WPT system, which consists of two separate shield coils with independent source. The shielding method was proved to have a minor impact on system transmission performance [9]. Li et al. proposed a double-coil dynamic shielding scheme based on active shielding technology, which adopts two half-loop structures set on the outside of the transmitting side coil, achieving dynamic shielding of EMF leakage while ensuring high transmission efficiency [10].

Passive shielding achieves a reduction of magnetic leakage field mainly by using high permeability ferromagnetic materials or high conductivity metal materials. The method is also widely used in electromagnetic exposure safety protection of WPT systems. Budhia et al. proposed a ferrite shielding composite structure consisting of six parts: plastic cover plate, coupling coil, frame, ferrite magnetic core, aluminum ring, and aluminum backplate, which features satisfactory performance of magnetic leakage shielding [11]. Zhu et al. proposed a shielding method that used aluminum strips applied on the outer side of the transmitting side coils, which reduces the negative impact of eddy current losses on system transmission performance [12]. Mohammad et al. discovered that ferromagnetic materials can effectively suppress the electromagnetic exposure of Double D coil based WPT systems. The experiment result shows that the peripheral magnetic leakage field can be effectively suppressed [13]. Gu et al. proposed combining soft magnetic materials and ferrite as the passive shielding structure of WPT, while retaining the electromagnetic shielding performance. The mechanical stability and thermal conductivity of the shielding structure also improved [14].

Let us now turn to research on hybrid active-passive shielding for WPT systems. Dai et al. proposed the active shielding structure of reverse-wound magnetic shielding coils in series with the main coil, as well as the passive shielding structure based on ferrite, which improved magnetic field distribution around the WPT system [15]. Li et al. proposed a composite electromagnetic shielding structure for WPT, which is composed of Tian-font magnetic shielding and anti-series active coils. The proposed hybrid structure minimizes material use while maintaining safe magnetic leakage levels [16]. Zhang et al. proposed a hybrid shielding system composed of single-source topology-integrated active suppression coils and adjustable ferrites, which generated canceling flux opposite to leakage flux as well as compensation flux consistent with the main flux [17]. Li et al. proposed a hybrid shielding structure consisting of a surrounding coil with a ring-shaped aluminum plate, effectively weakening the magnetic leakage in the edge position of the WPT system [18].

In order to further enhance the overall performance of the WPT system, many scholars conducted research on the application of optimization algorithms for the design of structure of WPT systems. Zhao et al. used a genetic algorithm to optimize metal aluminum shielding structural parameters, reducing the energy losses produced in the aluminum shielding plate of the WPT system [19]. Luo et al. proposed a multi-objective optimization method of a primary side ferrite layer for a Double D coil based WPT system, using the NSGA-II algorithm to optimize the geometrical parameters of ferrite, realizing the improvement of system coupling coefficient and the reduction of stray magnetic leakage fields [20]. Pei et al. proposed a multi-objective optimization method based on particle swarms coupled with the polynomial chaos expansion model to determine the optimal design parameters in the practical shielding design, which increases the system coupling coefficient while also reducing the shielding costs [21].

Compared to the existing literatures, this study effectively combines both active and passive shielding methods, realizing the reduction of the magnetic leakage field in the full place as well as transmission efficiency of the WPT system. This paper skillfully combines extreme learning machine (ELM) neural networks with multi-objective optimization algorithms to improving the overall performance of the WPT system. ELM is used to quickly construct a surrogate model of the optimization variables and objective functions in the shielding structure, and the multi-objective algorithm is used to search for the optimal solution of shielding structural parameters. This paper considers system transfer efficiency as well as the surrounding magnetic leakage flux density as the optimization objective, ultimately improving the overall performance of the WPT system.

The contents of the paper can be expressed as follows. Section II introduces the spatial magnetic field distribution of the studied coil type (circular coil), giving the mathematical model of magnetic induction intensity. Section III introduces the design idea of hybrid shielding structure and introduces the shielding principle of the proposed active and passive method. Section IV introduces the proposed optimization method, discussing the overall optimization design process of shielding structure. Section V is the specific numerical simulation part, verifying the feasibility of the proposed scheme. Section VI summarizes the research work of this paper.

II. ANALYSIS OF SPATIAL MAGNETIC FIELD OF WPT

The magnetic energy coil group is the main device for transmitting electricity in the WPT system, which

relies on a spatial alternating magnetic field to achieve WPT. Thus, the magnetic energy coil group determines magnetic field distribution in the transmitting channel as well as magnetic leakage field distribution in the surrounding environment to a large extent [22, 23].

The coil groups applied in the WPT system are usually composed of multiple independently insulated twisted wires wound together, which can be divided into the two categories of unipolar coil and bipolar coil according to the mode of magnetic field distribution [24]. The unipolar coil features only single magnetic pole direction, generating the magnetic flux component vertical to the plane of the coil. This type of coil usually features a relatively simple structure, such as circular and rectangular coils [25]. Different from a unipolar coil, the bipolar coil features two directions of magnetic pole, which produces two magnetic flux components that are respectively parallel and vertical to the plane of the coil. This type of coil usually features a complex structure, such as Double D coil or Bipolar coil [26]. The magnetic flux lines of the two types of coil structure are shown as Fig. 1.

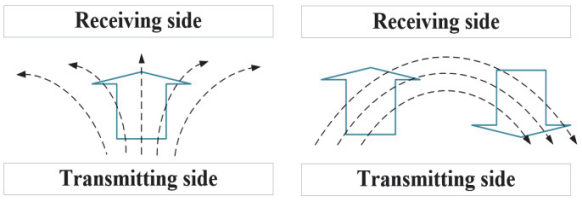

(a) (b)

Fig. 1. Magnetic flux distributions of different types of coils. (a) Unipolar coil and (b) bipolar coil.

This paper takes the circular coil as the research object. In the Cartesian coordinate system, the total magnetic field density of a certain spatial position can be composed of magnetic flux components in the x, y, z directions. As shown in Fig. 2, assuming that there exists a circular line current I on the plane of XOY, whose radius is R, $P(r, \theta, \varphi)$ is the spherical coordinate value of any point in the spatial domain.

Taking the center of the circular line current as coordinate origin, the magnetic vector potential of the circular line current at any spatial point can be expressed as:

$$A(r,\theta,\varphi) = \frac{\mu_0 \cdot I}{4\pi} \oint \frac{\mathrm{d}l}{|r-r'|}, \tag{1}$$

where μ_0 represents vacuum permeability $4\pi \times 10^{-7}$ H/m. dl represents the differential line element of the current element $I \cdot \mathrm{d}l$, whose spherical coordinate value can be expressed as $(r', \varphi', 0)$. According to the relationship between magnetic flux density and magnetic vector potential, the component of the magnetic

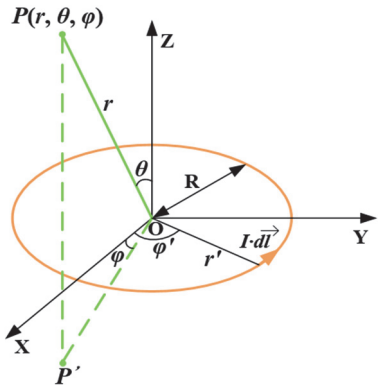

Fig. 2. Basic model of circular line current.

field density of a circular coil at any point in the Cartesian coordinate system can be calculated as [27]:

$$\begin{cases} B_x = \dfrac{\mu_0 \cdot I}{2\pi} \cdot \dfrac{z}{p\sqrt{[(p+R)^2+z^2]}} \\ \quad \cdot \left[-K + \dfrac{R^2+p^2+z^2}{(p-R)^2+z^2} \cdot E\right] \cdot \cos\varphi, \\ B_y = \dfrac{\mu_0 \cdot I}{2\pi} \cdot \dfrac{z}{p\sqrt{[(p+R)^2+z^2]}} \\ \quad \cdot \left[-K + \dfrac{p^2+z^2+R^2}{(p-R)^2+z^2} \cdot E\right] \cdot \sin\varphi, \\ B_z = \dfrac{\mu_0 \cdot I}{2\pi} \cdot \dfrac{1}{\sqrt{[(p+R)^2+z^2]}} \\ \quad \cdot \left[K + \dfrac{R^2-p^2-z^2}{(p-R)^2+z^2} \cdot E\right]. \end{cases} \tag{2}$$

In the above equation, p, K, E, and k can be further expressed as:

$$p = \sqrt{x^2+y^2+z^2}, \tag{3}$$

$$K = \int_0^{\frac{\pi}{2}} \frac{\mathrm{d}\varphi}{\sqrt{1-(k\cdot\sin\varphi)^2}}, \tag{4}$$

$$E = \int_0^{\frac{\pi}{2}} \sqrt{1-(k\cdot\sin\varphi)^2}\,\mathrm{d}\varphi, \tag{5}$$

$$k = \sqrt{\frac{4rR\sin\theta}{r^2+R^2+2rR\sin\theta}}. \tag{6}$$

If we assume that the turns of the transmitting and receiving side coil groups are respectively n and m, the magnetic field generated by each single turn coil at the spatial point P can be expressed as $B_{t,1}, B_{t,2}, \ldots, B_{t,n}$

as well as $B_{r,1}, B_{r,2}, \ldots, B_{r,m}$. The magnetic flux density generated by a single-turn coil is the basis for calculating the total field strength:

$$B_{total} = \sum_{i=1}^{n} B_i + \sum_{j=1}^{m} B_j. \tag{7}$$

III. PROPOSED HYBRID SHIELDING FOR MAGNETIC LEAKAGE FIELD MITIGATION

This section proposes a hybrid electromagnetic shielding structure that combines active and passive shielding methods, cutting off the EMF leakage path of the WPT system, while improving the magnetic field distribution in the system transmission region. As shown in Fig. 3, the purpose of the proposed hybrid shielding structure in this paper is to reduce the magnetic flux in regions ② and ③, while maintaining the magnetic flux in region ①.

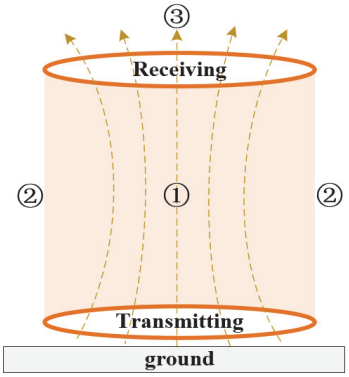

Fig. 3. Electromagnetic field distribution diagram of WPT.

A. Magnetic guidance of lightweight ferrite

Passive shielding achieves constraint of the magnetic field mainly through using a ferromagnetic or metal material. Ferromagnetic materials can construct a low magnetic resistance path for magnetic flux, to guide the magnetic flux lines to converge towards the transmission channel [28], i.e. region ① in Fig. 3. Calculation of a magnetic path can be solved using Ohm's law of magnetic paths [29]:

$$\Phi = \frac{F}{R_m}, \tag{8}$$

where Φ is magnetic flux volume, F is magnetomotive force, and R_m is resistance of the magnetic path. If we assume that the magnetic circuit interface is uniform, then R_m can be expressed as:

$$R_m = \frac{l}{\mu \cdot S}, \tag{9}$$

where μ is magnetic permeability, l is length of magnetic circuit, and S is cross-section area of the magnetic circuit. From Equation (9), the higher the magnetic permeability, the lower the magnetic resistance. The magnetic flux would mainly pass through the path with lower resistance. Thus, priority should be given to using high magnetic permeability materials for shielding. At present, ferrite is widely used for passive shielding of WPT systems, due to its high permeability, high saturation magnetic density, and high resistivity [30].

This paper suggests a novel passive shielding structure based on ferrite materials. The central part is hollowed out to form the groove architecture. The WPT coil groups are embedded inside the ferrite magnetic core in the actual application. The coil groups are enclosed by the ferrite ring, shown in Fig. 4. Compared with an entire ferrite disk, the new structure saves on materials, effectively reducing costs.

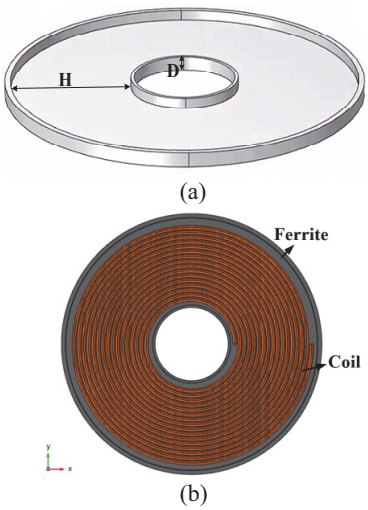

Fig. 4. Proposed ferrite groove structure. (a) Basic appearance of the ferrite groove and (b) assembly of the ferrite groove and WPT coils.

In Fig. 4, H is width of the ferrite groove, D is depth of ferrite groove. The special structure facilitates the practical placement of the coil groups. The paper applies the ferrite groove structure to the receiving side of the WPT system, which can concentrate the magnetic in region ① and reduce the magnetic leakage in region ③.

B. Magnetic flux interaction of the shield coil

The principle of an active shielding method is to use auxiliary coils to generate a reverse magnetic field, thereby offsetting magnetic leakage field at the target position [7]. A traditional active shielding system usually consists of a main coil of WPT and a shield coil, where the current direction of the shield coil is opposite

to that of the main coil, thereby forming a magnetic field direction opposite to that of the main coil [31]. Though the magnetic leakage field in the protective area is weakened, the direction of shielding current remains constant, which reduces the transmission efficiency of the WPT system [32, 33].

This study proposes laying the four shield coils on the transmitting side of the WPT system, which all have independent power supply. A top-down perspective is shown in Fig. 5.

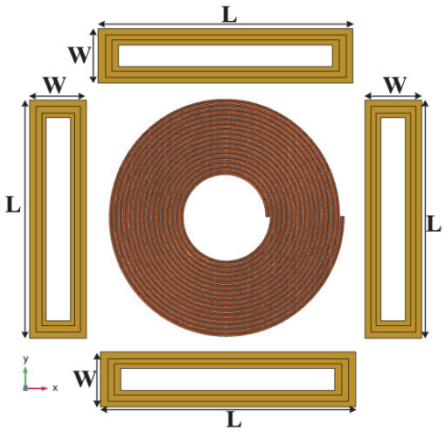

Fig. 5. Diagram of the surrounding shield coil.

Here, L and W represent the length and width of the shield coil. By adjusting the power supply of the shield coil, the current of the shield coil is in phase opposition to the current of the WPT transmitting main coil. Adjacent to the main coil, the shield coil can generate a magnetic field in phase with the main coil. Outside the main coil, the shield coil can generate a magnetic field in phase opposition to the main coil.

Taking a cross-section of the WPT system as the observation plane, Fig. 6 represents the magnetic superposition after adding the shield coils. Figure 6 divides the overall area into energy transmission area and magnetic leakage protection area. The lines in Fig. 6 represent the distribution of magnetic flux lines produced by the main coils and the shield coils.

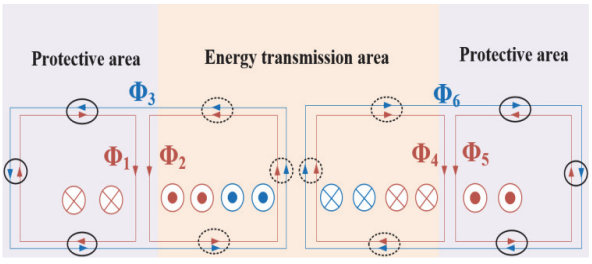

Fig. 6. Cross-section diagram of shield coil and main coil.

Assuming that the magnetic flux components generated by the WPT coil are Φ_3, Φ_6, the magnetic flux components generated by the shield coil on two sides are $\Phi_1, \Phi_2, \Phi_4, \Phi_5$. It can be seen that the magnetic flux caused by the shield and WPT coil are mutually cancelled out in the outer region, which can effectively weaken the magnetic leakage, while the magnetic flux caused by shield and WPT coil are mutually superimposed in the middle region, which can improve the transmission performance of the WPT system. Magnetic flux in the different regions can be expressed as:

$$\begin{cases} \Phi_{in} = \Phi_3 + \Phi_2 \\ \Phi_{in} = \Phi_6 + \Phi_4 \\ \Phi_{out} = \Phi_3 - \Phi_1 \\ \Phi_{out} = \Phi_6 - \Phi_5 \end{cases}, \tag{10}$$

where Φ_{in} and Φ_{out} represent the total magnetic flux in the middle and outer regions. Combining the initial design idea of electromagnetic shielding structures mentioned in section III, it can be theoretically concluded that the active coil structure can reduce the magnetic flux in region ② while supplementing the magnetic flux in region ①, achieving the dual effect of electromagnetic shielding and transfer performance.

The passive and active shielding structures in this study are made of Mn-Zn ferrite and copper, respectively. The general price range of Mn-Zn ferrite is US$10–30 per kilogram. Due to the lightweight nature of ferrites and the groove shape designed in this study saving on material usage, the cost is not high. The cost of active shielding depends on the volume of copper material, which can be reduced by reducing the number of turns and reducing the wire diameter of the shield coils; the cost range for cheaper copper material is generally US$10–20.

IV. MULTI OBJECTIVE OPTIMIZATION SURROGATE MODEL FOR SHIELD STRUCTURE

A. Extreme learning surrogate model

In the numerical simulation model of electromagnetic shielding structures there exists a stronger nonlinearity relationship between the shielding structural parameters and system optimization objectives [34]. To build the mapping relationship between the two for rapid optimization, this study establishes a surrogate model based on ELM, whose input variables are the optimization parameters of the electromagnetic shielding structure. The output variables are the objectives that need to be optimized including system transfer efficiency as well as magnetic leakage flux density. As shown in Fig. 7, this paper sets two observation planes of magnetic leakage,

which are at the side and back of the WPT system, namely regions ② and ③ in Fig. 3.

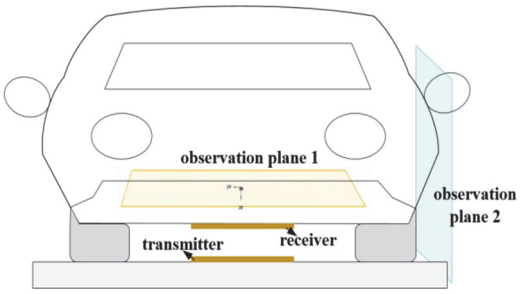

Fig. 7. Target plane of magnetic leakage around the vehicle.

Different from the back propagation neural network, the weight values on the hidden layer of ELM do not need to be adjusted during the training process, featuring high solution efficiency and satisfactory performance of generalization [35]. The principle of ELM can be described as follows. For each input sample x_i, the activation values of the neurons on the hidden layer can be expressed as:

$$h_{il} = g(a_l^T x_i + b_l), \tag{11}$$

where $g(\cdot)$ represents the activation function, a_l represents the input weight vector of the l-th neuron, and b_l represents the corresponding bias term, which are all randomly initialized and remaining constant during the training process of the model. The main task of ELM is to calculate the optimal weight values from hidden layer to output layer. Output can be expressed as a form of linear combination:

$$\beta = [\beta_1, \beta_2, \ldots, \beta_L], \tag{12}$$

$$\gamma_i = \sum_{l=1}^{L} \beta_l h_{il} = \beta^T h_i. \tag{13}$$

To minimize the overall prediction error of the samples, the optimal weight matrix β can be derived as:

$$\beta_{opt} = (H^T H)^{-1} H^T T, \tag{14}$$

where $H = [h_1, h_2, \ldots, h_N]^T$ represents the matrix of hidden layer activation values and $T = [t_1, t_2, \ldots, t_N]^T$ represents the target output matrix. In the ELM surrogate model established in this paper, the length of the shield coil L, the width of the shield coil W, the ring width of the ferrite groove H, and the depth of the ferrite groove D are taken as the input variables of the neural network model. The output variables include system transmission efficiency as well as maximum leakage flux density on observation planes 1 and 2. Thus, the number of nodes of the input and output layers of the neural network are set as 4 and 3. The modeling of ELM is the first step in the optimization design process of the electromagnetic shielding structure, which lays the foundation for the subsequent use of the optimization algorithm.

B. Multi-objective optimization process

As mentioned in the previous section, due to the multiple optimization objectives analyzed, this paper uses the multi-objective algorithm to solve the optimization design issue of the electromagnetic shielding structure.

The multi-objective particle swarm optimization (MOPSO) is an evolutionary algorithm improved on the basis of ordinary PSO, featuring better global search and convergence performance, which has been widely used in the solution of complex engineering problems. In this study, MOPSO is used for the optimization design of active and passive shielding structures. The basic idea of MOPSO is to divide the solution space into multiple sub-regions and search within each sub-region. Different from traditional PSO, MOPSO uses the relationship of Pareto dominance to evaluate the fitness of a particle [36, 37]. One particle is defined as dominating another particle if it outperforms the other particle on all objective functions. Only non-dominated particles can enter into the Pareto front. The solution process of MOPSO can be described as follows:

(1) Randomly initialize the position of the individual particles.
(2) Calculate the fitness of each individual particle and determine the non-dominated individuals according to the relationship of Pareto dominance. For a certain individual particle, the dominated set indicates the set of particles with worst fitness, and the non-dominated set indicates the set of particles with best fitness.
(3) Update the step size and position of each individual particle. The new step size and position of each particle is calculated according to the current status, then the fitness of particles and Pareto front are updated according to the relationship of Pareto dominance. If one certain particle becomes the new Pareto optimal solution, it will be added to the Pareto front; the solutions dominated will be removed.
(4) Repeat steps (2) and (3) until termination conditions are reached.

In summary, the steps of the optimization method can be described as follows. First, the optimization variables of shielding structure as well as the system optimization objectives are sampled through numerical simulation, which are taken as the training samples for the ELM surrogate model. When the training accuracy

of the model reaches the requirements, the optimization objective value can be accurately predicted. The MOPSO algorithm is combined to search the optimal shielding structural variables under the premise of considering system transfer efficiency as well as the magnetic leakage flux density as the optimization target. We will eventually obtain the ideal optimization design parameters of the shielding structure. The overall procedure of the optimization method is depicted in Fig. 8.

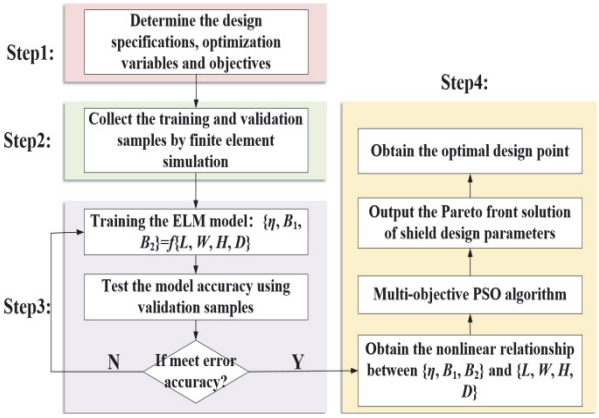

Fig. 8. Overall optimization framework of hybrid shielding structure.

V. PERFORMANCE VERIFICATION

This paper establishes the finite element method (FEM) numerical simulation model of an electric vehicle's WPT system in COMSOL software, which is shown in Fig. 9. The parameters of the vehicle's body size are as follows: length of 4.5 m, width of 2 m, height of 1.5 m, which are consistent with the volume size of common domestic vehicles on the market [38]. The material of the vehicle's body is set as aluminum, the materials of the tires and windows of the vehicle are respectively set as rubber and tempered glass, and the material of the coil groups is set as copper.

This paper establishes the human body model of adult male for analyzing the impact of the WPT system on human electromagnetic exposure safety, whose height and weight are respectively set as 1.8 m and 75 kg. The working frequency of the electric vehicle's WPT system is set as 85 kHz, corresponding to human body tissue's conductivity and relative permittivity respectively as 0.27 S/m and 5400 [39]. The electromagnetic exposure dose of human body is quantified using multi-physics field FEM, which is used to evaluate whether there exists potential threats to human health.

According to the relevant test standards specified in SAETIRJ954, the test plane of magnetic leakage field is set on the side and above the WPT system in the practical

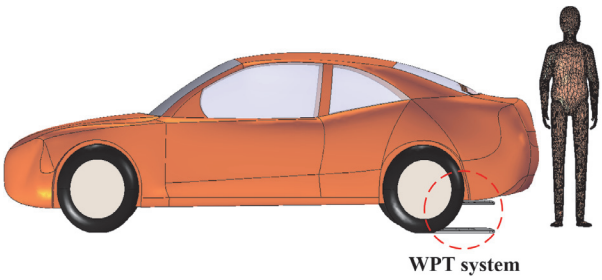

Fig. 9. Simulation model of wireless power transmission scenario of electric vehicle.

scenario, respectively as 0.8 m away from the central WPT system coupling mechanism [40], whose position is shown in Fig. 7.

To verify the electromagnetic shielding effect of the proposed active and passive shielding structure in this study, this section arbitrarily sets the initial structural design parameters of the shielding structure as shown in Table 1. It should be noted that the structural parameters in Table 1 are not the eventual optimized design results, just for verifying whether the proposed shielding structure has the effect of weakening the magnetic leakage field for the WPT system.

Table 1: Initial structural parameters of active and passive shielding

Active Shielding	L	273 mm
	W	38 mm
Passive Shielding	D	23 mm
	H	127 mm

The simulation results of the magnetic leakage field distribution are as follows. On observation plane 1, comparison results of magnetic flux with and without ferrite groove passive shielding are depicted in Fig. 10.

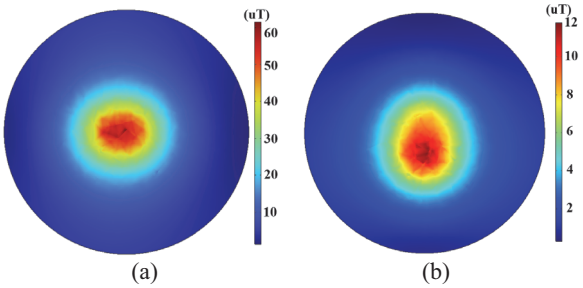

Fig. 10. Comparison of magnetic leakage flux on plane 1 (a) without ferrite and (b) with ferrite.

It can be seen that the magnetic flux density of observation plane 1 is decreased by 80%, thus the ferrite groove can weaken the leaking electromagnetic

magnetic field of the area above the WPT system. When passengers sit in the back seats of the vehicle, the electromagnetic exposure safety issues are alleviated. On the observation plane 2, the comparison results of magnetic leakage flux with and without active shielding coils are shown in Fig. 11.

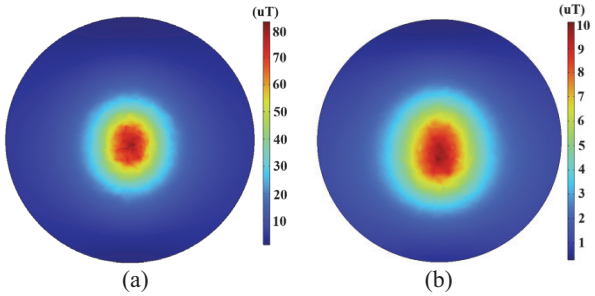

Fig. 11. Comparison of magnetic leakage flux on plane 2 (a) without shield coil and (b) with shield coil.

It can be seen that the magnetic leakage flux density of observation plane 2 is decreased by 87.5%. Thus, the shield coils can effectively suppress the lateral leaking EMF. Combined with actual scenarios, when passengers stand at the side of the vehicle, electromagnetic radiation hazards are reduced.

Considering that the varying environmental temperatures in real situations may affect the performance of the shielding structure, this paper builds a temperature coupled physical field in the numerical simulation, analyzing the varying characteristics of the maximum magnetic leakage flux density on the target plane with changes of temperature, shown in Fig. 12.

It can be concluded that the change of external temperature has minimal impact on the performance of the proposed electromagnetic shielding structures, reflecting robustness for change of environment conditions. In the analysis of shielding structure optimization design, ELM is used for predicting the optimization objectives. To verify the performance of the trained ELM model, this paper uses the test sample to obtain the output values of the model and comparing it with the FEM results, as shown in Fig. 13.

This paper takes the determination coefficient (R^2) as an evaluation indicator for ELM model performance, which can intuitively reflect regression quality and prediction error distribution of the surrogate model [41]. A total of 30 sample points were tested and it can be seen that FEM and ELM have almost the same solution accuracy for each optimization objective, demonstrating the effectiveness of the ELM prediction method.

On this basis, the MOPSO algorithm was adopted for optimization of electromagnetic shielding structural parameters. The intervals of the selected optimization

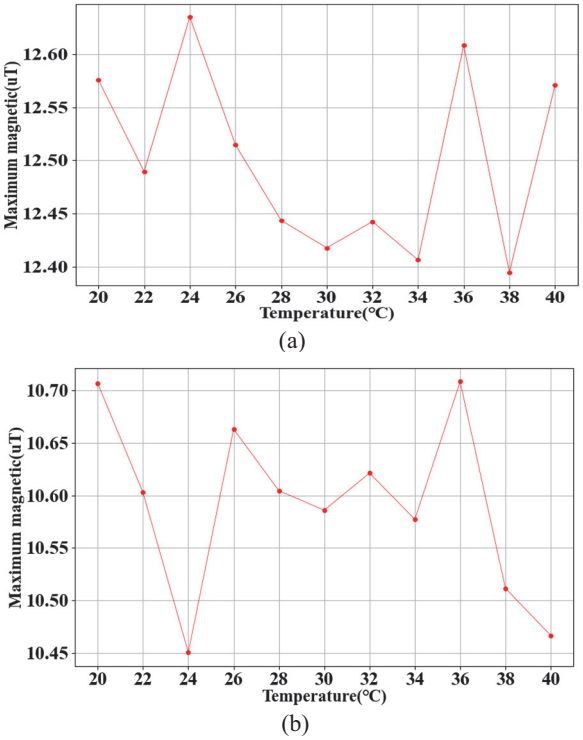

Fig. 12. Analysis of the influence of environmental temperature on electromagnetic shielding performance. (a) Varying magnetic leakage with the temperature on plane 1 and (b) varying magnetic leakage with the temperature on plane 2.

variables L, W, D, and H were set as [270 mm, 280 mm], [35 mm, 45 mm], [15 mm, 25 mm], and [120 mm, 130 mm], respectively. This paper set population size and maximum iteration times of the algorithm as 30 and 50. Implementing the optimization calculation can obtain the Pareto front solution results of each objective, shown in Fig. 14.

The optimal solution of shielding design parameters is marked by a cross in Fig. 14, which features higher transfer efficiency and lower electromagnetic exposure indicators, which is more in line with the needs of electric vehicle users. Table 2 shows the shielding structural parameter groups before and after optimization as well as the corresponding optimization target values.

In practical situations, there exist factors that could affect the electrical performance of the WPT system. Thus, it is necessary to carry out uncertainty quantification analysis for the work scenario of the WPT system [42]. Considering the spatial dislocation scenario of the coil groups of the WPT coupling mechanism, this study lists the relevant random variables as follows: transmission distance d, horizontal displacement of the coil groups Δx, Δy, and deviation angle of the coil groups α, which are shown in Table 3. U represents uniform

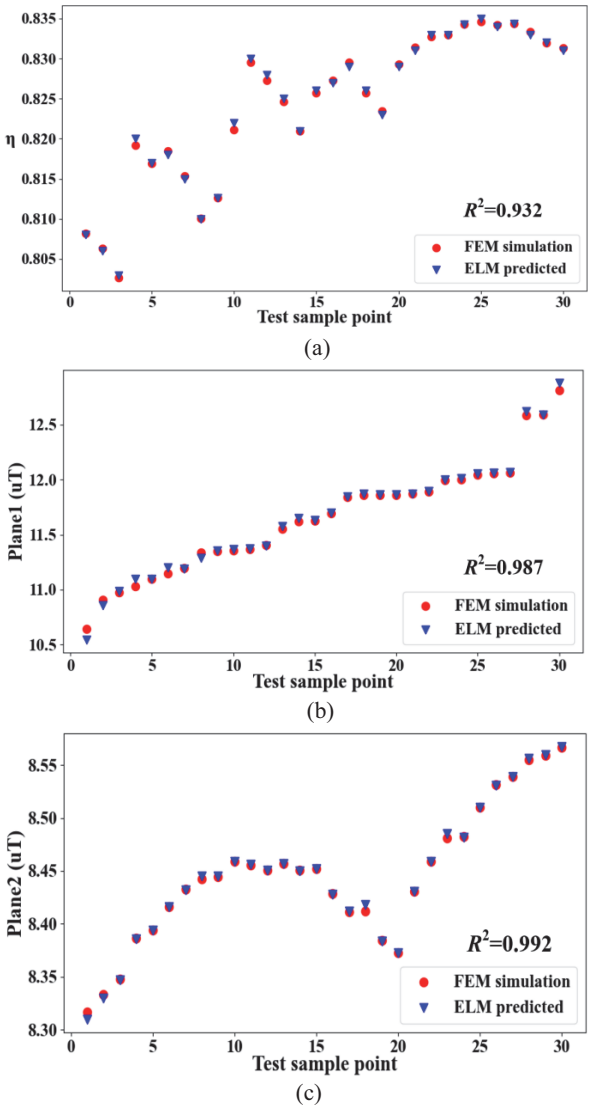

Fig. 13. Comparison of ELM prediction and FEM simulation results. (a) Comparison results of system transfer efficiency, (b) comparison results of leakage flux on plane 1, and (c) comparison results of leakage flux on plane 2.

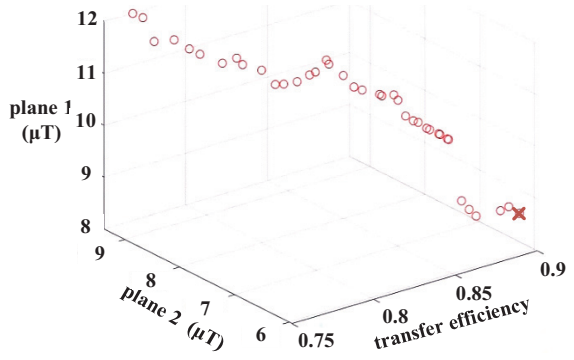

Fig. 14. Pareto front solution results of three-objective PSO.

Table 2: Comparison of various parameter indicators before and after optimization

	L (mm)	W (mm)	D (mm)	H (mm)	η	B_1 (μT)	B_2 (μT)
Original	273	38	23	127	0.79	11.3	9.7
Optimized	275	36	19	124	0.91	7.5	6.2

distribution, the Latin hypercube method is used for sampling the uncertain variables in this study, and the comparison results of various optimization objective's probability distribution before and after optimization are shown in Fig. 15.

Table 3: Uncertain variables considered in the practical application of the WPT system

Variables	Distribution Range	Unit
d	U (0.19, 0.21)	m
Δx	U (0, 0.02)	m
Δy	U (0, 0.02)	m
α	U (0, 90)	°

It can be concluded that under the interference of external uncertain factors, the transfer efficiency of the WPT system is more likely to be at a higher level after optimization. Meanwhile the risk of electromagnetic exposure is also decreased. Average transfer efficiency before and after optimization is 0.78 and 0.93, respectively, which is enhanced by 19.2%. Maximum magnetic leakage field density on observation plane 1 is 11.37 μT and 7.66 μT, respectively, before and after optimization, which is reduced by 35.1%. Maximum magnetic leakage field density on observation plane 2 is 9.35 μT and 6.07 μT, respectively, before and after optimization, which is reduced by 32.6%. Intensity of magnetic leakage field around the vehicle body are far less than the threshold (27 μT) specified by ICNIRP guidelines, which improves the electromagnetic exposure safety protection effect.

In addition, this study takes the scene of a passenger standing near the vehicle as the research case, calculating the specific absorption ratio (SAR) value distribution of the whole human body by finite element numerical simulation Comparison results before and after optimization are depicted in Fig. 16.

SAR value can accurately reflect the electromagnetic radiation dose absorbed by unit mass of human tissue in unit time [43]. Taking SAR value as the evaluation indicator can more scientifically reflect the impact of external EMFs on human health.

From the above comparison results, it can be seen that the negative impact of a WPT system on the electromagnetic exposure safety of a human body is reduced after optimization, which features practical significance

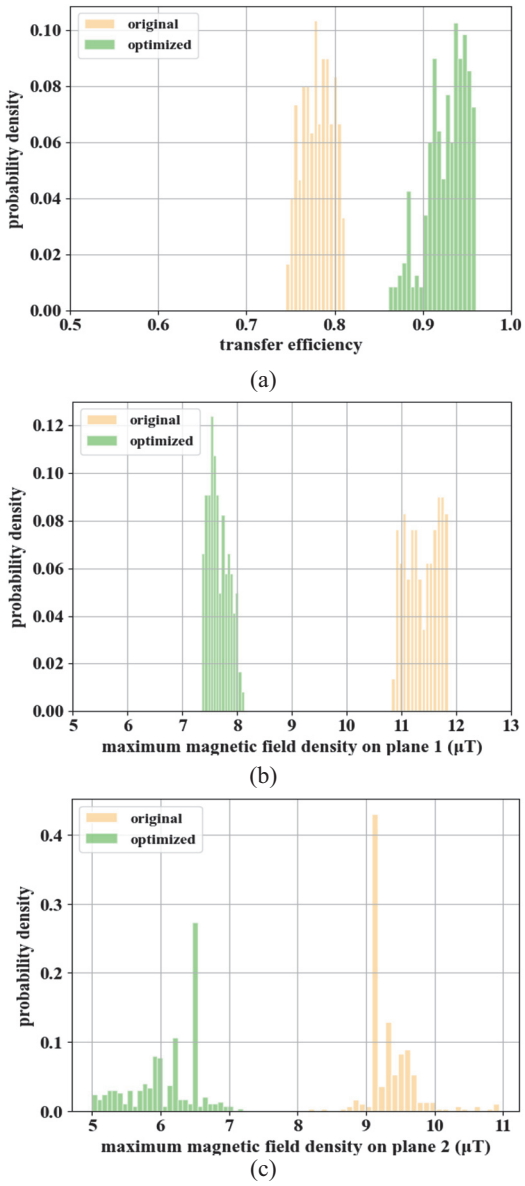

Fig. 15. Probability distribution of various optimization target values before and after optimization. (a) Comparison of probability distribution of transfer efficiency, (b) comparison of probability distribution of maximum magnetic leakage flux density on plane 1, and (c) comparison of probability distribution of maximum magnetic leakage flux density on plane 2.

for electromagnetic safety protection of drivers or passengers in daily situations.

Thus, the proposed active and passive shielding structure and its multi-objective optimization method can effectively improve the comprehensive performance of the WPT system, which provides efficient solutions for the design of shielding structures of electric vehicle's WPT systems. In the long term, improvement of

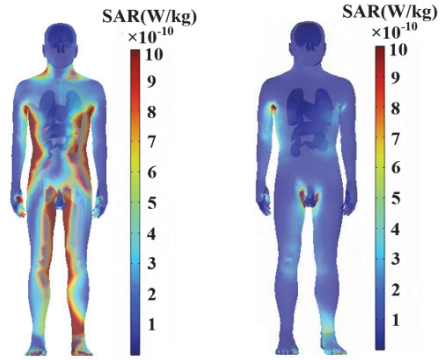

Fig. 16. SAR value distribution of human body near the WPT system (a) non-optimized and (b) optimized.

electromagnetic shielding measures can promote faster development of WPT technology of electric vehicle, which is in line with the future trend of intelligent transportation developments.

VI. CONCLUSION

This paper proposes a hybrid active and passive shielding method for mitigating the leaking magnetic field from an electric vehicle's WPT system. The ferrite grooves are covered on the back of the WPT receiving coil, realizing reduction of the vertical magnetic leakage field above the coupling mechanism. The shield coils are placed on four sides of the WPT transmitter, effectively reducing the lateral magnetic leakage field outside the coupling mechanism. Moreover, this paper establishes the optimization framework based on multi-objective particle swarm and ELM surrogate model, carrying out the optimization of hybrid shielding structural parameters, realizing the enhancement of transfer capability and electromagnetic shielding performance. In addition, combined with practical scenarios of electric vehicle charging, the paper also conducts uncertainty quantification analysis for the electrical performance of the WPT system, comparing the probability density distribution of various target values before and after optimization. Average transfer efficiency is improved by 19.2%, average value of vertical and lateral magnetic leakage field density are reduced by 35.1% and 32.6%, respectively, and the electromagnetic exposure indicator of a human body near the WPT system is significantly reduced.

ACKNOWLEDGMENT

This work was supported in part by the Jilin Scientific and Technological Development Program under Grant 20240101117JC, and by Key Laboratory for Comprehensive Energy Saving of Cold Regions

Architecture of Education, Jilin Jianzhu University under Grant JLJZHDKF202203.

REFERENCES

[1] K. Chen, J. Pan, Y. Yang, and K. Cheng, "Stability improvement and overshoot damping of SS compensated EV wireless charging systems with user-end buck converters," *IEEE Transactions on Vehicular Technology*, vol. 71, no. 8, pp. 8354–8366, Aug. 2022.

[2] O. N. Nezamuddin, C. L. Nicholas, and E. C. dos Santos, "The problem of electric vehicle charging: State-of-the-art and an innovative solution," *IEEE Transactions on Intelligent Transportation Systems*, vol. 23, no. 5, pp. 4663–4673, May 2022.

[3] J. Liu, Z. Liu, W. Chen, X. Sun, and H. Su, "An optimized coil array and passivity-based control for receiving side multilevel connected DC-DC converter of dynamic wireless charging," *IEEE Transactions on Vehicular Technology*, vol. 71, no. 4, pp. 3715–3726, Apr. 2022.

[4] Z. Luo, Y. Zhao, M. Xiong, X. Wei, and H. Dai, "A self-tuning LCC/LCC system based on switch-controlled capacitors for constant-power wireless electric vehicle charging," *IEEE Transactions on Industrial Electronics*, vol. 70, no. 1, pp. 709–720, Jan. 2023.

[5] M. Mohammad, E. T. Wodaj, S. Choi, and M. E. Elbuluk, "Modeling and design of passive shield to limit EMF emission and to minimize shield loss in unipolar wireless charging system for EV," *IEEE Transactions on Power Electronics*, vol. 34, no. 12, pp. 12235–12245, Dec. 2019.

[6] S. Cruciani, T. Campi, F. Maradei, and M. Feliziani, "Active shielding design for wireless power transfer systems," *IEEE Transactions on Electromagnetic Compatibility*, vol. 61, no. 6, pp. 1953–1960, Dec. 2019.

[7] S. Cruciani, T. Campi, F. Maradei, and M. Feliziani, "Active shielding design and optimization of a wireless power transfer (WPT) system for automotive," *Energies*, vol. 13, no. 21, pp. 1–12, Oct. 2020.

[8] M. Mi, Q. Yang, Y. Li, P. Zhang, and W. Zhang, "Multi-objective active shielding coil design for wireless electric vehicle charging system," *IEEE Transactions on Magnetics*, vol. 58, no. 2, pp. 1–5, Feb. 2022.

[9] T. Campi, S. Cruciani, F. Maradei, and M. Feliziani, "Magnetic field mitigation by multicoil active shielding in electric vehicles equipped with wireless power charging system," *IEEE Transactions on Electromagnetic Compatibility*, vol. 62, no. 4, pp. 1398–1405, Aug. 2020.

[10] Y. Li, S. Zhang, and Z. Cheng, "Double-coil dynamic shielding technology for wireless power transmission in electric vehicles," *Energies*, vol. 14, no. 17, pp. 1–20, Sep. 2021.

[11] M. Budhia, G. A. Covic, and J. T. Boys, "Design and optimization of circular magnetic structures for lumped inductive power transfer systems," *IEEE Transactions on Power Electronics*, vol. 26, no. 11, pp. 3096–3108, Nov. 2011.

[12] Q. Zhu, D. Chen, L. Wang, C. Liao, and Y. Guo, "Study on the magnetic field and shielding technique for an electric vehicle oriented wireless charging system," *Transactions of China Electrotechnical Society*, vol. 30, pp. 143–147, 2015.

[13] M. Mohammad, O. C. Onar, V. P. Galigekere, G. Su, and J. Wilkins, "Magnetic shield design for the double-D coil-based wireless charging system," *IEEE Transactions on Power Electronics*, vol. 37, no. 12, pp. 15740–15752, Dec. 2022.

[14] B. S. Gu, T. Dharmakeerthi, S. Kim, M. J. O'Sullivan, and G. A. Covic, "Optimized magnetic core layer in inductive power transfer pad for electric vehicle charging," *IEEE Transactions on Power Electronics*, vol. 38, no. 10, pp. 11964–11973, Oct. 2023.

[15] Z. Dai, X. Zhang, T. Liu, C. Pei, T. Chen, R. Dou, and J. Wang, "Magnetic coupling mechanism with omnidirectional magnetic shielding for wireless power transfer," *IEEE Transactions on Electromagnetic Compatibility*, vol. 65, no. 5, pp. 1565–1574, Oct. 2023.

[16] Z. Li, W. Zhang, Z. Gan, and B. Li, "Study on composite structure of tian-font magnetic shielding and anti-series active coils for wireless power transfer system," *CPSS Transactions on Power Electronics and Applications*, vol. 10, no. 1, pp. 97–109, Mar. 2025.

[17] X. Zhang, S. Liu, R. Dou, C. Hao, L. Zhao, P. Zhang, and Q. Yang, "A novel hybrid shielding method with single-source active topology and efficiency stability for wireless power transfer," *IEEE Transactions on Magnetics*, vol. 59, no. 11, pp. 1–6, Nov. 2023.

[18] Y. Li, K. Xie, Y. Ying, and Z. Li, "An improved hybrid shielding with LC coil for wireless power transfer system," *IEEE Transactions on Electromagnetic Compatibility*, vol. 64, no. 3, pp. 720–731, June 2022.

[19] H. Zhao, K. Liu, S. Li, F. Yang, S. Cheng, H. H. Eldeeb, J. Kang, and G. Xu, "Shielding optimization of IPT system based on genetic algorithm for efficiency promotion in EV wireless charging applications," *IEEE Transactions on Industry Applications*, vol. 58, no. 1, pp. 1190–1200, Jan. 2022.

[20] Z. Luo, X. Wei, M. G. S. Pearce, and G. A. Covic, "Multi-objective optimization of inductive power transfer double-D pads for electric vehicles," *IEEE Transactions on Power Electronics*, vol. 36, no. 5, pp. 5135–5146, May 2021.

[21] Y. Pei, L. Pichon, B. Y. Le, M. Bensetti, and P. Dessante, "Fast shielding optimization of an inductive power transfer system for electric vehicles," *IEEE Access*, vol. 10, pp. 91227–91234, Sep. 2022.

[22] J. Yi, P. Yang, Z. Li, P. Kong, and J. Li, "Mutual inductance calculation of circular coils for an arbitrary position with a finite magnetic core in wireless power transfer systems," *IEEE Transactions on Transportation Electrification*, vol. 9, no. 1, pp. 1950–1959, Mar. 2023.

[23] T. Zhang, G. Wei, R. Li, J. Feng, and C. Zhu, "Completely analytical model of inductance for circular coils with bilateral finite magnetic cores and Al plates in WPT systems," *IEEE Transactions on Transportation Electrification*, vol. 10, no. 3, pp. 6129–6140, Sep. 2024.

[24] R. Xie, R. Liu, X. Chen, X. Mao, X. Li, and Y. Zhang, "An interoperable wireless power transmitter for unipolar and bipolar receiving coils based on three-switch dual-output inverter," *IEEE Transactions on Power Electronics*, vol. 39, no. 2, pp. 1985–1989, Feb. 2024.

[25] G. Rituraj, B. K. Kushwaha, and P. Kumar, "A unipolar coil arrangement method for improving the coupling coefficient without ferrite material in wireless power transfer systems," *IEEE Transactions on Transportation Electrification*, vol. 6, no. 2, pp. 497–509, June 2020.

[26] Z. Luo, S. Nie, M. Pathmanathan, W. Han, and P. W. Lehn, "3-D analytical model of bipolar coils with multiple finite magnetic shields for wireless electric vehicle charging systems," *IEEE Transactions on Industrial Electronics*, vol. 69, no. 8, pp. 8231–8242, Aug. 2022.

[27] Z. Luo and X. Wei, "Analysis of square and circular planar spiral coils in wireless power transfer system for electric vehicles," *IEEE Transactions on Industrial Electronics*, vol. 65, no. 1, pp. 331–341, Jan. 2018.

[28] G. Rituraj and P. Kumar, "A new magnetic structure of unipolar rectangular coils in WPT systems to minimize the ferrite volume while maintaining maximum coupling," *IEEE Transactions on Circuits and Systems II: Express Briefs*, vol. 68, no. 6, pp. 2072–2076, June 2021.

[29] H. Zhuang, W. Wang, and G. Yan, "Ferrite concentrating and shielding structure design of wireless power transmitting coil for inductively coupled capsule robot," *IEEE Transactions on Biomedical Circuits and Systems*, vol. 17, no. 1, pp. 45–53, Feb. 2023.

[30] J. Shin, S. Shin, Y. Kim, S. Ahn, S. Lee, G. Jung, S. J. Jeon, and D. H. Cho, "Design and implementation of shaped magnetic-resonance-based wireless power transfer system for roadway-powered moving electric vehicles," *IEEE Transactions on Industrial Electronics*, vol. 61, no. 3, pp. 1179–1192, Mar. 2014.

[31] A. Tejeda, C. Carretero, J. T. Boys, and G. A. Covic, "Ferrite-less circular pad with controlled flux cancelation for EV wireless charging," *IEEE Transactions on Power Electronics*, vol. 32, no. 11, pp. 8349–8359, Nov. 2017.

[32] S. Y. Choi, B. W. Gu, S. W. Lee, W. Y. Lee, J. Huh, and C. T. Rim, "Generalized active EMF cancel methods for wireless electric vehicles," *IEEE Transactions on Power Electronics*, vol. 29, no. 11, pp. 5770–5783, Nov. 2014.

[33] W. Zhang, J. C. White, R. K. Malhan, and C. C. Mi, "Loosely coupled transformer coil design to minimize EMF radiation in concerned areas," *IEEE Transactions on Vehicular Technology*, vol. 65, no. 6, pp. 4779–4789, June 2016.

[34] Y. Pei, L. Pichon, B. Y. Le, M. Bensetti, and P. Dessante, "Fast shielding optimization of an inductive power transfer system for electric vehicles," *IEEE Access*, vol. 10, pp. 91227–91234, Aug. 2022.

[35] N. Liu and H. Wang, "Ensemble based extreme learning machine," *IEEE Signal Processing Letters*, vol. 17, no. 8, pp. 754–757, Aug. 2010.

[36] A. Elhossini, S. Areibi, and R. Dony, "Strength Pareto particle swarm optimization and hybrid EA-PSO for multi-objective optimization," *Evolutionary Computation*, vol. 18, no. 1, pp. 127–156, Mar. 2010.

[37] S. Wang and A. Zhou, "Leader prediction for multiobjective particle swarm optimization," *IEEE Transactions on Evolutionary Computation*, vol. 29, no. 4, pp. 1356–1370, Aug. 2025.

[38] Q. Wang, W. Li, J. Kang, and Y. Wang, "Electromagnetic safety evaluation and protection methods for a wireless charging system in an electric vehicle," *IEEE Transactions on Electromagnetic Compatibility*, vol. 61, no. 6, pp. 1913–1925, Dec. 2019.

[39] A. Arduino, O. Bottauscio, M. Chiampi, L. Giaccone, I. Liorni, N. Kuster, L. Zilberti, and M. Zucca, "Accuracy assessment of numerical dosimetry for the evaluation of human exposure to electric vehicle inductive charging systems," *IEEE Transactions on Electromagnetic Compatibility*, vol. 62, no. 5, pp. 1939–1950, Oct. 2020.

[40] Y. Li, K. Xie, Y. Ying, and Z. Li, "An improved hybrid shielding with LC coil for wireless power transfer system," *IEEE Transactions on Electromagnetic Compatibility*, vol. 64, no. 3, pp. 720–731, June 2022.

[41] Y. Wang, F. Wang, Y. Tian, A. N. Sun, and B. Liu, "Surrogate-assisted multiobjective optimization of double-D coil for inductive power transfer system with LCC-LCC compensation network," *IEEE Transactions on Industrial Electronics*, vol. 71, no. 9, pp. 10612–10624, Sep. 2024.

[42] T. Wang, Q. Yu, B. Li, G. Lv, Y. Wu, and S. Guan, "Uncertainty quantification of human

electromagnetic exposure from electric vehicle wireless power transfer system," *IEEE Transactions on Intelligent Transportation Systems*, vol. 24, no. 8, pp. 8886–8896, Aug. 2023.

[43] A. A. S. Mohamed, A. Meintz, P. Schrafel, and A. Calabro, "Testing and assessment of EMFs and touch currents from 25 kW IPT system for medium duty EVs," *IEEE Transactions on Vehicular Technology*, vol. 68, no. 8, pp. 7477–7487, Aug. 2019.

Yangyun Wu received the B.S. degree in architectural electricity and intelligence from the College of Electrical and Informational Engineering, Jilin University of Architecture and Technology, Changchun, Jilin, China, in 2018, the M.S. degree in electrical engineering from the College of Electrical and Computer Science, Jilin Jianzhu University, Changchun, Jilin, in 2021. He is currently working toward the Ph.D. degree in electrical engineering from the College of Instrumentation and Electrical Engineering, Jilin University. His research interests include the uncertainty quantification and optimal design strategy of EV's wireless power transfer system.

Tianhao Wang received the B.S. degree in electrical engineering and the Ph.D. degree in vehicle engineering from Jilin University, Changchun, Jilin, China, in 2010 and 2016, respectively. From 2016 to 2019, he was a Postdoctoral Researcher with the Department of Science and Technology of Instrument, Jilin University. He is currently an Assistant Professor with the College of Instrumentation and Electrical Engineering, Jilin University. His research interest includes numerical and experimental studies of crosstalk in complex cable bundles, with a particular emphasis on considering parameter variability using efficient statistical approaches.

Quanyi Yu received the B.S. and the M.S. degrees from the College of Communication Engineering, Jilin University, Changchun, Jilin, China, in 2016 and 2020, respectively, where he is pursuing the Ph.D. degree. His research interests include uncertainty quantification and electromagnetic compatibility of EVs.

Gang Lv received the master degree of electronic circuit and system in college of electronic science & engineering, Jilin University, Changchun, Jilin, China, in 2008. He came on board into National Automotive Quality supervision & Inspection Center (Changchun) after graduated. He is currently the head of the EMC department. He is mainly in charge of the EMC performance in vehicle type approval under the direction of Ministry of Industry and Information Technology (MIIT) and Certification and Accreditation Administration of the P.R.C. He always focuses on test methods improving and National Standards edit and amendment in EMC domain.

He has joined teams to be responsible for EMC part of "Test and Evaluation of autonomous electric vehicle" subject which is released by Ministry of Science and Technology (MOST) and "Research on real-time concurrent Simulation test technology of Multi-source Sensor information of Intelligent Networked Vehicle" which is released by Science and Technology Department of Jilin Province.

Yaodan Chi received the B.S. degree in electronic information engineering from the Jilin University of Technology, Changchun, Jilin, China, in 1998, and the master's degree in testing and measuring technology and instruments and the Ph.D. degree in science and technology of instrument from Jilin University, Changchun, Jilin, in 2004 and 2018, respectively. She is currently the Vice Director of the Jilin Provincial Key Laboratory of Architectural Electricity and Comprehensive Energy Saving. Her research interests include the uncertainty analysis approaches in electromagnetic compatibility simulation and building equipment intelligent integration technology.

Shanshan Guan received the B.S. degree in precision instruments and machinery and the Ph.D. degree in measurement technology and instruments from Jilin University, Changchun, Jilin, China, in 2008 and 2012, respectively. In 2019, she was a Visiting Scholar at the Southern University of Science and Technology, Shenzhen. She is currently an Associate Professor with the College of Instrumentation and Electrical Engineering, Jilin University. Her research interests include forward modeling and inverse algorithms of EM fields, and the development of electromagnetic instruments.